eman ta zabal zazu

Universidad del País Vasco Euskal Herriko Unibertsitatea

Non-Aqueous Li- and Na-O$_2$ Batteries: Study and Analysis of Electrochemical Processes

by

Imanol Landa Medrano

Thesis advisor:

Dr. Idoia Ruiz de Larramendi Villanueva

14th of December, 2016

Abstract

The high theoretical energy density of alkali-oxygen batteries compared to their corresponding alkali-ion batteries has attracted the interest of the research community. Lithium-oxygen (Li-O_2) batteries with non-aqueous electrolyte have been exhaustively studied due to their high energy density based on the electrochemical reduction of dioxygen (O_2) gas to lithium peroxide (Li_2O_2). Twenty years after their development, however, their transference from laboratories to commercially available systems is under debate as experimental results have not matched the expectations; advances in the electrochemical performance are usually accompanied by new drawbacks due to the tricky chemistry of these batteries.

In furtherance of overcoming the issues associated to the use of Li analogous sodium-oxygen (Na-O_2) batteries were reported five years ago. However, the alkali metal substitution was not that simple and the understanding of the cell chemistry in these batteries has lead to several discussions. Moreover, the discharge product most commonly reported, sodium superoxide (NaO_2), involves the transfer of a single electron per oxygen molecule and is therefore less attractive for practical applications than peroxide due to its lower energy density.

Despite this pessimistic scenario alkali-metal batteries continue being investigated by several research groups as the correct combination of battery components can lead to overcoming the difficulties related to each of them; the development of a successfully operating alkali-metal battery can stir up, for example, the automotive market. Consequently, the procedure followed in this thesis has been: (i) initial understanding of the system followed by (ii) strategies to improve it. This strategy has been followed for both Li- and Na-O_2 batteries.

First battery type analyzed has been Li-O_2 one. In Chapter 3 a detailed study of this system is performed based on galvanostatic cycling and electrochemical impedance

spectroscopy (EIS), both carried out at CIC Energigune, and discharge product characterization techniques such as X-ray diffraction (XRD), scanning electron microscope (SEM) and X-ray photoelectron spectroscopy (XPS). It is determined that oxygen diffusion is one of the key parameters limiting the battery performance together with side reactions. In addition, it is confirmed that EIS is a valuable technique to analyze the accumulation and elimination of the discharge products in the electrode surface.

After the analysis of the Li-O_2 system Chapter 4 is focused on the development of strategies to improve the electrochemical performance. For that aim heterogeneous catalysts, carbon-free oxygen electrodes (both at CIC Energigune) and homogeneous catalysts (at Institut de Ciencia de Materials de Barcelona, ICMAB) are explored. Although the system initially seems to benefit from the addition of heterogeneous catalysts an exhaustive analysis by EIS calls into question such improvement. In addition, attempts carried out using carbon-free electrodes are completely unsuccessful. On the other hand, the addition of iodide RM and potassium ions as discharge products stabilizing agents to the electrolyte has a positive impact in the cell performance, leading to an enhanced cycle life of the cell.

Regarding Na-O_2 batteries, study of the system has been linked to the analysis of the composition of the discharge products, their evolution after the electrochemical reduction and their stability. Chapter 5 gives a first approach to the identification of NaO_2 as the discharge product by means of Raman spectroscopy, electron paramagnetic resonance (EPR) and monitoring the gas pressure evolution during discharge. In addition, discharge product stability in the battery system is called into question based on the same pressure evolution characterization coupled with Raman spectroscopy and energy dispersive X-ray (EDX). Moreover, migration of the electrochemically generated superoxide radical is also identified as a factor limiting the Coulombic efficiency of the cell. This study was carried out during my stays at Argonne

National Laboratory and the University of Southampton. On the other hand, discharge product deposits are analyzed by means of synchrotron based transmission X-ray microscopy (TXM) in Chapter 6. Unexpectedly, sodium peroxide (Na_2O_2) is also detected in these deposits. In order to shed some light on the aforementioned irregularity experimental factors that could affect the composition of the products such as moisture, leaks and synchrotron beam radiation were explored (performed at ICMAB and Alba Synchrotron), being all the tests negative for Na_2O_2 accumulation. Reduction to peroxide catalyzed by the Au TEM grid used for the material characterization appears as the most likely option, as will be discussed in Chapter 6.

Finally, ethyl viologen ditriflate ($EtV(OTF)_2$) is studied as a discharge RM in Chapter 7 in furtherance of providing an improvement strategy for $Na-O_2$ batteries. Firstly, EtV^{2+} is demonstrated to be chemically reduced and oxidized in Na^+ media, being its oxidation promoted by the addition of dioxygen gas. After confirming its reversibility, this compound is tested as a discharge RM in a $Na-O_2$ cell, unequivocally improving the oxygen reduction reaction rate capability and the discharge capacity. This Chapter was entirely carried out at the University of Southampton.

Laburpena

Metal-oxigeno (M-O$_2$) baterien energia dentsitate teoriko altuak komunitate zientifikoan interes handia eragin eta ikerketa talde askoren interesa bereganatu du. Elektrolito organikodun litio-oxigeno (Li-O$_2$) bateriek energia dentsitate teoriko bereziki altua dute: 3458 W h kg^{-1} oxigenoaren erredukzioaren ondorioz litio peroxidoaren formazio erreakzioan kalkulatutakoa (O$_2$ + 2Li$^+$ + 2e$^-$ → Li$_2$O$_2$). Bizkitartean, 20 urte igaro dira Li-O$_2$ baterien sorpenetik eta, oraindik ere, dentsitate energetikora praktikoki gerturatu eta produktu komertzial bilakatu ahal izango diren eguna urrun dago; euren kimika berezia dela eta hauen ikerkuntzan emandako aurrerapauso bakoitzak zalantza eta arazo berrien sorpena eragin izan du. Bateria hauen arazo nagusienetako batzuk karga erreakzioaren gain-potentzial handia, albo-erreakzioen presentzia nabarmena eta deskarga-karga ziklo efizienteak egiteko gaitasun mugatua dira. Izan ere, bateriaren deskargan katodoan pilatzen den produktua, litio peroxidoa, isolatzaile elektronikoa da eta hura ezabatzeko gain-potentzial handiak behar dira. Potentzial handietan Li$_2$O$_2$-aren eliminazioarekin batera elektrolitoaren eta karbonoz egindako elektrodoen degradazioa gertatzen da, karbonatoak sortu eta pilatuz. Karbonato hauen pilaketak elektrodoaren gune aktiboak pasibatzen dira, hurrengo zikloetako eraginkortasuna baldintzatuz. Zikloekin egoerak okerrera egiten du, albo-produktuak pilatzen diren heinean. Karga ez-eraginkor honi aurre egiteko estrategiarik arrakastatsuena, oraingoz, erredox bitartekarien erabilpena izan da (aurrerago euren erabilera modu zehatzagoan azalduko da). Dena den, zenbait kasutan euren kimika eta albo-kalteak azaltzeke daude, emaitza elektrokimikoen hobekuntza nabarmena eragin badute ere.

Li-O$_2$ baterien perspektiba etsigarri honen ondorioz hainbat ikerketa taldek metal alkalinoa aldatu eta sodio-oxigeno (Na-O$_2$) baterien aldeko apustua egin dute azken bost urteotan. Apustu honen lehen desabantaila garbia energia dentsitatearen txikiagotzea da, zeina %54 murrizten den oxigenotik peroxidoa lortzeko erreakzioan (3458 vs 1605 W h kg^{-1} litio eta sodioarentzat, hurrenez hurren). Hala ere, katioi

metalikoen ordezkapenak zalantza berriak sortu ditu, nabarmenena bateriaren deskargan sortutako produktuaren identifikazioa izanik. Alde batetik, talde gehienek bateria hauetan sortutako deskarga produktua sodio superoxidoa (NaO_2) dela zabaldu dute. Bestetik, badira sodio peroxido (Na_2O_2) eta sodio peroxido dihidratatuaren ($Na_2O_2 \cdot 2H_2O$) formazioa erakutsi dutenak ere. Aipagarria da NaO_2 formazioa erakusten duten lanetan emaitza elektrokimikoak hobeak direla, karga erreakzioa gain-potentzial txikiagoarekin gauzatuz eta albo-erreakzioak murriztuz. Haatik, oxigenoa superoxidora erreduzitzeak oxigeno bakoitzeko elektroi bakar bat kontsumitzen dela esan nahi du (peroxidoaren kasuan bi elektroi erabiltzen dira) eta, ondorioz, energia dentsitatea txikiagoa da (1108 W h kg^{-1}). Beraz, erreakzio sekundarioen presentzia murrizten bada ere, litioa sodioz ordezkatzeak bateria hauen abantaila nagusiaren, energia dentsitate altuaren, apaltze nabarmena eragiten du.

M-O_2 baterien etorkizuna beltza dela dioenik badago ere, talde ugarik jarraitzen dute bateria hauen inguruko ikerkuntza burutzen, helburua zaila izan arren hura erdietsiz gero lortutako saria oparoa izan baitaiteke: auto elektrikoetan aplikagarria izan daitekeen bateria ekoiztea. Hala ere, aurrerapauso nabarmen hori emateko bateria hauen oinarrizko erreakzioak ondo ulertu behar dira eta, horregatik, tesi honetan jarraitutako prozedura honako hau da: lehenik, bateria bakoitzaren erreakzioen azterketa egin da eta, jarraian, aurkitutako ahuleziak gainditzeko estrategiak proposatu eta aztertu dira. Prozedura hau litio eta sodio baterietan jarraitu da: alde batetik, 3. eta 4. kapituloak Li-O_2 baterien ingurukoak dira eta, bestetik, 5., 6. eta 7. kapituluek Na-O_2 baterien ikerketa jorratzen dute.

Tesi honetako 3. kapituluan Li-O_2 sistemen analisi zehatza aurkezten da. Horretarako, alde batetik, baterion analisi elektrokimikoa egin zen kronopotentziometria (ziklo galvanostatikoak) eta inpedantzia elektrokimiko espektroskopia (EIS) teknikak erabiliz. Bestetik, sortutako deskarga produktuen analisia burutu zen X-izpien difrakzioa (XRD), ekortze mikroskopia elektronikoa (SEM) eta X-izpien foto-elektroi espektroskopia

(XPS) teknikez baliatuz. Lehenik eta behin, oxigenoak elektrolitoan daukan difusio gaitasuna bateriek eman dezaketen deskarga kapazitate maximoa baldintzatzen duen faktore erabakigarria dela ondorioztatu zen; horretarako lodiera ezberdineko elektrodoak erabili ziren. Oxigeno gordailutik urrutien zeuden elektrodo-gainazaletan produktu gutxiagoren akumulazioa gertatzen zela ikusi zen. Baterien kapazitatea elektrodoaren pisuaren baitako unitateen arabera aurkezten denez, elektrodoa loditu ahala erabili gabe geratutako elektrodo masa guzti horrek kapazitate erreala gutxiestea dakar, kalkuluetan kontutan hartzen baita. Hala ere, ziklo kopuruak aurrera egin ahala aurrez erabili gabeko elektrodo zonalde hauek bateria gauzatzeko gai den ziklo kopurua handitzea ahalbidetzen dute, aurrez erabilitakoak albo-erreakzioak jasaten baitituzte. Bidenabar, deskarga produktuen eta albo-produktuen formazioa eta eliminazioa EIS bidez monitorizatu ziren, M-O$_2$ baterien prozesuen azterketa *in situ* jarraitzeko teknika erabilgarria dela frogatuz.

Li-O$_2$ sistemen erreakzioen analisia egin ondoren, 4. kapituluan baterion errendimendua hobetzeko hainbat estrategia aztertzen dira. Lehenik jarraitutakoa bibliografian ohikoak diren katalizatzaile heterogeneoen erabilera izan zen; manganeso (IV) oxidoak (MnO$_2$), urreak eta paladioak oxigenoaren erredukzioan eta peroxidoaren oxidazioan izan dezaketen ahalmen katalizatzailea aztertu zen EIS teknikaren bidez. Emaitzak, tamalez, ez ziren gogobetegarriak izan eta euren eragina albo-erreakzioak bideratzea mugatzen zirela ondorioztatu zen. Bigarren saiakera batean, katalizatzaileak alde batera utzi eta albo-erreakzioak jasaten dituen karbono elektrodoa bibliografian aztertuak izan diren titanio karburo (TiO), kobalto oxido (Co$_3$O$_4$) eta nikel oxido (NiO) elektrodoz ordezkatu zen. Oraingo honetan ere emaitzak etsigarriak izan ziren, kapazitateak txikiegiak eta kargak mespretxagarriak izanik. Azkenik, katalizatzaile homogeneoak aztertu ziren, hau da, elektrolitoan disolbaturik bateriaren eraginkortasuna hobetzen duten katalizatzaileak. Alde batetik, potasio ioiak (K$^+$) gehitu ziren elektrolitora honen azidotasunean eragina izan eta deskargan sortutako

produktuak egonkortzeko gaitasuna handitzeko. Bestetik, I⁻ ioiak gehitu ziren karga erreakzioan erredox bitartekari gisa jokatzeko; I⁻ elektrokimikoki potentzial baxuan oxidatu daiteke I_2 sortuz eta azken hau disoluzioan zehar barreia daiteke, deskarga produktuekin kontaktuak kimikoki erreakzionatu eta oxigenoa eta I⁻ askatzeko. Estrategia biak arrakastatsuak izan ziren, eta euren efektu konbinatuak bateriaren jarduera nabarmenki hobetu zuen. Azkenik, I⁻ gehikuntzaren albo-efektuak aztertu ziren, hala nola erreakzio sekundarioak eta *shuttling* efektua. Horretarako gelaxka elektrokimiko barneko presioaren jarraipena, elektrolitoaren infragorri espektroskopia (IR) eta elektrodoen XRD egin ziren. Gainera, I_2 oxidazio produktuaren argi-absortzio gaitasuna dela eta argi ultramore eta ikusgarri espektroan absortzioa neurtzeko gelaxka bat diseinatu eta eraiki genuen, I_2 formazio eta eliminazioa *in situ* jarraitzea ahalbidetuz. Emaitza elektrokimikoek iradokitzen zuten bezain baikorra ez dela frogatu arren, I⁻ erredox bitartekariaren gehikuntzaren efektua oro har positiboa dela esan daiteke.

Li-O_2 bateriak alde batera utzita, 5. eta 6. kapituluetan Na-O_2 baterien inguruko prozesuak aztertzen dira. 5. kapituluan deskarga produktuen identifikazioa burutzen da lehendabizi, Raman espektroskopia, gas presioaren neurketa eta elektroi paramagnetiko erresonantzia (EPR) erabiliz. Gure produktua NaO_2 zela jakin ondoren konposatu honek gelaxka elektrokimikoan duen egonkortasuna aztertu zen, aurretik aipatutako teknikak SEM eta energia dispertsio X-izpi espektroskopiaz (EDX) osatuz. Bi efektu nabarmen aurkitu ziren: lehenik, sortutako NaO_2 deposituek birdisolbatzeko joera zutela ikusi genuen, efizientzia elektrokimikoan eragin zuzena izanik. Bestalde, birdisolbatu gabeko deposituak oxigenoa askatu eta pasibatzeko joera zutela frogatu genuen. Gainera, deskarga produktuez gain fase sekundarioen formazioa ere *in situ* jarraitu genuen EIS eta kuartzo kristal mikrobalantza (QCM) erabiliz.

6. kapituluan, 5.ean bezala, gure ikerketa objektua Na-O_2 baterien deskarga produktua da. Kasu honetan, produktuak transmisio X-izpi mikroskopia (TXM) izeneko sinkrotroi

teknikaren bidez aztertu ziren. Ezustean, sodio peroxidoa aurkitu zen deskarga deposituetan superoxidoarekin batera. 5. kapituluan peroxido formaziorik antzeman ez izanak produktu honen jatorriaren inguruan arakatzera bideratu gintuen, faktore gertagarrienak urarekiko, airearekiko eta X-izpiekiko esposizioa izanik. Esperimentuek, bizkitartean, peroxidoaren jatorriak faktore hauekin zerikusia zuenik ezeztatu zuten, eta neurketetan erabilitako urrezko euskarriak 2 elektroietako erredukzio erreakzioaren erantzule izaterik ote zuten iradoki zen. Azken ikerketek aukera hori babesten dutenez, etorkizunean interesgarria izan daiteke katalizatzaile ezberdinak aztertzea bateria hauen bidez lor daitekeen energia dentsitatea handitzeko asmoz. Bestalde, NaO_2 eta Na_2O_2 produktuen karga erreakzioak ere aztertu ziren. Hainbat autorerekin kontrajarrian, peroxidoa eta superoxidoa gain-potentzial berberarekin oxidatu daitezkeela frogatu genuen. Peroxidoa gain-potentzial txikiarekin eliminatu ahal izatea garrantzia handiko faktorea da katalizatzaile bidez 2 elektroiko oxigenoaren erredukzioa bultzatze aldera. Hala ere, zikloekin peroxidoaren itzulgarritasuna superoxidoarena baina txikiagoa zela frogatu zen, zikloekin elektrodoan pilatuz.

Azkenik, 7. kapituluan etil viologen ditriflatoak ($EtV(OTF)_2$), $Li-O_2$ baterietan modu arrakastatsuan frogatutako deskarga erredox bitartekariak, $Na-O_2$ sistemetan izan dezakeen efektu onuragarria aztertzen da. Lehenik eta behin, EtV^{2+}/EtV^+ erredox parearen itzulgarritasuna kimikoki aztertu zen, oxidatzaile eta erreduktore bezala oxigenoa (O_2) eta litio titanato litiatua ($Li_{6.8}Ti_5O_{12}$, LTO) erabiliz, hurrenez hurren. Emaitzak positiboak izanik, erredox bitartekaria $Na-O_2$ gelaxketan frogatu zen oxigeno erredukzio erreakzioa hobetuz: bitartekariaren presentzian voltamperometria ziklikoetan lortutako korronte maximoa eta ziklo galvanostatikoetan erdietsitako kapazitateak modu nabarmenean hobetu ziren. EtV^{2+}/EtV^+ erredox pareak $Na-O_2$ baterien etorkizunean zeresana emango duela aurreikus daiteke, aurkeztutako emaitzetan oinarrituta.

x

Comencé este camino contigo. Sumas, restas, multiplicar, dividir, letras, palabras, leer, escribir. Llegó un momento en el que decías que no entendías lo que yo te explicaba, "estas cosas tan difíciles", y supongo que te sentirías igual que yo cuando me sentaba en tu cocina y miraba aquellos cuadernos. Nunca he sido tan buen profesor como tú. Gustoso te regalaría este libro para que fuese uno más de los de tu estantería, aunque la estantería ya no está. Tú tampoco estás, pero sigues aquí. No hace falta que me hables para seguir aprendiendo de ti. Hemos recorrido juntos este camino, igual que cuando llegábamos a la gasolinera. Muchas gracias.

Acknowledgements

I would like to extend my appreciation to my supervisor, Dr. Idoia Ruiz de Larramendi, for her guidance and the confidence deposited on me throughout the course of this research project. I really appreciate her support after each decision I have taken. In addition, I am really grateful to all the present and past Inorganic Chemistry Department members, particularly to Prof. Luis Lezama and Prof. Teófilo Rojo for allowing me to join their group and for economically supporting my research. EPR experiments in this thesis were carried out with Prof. Lezama, so I want to express my gratitude to him also for these measurements. I am also grateful to Prof. José Ignacio Ruiz de Larramendi for *recruiting* me for research.

I would like to thank my thesis committee members: Drs. Aintzane Goñi, Nagore Ortiz-Vitoriano, Dino Tonti, Nuria García-Araez and Prof. Teófilo Rojo.

In furtherance of obtaining my Ph.D., I have had the opportunity of being hosted in several research centers. My first contact with metal-oxygen batteries was in CIC Energigune. I am very grateful to all the people I had the chance to know and work with, including the Scientific Director Teófilo Rojo and all the direction members for allowing me carrying out my experiments there, and also Begoña Acevedo for the SEM images in Chapter 3. After that I had the chance of joining Dr. Dino Tonti's group at ICMAB, learning from him and from Dr. Mara Olivares-Marín. It was such a fantastic stay that I was invited there again, this time to carry out the synchrotron experiments together with Dr. Andrea Sorrentino, from Alba facilities. Both stays were wonderful and I want to extend my gratitude to all the people I had the chance to work with.

My stays were not limited to Spanish borders; I had the chance to join Dr. Amine and Dr. Lu's group at Argonne National Laboratory. I want to extend my gratitude to both of them for allowing me to stay in one of the most outstanding research centers all over the world. Most of the experiments in Chapter 5 were performed during this fruitful stay.

I would like to thank my parents all the sacrifices done in order to give me the opportunity of reaching as far as I could in my student career. For having *duty is more important than pleasure* as their life-motto just to support my brothers and me. I want to extend my gratitude to all my family and to the people accompanying me in my travels pursuing my Ph.D., particularly to Olatz for her unconditional support and empathy.

Lastly, I wish to thank Dr. Ricardo Pinedo the incalculable time dedicated to this thesis, all his support and advises. Thanks for all the stimulating and frustrating discussions, for being available and working from Monday morning to Sunday evening and for questioning every single step forward we have given. Thank you for becoming my friend.

Table of contents

3. Investigations on ORR and OER in Li-O$_2$ systems

4. Strategies to improve the Li-O$_2$ battery performance

5. Analysis of the discharge products evolution in Na-O$_2$ batteries

6. Characterization of Na-O$_2$ discharge products by Synchrotron

X-ray Transmission Microscopy

7. Discharging a Na-O$_2$ cell using a redox mediator

Chapter 1 - Introduction

1.1. Metal-air batteries

Global warming, caused by greenhouse gas emissions, is one of the main concerns for humankind. Automotive transports based on fossil fuels combustion have been pointed as one of the most important agents causing such emissions and, therefore, many efforts are being made in order to decrease the dependence on this energy source. Investments on energy storage made by worldwide governments are an unequivocal indicative of the magnitude of the challenge we are facing: the U.S. Department of Energy spends between 10 and 20 million dollars per year in energy storage research, Germany has put aside 200 million euro in energy storage programs, and Japan has allocated similar amounts on the development of the New Energy and Industrial Technology Developments Organization (NEDO). In addition, EU has backed "Horizon 2020" in order to fund research into energy storage technologies.[1–3] Rechargeable batteries have been the main target of energy storage research. A clear example of this is the rechargeable Li-ion battery, which has facilitated the revolution of portable electronics. More than previous achievements, rechargeable batteries pose significant potential to bring a number of new economic and environmental benefits, such as replacing systems powered by fossil fuels and balancing the fluctuating generation of renewable power sources for their integration into the electrical grid.[4,5] The use of efficient rechargeable batteries would lead to important technological turning points in these industries. However, ubiquitous Li-ion batteries have almost reached their limits in terms of energy density (75-200 Wh kg^{-1}), cycle life (1000 cycles at > 80% of capacity), and charge / discharge rate capabilities (1C).[6,7] These values need to be increased in order to develop new emerging applications such as electric vehicle (EV) or stationary grid storage. For example, current Li-ion batteries for EVs offer a driving range of around 200 km. Hence, higher energy density batteries with superior performance are necessary in order to deploy EVs with the sufficient driving range to

compete with alternative technologies (fuel cells, non-renewable energy sources, etc.).

Metal-air (M-air) batteries are considered the most attractive alternative to Li-ion batteries when high energy density is a critical requirement. In Li-ion batteries, the energy is stored and released by the intercalation reaction of Li ion in both anode and cathode materials, hence such electrodes need to have a suitable chemical structure to host the Li ions. The chemical structure is not directly involved in the electrochemical reaction, only adding 'dead weight' to the battery. In contrast to conventional battery systems based on intercalation reactions,[8–10] M-air batteries rely on the electrochemical reduction of molecular oxygen at the cathode surface and are therefore also known as metal-oxygen (M-O_2) batteries. The advantages of M-O_2 batteries are that negligible amount of 'dead weight' is needed and the theoretical energy density is the highest among other battery systems (Figure 1.2).
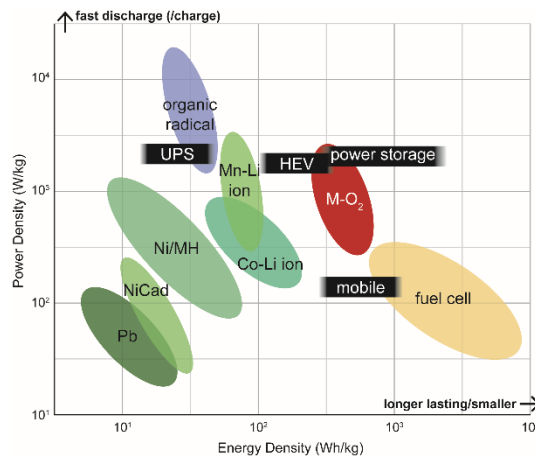
Figure 1.1. Practical energy density *vs.* power density for M-O_2 batteries and some other rechargeable batteries. The specifications of key applications is also highlighted: Uninterruptible Power Systems (UPS) is an electricity storage system that is used to reduce or avoid negative effects and costs associated with electrical service outgases and / or poor power quality; A hybrid electric vehicle (HEV) is a type of vehicle that combines a conventional internal combustion engine propulsion system with an electric propulsion system.

There are, however, noticeable differences on the energy density that M-O$_2$ batteries can provide depending on the metal used as negative electrode and, therefore, the discharge product formed on the oxygen electrode (Figure 1.2).[11]
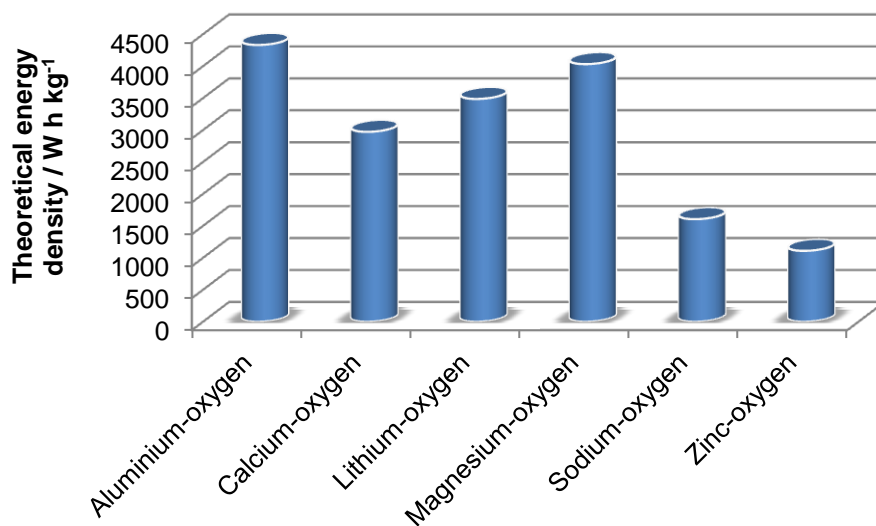
Figure 1.2. Theoretical energy densities calculated for aluminium-oxygen, calcium-oxygen, lithium-oxygen, magnesium-oxygen, sodium-oxygen and zinc-oxygen batteries based on the formation of Al$_2$O$_3$, CaO, Li$_2$O$_2$, MgO, Na$_2$O$_2$ and ZnO, respectively.

Gasoline, the dominant energy source for automotive transportation, has a theoretical energy density of 13000 W h kg^{-1}, significantly higher than that of the M-O$_2$ batteries presented in Figure 2. Only a small fraction of this energy density is, nevertheless, practically achieved (1700 W h kg^{-1}) by gasoline, comparable to the values observed for M-O$_2$ batteries and, therefore, making them candidates for their implementation in EVs and HEVs.[12]

In this work we have focused our interest in the analyses of lithium-oxygen (Li-O$_2$) and sodium-oxygen (Na-O$_2$) batteries. Our research started with Li-O$_2$ batteries as it has practically been demonstrated to deliver energy densities similar to those of gasoline[13]. Difficulties associated to the performance of such batteries (that will be discussed in

the text), however, lead us to the substitution of Li by Na and, therefore, the second part of this thesis is focused on Na-O$_2$ batteries.

1.2. Lithium-oxygen batteries

Li-O$_2$ batteries were originally proposed as EVs' and HEVs' energy sources in the 1970s due to their high theoretical energy density of ~ 3500 W h kg^{-1} for the reduction of molecular oxygen to lithium peroxide (Li$_2$O$_2$) and ~ 5000 W h kg^{-1} for the reduction to Li$_2$O[141516]. However, it was not until the late 90s when Abraham *et al.*[17] successfully introduced an organic solvent in these batteries avoiding the reaction of lithium metal with the aqueous electrolytes unsuccessfully tested until that work. Since that discovery the interest in Li-O$_2$ batteries was increased, particularly in the batteries with "non-aqueous" or "aprotic" electrolyte. At this point it is convenient to present the different types of Li-O$_2$ batteries (see Figure 1.3).
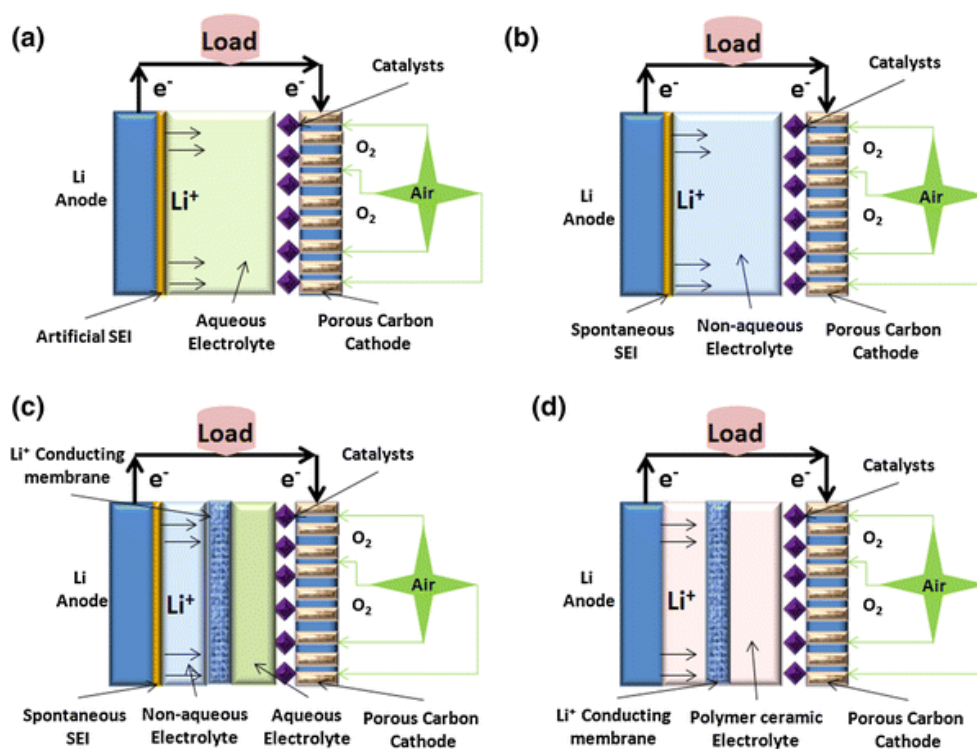
Figure 1.3. Schematic representation of the different types lithium-oxygen (Li-O$_2$) batteries: (a) aqueous,(b) non-aqueous, (c) hybrid, and (d) solid state. Reprinted with permission from Ref. 18. Copyright 2014 Springer.

In all the different set ups lithium metal and carbon are used as anode and cathode, respectively. Li from de anode is oxidized during the discharge of the cell and Li^+ ions are released to the electrolyte while electrons (e^-) are directed to the cathode by an external circuit. Electrons reaching to the cathode are used to reduce molecular oxygen (carbon electrode is also known as oxygen electrode due to the reaction taking place on its surface). The main difference arises from the electrolyte selected and $Li-O_2$ batteries are usually classified by the nature of the electrolyte used for Li^+ ion migration: aqueous, non-aqueous, hybrid and solid state (Figures 1.3.a, 1.3.b, 1.3.c and 1.3.d, respectively) can be differenced based on this criterion. Aqueous batteries (Figure 1.3.a), in which a Li^+ containing water solution is used as the electrolyte, require from an artificial SEI layer to protect Li metal from water. This SEI layer is spontaneously formed in non-aqueous and hybrid batteries (Figures 1.3.b and 1.3.c, respectively) as the electrolyte in contact with Li electrode is a Li+ containing organic solvent. In the case of these last type of batteries, the electrolyte facing the carbon electrode is an aqueous solution and anolyte and catholyte are separated by a Li^+ conducting membrane. Finally, solid state batteries (Figure 1.3.d) are based on a lithium conducting solid electrolyte.

1.2.1. The non-aqueous $Li-O_2$ battery

The most studied set up for $Li-O_2$ batteries has been the consisting of non-aqueous electrolyte (schematized in Figure 1.3.b). In these batteries molecular oxygen in the carbon electrode is reduced (oxygen reduction reaction, ORR) by the following reactions.[19,20]

Lithium electrode: $\qquad$ $Li \rightarrow Li^+ + e^-$ $\qquad$ [1.1]

Carbon electrode: $\qquad$ $O_2 + Li^+ + e^- \rightarrow LiO_2$ $\qquad$ [1.2]

$\qquad$ $2\ LiO_2 \rightarrow Li_2O_2 + O_2$ $\qquad$ [1.3]

$\qquad$ $LiO_2 + Li^+ + e^- \rightarrow Li_2O_2$ $\qquad$ [1.4]
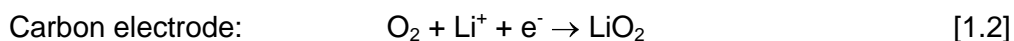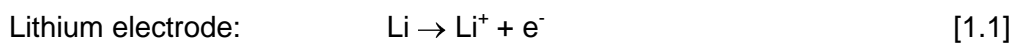
During the charge of the cell the peroxide generated in the previous discharge is oxidized to O_2 and Li^+ (oxygen evolution reaction, OER). There has been much controversy on the nature of the reaction of lithium superoxide (LiO_2) to form peroxide (Li_2O_2). Several authors have demonstrated that the first discharge product formed is LiO_2 (reaction 1.2), which later evolves to Li_2O_2 due to the instability of superoxide. This reaction can follow two distinct routes: (i) it can chemically disproportionate to Li_2O_2, which is much more stable in the battery environment (reaction 1.3), or be electrochemically reduced (reaction 1.4). Although these two mechanisms have been discussed as separated pathways, Luntz *et al.*[21] suggested that they are quite similar, as the only difference between them is the origin of the Li^+ added to LiO_2; in disproportionation reaction it comes from Li^+ adsorbed on the surface of the electrode, while in the electrochemically driven it comes from another LiO_2.

1.2.2. The discharge products: LiO_2 and Li_2O_2

The presence of the 1 e^- reduction product LiO_2 in the discharge product solid deposit has also been discussed in literature. Amine's group has been one of the research groups that have most intensely defended the presence of LiO_2 together with Li_2O_2 although pressure sensor measurements carried out in Li-O_2 cells point to a 2 e^- per O_2 molecule reaction.[22,23] Amine's group analyzed the presence of such superoxide by electrochemical,[24] Raman spectroscopy[25] and high energy X-ray diffraction and transmission electron microscopy.[26] Moreover, two significant works have recently been published related to the presence of LiO_2; Olivares-Marín *et al.*[27] detected,

6

quantified and localized with spatial resolution LiO_2 in the $Li-O_2$ discharge products by means of transmission soft X-ray microscopy and Lu et al.[28] were able to obtain crystalline superoxide as the discharge product using a reduced graphene oxide + iridium electrode. The presence of LiO_2 implies an improved electrochemical performance but the energy density obtainable by a 1 e$^-$ reduction is lower than by a 2 e$^-$ process and consequently hinders the main advantage of these batteries, their outstanding energy density.

Leaving behind the debate about the benefits and drawbacks of each discharge product and the reaction pathway for the conversion of LiO_2 to Li_2O_2, some authors have focused their research on the origin of the reaction; the instability of LiO_2. Johnson et al.[29] demonstrated by means of in situ Raman spectroscopy that high Gutmann Donor-Number (DN) electrolytes were able to stabilize the superoxide, leading to cluster-shaped Li_2O_2 discharge products, which can be reversed easier than film-shaped Li_2O_2 originated by low DN-based electrolytes. The relationship between discharge products morphology and reversibility had been previously studied by Adams et al.[30]; who correlated the discharge current density with the morphology of the discharge products, and later analyzed the influence of this morphology on charge potential of the cell. They demonstrated that at lower current density Li_2O_2 forms toroidal-shaped aggregates, while at higher current density Li_2O_2 was deposited forming a thin homogeneous film on the carbon surface. It was suggested that at lower current densities LiO_2 is solvated and chemically disproportioned to Li_2O_2, being precipitated once the solubility limit of the peroxide in the electrolyte was exceeded (solution mediated). In turn, they proposed that at higher current densities LiO_2 was formed and subsequently transformed to Li_2O_2 on carbon surface, leading to a film-like morphology (surface mediated). It was also observed that discharge capacity was reduced as current density was increased. Later, Lutz's group demonstrated that these

toroidal-shaped products were formed in presence of residual water, which leaded to a solution mediated ORR.[31]

Coming back to the stability of LiO_2 in the electrolyte, Abraham[19] emphasized the importance of such stabilization including the electrolyte (ions and solvent) in the ORR (reactions 1.5-1.7), Superoxide will be electrochemically formed and associated to the solvent. Afterwards, it will be chemically decomposed or electrochemically reduced (depending on the mechanism) precipitating as Li_2O_2.

$$O_2 + Li^+(solvent)_n + e^- \rightarrow Li^+(solvent)_nO_2^- \qquad [1.5]$$

$$Li^+(solvent)_nO_2^- \rightarrow Li_2O_{2(s)} + O_2 + n\ (solvent) \qquad [1.6]$$

$$Li^+(solvent)_nO_2^- + Li^+(solvent)_n + e^- \rightarrow Li_2O_{2(s)} + n\ (solvent) \qquad [1.7]$$
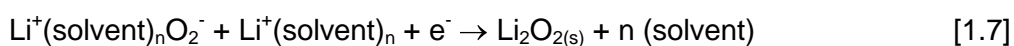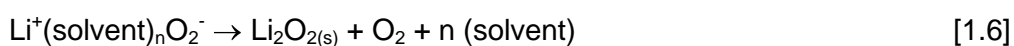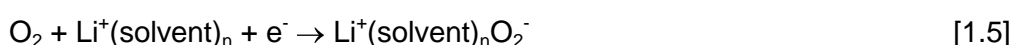
Considering that superoxide can react with the electrolyte resulting in the formation of lithium carbonate (Li_2CO_3)[27,32–35] due to its high instability, a complexed state would help to prevent the degradation of the cell components. In his work, Abraham[19] also analyzed the effect of the substitution of hard acid Li^+ by other monovalent cations: Na^+, K^+, EMI^+, PYR^+ and TBA^+ (sodium, potassium, 1-ethyl-3-methylimidazolium, 1-methyl-1-butyl-pyrrolidinium and tetrabutyl ammonium cations, respectively). It was observed that both oxygen reduction reaction (ORR) and oxygen evolution reaction (OER) were favored as the acidity of the cation was decreased (note that acidity decreases in the following order: $Li^+ > Na^+ > K^+ > EMI^+ > PYR^+ > TBA^+$) as O_2^- stronger coordinates with them based on Pearson's HSAB theory[36]. This was also observed by Johnson *et al.*[29] when measured the ORR and the OER activity with different Li^+/TBA^+ ratios in the electrolyte. They demonstrated that at higher Li^+ concentrations the discharge product LiO_2 evolved to Li_2O_2, which could only be removed at higher potentials. Zheng *et al.*[37] also observed a reduction of charge overpotential using tris(pentafluorophenyl) (TPFPB) as additive, which formed a complex with Li_2O_2 that was soluble in the electrolyte leading to faster kinetics and higher rate capability.

The nature of the products formed at the oxygen electrode during discharge reaction is, as mentioned, an important factor limiting the performance of the cell. Although the standard potential for ORR and OER is 2.96 V vs. Li/Li$^+$ (henceforth all the potentials will be referred to the Li/Li$^+$ pair potential) Li-O_2 cells usually exhibit significant overpotential during the charge of the cell;[38] whereas LiO_2 can be oxidized at ~3.5 V[28] removal of Li_2O_2 and Li_2CO_3 occurs between 3.8 and 4.5 V. At such high charging potentials Li_2O_2 has been demonstrated to react with the carbon electrode forming lithium carbonate:[39]

$$Li_2O_2 + 1/2 \ O_2 + C \rightarrow Li_2CO_3 \qquad\qquad [1.8]$$

Moreover, at ~4.5 V Li_2CO_3 evolves to CO_2[40] which can, in the subsequent cycles replace O_2 in the discharge of the cell leading to a gradual increase on the carbonate formation[41]. Cycling performance of the cell is, therefore, severely conditioned by the products that are formed in the oxygen electrode.

1.2.3. Carbon-free electrodes

Several strategies have been adopted in order to decrease the presence of side reactions and, consequently, improve the cycling performance of the battery. Some authors have focused their interest in the substitution of carbon by alternative materials in the oxygen electrode. Carbon has been the most widely used electrode material in Li–O_2 batteries[42,43]. The Li_2O_2 solid discharge product must be accumulated in a porous, conducting, inexpensive matrix, which makes carbon an excellent candidate.[44] However, as previously mentioned several studies show evidence of the unsuitability of carbon as the Li–O_2 positive electrode owing to its lack of stability during charge and the formation of intermediate products. The instability of carbon-based electrodes has motivated the selection of carbon-free electrode materials. This is considered a key factor for the development of commercially viable Li–O_2 batteries and an area where promising results are already reported[45–47]. The requirements of an air electrode

material include: sufficient electronic conductivity, low density, stability over the operating voltage (typically 2–4 V), stability towards nucleophilic attack (O_2^- and O_2^{2-}), non-toxicity, low cost, and ease of fabrication in porous structures.[46] Despite differences in the experimental conditions and other factors such as electrolytes and cell designs Table 1 has been built up in order to give a general overview of some of the electrochemical results of the discussed materials.

Table 1. Electrochemical results of the different combinations of noble metals and oxides as oxygen electrodes. Mass-normalized units are based in support materials with active material mass and area normalized are referred to geometric area of the electrode.

Author	Cui et al.[48]	Riaz et al.[49]	Lee et al.[50]	Yu et al.[51]	Hu et al.[52]	Lin et al.[53]	Kundu et al.[54]	Liao et al.[55]	Peng et al.[56]	Li et al.[57]	Zhao et al.[50]	Chen et al.[58]	Thotyil et al.[59]	Cui et al.[60].
Material	Co_3O_4	Co_3O_4	Co_3O_4	MnO_2	ε-MnO_2	$(Co,Mn)_3O_4$	Ti_4O_7	RuO_2	NPG	Ru+ITO	TiO_2+Pt	NPG + RuO_2	TiC	TPPy
Electrolyte	1 M $LiPF_6$ in PC	1 M LiTFSI in TEGDME	1 M $LiClO_4$ in DMSO	1 M $LiClO_4$ in PC/DEC (1:1)	1 M LiTFSI in TEGDME	1 M LiTFSI in TEGDME	0.5 LiTFSI in TEGDME	1 M $LiClO_4$ in DMSO	0.1 M $LiClO_4$ in DMSO	LiTFSA in G3 (1:5)	1 M LiTFSI in TEGDME	1 M $LiClO_4$ in DMSO	0.5 M $LiPF_6$ in TEGDME	0.1 M LiTFSI in DME
Current density	0.1 mA cm^{-2}	100 mA g^{-1}	0.05 mA cm^{-2}	0.3 mA cm^{-2}	500 mA g^{-1}	0.05 mA cm^{-2}	0.2 mA cm^{-2}	100 mA g^{-1}	500 mA g^{-1}	0.025 mA mA cm^{-2}	0.057 mA cm^{-2}	275 mA g^{-1}	0.5 mA cm^{-2}	0.5 mA cm^{-2}
First discharge capacity	1040 mA h g^{-1}	2280 mA h g^{-1}	4531 mA h g^{-1}	0.3 mA h cm^{-2}	6300 mA h g^{-1}	3605 mA h g^{-1}	1.2 mA h	1100 mA h g^{-1}	325 mA h g^{-1}	2.5 mA h cm^{-2}	0.1 mA h	275 mA h g^{-1}	555 mA h g^{-1}	1764 mA h g^{-1}
Cycling current density	0.1 mA cm^{-2}	100 mA g^{-1}	0.1 mA cm^{-2}	0.3 mA cm^{-2}	500 mA g^{-1}	0.05 mA cm^{-2}	-	500 mA g^{-1}	500 mA g^{-1}	0.15 mA cm^{-2}	0.057 mA cm^{-2}	275 mA g^{-1}	0.5 mA cm^{-2}	0.5 mA cm^{-2}
Number of cycles	5	50	19	50	120	50	-	50	100	50	150	55	100	6
Limited capacity	No	Yes	Yes	No	No	Yes	-	No	Yes	Yes	Yes	Yes	No	No
Capacity	> 1040 mA h g^{-1}	500 mA h g^{-1}	1 mA h	> 0.2 mA h cm^{-2}	> 1000 mA h g^{-1}	500 mA h g^{-1}	-	> 800 mA h g^{-1}	325 mA h g^{-1}	1.81 mA h cm^{-2}	0.1 mA h	275 mA h g^{-1}	> 500 mA h g^{-1}	> 1700 mA h g^{-1}

Table 1 evidences the difficulties of making reasonable comparisons related to the electrochemical data of discharge capacity and/or cycling performance reported by different authors. TiC[59] shows a good compromise between discharge capacity, current rate and number of cycles. However, the reproducibility of these results should be demonstrated for its implementation in commercial devices. Au nanoparticles[56] also

show an extraordinary electrochemical performance but the high cost of Au makes it inappropriate for commercial development. Finally, metal oxides[48,49,51,52] show outstanding discharge capacities and cyclability at low current rates, which make them interesting candidates for stationary energy storage applications. It is worth mentioning the extraordinary performance observed for MnO_2 with very good cyclability (120 cycles) and high-rate capability (500 mA g^{-1}).[52] Nevertheless, the lack of experimental data provided in the published works hinders the possibility of developing a deep study on these systems.

1.2.4. Heterogeneous and homogeneous catalysts

Although alternative electrode materials above presented have improved the battery performance by the decrease in the side reactions involving the oxygen electrodes, some authors have worked in the optimization of ORR and OER by the use of catalysts, being the most popular strategy the addition of heterogeneous catalysts that dispersed in the carbon electrode have improved the performance of the battery. Among them noble metals[61–64] and metal oxides[65–68] have been widely investigated. Remarkable improvements on the battery performance have been reported[69–72] although McCloskey *et al.*[73,74] suggested that the attained reduced overpotential could be indicative of the electrocatalysis related to electrolyte decomposition. In addition, these catalysts are normally dispersed through conventional carbons and the applied current density is set as a function of the carbon mass, even when catalyst-containing and catalyst-free cathodes are compared.[45]

Finally, homogeneous catalysts (or redox mediators, RM) have been studied by several researchers as an alternative to improve the cycling performance of Li-O$_2$ batteries. These compounds, which are dissolved in the electrolyte, can be oxidized (RM$^+$) at low overpotentials during charge and, as they are dissolved in the electrolyte, migrate to

the surface of non-conductive Li_2O_2 (or LiO_2) crystals, oxidizing them and returning to their initial state (RM):[75]

$$RM \rightarrow RM^+ + e^- \qquad\qquad [1.9]$$

$$2\ RM^+ + Li_2O_2 \rightarrow 2\ Li^+ + O_2 + 2\ RM \qquad [1.10]$$
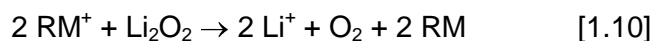
Several redox mediators have been proposed for charging nonaqueous LOBs, such as tetrathialfulvalene (TTF),[76] iron phthalocyanine (FePc),[77] 2,2,6,6-tetramethylpiperidinyloxyl (TEMPO)[78] and iodide (I^-)[75,79–81]. Apart from charge mediators, Yang *et al.*[82] analyzed the effect of viologen (EtV^{2+}) discharge mediator. Li_2O_2 discharge product is non-conductive and a severe and disordered deposition of this material can passivate the electrode reducing its capacity to accumulate peroxide. Viologen is supposed to mediate in the reduction of O_2 to LiO_2 and create a stable complex with superoxide and later reduce this superoxide to peroxide in an advantageous route improving the discharge capacity by 2.5 in their experiment. Charge capacity of the viologen-mediated cell was, however, exactly the same as the one without mediator although in the first battery much more Li_2O_2 should be formed (deduced from the enhanced discharge capacity). Similar effects have also been reported with other molecules that are reduced at voltages between 2.8 and 2.4 V vs. Li, such as quinones[83] and organic radicals.[84]

1.3. Sodium-oxygen batteries

As previously, worldwide researchers have mainly focused their efforts on the study of the $Li-O_2$ battery due to their high theoretical energy density. However, several underlying physical and chemical mechanisms during battery operation have prevented the system from achieving its potential[10]. These limitations are partially due to stability issues which include: (i) short circuit of the cell caused by Li metal anode upon cycling (precipitate growth of Li dendrites); (ii) reaction of Li metal with contaminants from air (*e.g.*, H_2O and CO_2) and some electrolyte molecules; (iii) positive oxygen electrode

reactions with the discharge product Li_2O_2 which can be further oxidized on charging (> 3.5 V); and (iv) electrolyte stability with oxygen reduction products or intermediates. In addition, the $Li-O_2$ battery presents low discharge / charge coulombic efficiency and poor cycle life.

1.3.1. Cell chemistry and comparison to $Li-O_2$ batteries

The substitution of lithium by sodium has recently emerged as a promising approach to surpass $Li-O_2$ battery limitations.[85] In its common configuration, the non-aqueous $Na-O_2$ battery comprises a sodium-containing anode (currently Na-metal), a sodium-conducting organic electrolyte and an air cathode. Cell discharge occurs when the Na metal anode electrochemically oxidizes and the Na^+ ions migrate across the electrolyte. It is believed that the reaction mechanism, as in the case of $Li-O_2$ batteries, involves the oxygen gas (O_2) dissolving in the regions of the electrolyte left exposed by the porous cathode (generally a carbonaceous material), forming superoxide species (O_2^-). In contrast to $Li-O_2$ batteries sodium superoxide (NaO_2) is formed as the final discharge product in a reaction between the Na^+ and O_2^-. This is subsequently decomposed upon charging, in the reverse reaction ($Na^+ + O_2 + e^- \leftrightarrow NaO_2$). Other discharge products such as sodium peroxide (Na_2O_2) and peroxide dehydrate ($Na_2O_2 \cdot 2H_2O$) have also been reported in literature which will be discussed below.

The main characteristics of $Na-O_2$ and $Li-O_2$ systems are compared in Table 2. In terms of cell chemistry, the theoretical energy density of a $Na-O_2$ battery is ~ 1108 Wh kg^{-1}, which is ~ 30% lower than that of a $Li-O_2$ cell.[86] One of the main advantages of a $Na-O_2$ battery is its much lower charge overpotential (< 100 mV) than those in typical $Li-O_2$ batteries (~ 1000 mV). Such low charging overpotential might be the result of cleaner cell chemistry compared with $Li-O_2$ batteries.[87] Another key benefit of $Na-O_2$ batteries is their higher coulombic efficiency (> 95% upon cycling)[85,88]compared to $Li-O_2$ batteries.

Table 2. Comparison of theoretical data between Na-O_2 and Li-O_2 batteries for different discharge products.

	Na-O_2	Li-O_2
Cell chemistry	$Na^+ + O_2 + e^- \rightarrow NaO_2$ $2Na^+ + O_2 + 2e^- \rightarrow Na_2O_2$	$2Li^+ + O_2 + 2e^- \rightarrow Li_2O_2$
Cell voltage	E° (2 NaO$_2$) = 2.27 V ($\Delta G° = -437.5$ kJ mol^{-1}) E° (Na$_2$O$_2$) = 2.33 V ($\Delta G° = -449.7$ kJ mol^{-1})	E° (Li$_2$O$_2$) = 2.96 V ($\Delta G° = -570.8$ kJ mol^{-1})
Overpotential (Discharge / Charge)	$\eta_{dis} < 100$ mV $\eta_{ch} \approx 30\text{-}100$ mV	$\eta_{dis} \approx 300$ mV $\eta_{ch} \approx 1300$ mV
Theoretical capacity	1165 mAh g^{-1} (Na) 488 mAh g^{-1} (NaO$_2$) 689 mAh g^{-1} (Na$_2$O$_2$)	3861 mAh g^{-1} (Li) 1168 mAh g^{-1} (Li$_2$O$_2$)
Energy density	1108 Wh kg^{-1} (NaO$_2$) 1605 Wh kg^{-1} (Na$_2$O$_2$)	3458 Wh kg^{-1} (Li$_2$O$_2$)

In terms of cost, substituting lithium by sodium offers additional benefits: (i) sodium salts used in the electrolyte are more abundant than equivalent lithium salts, making them both cheap and easily obtainable[89] and (ii) in contrast to lithium, sodium does not dissolve in aluminium, which enables the use of thin aluminium foil as a light and low-cost anode current collector (Li-O_2 batteries require the use of copper or nickel). In addition, the electrochemistry of a Na-O_2 cell might share similarities with that of Li-O_2 cells and, therefore, the extensive knowledge gathered during the last two decades on Li-O_2 batteries[21] can be applied, with a degree of caution, to Na-O_2 batteries. For

example, stability of electrolytes, effective architectures of cathode supports, and even some degradation aspects from Li-O$_2$ cells pave the way for the initial design of Na-O$_2$ systems. All these advantages make the development of a potentially sustainable and affordable Na-O$_2$ battery of high technological interest.

1.3.2. Controversy on the discharge products

The interest in Na-O$_2$ batteries has unequivocally increased since Peled *et al.*[90] reported the first cell in 2011 using molten Na as anode. High cell impedance and dendrite formation, previously reported for Li-O$_2$ batteries, were overcome at 100 °C leading to coulombic efficiencies of ~ 85%. In 2012, Prof. Janek's group successfully constructed a Na-O$_2$ battery at room temperature[85] where cubic NaO$_2$ was found as the sole discharge product. This is in contrast to Li-O$_2$ batteries where lithium peroxide (Li$_2$O$_2$) is the main discharge product. This was the first indication of the important differences between these two, otherwise similar, alkali M-O$_2$ systems, which prompted a flurry of interest.

NaO$_2$ is not, however, the sole discharge product described in literature since then. Several authors have reported the formation of Na$_2$O$_2$ on the cathode after discharge, usually crystallized with two water molecules (Na$_2$O$_2$·2H$_2$O)[91–94]. This has, therefore, motivated several works in order to clarify such controversy. Density functional theory (DFT) calculations performed by Kang *et al.*[95] argued that due to the very similar equilibrium potentials for the formation of both NaO$_2$ (2.27 V) and Na$_2$O$_2$ (2.33 V), the competition between surface and bulk energy should ultimately drive the preference to form one of them. These authors concluded that Na$_2$O$_2$ is the most stable bulk phase, whereas NaO$_2$ is preferred at the nanoscale. These results, however, are in contrast with the DFT results of Lee *et al.*,[96] where NaO$_2$ was predicted to be the most stable phase at standard conditions (300 K and 1 atm). From an experimental viewpoint, Yadegari *et al.*[97] found that both superoxide and peroxide were formed during

discharge. The charge profile revealed three plateaus, where the superoxide is firstly removed in the lower plateau, whereas peroxide oxidation takes place at higher potentials. This study is in stark contrast with those reported by Janek's,[98] Luntz's[22] and Shao-Horn's[99] groups where NaO_2 was the only discharge product. In addition, Janek *et al.*[98] compared different carbon electrodes (H2315, SFG-44, Super PLi, Kentjenblack EC 600JD, HSAG 500 and SCR-1) without any evidence of peroxide formation. Furthermore, McCloskey *et al.*[22] confirmed that both oxygen reduction reaction (ORR) and oxygen evolution reaction (OER) were 1 e$^-$ / O_2 processes by means of differential electrochemical mass spectrometry (DEMS), unequivocally demonstrating the exclusive formation and decomposition of NaO_2. In contrast, in the Li-O_2 cell, e$^-$ / O_2 ratio during OER increased evidencing the presence of side reactions. The lower efficiency in the Li-O_2 cell was attributed to the higher reactivity of the discharge product Li_2O_2 compared to NaO_2.

Ortiz-Vitoriano *et al.*[99] also showed NaO_2 as the only discharge product from Na-O_2 cells with carbon nanotubes from X-ray diffraction and Raman spectroscopy. $Na_2O_2 \cdot 2H_2O$ was, however, detected when operating at ambient air exposure, even though it was not found with up to 6000 ppm of H_2O added to the electrolyte.

Despite the evidence provided by Ortiz-Vitoriano *et al.,*[99] it cannot be ensured that the formation of $Na_2O_2 \cdot 2H_2O$ is due, in all cases, to water vapour contamination. What is clear is that both the overpotential and instability are lower when the discharge product is NaO_2[22,98,99] than $Na_2O_2 \cdot 2H_2O$[91–94]. This highlights the need to develop in situ methods to monitor and analyse the discharge product chemistry and to give insight into the poor cyclability of $Na_2O_2 \cdot 2H_2O$.

1.3.3. Insight into the reaction mechanism

Janek and coworkers have proposed two possible mechanisms for NaO_2 growth:[98,100] (i) a solution mediated path where superoxide ions formed on the electrode surface are

dissolved in the electrolyte until they precipitate and grow on previously formed nuclei; and (ii) a surface mediated path where the ORR directly occurs on the surface of these nuclei. An indispensable condition for the surface mechanism is that the discharge product has to conduct electrons from the electrode surface to the NaO_2 / electrolyte interface. However, DFT studies on the intrinsic conductivity of NaO_2 bulk, surface, and nanoparticles[101,102] have found that NaO_2 is an electronic insulator. The solution mediated mechanism, therefore, arises as the most realistic approach for NaO_2 growth, which has been recently confirmed by charge / discharge studies using a dual-working cell[29].

Interestingly, Nazar's group[103] investigated the role of residual water in the electrolyte and proposed a mechanism where oxygen is reduced on the electrode surface and "accommodated" in the solution forming HO_2 with protons of the residual water, driving to a solution mediated growth of NaO_2 crystals. Essentially, water acts as a phase-transfer catalyst on both ORR and OER. In absence of water, NaO_2 grows in thin-film shape, resulting in a negligible discharge capacity due to the insulating nature of NaO_2.

Another key aspect influencing battery performance is the design of the cathode. Janek and coworkers identified the limiting effect of oxygen transport in discharge capacity using Scanning Electron Microscopy (SEM) and Energy-dispersive X-ray spectroscopy (EDS)[85]. They concluded that electrode areas in direct contact with oxygen gas during discharge showed high concentrations of discharge product, while less oxygen-exposed areas showed negligible concentrations. This highlights the need for achieving an extensive utilization of the cathode material in order to maximize discharge capacity. Consequently, carbon electrode design has been widely optimized in this field to enhance the capacity and cycle life[93,104–106].

1.4. Summary

M-O$_2$ batteries are projected to be an alternative as suppliers for high energy demanding systems such as EVs and HEVs. Li-O$_2$ has been one of the most studied M-O$_2$ systems due to its high theoretical energy density, based on the reduction of molecular oxygen in a porous cathode leading to the formation of insoluble Li$_2$O$_2$ that is accumulated in this cathode and later oxidized again to O$_2$ during the recharge of the battery.

Although theoretically extraordinary, the practical performance of Li-O$_2$ batteries has not matched the expectations: the reactive nature of the oxygen reduction products has complicated the selection of an appropriate electrolyte due to the formation of hardly reversible carbonates. In addition, Li$_2$O$_2$ is an insulating product responsible for a high overpotential in charge reaction that leads to decomposition of the cell components (i.e. carbon electrode and electrolyte).

In the recent years, the initially intermediate-product considered LiO$_2$ has unexpectedly been detected in both the electrolyte and the discharge solid deposit. Superoxide can be reverted at lower overpotential and can therefore lead to an enhanced cyclability of the cell due to the decrease of side reactions. Nevertheless, LiO$_2$ is even more reactive than peroxide and its stabilization therefore plays a key role in the design of the cell. The improved reversibility obtained by superoxide, however, is traduced in a 1 e$^-$ reduction process (vs. the 2 e$^-$ reduction of Li$_2$O$_2$), what decreases the energy density of the battery, its main characteristic.

Two main strategies have been followed in order to improve the performance of the cell; on one hand, carbon has been substituted by alternative materials less susceptible to nucleophilic attack. On the other hand, catalysts have been used to improve ORR and OER. The analysis of heterogeneous catalysts has been a popular field in Li-O$_2$

research, while in the recent years homogeneous catalysts are gaining interest due to the improvement on OER and therefore on the cyclability of the cell.

Some other authors, due to the previously described difficulties, recently decided to replace lithium by sodium and study Na-O$_2$ batteries. Still in its early stages, one of the hotspot in these batteries has been the difference in the discharge products reported by different authors; NaO$_2$, Na$_2$O$_2$ and Na$_2$O$_2$·2H$_2$O have been reported as discharge products. Similarly to Li-O$_2$ technology superoxide has demonstrated to be reversible at lower overpotential. In addition, it has been confirmed that superoxide is formed in the oxygen electrode, stabilized in the electrolyte, and deposited in cubic morphology after saturation in the electrolyte, mediated by residual protons. In addition, this stabilization is considered the responsible for the "cleaner" cell chemistry of Na-O$_2$ batteries compared to Li-O$_2$. Nevertheless, as occurred for Li-O$_2$ batteries based on LiO$_2$ formation and removal, energy density is lower for 1 e$^-$ processes and become therefore less appealing for EV and HEV applications.

1.5. Scope of this thesis

Chapter 1 is a general introduction to the Li- and Na-O$_2$ research undertaken during the last years. Some of these paragraphs are reproduced from the following publications: Landa-Medrano, I.; Li, C.; Ortiz-Vitoriano, N.; Ruiz de Larramendi, I.; Carrasco, J.; Rojo, T. J. Phys. Chem. Lett. 2016, 7, 1161–1166 (Copyright 2016: American Chemical Society) and Landa-Medrano, I.; Pinedo, R.; Ortiz-Vitoriano, N.; Ruiz de Larramendi, I.; Rojo, T. ChemSusChem 2015, 8, 3932–3940 (Copyright 2015: Wiley Publishing Group). The experimental details and techniques required for the development of this thesis are overviewed in Chapter 2. Chapter 3 is a detailed analysis of the ORR and OER reactions in Li-O$_2$ batteries and has been published elsewhere: Landa-Medrano, I.; Ruiz de Larramendi, I.; Ortiz-Vitoriano, N.; Pinedo, R.; Ruiz de Larramendi, J. I.; Rojo, T. J. Power Sources 2014, 249, 110–117 (Copyright 2014: Elsevier) and Landa-

Medrano, I.; Pinedo, R.; Ruiz de Larramendi, I.; Ortiz-Vitoriano, N. J. Electrochem. Soc. 2015, 162 (2), 3126–3132 (Copyright 2015: The Electrochemical Society). Chapter 4 includes the strategies followed to improve the electrochemical performance of Li-O$_2$ batteries and part of its content was published in Landa-Medrano, I.; Olivares-Marín, M.; Pinedo, R.; Ruiz de Larramendi, I.; Rojo, T.; Tonti, D. Electrochem. Commun. 2015, 59, 24–27 (Copyright 2015: Elsevier). Chapter 5 explores the identification, evolution and stability of the discharge products in Na-O$_2$ and was partially published in Landa-Medrano, I.; Pinedo, R.; Bi, X.; Ruiz de Larramendi, I.; Lezama, L.; Janek, J.; Amine, K.; Lu, J.; Rojo, T. ACS Appl. Mater. Interfaces 2016, 8 (31), 20120–20127 (Copyright 2016: American Chemical Society). Chapter 6 includes the analysis of the composition of the Na-O$_2$ discharge deposits by transmission X-ray microscopy. The use of ethyl viologen ditriflate redox mediator in Na-O$_2$ batteries is explored in Chapter 7. Finally, Chapter 8 consists of a brief summary and the main conclusion of this thesis.

1.6. References

(1)   Borden, E.; Schill, W.-P. *Policy Efforts for the Development of Storage Technologies in the U.S. and Germany*; **2013**.

(2)   Commission, E. *Investing in European success. HORIZON 2020*; **2013**.

(3)   Grande, L.; Paillard, E.; Hassoun, J.; Park, J.-B.; Lee, Y.-J.; Sun, Y.-K.; Passerini, S.; Scrosati, B. *Adv. Mater.* **2014**, *27* (5), 784–800.

(4)   De Carolis, J. F.; Keith, D. W. *Energy Policy* **2006**, *34*, 395–410.

(5)   Barton, J. P.; Infield, D. G. *IEEE Trans. Energy Convers.* **2004**, *19*, 441–448.

(6)   Tarascon, J. M.; Armand, M. *Nature* **2001**, *414* (6861), 359–367.

(7)   Armand, M.; Tarascon, J.-M. *Nature* **2008**, *451* (7179), 652–657.

(8)   Goodenough, J. B. *J. Power Sources* **2007**, *174* (2), 996–1000.

(9)   Nazri, G.-A.; Pistoia, G. *Lithium Batteries: Science and Technology*; Springer Berlin,

2003.

(10)   Whittingham, M. S. *Chem. Rev.* **2004**, *104*, 4271–4302.

(11)   Rahman, A.; Wang, X.; Wen, C. *J. Electrochem. Soc.* **2013**, *160* (10).

(12)   Hassoun, J.; Jung, H.-G.; Lee, D.-J.; Park, J.-B.; Amine, K.; Sun, Y.-K.; Scrosati, B. *Nano Lett.* **2012**, *12* (11), 5775–5779.

(13)   Lu, J.; Li, L.; Park, J.; Sun, Y.; Wu, F.; Amine, K. *Chem. Rev.* **2014**, *114* (11), 5611–5640.

(14)   Bennion, D. N.; Littauer, E. L. *J. Electrochem. Soc.* **1976**, *123*, 1462–1469.

(15)   Littauer, E. L.; Tsai, K. C. *J. Electrochem. Soc.* **1976**, *123*, 771–776.

(16)   Gibian, M. J.; Sawyer, D. T.; Ungermann, T.; Tangpoonpholvivat, R.; Morrison, M. M. *J. Am. Chem. Soc.* **1979**, *101*, 640–644.

(17)   Abraham, K. M.; Jiang, Z. *Electrochem. Sci. Technol.* **1996**, *143* (1), 1–5.

(18)   Rahman, A.; Wang, X. *J. Appl. Electrochem.* **2014**, *1*, 5–22.

(19)   Abraham, K. M. *J. Electrochem. Soc.* **2014**, *162* (2), A3021–A3031.

(20)   O'Laoire, C.; Mukerjee, C. S.; Abraham, K. M.; Plichta, E. J.; Hendrickson, M. A. *J. Phys. Chem. C* **2009**, *113*, 20127–20134.

(21)   Luntz, A. C.; Mccloskey, B. D. *Chem. Rev.* **2014**, *114* (23), 11721–11750.

(22)   Mccloskey, B. D.; Garcia, J. M.; Luntz, A. C. *J. Phys. Chem. Lett.* **2014**, *5*, 1230–1235.

(23)   Giordani, V.; Bryantsev, V. S.; Uddin, J.; Walker, W.; Chase, G. V; Addison, D. *ECS Electrochem. Lett.* **2014**, *3* (1), 11–14.

(24)   Zhai, D.; Wang, H.; Yang, J.; Lau, K. C.; Li, K.; Amine, K.; Curtiss, L. A. *J. Am. Chem. Soc.* **2013**, *135*, 15364–15372.

(25)   Zhai, D.; Wang, H.; Lau, K. C.; Gao, J.; Redfern, P. C.; Kang, F.; Li, B.; Indacochea, E.;

Das, U.; Sun, H.; Sun, H.; Amine, K.; Curtiss, L. A. *J. Phys. Chem. Lett.* **2014**, *5*, 2705–2710.

(26)   Zhai, D.; Lau, K. C.; Wang, H.-H.; Wen, J.; Miller, D. J.; Lu, J.; Kang, F.; Li, B.; Yang, W.; Gao, J.; Indacochea, E.; Curtiss, L. a; Amine, K. *Nano Lett.* **2015**, *2014* (1), 1–6.

(27)   Olivares-Marín, M.; Sorrentino, A.; Lee, R.-C.; Pereiro, E.; Wu, N.-L.; Tonti, D. *Nano Lett.* **2015**, *15* (10), 6932–6938.

(28)   Lu, J.; Lee, Y. J.; Luo, X.; Lau, K. C.; Asadi, M.; Wang, H.; Brombosz, S.; Wen, J.; Zhai, D.; Chen, Z.; Miller, D. J.; Jeong, Y. S.; Park, J.; Fang, Z. Z.; Kumar, B.; Salehi-khojin, A.; Sun, Y.; Curtiss, L. A.; Amine, K. *Nature* **2016**, *529*, 377–382.

(29)   Johnson, L.; Li, C.; Liu, Z.; Chen, Y.; Freunberger, S. a.; Tarascon, J.-M.; Ashok, P. C.; Praveen, B. B.; Dholakia, K.; Bruce, P. G. *Nat. Chem.* **2014**, *6*, 1091–1099.

(30)   Adams, B. D.; Radtke, C.; Black, R.; Trudeau, M. L.; Zaghib, K.; Nazar, L. F. *Energy Environ. Sci.* **2013**, *6*, 1772–1778.

(31)   Aetukuri, N. B.; McCloskey, B. D.; García, J. M.; Krupp, L. E.; Viswanathan, V.; Luntz, A. C. *Nat. Chem.* **2014**, *7*, 50–56.

(32)   Freunberger, S. A.; Chen, Y.; Peng, Z.; Griffin, J. M.; Hardwick, L. J.; Bardé, F.; Novák, P.; Bruce, P. G. *J. Am. Chem. Soc.* **2011**, *133*, 8040–8047.

(33)   Schwenke, K. U.; Meini, S.; Wu, X.; Gasteiger, H. a; Piana, M. *Phys. Chem. Chem. Phys.* **2013**, *15* (28), 11830–11839.

(34)   Frith, J. T.; Russell, A. E.; Garcia-araez, N.; Owen, J. R. *Electrochem. commun.* **2014**, *46*, 33–35.

(35)   Kwabi, D. G.; Batcho, T. P.; Amanchukwu, C. V.; Ortiz-Vitoriano, N.; Hammond, P.; Thompson, C. V.; Shao-Horn, Y. *J. Phys. Chem. Lett.* **2014**, *5* (16), 2850–2856.

(36)   Pearson, R. G. *J. Am. Chem. Soc.* **1963**, *85* (22), 3533–3539.

(37)   Zheng, D.; Lee, H.-S.; Yang, X.-Q.; Qu, D. *Electrochem. commun.* **2013**, *28*, 17–19.

(38)   Højberg, J.; McCloskey, B. D.; Hjelm, J.; Vegge, T.; Johansen, K.; Norby, P.; Luntz, A. C. *ACS Appl. Mater. Interfaces* **2015**, *7*, 4039–4047.

(39)   McCloskey, B. D.; Speidel, A.; Scheffler, R.; Miller, D. C.; Viswanathan, V.; Hummelshøj, J. S.; Nørskov, J. K.; Luntz, A. C. *J. Phys. Chem. Lett.* **2012**, *3*, 997–1001.

(40)   McCloskey, B. D.; Valery, A.; Luntz, A. C.; Gowda, S. R.; Wallra, G. M.; Garcia, J. M.; Mori, T.; Krupp, L. E. *J. Phys. Chem. Lett.* **2013**, *4*, 2989–2993.

(41)   Lim, H.-K.; Lim, H.-D.; Park, K.-Y.; Seo, D.-H.; Gwon, H.; Hong, J.; Goddard, W. a; Kim, H.; Kang, K. *J. Am. Chem. Soc.* **2013**, *135* (26), 9733–9742.

(42)   Girishkumar, G.; McCloskey, B.; Luntz, A. C.; Swanson, S.; W. Wilcke. *J. Phys. Chem. Lett.* **2010**, *1*, 2193–2203.

(43)   Cao, R.; Lee, J.-S.; Liu, M.; Cho, J. *Adv. Energy Mater.* **2012**, *2* (7), 816–829.

(44)   Ottakam Thotiyl, M. M.; Freunberger, S. a; Peng, Z.; Bruce, P. G. *J. Am. Chem. Soc.* **2013**, *135* (1), 494–500.

(45)   Cui, Y.; Wen, Z.; Liu, Y. *Energy Environ. Sci.* **2011**, *4*, 4727–4734.

(46)   Peng, Z.; Freunberger, S. a; Chen, Y.; Bruce, P. G. *Science* **2012**, *337* (6094), 563–566.

(47)   Thotiyl, M. M. O.; Freunberger, S. A.; Peng, Z.; Chen, Y.; Liu, Z.; Bruce, P. G. *Nat. Mater.* **2013**, *4*, 1–16.

(48)   Cui, Y.; Wen, Z.; Liu, Y. *Energy Environ. Sci.* **2011**, *4*, 4727–4734.

(49)   Riaz, A.; Jung, K.-N.; Chang, W.; Lee, S.-B.; Lim, T.-H.; Park, S.-J.; Song, R.-H.; Yoon, S.; Shin, K.-H.; Lee, J.-W. *Chem. Commun.* **2013**, *49*, 5984–5986.

(50)   Lee, H.; Kim, Y.; Jin, D.; Song, J.; Min, Y. *J. Mater. Chem. A* **2014**, *2*, 11891–11899.

(51)   Yu, Y.; Zhang, B.; Xu, Z.-L.; He, Y.-B.; Kim, J.-K. *Solid State Ionics* **2013**, *4*, 2–6.

(52)   Hu, X.; Han, X.; Hu, Y.; Cheng, F.; Chen, J. *Nanoscale* **2014**, *6*, 3522–3525.

(53)   Lin, X.; Shang, Y.; Huang, T.; Yu, A. *Nanoscale* **2014**, *6*, 9043–9049.

(54)   Kundu, D.; Black, R.; Jämstorp, E.; Nazar, L. *Energy Environ. Sci.* **2014**, *8*, 1292–1298.

(55)   Liao, K.; Wang, X.; Sun, Y.; Tang, D.; Han, M.; He, P.; Jiang, X.; Zhang, T.; Zhou, H. *Energy Environ. Sci.* **2015**, *8*, 1992–1997.

(56)   Peng, Z.; Freunberger, S. A.; Chen, Y.; Bruce, P. G. *Science (80-.).* **2012**, *563*, 563–566.

(57)   Li, F.; Tang, D.; Zhang, T.; Liao, K.; He, P.; Golberg, D. **2015**, 2–7.

(58)   Chen, L.; Guo, X.; Han, J.; Liu, P.; Xu, X.; Hirata, A.; Chen, M. *J. Mater. Chem. A* **2015**, *3*, 3620–362.

(59)   Thotiyl, M. M. O.; Freunberger, S. A.; Peng, Z.; Chen, Y.; Liu, Z.; Bruce, P. G. *Nat. Mater.* **2013**, *12*, 1050–1056.

(60)   Cui, Y.; Wen, Z.; Liang, X.; Lu, Y.; Jin, J.; Wu, M.; Wu, X. *Energy Environ. Sci.* **2012**, *5* (7), 7893.

(61)   Lu, Y.-C.; Xu, Z. C.; Gasteiger, H. A.; Chen, S.; Hamad-Schifferli, K.; Shao-Horn, Y. *J. Am. Chem. Soc.* **2010**, *132*, 12170–12171.

(62)   Thapa, A. K.; Ishihara, T. *J. Power Sources* **2011**, *196*, 7016–7020.

(63)   Lu, Y.-C.; Gasteiger, H. a; Shao-Horn, Y. *J. Am. Chem. Soc.* **2011**, *133* (47), 19048–19051.

(64)   Harding, J. R.; Lu, Y.-C.; Tsukada, Y.; Shao-Horn, Y. *Phys. Chem. Chem. Phys.* **2012**, *14* (30), 10540–10546.

(65)   Zhang, W.; Zeng, Y.; Xu, C.; Tan, H.; Liu, W.; Zhu, J.; Xiao, N.; Hng, H. H.; Ma, J.; Hoster, H. E.; Yazami, R.; Yan, Q. *RSC Adv.* **2012**, *2* (22), 8508–8514.

(66)   Ryu, W.; Yoon, T.; Song, S. H.; Jeon, S.; Park, Y.; Kim, I. *Nano Lett.* **2013**, *13*, 4190–4197.

(67)   Lee, Y.; Suntivich, J.; May, K. J.; Perry, E. E.; Shao-horn, Y. *J. Phys. Chem. Lett.* **2012**, *3*, 399–404.

(68) Lu, J.; Qin, Y.; Du, P.; Luo, X.; Wu, T.; Ren, Y.; Wen, J.; Miller, D. J.; Miller, J. T.; Amine, K. *RSC Adv.* **2013**, *3*, 8276–8285.

(69) Zhao, Y.; Xu, L.; Mai, L.; Han, C.; An, Q.; Xu, X.; Liu, X.; Zhang, Q. *Proc. Natl. Acad. Sci. U. S. A.* **2012**, *109* (48), 19569–19574.

(70) Cao, Y.; Wei, Z.; He, J.; Zang, J.; Zhang, Q.; Zheng, M.; Dong, Q. *Energy Environ. Sci.* **2012**, *5*, 9765–9768.

(71) Shui, J.-L.; Karan, N. K.; Balasubramanian, M.; Li, S.-Y.; Liu, D.-J. *J. Am. Chem. Soc.* **2012**, *134* (40), 16654–16661.

(72) Wu, G.; Mack, N. H.; Gao, W.; Zhong, R.; Han, J.; Baldwin, J. K.; Zelenay, P. *ACS Nano* **2012**, *6* (11), 9764–9776.

(73) McCloskey, B. D.; Scheffler, R.; Speidel, A.; Bethune, D. S.; Shelby, R. M.; Luntz, A. C. *J. Am. Chem. Soc.* **2011**, *133*, 18038–18041.

(74) McCloskey, B. D.; Scheffler, R.; Speidel, A.; Girishkumar, G.; Luntz, A. C. *J. Phys. Chem. C* **2012**, *116*, 23897–23905.

(75) Lim, H.; Song, H.; Kim, J.; Gwon, H.; Bae, Y.; Park, K.; Hong, J.; Kim, H.; Kim, T.; Kim, Y. H.; Lepró, X.; Ovalle-, R.; Baughman, R. H.; Kang, K. *Angew. Chemie* **2014**, *126* (15), 4007–4012.

(76) Chen, Y.; Freunberger, S. A.; Peng, Z.; Fontaine, O.; Bruce, P. G. *Nat. Chem.* **2013**, *5*, 489–494.

(77) Sun, D.; Shen, Y.; Zhang, W.; Yu, L.; Yi, Z.; Yin, W.; Wang, D.; Huang, Y.; Wang, J.; Wang, D.; Goodenough, J. B. *J. Am. Chem. Soc.* **2014**, *136* (25), 8941–8946.

(78) Bergner, B. J.; Schürmann, A.; Peppler, K.; Garsuch, A.; Janek, J. *J. Am. Chem. Soc.* **2014**, *136* (42), 15054–15064.

(79) Kim, D. S.; Park, Y. J. *J. Alloys Compd.* **2014**, *591*, 164–169.

(80) Yu, M.; Ren, X.; Ma, L.; Wu, Y. *Nat. Commun.* **2014**, *5*, 5111–5116.

(81)   Liu, T.; Leskes, M.; Yu, W.; Moore, A. J.; Zhou, L.; Bayley, P. M.; Kim, G.; Grey, C. P. *Science* **2015**, *350* (6260), 530–533.

(82)   Yang, L.; Frith, J. T.; Garcia-Araez, N.; Owen, J. R. *Chem. Commun.* **2015**, *51*, 1705–1708.

(83)   Matsuda, S.; Hashimoto, K.; Nakanishi, S. *J. Phys. Chem. C* **2014**, *118*, 18397–18400.

(84)   Tesio, A. Y.; Blasi, D.; Olivares-Marín, M.; Ratera, I.; Tonti, D.; Veciana, J. *Chem. Commun.* **2015**, *51*, 17623–17626.

(85)   Hartmann, P.; Bender, C. L.; Vračar, M.; Dürr, A. K.; Garsuch, A.; Janek, J.; Adelhelm, P. *Nat. Mater.* **2013**, *12* (3), 228–232.

(86)   Bruce, P. G.; Freunberger, S. a; Hardwick, L. J.; Tarascon, J.-M. *Nat. Mater.* **2012**, *11*, 19–30.

(87)   McCloskey, B. D.; Garcia, J. M.; Luntz, A. C. *J. Phys. Chem. Lett.* **2014**, *5*, 1230–1235.

(88)   Ortiz-Vitoriano, N.; Batcho, T. P.; Kwabi, D. G.; Han, B.; Pour, N.; Yao, K. P. C.; Thompson, C. V.; Shao-Horn, Y. *J. Phys. Chem. Lett.* **2015**, *6*, 2636–2643.

(89)   Hueso, K.; Armand, M.; Rojo, T. *Energy Environ. Sci.* **2013**, *6*, 734–749.

(90)   Peled, E.; Golodnitsky, D.; Mazor, H.; Goor, M.; Avshalomov, S. *J. Power Sources* **2011**, *196* (16), 6835–6840.

(91)   Li, Y.; Yadegari, H.; Li, X.; Banis, M. N.; Li, R.; Sun, X. *Chem. Commun. (Camb).* **2013**, *49* (100), 11731–11733.

(92)   Kim, J.; Lim, H.-D.; Gwon, H.; Kang, K. *Phys. Chem. Chem. Phys.* **2013**, *15* (10), 3623–3629.

(93)   Jian, Z.; Chen, Y.; Li, F.; Zhang, T.; Liu, C.; Zhou, H. *J. Power Sources* **2014**, *251*, 466–469.

(94)   Liu, W.; Sun, Q.; Yang, Y.; Xie, J.-Y.; Fu, Z.-W. *Chem. Commun. (Camb).* **2013**, *49* (19), 1951–1953.

(95) Kang, S.; Mo, Y.; Ong, S. P.; Ceder, G. *Nano Lett.* **2014**, *14* (2), 1016–1020.

(96) Lee, B.; Seo, D.; Lim, H.; Park, I.; Park, K.; Kim, J.; Kang, K. *Chem. Mater.* **2014**, *26* (2), 1048–1055.

(97) Yadegari, H.; Li, Y.; Norouzi Banis, M.; Li, X.; Wang, B.; Sun, Q.; Li, R.; Sham, T.-K.; Cui, X.; Sun, X. *Energy Environ. Sci.* **2014**, *7*, 3747–3757.

(98) Bender, C. L.; Hartmann, P.; Vračar, M.; Adelhelm, P.; Janek, J. *Adv. Energy Mater.* **2014**, *4* (12), n/a – n/a.

(99) Ortiz-Vitoriano, N.; Batcho, T. P.; Kwabi, D. G.; Pour, N. *J. Phys. Chem. Lett. Phys.* **2015**, 1–13.

(100) Hartmann, P.; Heinemann, M.; Bender, C. L.; Graf, K.; Baumann, R.-P.; Adelhelm, P.; Heiliger, C.; Janek, J. *J. Phys. Chem. C* **2015**, *119* (40), 22778–22786.

(101) Yang, S.; Siegel, D. J. *Chem. Mater.* **2015**, *27* (11), 3852–3860.

(102) Arcelus, O.; Li, C.; Rojo, T.; Carrasco, J. *J. Phys. Chem. Lett.* **2015**, *6*, 2027–2031.

(103) Xia, C.; Black, R.; Fernandes, R.; Adams, B.; Nazar, L. F. *Nat. Chem.* **2015**, *7*, 496–501.

(104) Kwak, W.-J.; Chen, Z.; Yoon, C. S.; Lee, J.-K.; Amine, K.; Sun, Y.-K. *Nano Energy* **2015**, *12*, 123–130.

(105) Bender, C. L.; Bartuli, W.; Schwab, M. G.; Adelhelm, P.; Janek, J. *Energy Technol.* **2015**, *3* (3), 242–248.

(106) Sun, Q.; Yadegari, H.; Banis, M. N.; Liu, J.; Xiao, B.; Wang, B.; Lawes, S.; Li, X.; Li, R.; Sun, X. *Nano Energy* **2015**, *12*, 698–708.

Chapter 2 – Experimental methods

This thesis analyzes lithium- and sodium-oxygen batteries by means of multiple electrochemical and characterization techniques. Materials preparation, working conditions, electrochemical cells and experimental methods followed are detailed in this chapter.

2.1. Materials synthesis

NiO and Co_3O_4 used in Chapter 4 to replace carbon as electrode material were prepared following the experimental process reported by Lin *et al.*[1] 6 mmol of the corresponding nitrates (nickel(II) nitrate hexahydrate, ≥96%, Sigma-Aldrich and Cobalt(II) nitrate hexahydrate, ≥98%, Sigma-Aldrich) were dissolved together with 7.5 mmol ($CO(NH_2)_2$, Sigma-Aldrich) in 30 ml deionized water under stirring. Solutions were transferred to teflon-lined stainless steel autoclaves and heated at 90 °C for 8 hours. After that solutions were filtered and the precipitate was rinsed with ethanol and deionized water and dried at 80 °C overnight. Powder was finally calcined at 300 °C for 4 h in air.

The MnO_2 catalyst studied in Chapter 4 was synthesized by using mild hydrothermal conditions under autogeneous pressure. Stechiometric manganese (II) sulfate monohydrate ($MnSO_4 \cdot H_2O$ ≥98%, Sigma-Aldrich) and ammonium persulfate (($NH_4)_2S_2O_8$, 98%, Sigma-Aldrich) were dissolved in deionized water while stirring. The colorless solution was transferred into a Teflon-lined stainless steel autoclave and maintained at 120 °C for 2 hours. The black precipitate formed was filtered in vacuum and washed several times using deionized water and ethanol. The precipitate was dried in air at room temperature.

2.2. Electrochemical methods

2.2.1. Electrochemical cells

Different electrochemical cells have been used during the development of this thesis. These cells will be shown in the following lines.

2.2.1.1. 2-electrode cell

Experiments in Chapter 3 were performed using the modified Swagelok cell developed in collaboration with CIC Energigune and shown in Figure 2.1.
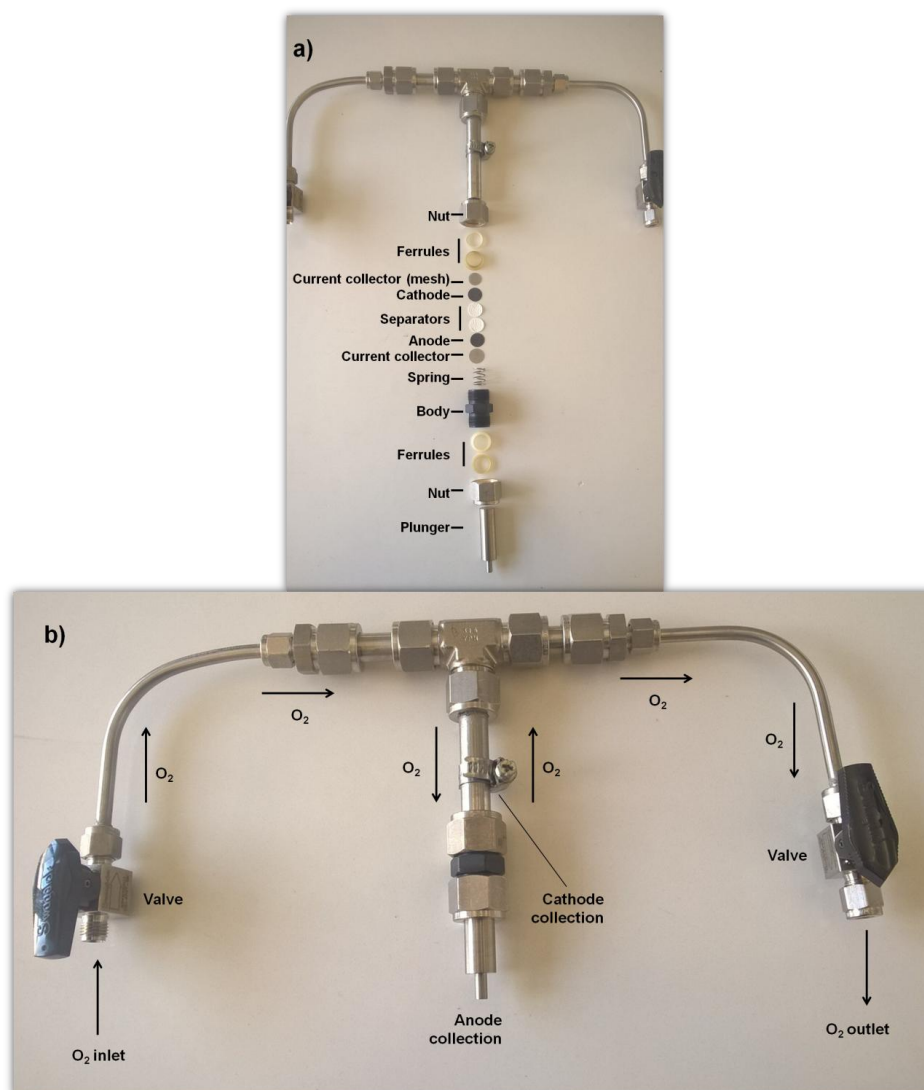

Figure 2.1. (a) Identification of the components of the 2-electrode Swagelok cell. (b) Picture of the cell assembled and schematic representation of the O_2 route when replacing Ar by O_2.

Figure 2.1.a shows the different components inside the 2-electrode cell. These components are placed in the cell following the order detailed in this figure. It is referred as 2-electrode cell as the lithium used as anode acts as both reference and counter electrode (RE and CE, respectively). On the other hand, a carbon electrode is used as working electrode (WE). These two electrodes are separated by two pieces of separator (Whatman, grade D) in order to avoid undesired short-circuits, being these electrodes wetted by 150 μL of electrolyte. The body of the cell was manufactured by Polifluor S.L. and was made of polypropylene also in furtherance of avoiding short-circuits. Cells were assembled in a glove box under Ar flux and this Ar was replaced by pure oxygen before the experiments (assembled cell in figure 2.1.b). O_2 was passed for 1 minute and after that the inlet and outlet valves were closed, being the cell ready for the experiments.

2.2.1.2. 3-electrode cell

3-electrode cell, developed in Justus-Liebig-Universität Gießen, is also a Swagelok-based cell, but has some differences compared to the aforementioned 2-electrode cell. Detail on the components is shown in Figure 2.2.a.
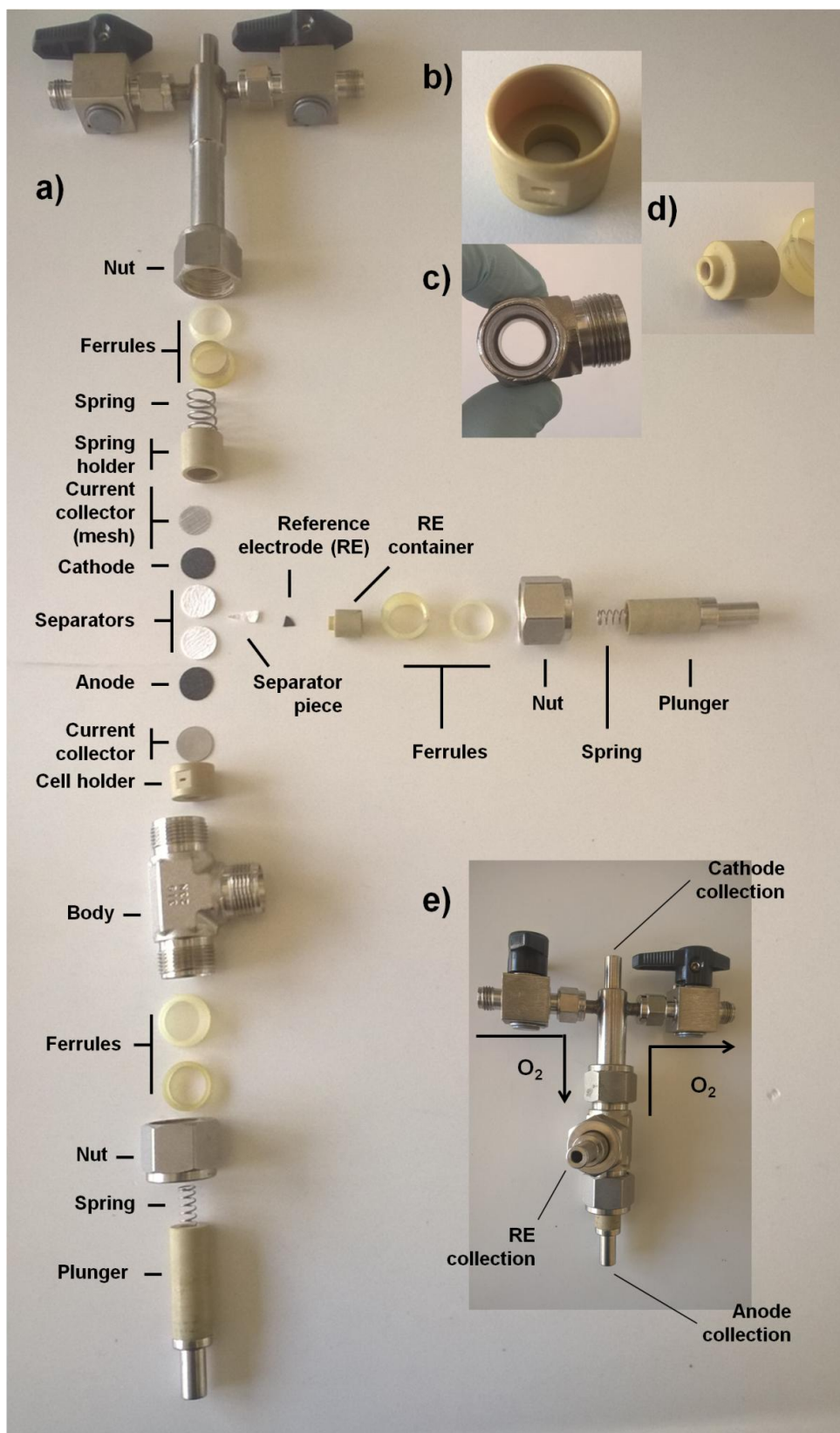
Figure 2.2. (a) Identification of the components of the 3-electrode Swagelok cell. Detail of (b) the cell holder, (c) the body and (d) the reference electrode container. (e) Picture of the 2-electrode cell assembled and schematic representation of the O_2 route when replacing Ar by O_2.

Main difference between 2- and 3-electrode cells relies on the presence of third electrode in this last one, which is used as a reference electrode. In addition, CE (anode), the two separators, WE (cathode) and both anode and cathode current collector are placed in a polyether ether ketone (PEEK) cell holder (see detail of the cell holder in Figure 2.2.b). This cell holder has a lateral hole that is used to intercalate a small piece of electrolyte-wetted separator that connects RE to the rest of the cell components. In addition, the cell body has a smaller diameter in one of its vertical entrances (detail in Figure 2.2.c) in order to keep the lateral hole of the cell holder aligned with the lateral entrance of the body where RE is placed. A small piece of the same metal used is the CE is placed in the RE container (Figure 2.2.d). Finally, Ar from the glovebox is replaced by Ar the same way as explained for the 2-electrode cell (Figure 2.2.e).

This electrochemical set up was used for the experiments in Chapters 4, 5 and 6; the presence of a third electrode that is not galvanostatically oxidized or reduced facilitates the analysis of the oxygen electrode as will be demonstrated in Chapter 5. The experiments in Charper 6 were performed using a 2 electrode set up as in this chapter the electrochemical performance is not analyzed in detail and the interest is focused on the composition of the discharge products.

2.2.1.3. *In situ* ultraviolet-visible (UV-vis) spectroscopy cell

In Chapter 4 a home-made cell was built up at ICMAB in furtherance of analyzing the I^-/I_2 redox pair mediation in OER. I_2 and some of its side products are known to absorb visible light and its formation and decomposition was followed using this tool.[2] A schematic representation and a picture of the cell are displayed in Figures 2.3.a and 2.3.b, respectively.
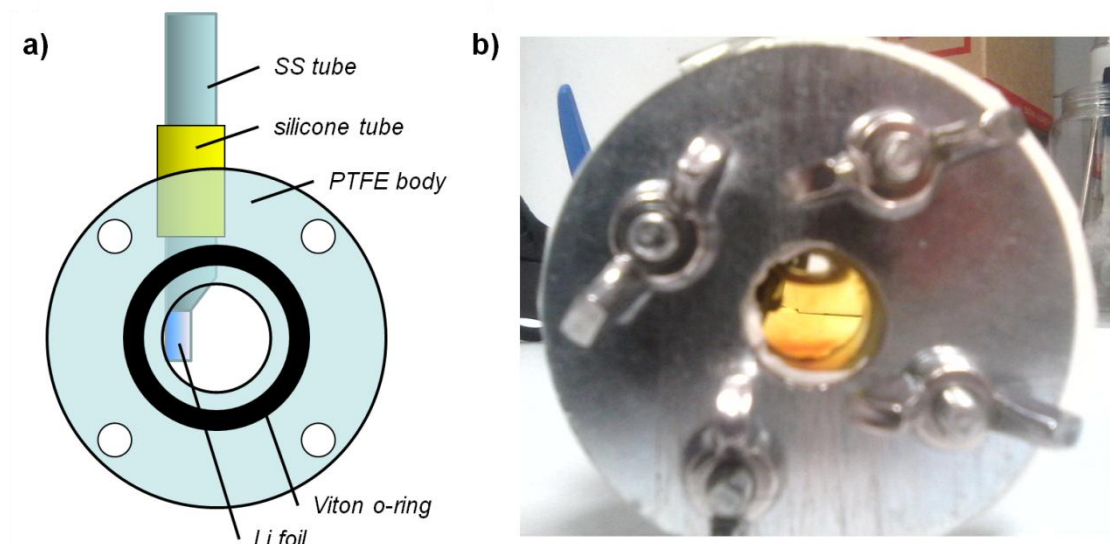
Figure 2.3. (a) Schematic representation and (b) picture of the of the cell used for the in-situ UV-visible spectroscopy.

The cell consisted of a ring-shaped polytetrafluoroethylene (PTFE) piece with a small lateral orifice designed to insert a stainless steel (SS) tube used to both lead oxygen to the electrolyte and electrical contact to the lithium metal anode (CE and RE). Both sides of the central aperture were closed by glass windows, one of them coated with indium-doped tin oxide (ITO), which was used as oxygen electrode (WE).[3] The cell was assembled to a UV-vis spectrophotometer and the formation and elimination of I_2 could be *operando* followed while a cyclic voltammetry was performed.

2.2.1.4. Quartz crystal microbalance (QCM) cell

In Chapter 5 the deposition and decomposition of discharge products in the oxygen electrode of a Na-O_2 battery is analyzed at the University of Southampton by means of the QCM cell shown in Figure 2.4.
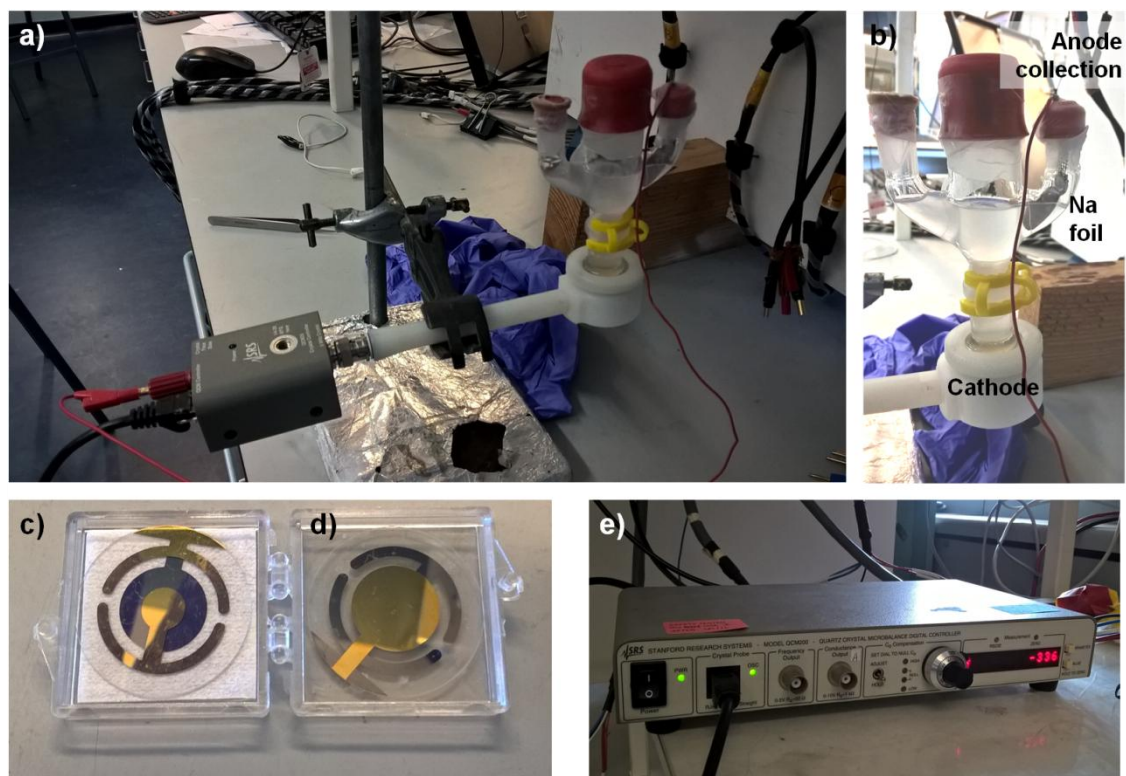
Figure 2.4. (a) Picture of the quartz crystal microbalance measurement system. (b) Picture of the electrochemical cell of the quartz crystal microbalance. (c) Back and (d) front faces of the quartz crystal used as oxygen electrode. (e) Picture of the digital frequency controller used in the measurements.

The complete measurement system (Figure 2.4.a) can be divided into two parts: the electrochemical cell and the frequency analyzer. The electrochemical cell (Figure 2.4.b) consists of a glass container coupled by its lower entrance to the oxygen electrode (WE) container, which is connected to the 5 MHz, 1 inch diameter, AT-cut Au-covered quartz crystal wafer (oxygen electrode) inserted into a holder. Figures 2.4.c and 2.4.d show the back and front face of the WE, respectively, being this last face in contact with the electrolyte.

All the upper entrances of the electrochemical cell were sealed using septum and plastic paraffin film (Parafilm); the central entrance was used to bubble pure oxygen into the electrolyte for 30 minutes by inserting SS needles. Additional SS needles were used to avoid overpressure inside the cell. Moreover, a SS wire was connected to a SS

mesh through the other small entrance and worked as the current collector and holder for the Na foil anode (CE and RE).

The cathode-containing holder was connected to a QCM 200 digital controller (Figure 2.4.e) and ultimately to the potentiostat in order to record concurrently both the frequency variation and the electrochemical experiment.

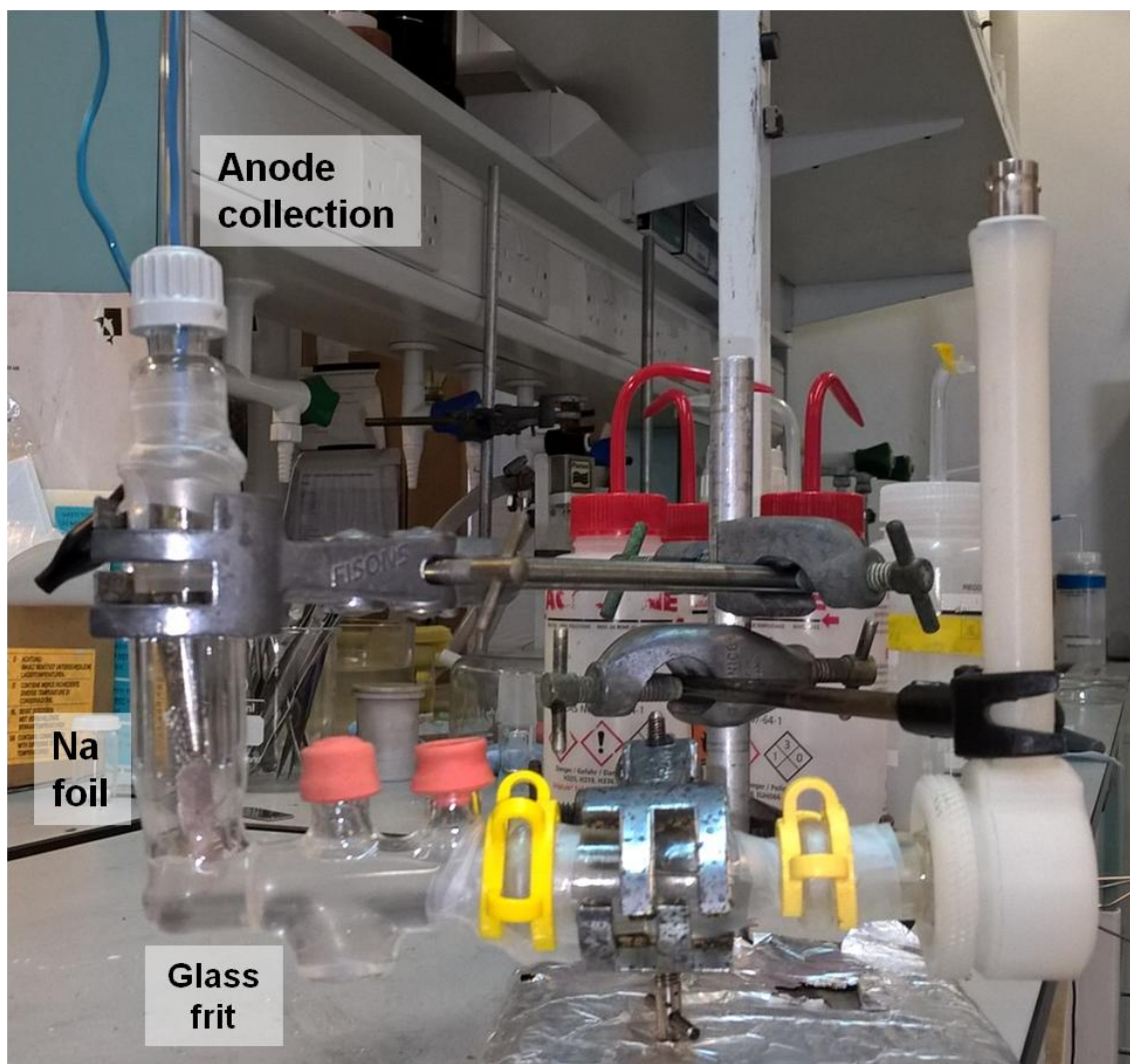The alternative QCM cell set up displayed in Figure 2.5 was also explored.

Figure 2.5. (a) Picture of the alternative electrochemical cell used for the quartz crystal microbalance experiments.

In this set up the glass body was replaced by a glass tube consisting of three different components connected. Oxygen was bubbled for 30 minutes into the cell introducing a

needle trough a septum. One of the main advantages of this set up is that Na electrode is separated from the rest of the cell by a glass frit hindering the migration of oxygen and/or superoxide to this electrode. On the other hand, the cell was electrochemically demonstrated to have leaks (Chapter 5) and was therefore used to analyze the accumulation and elimination of discharge products in presence of water.

<u>2.2.1.5. U-cell</u>

Cyclic voltammetry experiments in Chapters 5 and 7 were performed at the University of Southampton using the *U-cell* in Figure 2.6. This cell consisted of two glass compartments separated by a glass frit. A glassy carbon electrode and a Na foil pressed onto a SS mesh were used as cathode (WE) and anode (CE and RE), respectively. Both compartments had two entrances; the entrances in the cathode side were used to bubble oxygen for 10 minutes into the electrolyte and reduce overpressure same way as in the experiments with QCM.
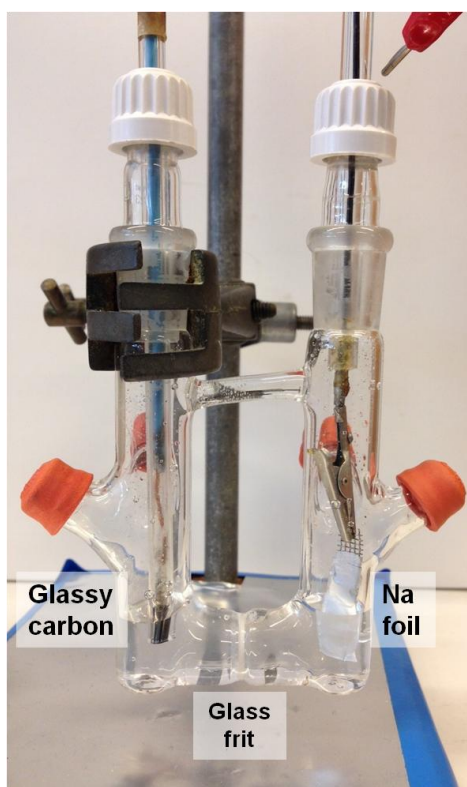

Figure 2.6. (a) Picture of U-cell used for CV experiments in Chapters 5 and 7.

2.2.2. Electrode preparation

2.2.2.1. Li-O_2 experiments (Chapters 3 and 4)

The oxygen electrodes in Chapter 3 consisted of carbon black (C-Nergy Super C-65) and PTFE (Sigma Aldrich) as the binder in a weight ratio of 9:1. Ethanol was used as the dispersing agent to form slurry that was kept under stirring overnight. The slurry was air-brushed over a stainless steel mesh (Alfa Aesar, 0.05 mm wire diameter), which works as current collector at the cathode side, and left drying at room temperature for a week in air. Finally, 10 mm diameter electrodes with carbon loadings between 0.20 and 1.32 mg were prepared and used in the study in Chapter 3. On the other hand, Carbon loading was evaluated using a XP6 microbalance (Metler Toledo) with a resolution of ±1.0 μg.

The carbon-free electrodes in Chapter 4 were prepared following the same methodology as that for the electrodes in Chapter 3 using commercial TiC (95 %, < 200 nm particle size, Sigma-Aldrich) and synthesized NiO and Co_3O_4 instead of carbon.

Cathodes for catalysis analysis in Chapter 4 were prepared at Massachussets Institute of Technology (MIT) from ultrasonicated inks containing carbon, catalyst, poly(vinylidene fluoride) (PVDF, Kynar) dissolved in N-methyl pyrrolidone (<50 ppm H_2O, Alfa Aesar). Inks were coated onto a separator foil, vacuum-dried at 70°C, and cut (15 mm diameter). Cathode carbon loadings were within 0.85 ± 0.15 mg (0.48 ± 0.08 mg/cm$_{electrode}^2$) at a PVDF/(carbon + catalyst) weight ratio of 3.6/1.

The carbon cathodes in redox mediation experiments in Chapter 4 were prepared by grinding in a mortar carbon black (Super P, M. M. M. Carbon) and polyvinilydene fluoride (PVDF, Sigma-Aldrich) in a weight ratio of 9:1 and adding N-methylpyrrolidone (NMP, Sigma-Aldrich). The slurry obtained was used to impregnate a stainless steel mesh (AIS416, 180 meshes per inch, Advent Research Materials Ltd.) and finally dried at 100 °C for 12 h. The electrode loading was of the order of 1 mg cm^{-2}. In addition,

carbon-coated Au TEM grids (200 mesh, 3.05 mm diameter, 16 µm metal thickness, CF200-Au from EMS) were also used directly as a cathode for synchrotron characterization in Chapter 4. TEM grids used as oxygen electrodes were coated following the same procedure. Total carbon mass in the electrode was around 0.03 mg.

Finally, *in situ* UV-vis experiments in Chapter 4 were performed using indium tin oxide (ITO, PSiOTec, Ltd., UK) 5 Ohm/square coated glass (Polished sodalime with SiO_2 barrier layer) as oxygen electrode (WE).[3]

All the experiments were carried out using Li foil (Sigma-Aldrich, 0.4 mm thick) as anode. Li was stored and manipulated into a Ar filled glovebox; as-received foil was brushed and 10 mm diameter pieces were punched and used as counter (and sometimes reference) electrodes. In the *in situ* UV-vis experiments a piece of lithium was cut and pressed on the SS tube used for introducing oxygen to the cell, which also acted as the anode current collector.

2.2.2.2. Na-O_2 experiments (Chapters 5, 6 and 7)

Electrochemical experiments in the Swagelok cell in Chapter 5 were performed using 11 mm diameter carbon paper electrodes (H2315, Freudenberg) as WE. Experiments in Chapter 6 were also carried out using carbon paper electrodes; however, there are two differences: (i) Au TEM grids were placed on the top part of the carbon paper electrodes in order to analyze these grids by synchrotron techniques and (ii) the carbon paper in this experiments was Toray TGP-060, with a surface area much lower than that of the H2315. Consequently, discharge capacities were much lower.

The glassy carbon macrodisc electrodes used in the U-cell in Chapters 5 and 7 were constructed by sealing glassy carbon rods in glass. Prior to each experiment, the working electrodes were polished with 0.3 µm and 0.05 µm alumina powder (Buehler), and rinsed and sonicated with acetone and water. The radius of the macrodisc glassy carbon electrode was 1.5 mm.

QCM experiments were performed using a 5 MHz, 1 inch diameter, AT-cut Au covered quartz crystal wafer, as explained in section 2.2.1.4.

Finally, sodium electrodes used in the Swagelok-type cell were obtained by laminating Na cubes purchased from Sigma-Aldrich (99.9 %) and punching 11 mm diameter pieces. On the other hand, Na electrodes in the U-cell and the QCM were prepared cutting a rectangular piece of the laminated Na foil and pressing it on a SS mesh piece.

2.2.3. Electrolyte preparation

Lithium and sodium salts used for electrolyte preparation were dried in a Buchi oven at 120 °C under vacuum for at least 48 h. After that it was introduced to the glovebox and dissolved in the corresponding solvent. Prior to use, the electrolyte was dried using 4 Å type molecular sieves (Sigma-Aldrich) and water content was measured using a Mettler−Toledo Karl Fischer titration apparatus being always lower than 20 ppm. The electrolytes used in this thesis have been:

a) *Chapter 3.* 0.1M $LiClO_4$ (99.99%, Sigma-Aldrich) in 1,2-Dimethoxyethane (DME, anhydrous, 99.5 %, Sigma-Aldrich).

b) *Chapter 4.* 1 M lithium trifluoromethanesulfonate (LiOTF, 99.995% trace metal bases, Sigma-Aldrich) dissolved in tetraethylene glycol dimethyl ether (TEGDME, ≥99%, Sigma-Aldrich). In order to analyze the effect of K^+ addition to the containing LiOTF electrolyte a 0.1 M potassium trifluoromethanesulfonate (KOTF, 98%, Sigma-Aldrich) and 1 M LiOTF TEGDME-based electrolyte was prepared. For redox mediated measurements 100 mM of potassium iodine (KI, Sigma-Aldrich) were added to the electrolyte. Lithium iodine (LiI, Sigma-Aldrich) containing electrolyte was also prepared for comparison with KI.

c) *Chapters 5 and 6.* Sodium trifluoromethanesulfonate (NaOTF, 98%, Sigma-Aldrich) 0.5 M in diethylene glycol dimethyl ether (DEGDME, anhydrous, 99.5%, Sigma-Aldrich).

d) *Chapter 7.* Ethyl viologen ditriflate (EtV(OTF)$_2$) 1 mM and sodium trifluoromethanesulfonate (NaOTF, 98%, Sigma-Aldrich) 0.5 M in diethylene glycol dimethyl ether (DEGDME, anhydrous, 99.5%, Sigma-Aldrich). NaOTF 0.5 M in DEGDME (Without EtV^{2+}) was also prepared for comparison. Ethyl viologen ditriflate (EtV(OTF)$_2$) was provided by Prof. Owen and Dr. García-Aráez's group. It was prepared by the reaction of the diiodide salt with a stoichiometric amount of silver triflate (AgOTF, Sigma-Aldrich) in aqueous solution. The solution was separated from the AgI precipitate and the water was removed under reduced pressure. The solid EtV(OTf)$_2$ was purified by recrystallization from ethanol and was dried under vacuum as described above.

2.2.4. Chronopotentiometry/Galvanostatic cycling

Chronoampotentiometry (also known as galvanostatic cycling) is based on the application of a constant current (Figure 2.7.a) in order to monitorize the potential variation of the cell. The application of a negative current drives to a decrease in the cell potential in a process known as discharge. On the other hand, applying a positive current leads to charge being cell potential increased. The occurrence of electrochemical processes in both electrodes keeps the potential of the cell invariable until one of the processes is interrupted. That unvaried potential part of the charge/discharge process will be known as *potential plateau* (see Figure 2.7.b) and the potential at which is placed will be determined by the potential of the reactions (ΔE) at the reference and the working electrode and the IR drop:[4]

$$\Delta V = \Delta E - IR \qquad\qquad [2.1]$$

IR drop will depend on several factors such as the concentration of the electroactive species, the mass transport conditions or the working current.
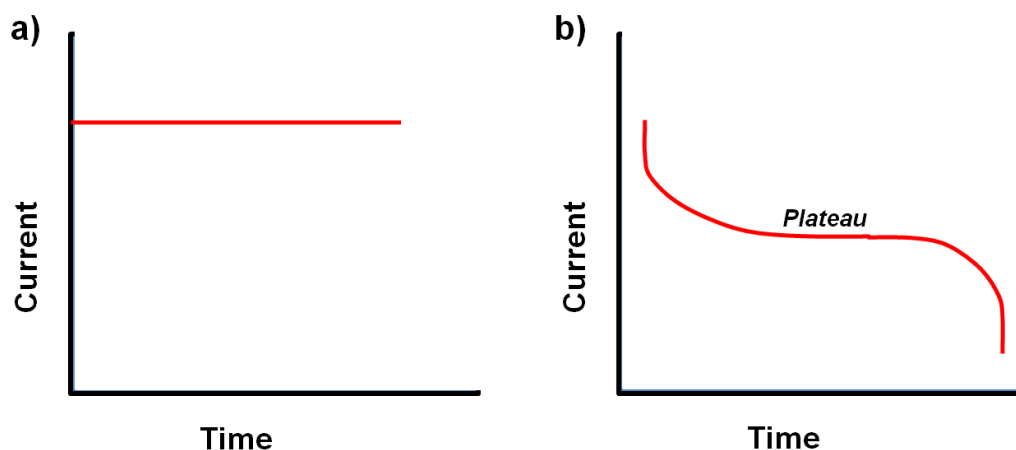
Figure 2.7. (a) Current-time profile in chronopotentiometry experiments. (b) Example of the current to time response in a discharge chronopotentiometry experiment.

Galvanostatic cycling is used in Chapters 3, 4, 5, 6 and 7 of this thesis. A Biologic-sas VMP control potentiostat was used for the experiments in Chapters 3, 4, 6 and 7, while experiments in Chapter 5 were performed using a Maccor Series 4000 potenciostat.

2.2.5. Electrochemical impedance spectroscopy

In EIS experiments the current generated by the application of a small AC potential is measured. The AC potential is applied as a sinusoidal excitation within a set frequency range and the resultant AC current signal is analyzed as a sum of sinusoidal functions. The perturbation potential applied to the cell is small so that the cells response is pseudo-linear.[5]

In this thesis, EIS measurements are represented by Nyquist and Bode plots. Nyquist plots are obtained graphing imaginary impedance (Z'') vs. real impedance (Z') and can be fitted by an equivalent circuit in order to discern between the different components contributing to the total impedance. On the other hand, Bode plots show the imaginary impedance variation with the frequency of the sinusoidal excitation. The impedance spectra in Chapters 3, 4 and 5 were recorded using a Biologic-sas VMP control potentiostat in the frequency range between 10^6 and 0.01 Hz with perturbation

amplitude of 10 mV. Impedance spectra were analyzed using a Scribner Associates'
Zview software.

2.2.6. Cyclic voltammetry (CV)

CVs are based on the recording of the current obtained in a scan trough a potential
window in which the target reaction occurs, followed by the scan in the opposite
direction once the a selected potential is reached (Figure 2.8.a).[4] The information
obtainable by this technique is determined by the potential limits, potential scan rate
and whether a first scan or multiple cycles are recorded. A schematic representation of
the typical shape of a CV is shown in Figure 2.8.b. By this technique it is possible to
obtain information related to the oxidation and reduction reactions in the selected
potential region based on the number of peaks on both the forward and reverse scan,
the shapes of the peaks, the peak potentials, current densities and the differences in
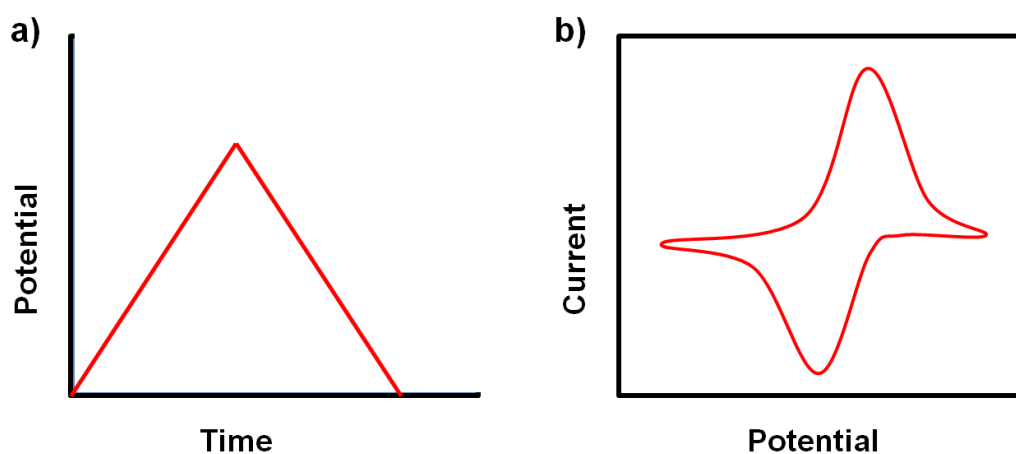the scans obtained in multiple cycles.[4]

Figure 2.8. (a) Potential-time profile in CV experiments. (b) Example of the current to potential
response in a CV experiment.

CVs in Chapters 4 and 7 were performed using a Biologic-sas VMP control
potentiostat, while those in Chapter 5 were carried out with a Solartron Analytical SI

1287 Electrochemical Interface, coupled with a SI 1260 impedance/gainphase analyzer used for impedance spectroscopy.

2.2.7. Quartz crystal microbalance (QCM)

QCM is an instrument capable of measuring a frequency of a quartz crystal resonator as resonance is disturbed by the deposition or removal of small mass of this quartz crystal. QCM experiments can be performed in metal-oxygen batteries in order to monitorize the formation/decomposition of discharge products using the quartz crystal as the oxygen electrode. The deposition of ORR products leads to a decrease in the resonance frequency that can be used to determine the amount of discharge product deposited in the electrode, based on Sauerbrey's equation:[6]

$$\Delta f = -2 \cdot f_0^2 \cdot A^{-1} \cdot \rho_q^{-1/2} \cdot \mu_q^{-1/2} \cdot \Delta m \qquad [2.2]$$

Being Δf the frequency change in Hz, f_0 the resonant frequency in Hz, A the piezoelectrically active crystal area in cm^2, ρ_q the density of quartz (2.648 g cm^{-3}), μ_q the Shear modulus of quartz AT-cut crystal (2.947×10^{11} g cm^{-1} s^{-2}) and Δm the mass variation. This equation can be reformulated in order to group together all the parameters associated to the quartz resistor:

$$\Delta f = -C \cdot \Delta m \qquad [2.3]$$

C is the sensitivity factor for the crystal, namely 56.6 Hz μg^{-1} cm^2 for a 5 MHz crystal at room temperature for the instrument used for the experiments in Chapter 5, based on the information provided by the manufacturer. These experiments were carried out using a QCM200 Quartz Crystal Microbalance Digital Controller (Stanford Research Systems) coupled with a Biologic-sas VMP control potentiostat.

2.2.8. Chronoamperometry (CA)

CA is based on setting a fixed potential (see Figure 2.9.a) at which a compound in the electrochemical cell is oxidized or reduced obtaining a positive or negative current response, respectively. Current is plotted against time as shown in Figure 2.9.b. In the early stages of the process species in the Nerst layer will react leading to a high current response. Nevertheless, this current will be decreased as the reacting specie inside the layer gets consumed and diffusion of the specie to the surface limits the reaction.[4]
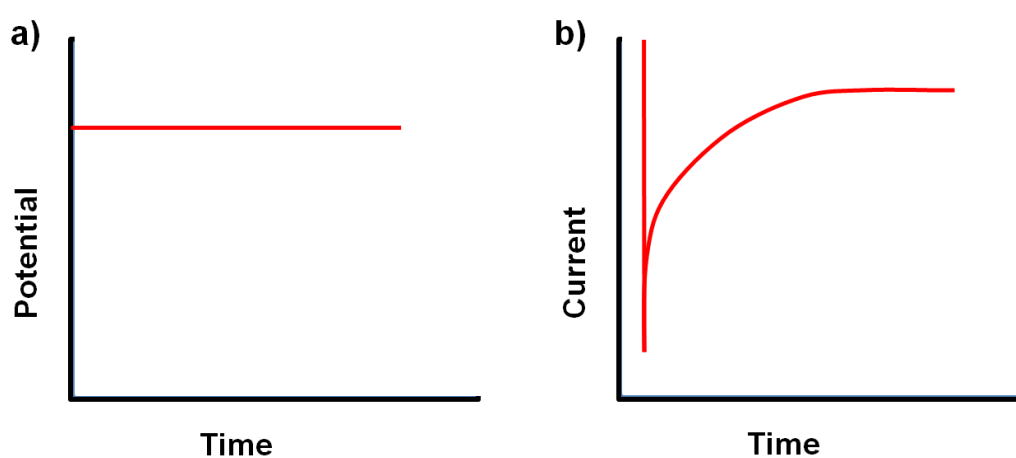

Figure 2.9. (a) Potential-time profile in CA experiments. (b) Example of the current to time response in a CA reduction experiment.

CAs in Chapter 7 were performed using a Biologic-sas VMP control potentiostat.

2.3. Characterization techniques

2.3.1. X-ray diffraction

X-ray diffraction (XRD) is a widely used technique for crystalline solids characterization. The sample is irradiated by a highly energetic X-ray beam with a specific wavelength and intensity. X-rays will be dispersed in certain directions depending on the crystal structure of the material as schematized in Figure 2.10:[7]
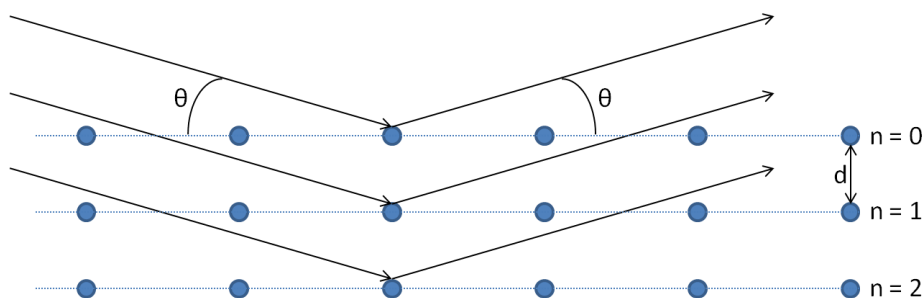
Figura 2.10. Schematic representation of the X-ray diffraction in a crystalline sample.

Angles at which waves can be detected after diffracting in the material are determined by Bragg's law:[7]

$$n \cdot \lambda = 2 \cdot d \cdot \sin \theta \qquad [2.4]$$

λ is the wavelength of the beam, *n* an integer number referring to the diffraction order, *d* the spacing between the planes in the atomic lattice and θ the angle between the incident ray and the scattering planes. Intensity and diffraction angle of the diffracted X-rays arte recorded by the detector and represented in a intensity vs. 2θ plot called diffractogram.[7]

Discharge products in Chapters 3 and 4 and metal oxides in Chapter 4 were characterized by means of X-ray powder diffraction (XRD) using a Phillips PW1710 diffractometer with Cu Kα (λ = 1.5418 Å) radiation. XRD pattern was recorded using a gastight sample holder in the case of the discharge products to prevent reaction of Li_2O_2 with moisture and CO_2. Diffractograms were recorded in the 20–60° 2θ range (0.02° step) and the obtained data were fitted using the FULLPROF program.[8]

2.3.2. Electron microscope

In this section the different imaging tools used in this thesis are presented. These techniques are usually used for obtaining information on the particle size, morphology and distribution of materials.[9] In electronic microscopes an electron beam is focused on

the materials being these electrons absorbed or scattered; being secondary electrons, backscattered electrons and characteristic X-rays produced.[5]

2.3.2.1. Scanning electron microscope (SEM)

Using a SEM it possible to reproduce the morphology of the material on an electron-sensitive photographic plate using the electrons generated.[9] The morphology of the electrodes and the reaction products in Chapter 3 were examined using a SEM Quanta 200 FEG operated in low vacuum mode at an accelerating voltage of 20.0 kV. On the other hand, metal oxides Chapter 4 were analyzed with a Hitachi S-4800. Finally, morphology of the discharge products in Chapter 5 was studied using a Hitachi S-4700 microscope equipped with energy dispersive X-ray spectroscopy instrumentation, respectively.

2.3.2.2. Energy dispersive X-ray (EDX)

As previously mentioned, X-rays can be generated from the sample when it is irradiated with the electron beam. These X-rays are characteristic from the emitting material and can therefore be used to determine the composition of the material analyzed.[10] This technique is used in Chapter 5 to determine the composition of the discharge products in $Na-O_2$ batteries after aging. As mentioned, a Hitachi S-4700 microscope equipped with energy dispersive X-ray spectroscopy instrumentation was used in that chapter.

2.3.2.3. Transmission electron microscope (TEM)

A TEM operates at higher voltage than a SEM and can provide diffraction information apart from imaging. This high voltage allows the electron beam cross the sample if this is thin enough. TEM images in Chapter 4 were obtained using a Phillips CM200 microscope.

2.3.3. X-ray photoelectron spectroscopy (XPS)

In this technique the material is irradiated with an X-ray beam while the kinetic energy and number of electrons that escape from the surface of the material (0 to 10 nm) are analyzed (see Figure 2.11.a). The detection of the ejected electrons allows the recording of a photoelectron spectrum in which energies are related to the emitting atoms and their chemical stated, electronic state and chemical bonds (Figure 2.11.b). By this technique it is therefore possible to obtain information on the chemical composition of the surface of the materials.[11]
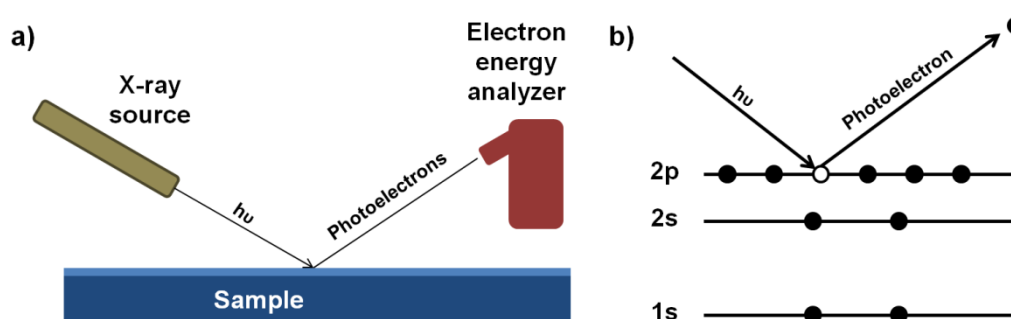

Figura 2.11. Schematic representation of (a) the XPS spectrometer operation basics and (b) the photoelectron emission process.

In this thesis XPS is used to characterize the discharge products deposited on the oxygen electrode in Chapter 3 and to analyze the interaction of iodide with lithium anode in chapter 4. Oxygen electrode analyses were performed in a SPECS (Berlin, Germany) system equipped with a Phoibos 150 1D-DLD analyzer and monochromatic Al Kα radiation (1486.6 eV).An initial analysis of the present elements was conducted at wide scan mode (step energy 1 eV, dwell time 0.1 s, pass energy 40 eV) and after that, high-resolution spectra of the found elements were acquired (step energy 0.1 eV, dwell time 0.1 s, pass energy 20 eV) with an electron take-off angle of 90∘. On the other hand, anode characterization measurements were carried out with a PHI5000 Versa Probe spectrometer using a monochromatic Al Kα radiation (hv = 1486.6 eV). The peaks were recorded with constant pass energy of 23.5 eV. The diameter of the

irradiated area was ~ 200 μm. To minimize charging effects a dual beam charge neutralization system was used. Photoelectron spectra were fitted with a Casa XPS software with Shirley backgrounds and 100% Gaussian curves. All spectra were charge corrected to a binding energy from hydrocarbons contamination on top of the surface using the C 1s peak at 284.8 eV.

2.3.4. Synchrotron X-ray Transmission Microscopy (TXM)

In TXM a light source emits photons that are collected by a condenser and redirected onto the sample and subsequently focused by an objective onto a camera. They are usually operated in the spectral range of absorption of K-edges of carbon (284 eV) and oxygen (543 eV) making it suitable for applications related to biochemistry.[12]

Soft X-rays are strongly absorbed by all materials. This phenomenon, also known as photoionization, takes place when an incident photon with enough energy to overcome the binding energy of a core or near-core electron hits an uncharged atom. Consequently, a photon with the energy difference between the incident photon and the binding energy is emitted, being the core vacancy filled by an electron from a higher shell leading to the emission of an Auger electron or fluorescence radiation.[12] Consequently, it is possible to have access to the chemical state, spatial distribution and morphology at a single particle scale of the oxygen-based discharge products of the sample depending on the photon energy obtained after the interaction of the incident photons with our samples.[13] For that aim we placed Au-coated TEM grids onto the carbon papers used as oxygen electrodes being those TEM grids analyzed by TXM.

Experiments were performed at ALBA's MISTRAL beamline.[14,15] Representative regions of the samples were selected from areas of 100 μm × 100 μm recorded at different zones of the sample by the means of composite or "mosaic" images just at two energies, above and below the O K- edge for a first localization of oxygen compounds.

On the selected areas 2D XANES images (2 s exposure time, effective pixel size 10 nm, field of view (FOV) 10 μm × 10 μm) were collected from 520 eV to 550 eV in 120 steps, varying the energy across the O K-edge with a spectral sampling of 0.25 eV. The objective zone plate lens (outermost zone width of 40 nm, 937 zones) and the CCD detector positions were automatically adjusted to maintain focus and constant magnification. In this way, we have obtained 2D maps of the oxygen chemical state of the principal possible reaction products involved, with a full XANES spectrum at each pixel. The total acquisition time necessary to acquire a full XANES TXM spectrum is about 1 hour, including the flat field acquisition at each energy step. Washed samples were stored under Ar in cryogenic vials, which were dipped in liquid nitrogen, transported to ALBA and transferred in the MISTRAL microscope in cryogenic condition (T<110 K) under N_2 vapor to minimize atmospheric contamination. The samples were kept at cryogenic temperature and under high vacuum conditions during all the measurements. The exposure time for the single image (typically 2s) was chosen to avoid possible saturation of the CCD camera.

For XANES microscopy we align the images of the energy stack using an in-house software called aligntomo. The input is an HDF5 file containing the normalized spectroscopy stack of images. Each image is aligned taking as reference the first image (another option of alignment exists, by taking as reference the previous image). The alignment is done by taking a central region of interest (ROI) of 300 pixels of width and 500 pixels of height. The ROI of a single image is compared with the ROI of the first image and thanks to the Python library of cv2 (Open Computer Vision: OpenCV) the software uses the normalized cross-correlation of both ROIs to detect the best matching between them (the function used is 'cv2.matchTemplate()'). Once this best matching is detected, the image is shifted the number of pixels calculated in the precedent operation. This process is repeated for each image of the energy stack.

XANES spectra were extracted from the TXM aligned energy stacks absorbance images using the function "get XANES of ROI" of the SW TXM Xanes Wizard.[16]

Product quantification in the TEM grids was carried out following the same procedure presented by Tonti's group in a previous work.[13] The relative content of each product was calculated based on the maximums and minimums (I_{max}) in the O K-edge spectra of the reference materials. Quantification was carried out as follows:

i. MO_2 % = ($I_{max}MO_2$ - $I_{BL}MO_2$) / ($I_{max}MO_2$ - $I_{BL}MO_2$ + $I_{max}M_2O_2$ - $I_{BL}M_2O_2$ + $I_{max}SP$ - $I_{BL}SP$)

ii. M_2O_2 % = ($I_{max}M_2O_2$ - $I_{BL}M_2O_2$) / ($I_{max}MO_2$ - $I_{BL}MO_2$ + $I_{max}M_2O_2$ - $I_{BL}M_2O_2$ + $I_{max}SP$ - $I_{BL}SP$)

iii. SP % = ($I_{max}SP$ - $I_{BL}SP$) / ($I_{max}MO_2$ - $I_{BL}MO_2$ + $I_{max}M_2O_2$ - $I_{BL}M_2O_2$ + $I_{max}SP$ - $I_{BL}SP$)

It is worth mentioning that BL refers to baseline and M to the metal cation in each experiment; in Chapter 4 this technique is used to distinguish between the discharge products in a Li-O_2 cell (M = Li) in presence of iodide while in Chapter 5 Na-O_2 (M = Na) discharge products are characterized. In addition, Li_2CO_3 was found as the sole SP in Chapter 4 and it was impossible to distinguish between NaOH and Na_2CO_3 in Chapter 5.

2.3.5. Fourier transformed infrared spectroscopy (FTIR)

FTIR is based on passing infrared radiation through a sample; part of the radiation absorbed and some transmitted. The absorption of this radiation can generate tension and flexion vibrations in some molecules. Each periodic vibration movement can be described by two parameters: frequency and amplitude. Frequency describes the number of times the movement is repeated in a period of time and amplitude is related to the length of the displacement.[17] Each molecule has a different vibrating mode and the spectrum obtained represents the absorption and transmission of the infrared

radiation by the sample. This spectrum represents the absorbance or the transmission intensity vs. the wavenumber (analogous to frequency) and is known as the *fingerprint* of the sample as no two unique molecules produce the same spectrum. The obtained raw data requires from a mathematical process called Fourier transform in order to be converted in a spectrum.[18]

FTIR analyses in this thesis were carried out after dissembling the cell inside the glovebox and washing the electrodes with DEGDME using an attenuated total reflection (ATR) apparatus scanning between 650 and 3500 cm^{-1}.

2.3.6. Ultraviolet-visible spectroscopy (UV-vis spectroscopy)

The application of UV-vis radiation to a sample can generate an electronic transition in the molecules present in the sample by the absorbance of the energy of the incident radiation. In addition, elements that have *d* and *f* atomic orbitals such as transition metals can also absorb UV-vis photons. If radiation energy matches the characteristic energy required for the electronic transition that specie will absorb photons.[17] Beer-Lambert's law specifies that at a specific wavelength in which the sample absorbs radiation the total absorbance will depend on the number of absorbing molecules in the sample:[17]

$$A = \varepsilon \cdot c \cdot l \qquad\qquad [2.5]$$

A is the absorption, which is described as the inverse logarithm of the transmittance (*T*, A = -log T). In turn, transmittance is a relative parameter that relates the radiation intensity that reaches to the detector in presence (*P*) and absence (*P$_0$*) of the sample (T = P/P_0). Turning back to Beer-Lambert's law, *l* refers to the optical path length (the thickness of the cuvette that contains the sample), *c* the concentration of the absorbing specie and *ε* the extinction coefficient, a parameter defining how strongly a substance absorbs light at a given wavelength.[17]

In this thesis UV-vis spectroscopy is used to analyze the presence of the absorbing iodide (Chapter 4) and ethyl viologen (Chapter 7) redox mediators. Evolution of iodide concentration in Chapter 4 was carried out using a Varian Cary 5 two double beam UV-Vis-NIR spectrophotometer in the in-situ cell described in section 2.2.1. Scans were repeated every 60 seconds in the wavelength range between 350 and 550 nm. On the other hand, experiments in Chapter 7 were performed using a Lambda Bio XLS spectrophotometer in the wavelength range between 200 and 900 nm.

2.3.7. Electron paramagnetic resonance (EPR)

EPR is a technique used for the analysis of samples containing molecules with unpaired electrons. The application of an external magnetic field B_0 generates the alignment of the unpaired electron in either in parallel or anti-parallel to the field with a specific energy (E) according to Zeeman's effect:[19]

$$E = m_s \cdot g_e \cdot \mu_B \cdot B_0 \qquad\qquad [2.6]$$

m_s refers to the magnetic moment (+1/2 and -1/2 for parallel and anti-parallel alignments, respectively), g_e is the g-factor (g_e = 2.0023 for free electrons) and μ_B the Bohr magneton. It is therefore possible to detect superoxide radical by this technique due to the presence of an unpaired electron in its electronic configuration (see the Lewis configuration in Figure 2.12).[20]
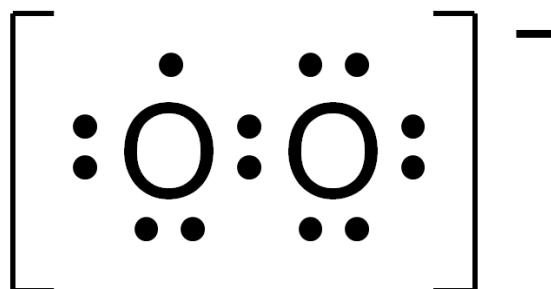

Figura 2.12. Lewis configuration of the superoxide radical.

EPR measurements in Chapters 5 and 6 were carried out on a Bruker ELEXSYS 500 spectrometer equipped with a superhigh-Q resonator ER-4123-SHQ, a maximum available microwave power of 200 mW and standard Oxford Instruments low temperature devices. Samples were placed in quartz tubes, and spectra were recorded at different temperatures between 5 and 300 K using a modulation amplitude of 0.1 mT at a frequency of 100 kHz. The magnetic field was calibrated by an NMR probe and the frequency inside the cavity ($\sim$9.4 GHz) was determined with an integrated MW-frequency counter. Discharged cells were dissembled in the glovebox, and two different procedures were followed for preparing the samples: first the carbon cathodes were washed with diglyme (previously dried for several weeks with molecular sieves) and then dried under vacuum to remove the solvent. For the electrolyte analyses, separators were rinsed with 2 mL dried diglyme and then this solution was analyzed.

2.3.8. Raman spectroscopy

When a sample is irradiated by monochromatic photons some of this radiation is dispersed by the molecules. This dispersed radiation has the same wavenumber (and consequently the same energy) as the original radiation and the radiation to sample interaction is known as *elastic*. Nevertheless, there some photons in which slight variations in the wavenumber can be appreciated meaning that there has been energy exchange between the photons and the sample molecules, *inelastic* interactions. This effect is known as *Raman Effect*. Resultant photons can therefore have the same (elastic interaction, *Rayleigh dispersion*), lower (*Raman-Stokes dispersion*) or higher (*Raman-anti-Stokes dispersion*) energy than before the interaction (Figure 2.13). In Raman Effect the energy of a photon absorbed by a molecule in a IR transition matches the energy difference between the excitation photon and the emitted photon. The difference between FTIR and Raman is that in the first one the photon used for the transition is a low-energy photon from a IR wavelength, while that the photons used for

Raman Effect are more energetic (usually from the region of visible light), almost capable of producing an electronic transit (see Figure 2.13).[17]
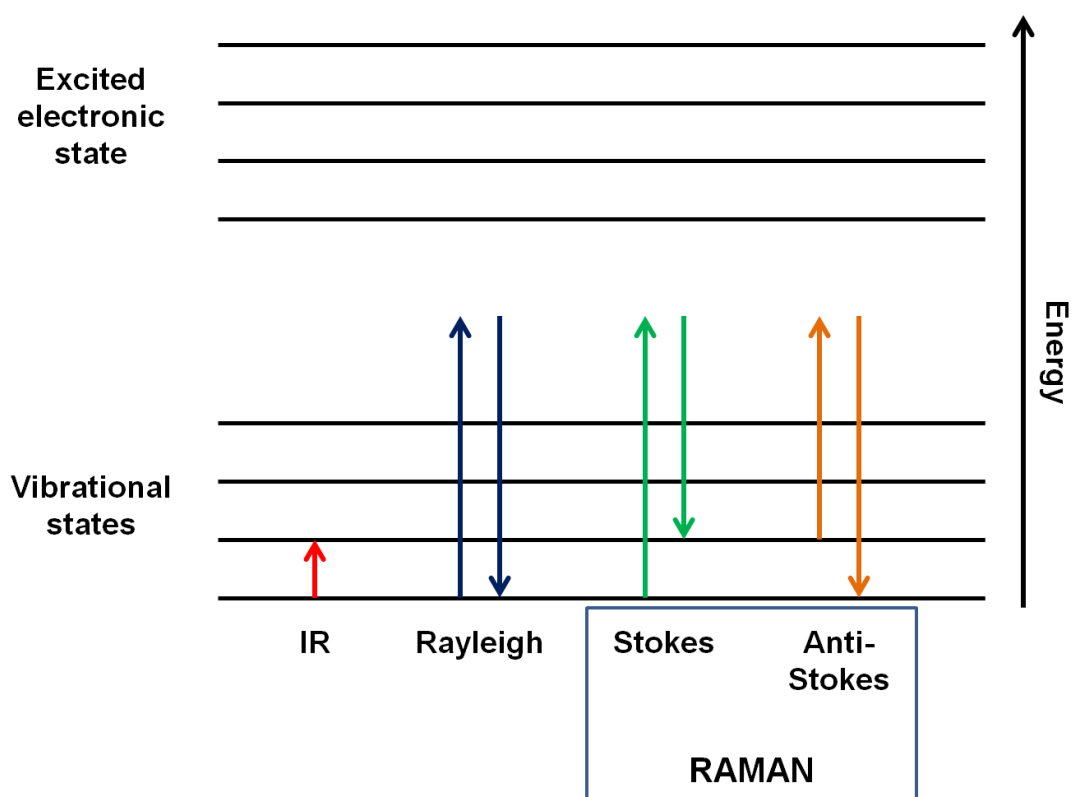

Figura 2.13. Schematic representation of IR absorption, Rayleigh elastic dispersion and Stokes and anti-Stokes Raman dispersions.

In the experiments in Chapter 5 a Renishaw in Via Raman Microscope was used coupled to a Renishaw RL633 laser recording the Raman spectra between 100 and 3500 cm^{-1}.

2.3.9. Cell-pressure evolution analysis

Formation and decomposition of discharge products in $M-O_2$ batteries involve the elimination and generation of dioxygen gas, respectively. Measuring the pressure in the electrochemical cell during the galvanostatic cycle can therefore provide valuable information on the reaction occurring in the cell, by coupling the electrochemical data recorded and the gas mol generated/consumed, based on the ideal gas law:

$$p \cdot V = n \cdot R \cdot T \qquad\qquad [2.7]$$

p and *n* are the pressure and the gas mol in the cell, respectively. *V* is the volume of this cell, *T* is the temperature at which experiments are performed and R refers to the ideal gas constant.

In Chapters 4 and 5 pressure data were recorded using a PAA-33X absolute pressure sensor adapted to the electrochemical cell, a K104B USB computer adapter, and the software Read30 v2.10 (all from Omega Engineering). The volumes of the different gas reservoirs were determined by parallel use of the pressure sensor and a calibrated syringe (Hamilton).

2.4. References

(1)   Lin, X.; Shang, Y.; Huang, T.; Yu, A. *Nanoscale* **2014**, *6*, 9043–9049.

(2)   Landa-Medrano, I.; Olivares-Marín, M.; Pinedo, R.; Ruiz de Larramendi, I.; Rojo, T.; Tonti, D. *Electrochem. commun.* **2015**, *59*, 24–27.

(3)   Yamada, A.; Zhou, H. *Nano Lett.* **2013**, *13*, 4702–4707.

(4)   Pletcher, D. *A First Course in Electrode Processes*; RSC Publishing, **2009**.

(5)   Adams, B. Development of the Aprotic Lithium-Oxygen Battery System by, University of Waterloo, **2015**.

(6)   Sauerbrey, G. *Zeitschrift Für Phys.* **1959**, *155*, 206–222.

(7)   Barrow, G. M. *Química física para las ciencias de la vida*; Reverté, **1977**.

(8)   Rodriguez-Carvajal, J. *Phys. B Condens. Matter* **1993**, *192*, 55–69.

(9)   Fernández-Ropero, A. J. Synthesis and characterization on low-cost materials for aqueous Na-ion batteries, Universidad del País Vasco / CIC energigune,

2016.

(10)   Goldstein, J. *Scanning Electron Microscopy and X-Ray Microanalysis*; Springer, 2003.

(11)   Smart, R.; Mcintyre, S.; Bancroft, M.; Bello, I. *X - ray Photoelectron Spectroscopy*; Hong Kong, 2016.

(12)   Seim, C. Laboratory Full-Field Transmission X-Ray Microscopy and Applications in Life Science, Technische Universität Berlin, 2014.

(13)   Olivares-Marín, M.; Sorrentino, A.; Lee, R.-C.; Pereiro, E.; Wu, N.-L.; Tonti, D. *Nano Lett.* **2015**, *15* (10), 6932–6938.

(14)   Pereiro, E.; Nicolas, J.; Ferrer, S.; Howells, M. *J. Synchrotron Radiat.* **2009**, *16*, 505–512.

(15)   Sorrentino, A.; Nicolás, J.; Valcárcel, R.; Chichón, F. J.; Rosanes, M.; Avila, J.; Tkachuk, A.; Irwin, J.; Ferrer, S.; Pereiro, E. *J. Synchrotron Radiat.* **2015**, *22*, 1112–1117.

(16)   Meirer, F.; Cabana, J.; Liu, Y.; Mehta, A.; Andrews, J. C.; Pianetta, P. *J. Synchrotron Radiat.* **2011**, *18*, 773–781.

(17)   Gavira Vallejo, J. M.; Herranz Gismero, A. *Técnicas Fisicoquímicas en Medio Ambiente*; UNED: Madrid, 2007.

(18)   Thermo Nicoret. *Introduction to Fourier Transform Infrared Spectrometry*; 2001.

(19)   Odom, B.; Hanneke, D.; Urso, B. D.; Gabrielse, G. *Phys. Rev. Lett.* **2006**, *97*, 6–9.

(20)   Cao, R.; Walter, E. D.; Xu, W.; Nasybulin, E. N.; Bhattacharya, P.; Bowden, M. E.; Engelhard, M. H.; Zhang, J.-G. *ChemSusChem* **2014**, *99354*, 1–6.

Chapter 3 – Investigations on ORR and OER in Li-O$_2$ systems

Oxygen reduction reaction has been a widely studied research field in order to optimize the performance of Li-O$_2$ batteries. In this chapter we focus our efforts in the analysis of the discharge product formation and removal in the oxygen electrode using different characterization techniques.

3.1. Introduction

Theoretical energy density based on the reduction of molecular oxygen to Li$_2$O$_2$ has not been practically matched due to inefficiencies in ORR and side reactions.[1] Solubility and diffusion rate of oxygen in the electrolyte play key roles in determining battery performance.[2,3] Zhang *et al*. proposed a liquid-solid "two-phase reaction zone" where ORR occurs on the electrolyte-carbon interface.[4] They claimed that the status of electrolyte-filling plays an essential role in the specific capacity and power capability in Li-O$_2$ cells. The nanostructure of carbon also plays an important role in the performance of Li-O$_2$ batteries. Several authors have reported an increase in the specific energy of these batteries with increasing carbon mesopore volume in the air electrode.[5–7] In this respect, some approaches can be defined to improve oxygen diffusion across the electrode: (i) reduction of the electrode thickness in order to minimize the oxygen diffusion distance, and (ii) minimization of electrode pore overflow to allow the diffusion of oxygen.[8] Local oxygen concentration was also found to be a limiting factor for ORR by Andrei *et al*.[9] when they modeled, for the first time, the influence of oxygen diffusion and the distance from the O$_2$/electrolyte interface. In addition, the type of carbon was also found to influence the electrochemical performance;[10] it was determined that some carbons have better mass transfer because of their moderate compatibility with the electrolyte preventing them from overflow and achieving better use of the internal pores and the whole electrode

volume. They also demonstrated that higher discharge capacities can be achieved by increasing oxygen partial pressure due to increased oxygen solubility in the electrolyte.

In this chapter the first galvanostatic cycle is studied in detail. Firstly, specific capacities during discharge, with different carbon loadings, have been studied in order to compare the influence of this loading on the electrochemical performance of Li-O$_2$ batteries. To date, no testing protocol has been established, making the comparison of results between different authors difficult. One of the main disagreements is related to the charge-discharge current density units, normally expressed as intensity per active mass (mA g^{-1}) or intensity per electrode area (mA cm^{-2}).[5] In addition, the specific capacity is usually given by intensity and time per active material mass (mA h g^{-1}), intensity and time per electrode area (mA h cm^{-2}) or intensity and time (mA h). To calculate the capacity of the cathode, the carbon or catalyst/carbon loading are taken into account, assuming therefore that the reaction occurs on the entire electrode area. Several studies suggest that the active area of the electrode differs from the surface area leading to underestimated values.[11,12] As previously commented in Chapter 1, Li$_2$O$_2$ and Li$_2$CO$_3$ are formed and can be detected in the oxygen electrode after discharge, being removed after charge. Discharge product distribution, determined by characterization techniques coupled with the electrochemical results, points differences in oxygen distribution throughout the carbon electrode. This fact has been attributed to the poor solubility of oxygen in the electrolyte, as the main responsible for the differences in the discharge capacities observed for electrodes with different thickness. Finally, discharge product formation and accumulation is *in situ* monitored by means of electrochemical impedance spectroscopy (EIS), which has been proved to be a valuable technique to analyze the processes occurring in the oxygen electrode.[13,14]

3.2. Influence of carbon loading in the electrochemical performance

It is difficult to compare galvanostatic results of different authors in literature as they usually differ in protocols, electrolytes, cells and carbon types used. In addition, most appropriate units to express capacity and current density are not either established. Our research started at this point, analyzing the influence of the use of different units in the experimental results. Oxygen electrodes with varying carbon mass and the same diameter of 1 cm were prepared in order to compare their discharge performances in a Swagelok based Li-O_2 cell. Table 3.1 summarizes the carbon loading for each sample, the applied current density and the first discharge specific capacity expressed in different units. The corresponding discharge profiles are shown in Figure 3.1. The onset potential is between 2.6 and 2.65 V and most of the discharge reactions take place between 2.68 and 2.5 V, similarly to those observed in the literature.[15–17]

Table 3.1: Carbon mass loaded in each electrode, current density applied, and the respective specific capacity obtained after first discharge, expressed in different units.

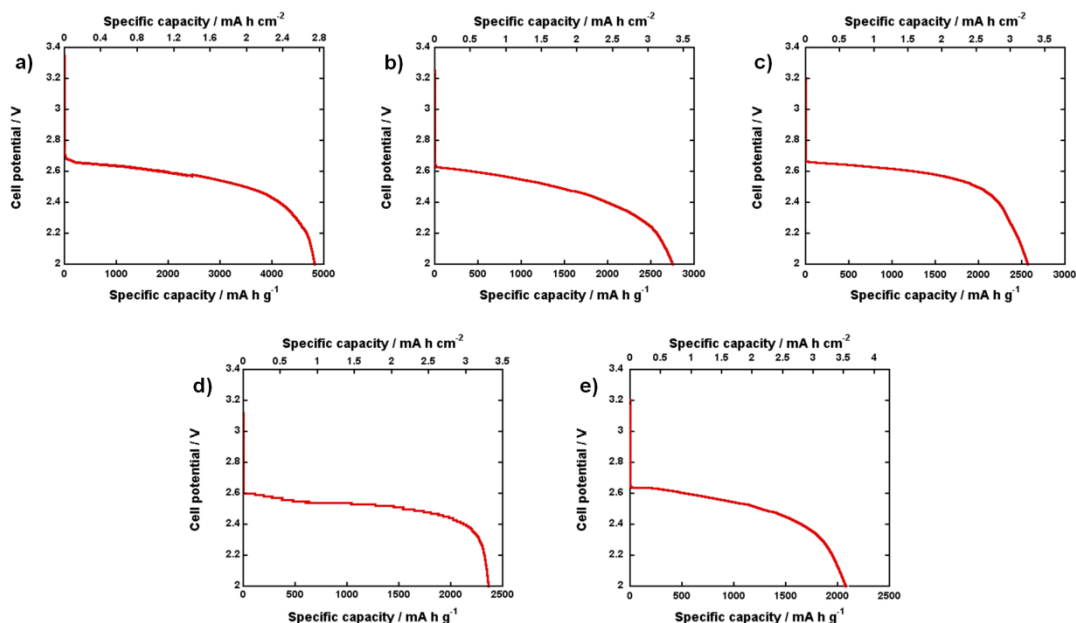| Sample	Carbon loaded [mg]	Current density [mA g^{-1}]	Current density [mA cm^{-2}]	Specific capacity [mA h g^{-1}]	Specific capacity [mA h cm^{-2}]	Specific capacity [mA h]
A	0.45	90	0.0571	4822	2.75	2.16
B	0.96	90	0.1223	2751	3.36	2.64
C	1.01	90	0.1281	2587	3.31	2.60
D	1.11	90	0.1412	2363	3.34	2.62
E	1.32	90	0.1513	2101	3.53	2.77
F	0.71	135	0.1223	2991	2.80	2.20

Figure 3.1. Voltage vs. specific capacity (mA h g^{-1} and mA h cm^{-2}) of (a) A, (b) B, (c) C, (d) D and (e) E electrodes discharged at 90 mA g^{-1}.

When capacity is expressed in mA h g^{-1} sample A presents the better performance. As shown in Table 3.1, specific capacity (mA h g^{-1}) decreases as the mass of carbon increases. However, when current density is expressed in mA cm^{-2} and capacity in either mA h cm^{-2} or mA h units, the highest specific capacity is obtained for sample E, which corresponds to the highest carbon loading and current density.

Different specific capacities have been obtained for the electrodes. All electrodes were, however, cycled at the same intensity per carbon mass, suggesting that the entirety of the cathode material is not necessarily active. Furthermore, the fact that the thinner cathodes exhibit a higher specific capacity in mA h g^{-1} while the thicker electrodes present higher specific capacities in mA h cm^{-2} and mA h, evidences a difference on the ability towards ORR as the carbon amount increases. In order to shed some light on this point, an additional discharge (sample F in Table 3.1) was performed. The current rate in mA cm^{-2} was the same as sample B (0.1223 mA cm^{-2}), but with only half of the carbon mass, and consequently the current rate in mA g^{-1} significantly differs from sample B (90 vs. 135 mA g^{-1}, respectively). A comparison of the discharge profiles

is shown in Figure 3.2. The battery discharged at higher current density delivered lower specific capacity in mA h cm^{-2} units (Figure 3.2.a). This trend, however, was inverted when specific capacity was expressed in mA h g^{-1} (Figure 3.2.b). It can therefore be concluded that when the specific capacity of B is expressed in mA h g^{-1} non-active carbon mass is included in the capacity calculations, leading to an underestimation of its real capacity.
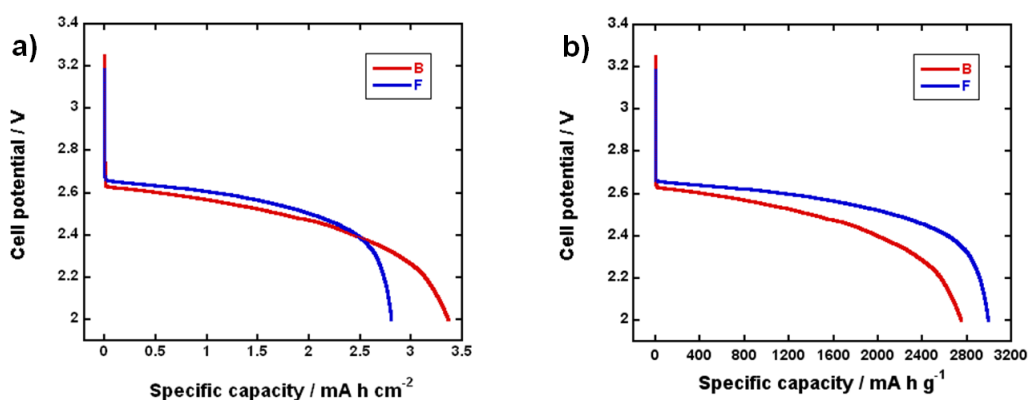

Figure 3.2. Voltage vs. specific capacity of B and F electrodes expressing the capacity in (a) mA h cm^{-2} and (b) mA h g^{-1}.

As previously mentioned, oxygen solubility in the electrolyte is an important factor that influences the active electrode area in the discharge reaction. Figure 3.3.a shows the schematic representation of the cathode before discharge. A significantly lower concentration of oxygen is observed at the electrode/separator interface compared to the O_2/electrode interface due to limited oxygen mass transport to the reaction site in the liquid electrolyte present in the pores.[4] Thus, oxygen concentration is higher at the O_2/electrode interface and the concentration is reduced as the distance from this interface increases. Consequently, there are more oxygen molecules available for the ORR in the proximities of the O_2/electrode interface. Discharge products are therefore favorable to be formed in the proximities of the surface exposed to the stainless steel mesh compared to the surface exposed to the separator. The accumulation of discharge products at the O_2/electrode interface leads to pore clogging (Figure 3.3.b),

63

resulting in the capacity fade observed in the final stages of the discharge profile shown in Figure 3.1.
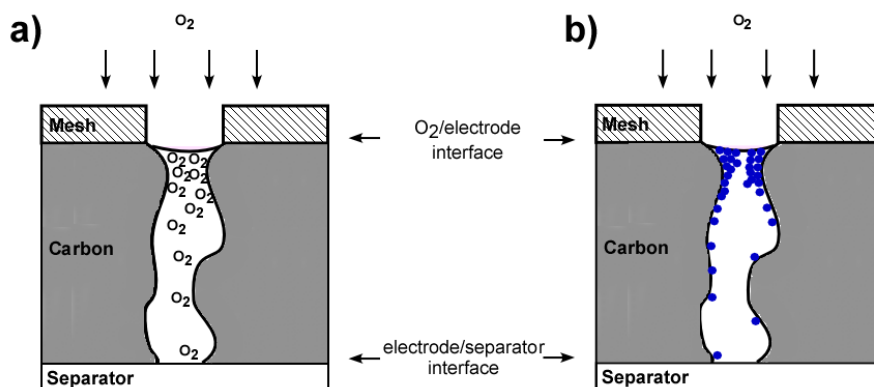

Figure 3.3. Schematic representation of the oxygen electrode (a) before discharge and (b) after discharge.

Finally, the effect of carbon loading and current rate on the cyclability was evaluated. Electrodes of 1 cm diameter loaded with 0.2 and 0.4 mg of carbon were cycled in the voltage window of 2-4.5 V with a fixed discharge capacity of 0.235 mA h cm^{-2} at a current rate of 0.045 mA cm^{-2} (Figure 3.4.a). The battery loaded with higher carbon mass was able to perform 21 cycles before capacity fade while the battery loaded with 0.2 mg of carbon was only able to perform 11 cycles. This could be attributed to the blocking of the active area with increasing cycle numbers due to the non-reversibility of the side products. As previously discussed, the entire electrode is not active for ORR during the first discharge as the discharge products are mainly formed at the oxygen/electrode interface where the oxygen concentration is higher,[18] filling the pores of the carbon particles. The formed toroid-shaped products gradually block the oxygen diffusion paths into the interior of the cathode leading to incomplete utilization of the cathode pore volume. However, during charge the formation of insulator products (e.g. Li_2CO_3) could result in a partial pore blocking avoiding the restriction of the ORR to the top of the oxygen side of the electrode.[19] The formation of Li_2O_2 even at the

cathode/separator interface of the thicker electrodes can therefore occur. Finally, the progressive accumulation of side products results in the capacity fade where thicker electrodes are able to deliver the selected specific capacity during higher number of cycles. In addition, batteries with similar carbon loadings (0.4 mg) were cycled at different current rates (0.045, 0.090 and 0.225 mA g^{-1}) with a fixed discharge capacity of 0.235 mA h cm^{-2} (Figure 3.4.b).
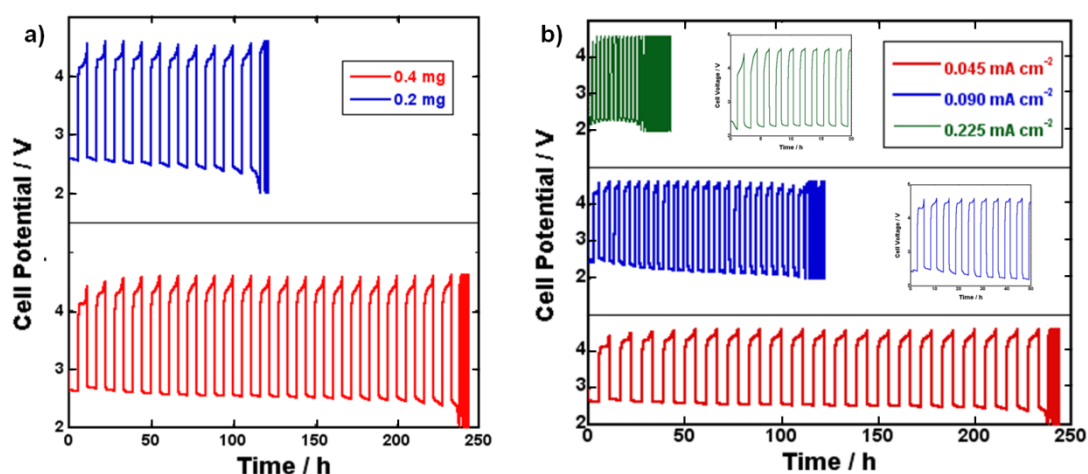

Figure 3.4. Comparison of the cycling performance of cells with a fixed discharge capacity of 0.235 mA h cm^{-2} in the voltage range of 2 and 4.5 V (a) with 0.2 (blue) and 0.4 (red) mg of carbon loaded on the oxygen electrode at a current rate of 0.045 mA cm^{-2} and (b) using electrodes of the same mass (0.4 mg) cycled at 0.225 (green), 0.090 (blue) and 0.045 (red) mA cm^{-2}.

It was therefore confirmed that low current rates enhance the lifetime of the battery, as lifetime in the battery cycled at 0.045 mA cm^{-2} was over 4 times the battery cycled at 0.225 mA cm^{-2}. This fact can be ascribed to two factors. First, higher discharge rates lead to larger gradient of the oxygen concentration across the carbon cathode, which restricts the reaction to the region close to the gas phase/cathode interface.[18] Second, the difficulties for removing discharge products at higher current densities, as has been demonstrated by Adams *et al.*[16] and Wang *et al.*,[20] are expected to reinforce this decrease on the performance.

3.3. Discharge products characterization and oxygen solubility hypothesis

A post-mortem analysis of the E electrode (see Table 3.1) was conducted in order to prove the hypothesis of the different activity in both sides of the carbon electrode. The choice of this electrode is due to its highest carbon loading among all the studied samples and, therefore, the effect of the oxygen solubility on the electrode/separator interface, due to the longer pathway of oxygen molecules to reach to this interface, should be more noticeable for this sample.

Initially discharge product identification was carried out, without differencing between both sides of the electrode, by XRD. The objective of this characterization was to validate the electrochemical discharges by the detection of ORR product Li_2O_2. Figure 3.5.a shows the XRD patterns (2θ = 20-60º) of the cathode after discharge and the protective polymer film used for the air-tight oxygen system.
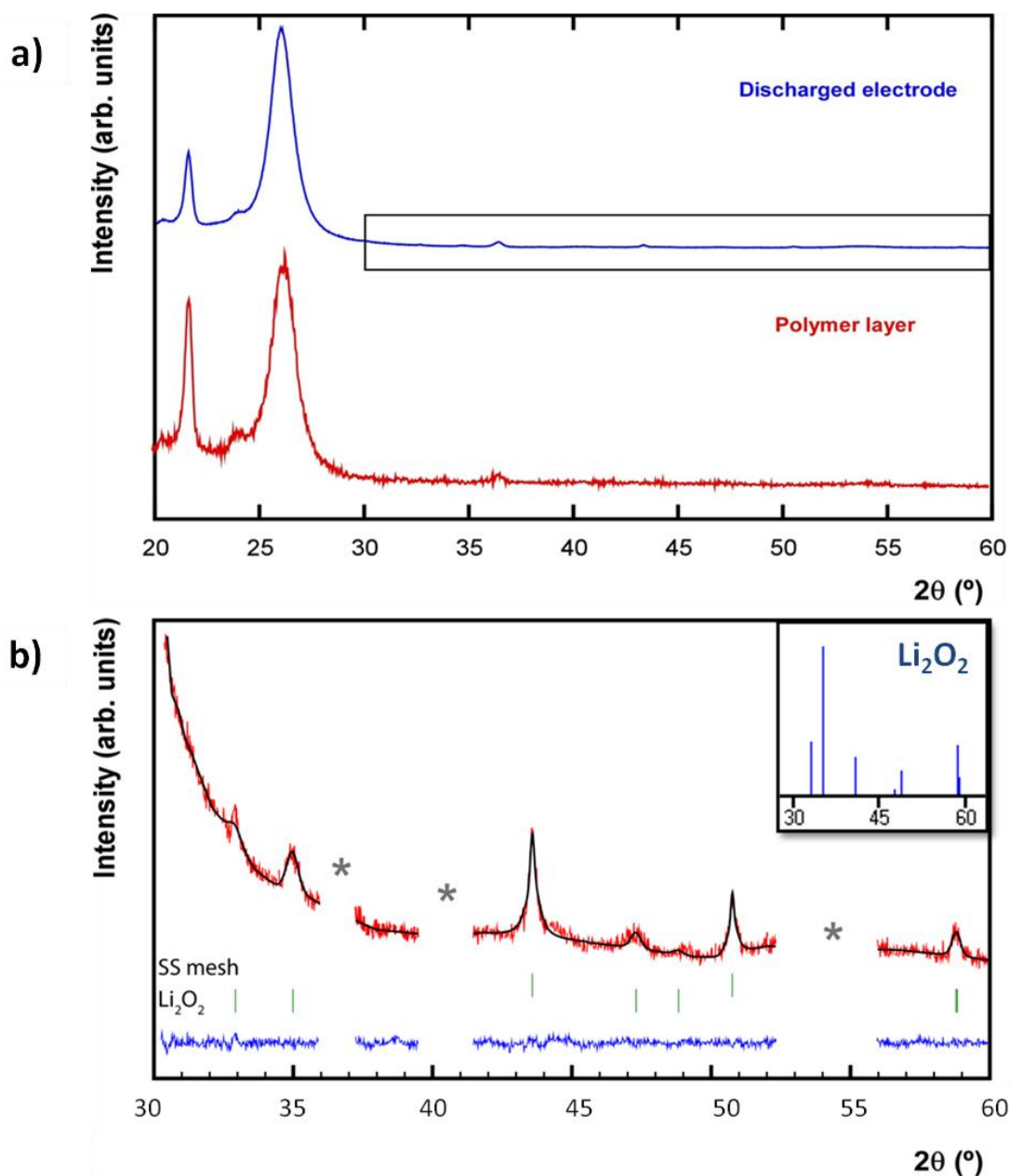
Figure 3.5. (a) XRD diffraction pattern of the protective polymer film and the discharged electrode; (b) Fitted diffraction profile of the electrode showing observed (red line), calculated (black line) and difference (lower line) profiles (* corresponds to diffraction reflections of protective polymer film). Inset in Figure 3.5.b shows the theoretical relative intensities of the reflections for hexagonal Li_2O_2.

The existence of strong reflections from the polymer film on the discharged electrode at $2\theta = 21.7°$ and $26.7°$ makes the characterization of the discharge products difficult. Consequently, the refinement was performed in a 2θ range between $30°$ and $60°$ in

order to identify the discharge product structure (Figure 3.5.b). Within this range, six distinct reflections (2θ = 32.92°, 34.99°, 47.31°, 48.83°, 58.78°, 58.83°) are found which correspond to the formation of hexagonal Li_2O_2 (JCPDS 74-0115). Additional reflections at 2θ ~36.4°, 40.3° and 54.3° can be attributed to the polymer foil used in the air-tight system and, due to the absence of crystallographic information, have been excluded from the refinement. Furthermore, two reflections (2θ = 43.58°, 50.76°) from the stainless steel mesh were identified and taken into consideration. From the residual plot, a mismatch in the relative intensities of the Li_2O_2 reflections at lower diffraction angles compared to theoretical relative intensities of hexagonal Li_2O_2 (see inset in Figure 3.5.b) becomes obvious, i.e. the first reflection at 2θ = 32.92° shows considerably lower intensity than expected. This observation can be attributed to the electrode configuration in which the stainless steel mesh is located on top of the C-based electrode. As the measurement was conducted in Bragg-Brentano geometry, diffraction at lower angles was most likely influenced by the relative height of the materials. Thus, the stainless steel mesh acted as a physical barrier for part of the radiation diffracted by the Li_2O_2-phase leading to lower absolute intensities. At higher diffraction angles, this effect disappears and a normal behavior of the intensities is observed. Hence, it can be concluded that Li_2O_2 is the main discharge product, and further evidence is provided in the following sections. It is also worth noting that no Li_2CO_3 side-reaction product was observed although it is widely accepted that the Li_2O_2 formed during the discharge process can subsequently react with the electrolyte leading to the formation of Li_2CO_3.[17,21,22] As expected, the rarely reported LiO_2 was neither detected.[23]

SEM was used to locate the discharge products. Discharge products accumulated in the O_2-electrode interface are shown in Figure 3.6. The toroidal-shaped characteristic Li_2O_2 particles with a diameter of 2-3 µm are found. This type of discharge product has been widely described by several authors at low discharge rate currents.[16,24–26] Aetukuri

et al.[27] attributed this discharge product morphology to the presence of water in the electrolyte when DME solvent was used. Nevertheless, water content in the electrolyte was controlled to be less than 10 ppm by Karl-Fisher measurements. In addition, the toroidal-shaped discharge products observed by Aekuturi *et al.* can be described as aggregates of flat discs forming toroid-like structures which differ from those in Figure 3.6.[27] No discharge products were observed on the electrode-separator interface after first discharge which supports the described hypothesis.
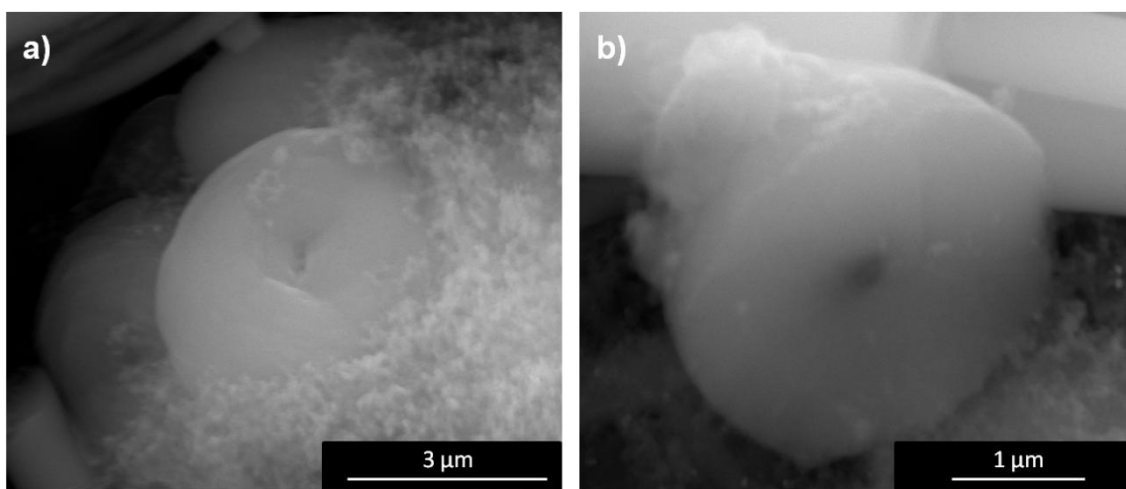

Figure 3.6. SEM images of different toroid-shaped Li_2O_2 particles formed on the O_2-electrode interface.

In order to definitely compare the activity towards ORR of these two surfaces by the accumulation of the discharge products XPS measurements were carried out. The results are shown in Figure 3.7.
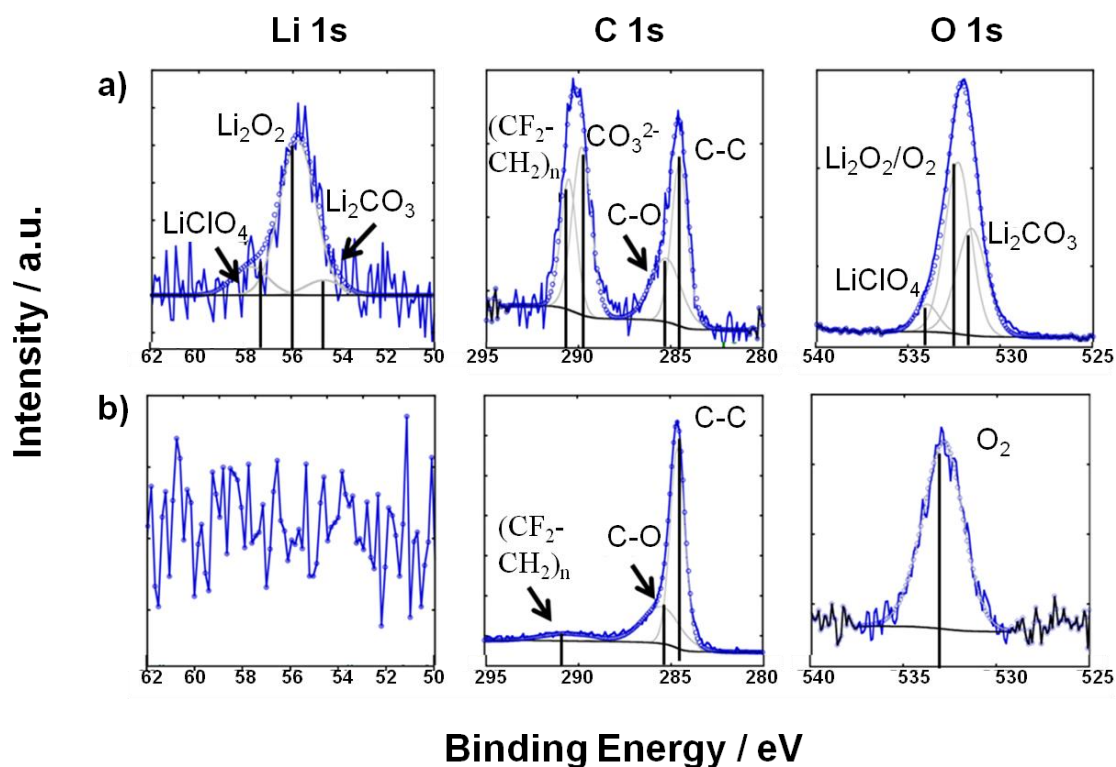
Figure 3.7. XPS data collected on the E discharged electrode surface exposed to (a) the stainless steel mesh and (b) the separator. Continuous lines denote the experimental data (blue), the different contributions of each spectrum (grey) and the background (black), while the open circles are referred to the attained fit.

Figure 3.7.a shows the XPS spectrum at the O_2/electrode interface. The presence of the Li_2O_2 discharge product detected by XRD was confirmed at the O_2/electrode interface at ~56 eV in the Li 1s spectra. The existence of Li_2CO_3 (at ~290 eV in the C 1s spectra) in the interface was also found. On the other hand, in Figure 3.7.b at the electrode/separator interface no discharge product (Li_2O_2) or side reaction (Li_2CO_3) products were detected, proving the inactivity of this surface. In summary, the XPS measurements confirm that each surface of the positive electrode shows different activity towards ORR, consistent with the SEM analysis. Thus, it can be concluded that the activity of the cathode towards ORR is reduced as the distance from the oxygen gas-electrolyte interface is increased. Finally, activity of the carbon electrode side

facing the separator after several cycles was demonstrated by means of SEM and XPS (Figure 3.8).
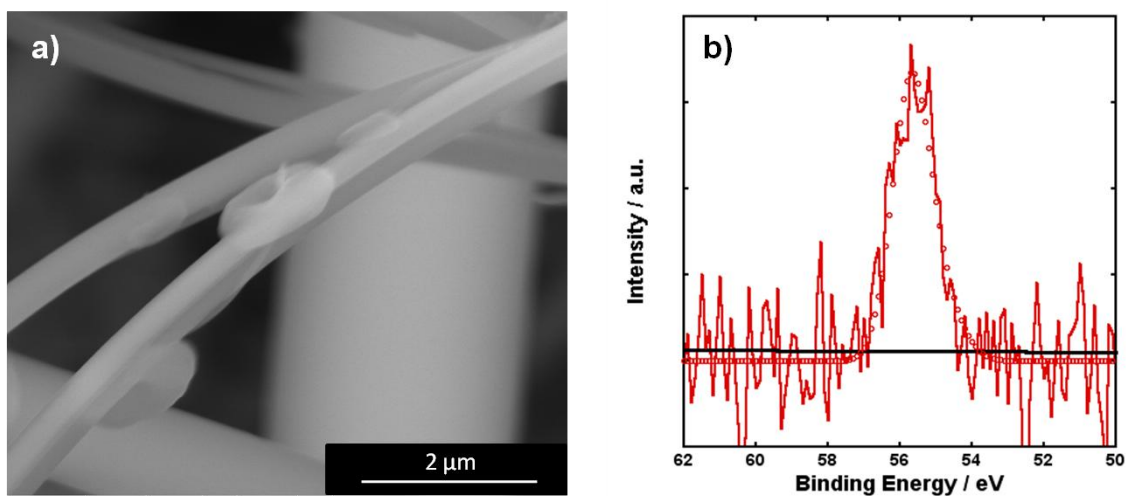

Figure 8. (a) SEM images of the toroid-shaped Li_2O_2 particles formed on the separator-electrode interface after several cycles; (b) Li 1s spectra of the separator-electrode interface after several cycles. Continuous lines denote the experimental data (red), and the background (black), while the open circles are referred to the attained fit.

Toroid formation was observed in the oxygen electrode side facing the separator after several discharge-charge galvanostatic cycles. These toroids (Figure 3.8.a), however, were noticeable smaller than the observed in Figure 3.6 which could be attributed to the lower oxygen presence in this side of the electrode. In addition, lithium discharge product presence was confirmed by means of XPS (Figure 3.8.b).

3.4. *In situ* discharge and charge reactions monitoring by electrochemical impedance spectroscopy

Once the presence of discharge products after discharge was demonstrated, the formation and removal of these products was *in situ* monitored by means of EIS. The initial hypothesis is that the variations in the electrolyte/electrode interface resistance originated by the discharge product deposition and side-reactions could be monitored by this technique. For this aim the cell was galvanostatically cycled and stopped at 2.6,

2.5, 2.4, 2.3 and 2.0 V during the discharge of the cell performing impedance measurements at those potentials. After discharge to 2.0 V the strategy was repeated for the recharge of the cell at 4.3, 4.4 and 4.6 V. The galvanostatic cycle is shown in Figure 3.9.
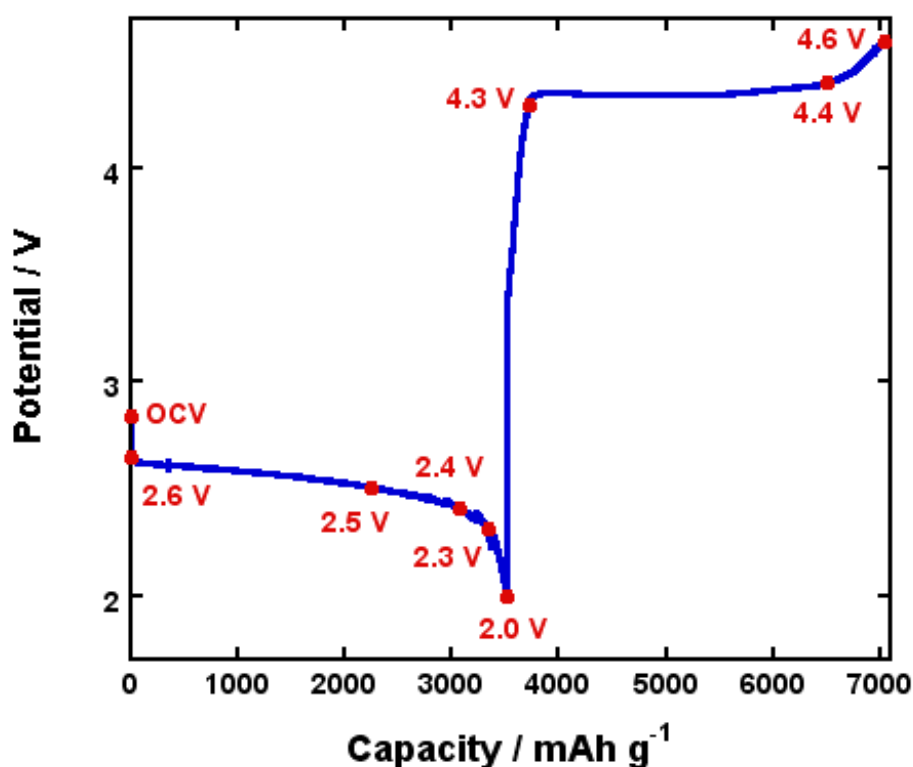

Figure 3.9. Discharge and charge galvanostatic cycle of a Li-O$_2$ cell. Potentials in which impedance measurements were carried out are indicated.

A long plateau similar to the presented in Figure 3.1 could be observed during the discharge of the cell reproducing the voltage profile usually observed for full discharge.[28,29] During charge process a long plateau was observed between 4.3 and 4.4 V usually reported for OER[16] after which potential was rapidly increased to 4.6 V, similarly to the drop of potential observed in the last stages of the discharge. The polarization of the galvanostatic cycle was ~1.85 V, in good agreement with the values typically reported in literature for catalyst-free cells.[16,30] The impedance spectra for the different measurements during the galvanostatic cycle is presented in Figure 3.10.
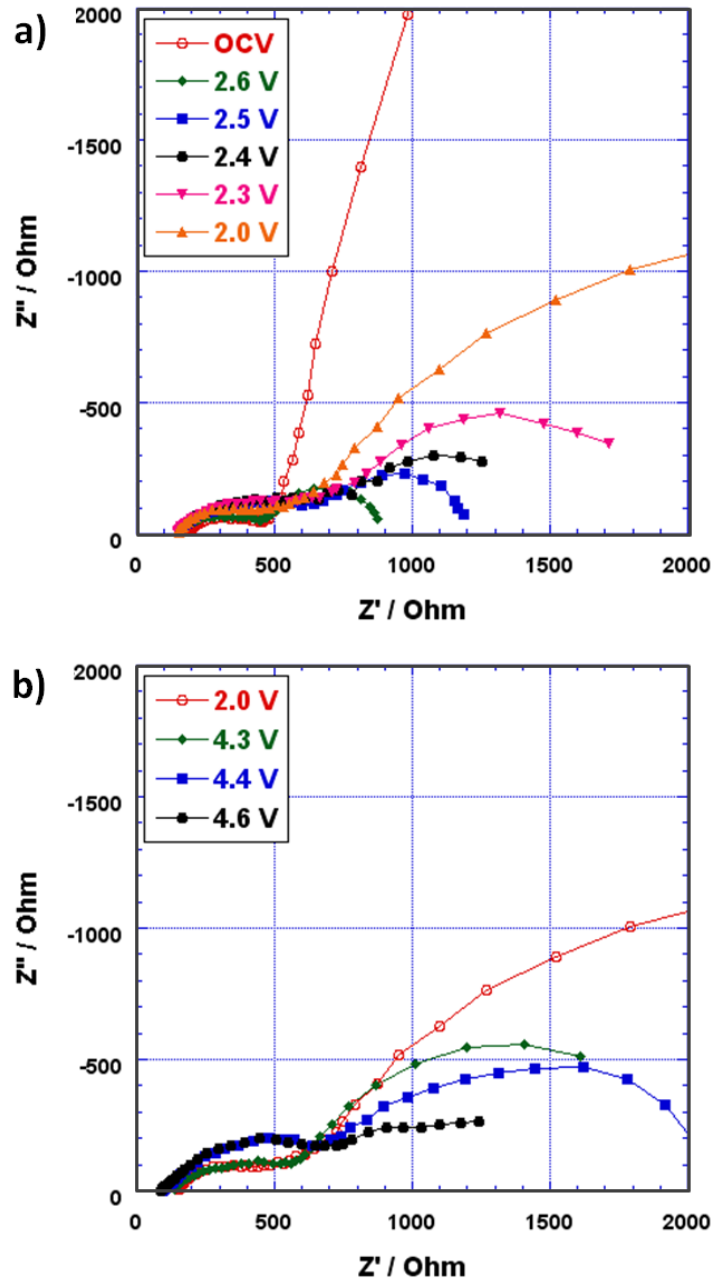
Figure 3.10. Nyquist plots of impedance response recorded during the galvanostatic cycle at the indicated potentials during (a) discharge and (b) charge.

At OCV the sole semicircle represents the processes at high frequencies (~10^3 Hz) in the Nyquist plot as for the processes at low frequencies (~1 Hz) only diffusion is observable. For the remaining voltages, however, a second semicircle appears at low frequencies. The high and low frequency semicircles consist of several overlapped contributions making their analysis more difficult. The accurate differentiation of these contributions, however, is considered a key factor for the development of an equivalent

circuit model capable of simulating and explaining the electrochemical processes taking place in the cell. The first step towards the achievement of this goal focuses on discerning the number of processes taking place at each voltage. This can be better analyzed through the use of Bode plots (Figure 3.11).
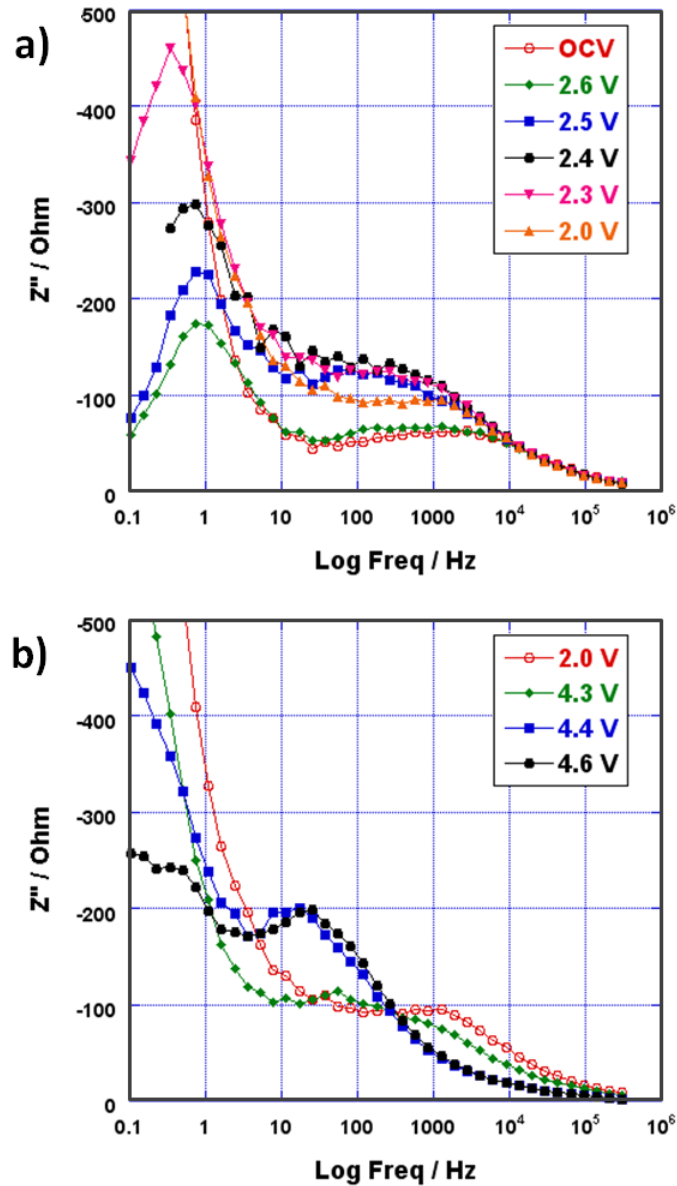

Figure 3.11. Bode plots of impedance response at the selected potentials during (a) discharge and (b) charge.

The Bode plot shows the presence of two processes at high (10^3 Hz) and low frequencies (10 Hz). Asymmetric peaks are observed for both cells suggesting the

presence of multiple processes at high and low frequencies. At least two processes at high frequencies and another two at low frequencies can be, therefore, assigned. During charging the high frequency process shifts to lower frequencies (10-100 Hz). This can be associated with the formation and/or precipitation of secondary reaction products discussed in literature[31] at the electrolyte/electrode interface, increasing their resistances. This fact is explained in more detail later. The analysis of the low frequency region of the impedance spectra during charge is more complicated due to the strongly overlapping processes and limitation of the data measured. The developed model for the discharge processes, however, will be applied to the charge processes in order to provide validation. The overlapping observed in both Bode and Nyquist plots at OCV and 2.6 V at high frequencies (10^2-10^6 Hz) reveals that no reaction has occurred in the cell. In turn, at voltages lower than 2.6 V, where the discharge plateau starts, the resistance associated with high frequencies (R_{HF}) increases up to a maximum when the discharge finishes (2.0 V). Regarding the charging processes, R_{HF} remains constant between 2.0 and 4.3 V (where no charging plateau is observed) and increases to 4.4 V, and then remains constant for the end of the charge. The resistance associated with low frequency processes (R_{LF}) increases during discharge between 2.6 and 2.3 V, up to a maximum at 2.0 V, and during charge a decrease of R_{LF} is observed. It is noteworthy that the presence of discharge products at the cathode surface reduces the active cathode area, limiting the ORR.[28]

As discussed previously, through the analysis of the Bode plots it is possible to distinguish at least two processes overlapped at both high and low frequencies, however these processes are overlapping. Figure 3.12 shows a schematic of the proposed electrochemical model (R_1-R_2CPE_2-R_3CPE_3-R_4CPE_4-R_5CPE_5). The first element, R_1, is associated with the ohmic resistance, which includes the electrolyte contribution (physical and chemical changes), current collectors and cell contacts and its numerical value is calculated from the high frequency intercept on the Z' axis. The

four subsequent elements in series consist of a resistor (R) in parallel with a constant phase element (CPE) (R‖CPE). Each of these R‖CPE elements must be associated with a process in order to validate the proposed model.
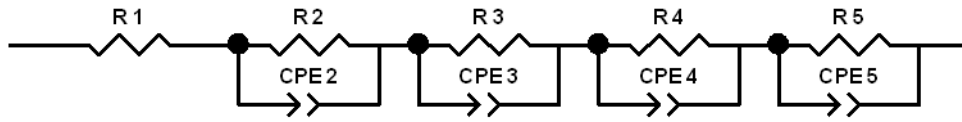

Figure 3.12. Schematic of the proposed equivalent circuit.

The constant phase element (CPE) is a simple distributed element which produces impedance having a constant phase angle in the complex plane.[32,33] A CPE is often used in a model in place of a capacitor to compensate the non-homogeneity in a system. For example, a rough or porous surface can cause a double-layer capacitance to appear as a constant phase element with a CPE-P value between 0.9 and 1. In fact, a capacitor is actually a constant phase element - one with a constant phase angle of 90°. From the impedance associated with each CPE element, $Z = 1/T(j\omega)^P$ (where ω is the angular frequency and T and P are constants), it is possible to obtain the degree of distortion of the impedance spectrum. When P = 1 the CPE will act as a capacitor and T will be its capacity value. In this study, the P value is between 0.556 and 1. For the fitting of OCV, 4 and 5 data processes were replaced by a finite length Warburg element (R_1-R_2CP_2-R_3CP_3-W) used when charge carriers diffuse through a material. This way, the contribution at lower frequencies corresponds to diffusion processes deeper into the material. Figure 3.13 presents some of the fittings obtained with the equivalent circuit shown in Figure 3.12. These fittings are representative of the rest of the data obtained. The model fits well with the experimental data recorded, for both discharge and charge.
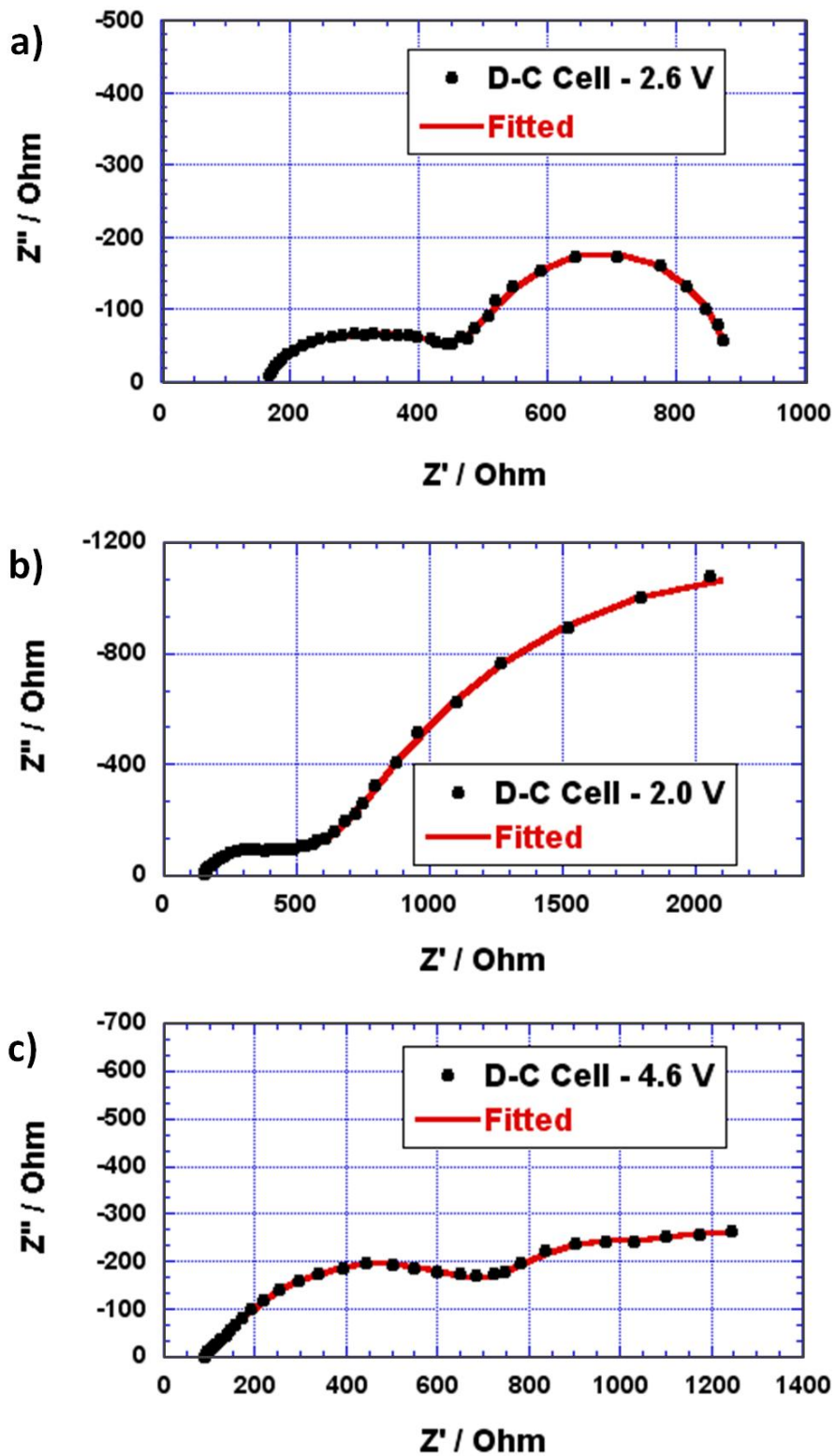
Figure 3.13. Fitting of the impedance spectra using the proposed equivalent circuit.

The evolution of the resistances obtained from the fitting of the data with the equivalent

circuit at different voltages is presented in Figure 3.14. When analyzing these results,

the individual resistances (R_4 and R_5) as well as the sum of both ($R_4 + R_5$) will be taken into account. The changes on the ohmic resistance are associated with the chemical and physical properties of the electrolyte, and this resistance remains almost constant throughout the complete experiment. On the other hand, the high frequency processes have been fitted through the deconvolution of two processes. R_2 presents low resistance values remaining constant during the study of the cell. The capacitance value of CPE_2 is 10^{-7} F, which can be associated with charge transference at the anode surface (anode/electrolyte interface). Changes in R_2 are not appreciable but this is expected to increase during cycling due to the formation of dendrites at the anode surface or the formation of Solid Electrolyte Interphase (SEI) layer.[34][35] The capacitance value of CPE_3, observed at high frequencies, is on the order of 10^{-6} F. This contribution is ascribed to charge transference through the electrolyte/cathode interface.[17] Kichambare *et al.* also ascribed the resistances associated with the high frequency semicircle to charge-transfer processes and a higher resistance was obtained when discharge products were deposited on the pores of the cathode.[36] R_3 remains constant up to the discharge plateau (2.6 V) when it sharply increases. This behavior is due to the formation of reaction products when the discharge plateau is reached, as has been reported by other authors.[37][38][39]
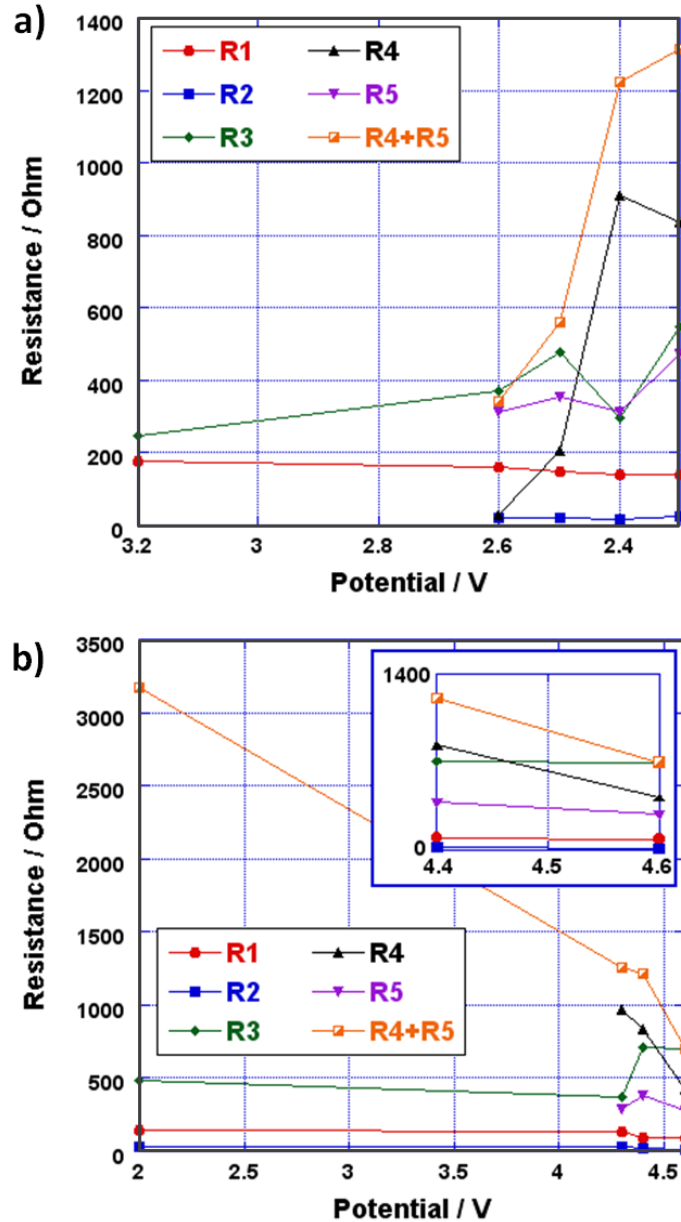
Figure 3.14. Resistances obtained using the fitting of the impedance data to the equivalent circuit proposed in this work during (a) discharge and (b) charge.

The formation of reaction products with low conductivity values [$\sigma(Li_2O_2) = 2\cdot10^{-13}$ S cm^{-1}; $\sigma(Li_2CO_3) = 5\cdot10^{-9}$ S cm^{-1}] blocks the electrolyte/cathode interface increasing the resistance associated with those processes (R_3). In addition, it is known that side reactions involving the formation of Li_2CO_3 can occur when charge process is carried out at high potentials (4.3 - 4.4 V). This would explain the resistance observed during the charge of the cell. R_4 and R_5 contributions are ascribed to oxygen diffusion from

outer atmosphere to oxygen-electrode surface and oxygen dissociative adsorption together with the charge-transfer resistance of electrochemical reduction of oxygen species. The contributions at lower frequencies are normally associated with lithium and oxygen diffusion controlled processes.[36,40] CPE_4 and CPE_5 capacitance values are on the order of 10^{-4} F, which is in good agreement with the described electrochemical processes. During discharge, a gradual increase of the contribution associated with discharge product deposition is observed for both cells, becoming the dominant process in the electrochemical response. During charge, however, these resistances decrease, implying that the oxidation process is favored as the voltage increases. As the charge progresses, the products formed during discharge are decomposed.

After the charging process, the resistance (R_4 + R_5) associated with the oxygen electrode does not return to its initial value. This is possibly related to residual traces of Li_2O_2 and Li_2CO_3 discharge products on the air electrode which have not been fully decomposed. The presence of these products at the carbon electrode surface will lead to greater resistance values due to the reduction of active sites.

3.5. Conclusions

To sum up, it has been electrochemically demonstrated that oxygen solubility and diffusion are limiting factors that hinder the comparison of electrochemical results obtained under different conditions (i.e. cell designs, solvents, electrode thickness…). In addition, it has been demonstrated that regions of the oxygen electrode closer to the O_2/electrode interface are more active towards ORR due to the mentioned O_2 solubility and diffusion and, therefore, some regions of the cathode evidence negligible activity. This hypothesis has been supported by means of SEM and XPS characterization techniques as, following the same procedure followed for the O_2/electrode interface, no discharge product evidence was detected in the separator/electrode interface. Moreover, it was demonstrated that ORR is successfully performed as Li_2O_2 was

observed as the main discharge product. It has also been demonstrated that the thicker the oxygen electrode, the better cyclability of the cell; the detection of discharge products in the electrode side facing the separator evidences that although not active in the first cycles some regions of the electrode become useful for ORR as other regions previously active become passivated. Besides, the formation and decomposition of this Li_2O_2 has been in situ monitored by means EIS. A galvanostatic cycle has been carried out stopping the current at different cell potentials and measuring impendance at those points. It was possible to distinguish 5 different contributions and built up the R_1-R_2CP_2-R_3CP_3-R_4CP_4-R_5CP_5 equivalent circuit. R_1 was associated with the ohmic resistance, which includes the electrolyte contribution, current collectors and cell contacts. The subsequent elements in series consisted of a resistor in parallel with a constant phase element. R_2CPE_2 and R_3CPE_3 were ascribed to anode/electrolyte and electrolyte/cathode interface processes, respectively. The latter contribution increased in resistance on discharge, as the reaction products form, and decreased on charging due to their decomposition. At high voltages a small increase in the resistance associated with formation of salt of the electrolyte was observed. Finally, the last two processes were related to electrochemical reactions associated with the ORR and OER. EIS has therefore been demonstrated to be a valuable technique in order to monitorize the formation and removal of discharge products and applying this model to Li-air batteries will allow the in situ investigation of the fundamental electrochemical mechanisms of the different components, as well as allow the evaluation of the behaviour of cathode catalysts through the analysis of their effect on the resistance associated with ORR and OER.

3.6. References

(1)   Song, M.-K.; Park, S.; Alamgir, F. M.; Cho, J.; Liu, M. *Mater. Sci. Eng. R Reports* **2011**, *72* (11), 203–252.

(2)   Read, J.; Mutolo, K.; Ervin, M.; Behl, W.; Wolfenstine, J.; Driedger, A.; Foster, D. *J. Electrochem. Soc.* **2003**, *150*, A1351–A1356.

(3)   Sandhu, S. S.; Fellner, J. P.; Brutchen, G. W. *J. Power Sources* **2007**, *164*, 365–371.

(4)   Zhang, S. S.; Foster, D.; Read, J. *J. Power Sources* **2010**, *195* (4), 1235–1240.

(5)   Xiao, J.; Wang, D.; Xu, W.; Wang, D.; Williford, R. E.; Liu, J.; Zhang, J.-G. *J. Electrochem. Soc.* **2010**, *157* (4), A487–A492.

(6)   Wang, F.; Xu, Y.; Luo, Z.; Pang, Y.; Wu, Q.; Liang, C.; Chen, J.; Liu, D.; Zheng, X. *J. Power Sources* **2014**, *272*, 1061–1071.

(7)   Xue, K.-H.; Nguyen, T.-K.; Franco, A. A. *J. Electrochem. Soc.* **2014**, *161* (8), E3028–E3035.

(8)   Baturina, O. A.; Smirnova, A. E. *New and Future Developments in Catalysis, Batteries, Hydrogen Storage and Fuel Cells*; Suib, S. L., Ed.; Elsevier, 2013.

(9)   Andrei, P.; Zheng, J. P.; Hendrickson, M.; Plichta, E. J. *J. Electrochem. Soc.* **2010**, *157* (12), A1287–A1295.

(10)   Zhang, Y.; Zhang, H.; Li, J.; Wang, M.; Nie, H.; Zhang, F. *J. Power Sources* **2013**, *240*, 390–396.

(11)   Meini, S.; Piana, M.; Beyer, H.; Schwaemmlein, J.; Gasteiger, H. A. *J. Electrochem. Soc.* **2012**, *159*, A2135–A2142.

(12)   Xia, C.; Bender, C. L.; Bergner, B.; Peppler, K.; Janek, J. *Electrochem. commun.*

2013, *26*, 93–96.

(13)　Højberg, J.; McCloskey, B. D.; Hjelm, J.; Vegge, T.; Johansen, K.; Norby, P.;
　　　　Luntz, A. C. *ACS Appl. Mater. Interfaces* **2015**, *7*, 4039–4047.

(14)　Christensen, A. E.; Højberg, J.; Norby, P.; Vegge, T. *J. Electrochem. Soc.* **2015**,
　　　　162 (10), A2075–A2079.

(15)　Ogasawara, T.; Débart, A.; Holzapfel, M.; Novák, P.; Bruce, P. G. *J. Am. Chem.*
　　　　Soc. **2006**, *128* (4), 1390–1393.

(16)　Adams, B. D.; Radtke, C.; Black, R.; Trudeau, M. L.; Zaghib, K.; Nazar, L. F.
　　　　Energy Environ. Sci. **2013**, *6*, 1772–1778.

(17)　Freunberger, S. a; Chen, Y.; Drewett, N. E.; Hardwick, L. J.; Bardé, F.; Bruce, P.
　　　　G. *Angew. Chem. Int. Ed. Engl.* **2011**, *50* (37), 8609–8613.

(18)　Read, J. *J. Electrochem. Soc.* **2002**, *149* (9), A1190–A1195.

(19)　Xia, C.; Waletzko, M.; Peppler, K.; Janek, J. *J. Phys. Chem. C* **2013**, *117*,
　　　　19897–19904.

(20)　Wang, F.; Xu, Y.-H.; Luo, Z.-K.; Pang, Y.; Liang, C.-S.; Chen, J.; Liu, D.; Zhang,
　　　　X. *J. Power Sources* **2014**, *272*, 1061–1071.

(21)　McCloskey, B. D.; Scheffler, R.; Speidel, A.; Girishkumar, G.; Luntz, A. C. *J.*
　　　　Phys. Chem. C **2012**, *116*, 23897–23905.

(22)　Peng, Z.; Freunberger, S. A.; Hardwick, L. J.; Chen, Y.; Giordani, V.; Barde, F.;
　　　　Novak, P.; Graham, D.; Tarascon, J. M.; Bruce, P. G. *Angew. Chem. Int. Ed.*
　　　　Engl. **2011**, *50*, 6351–6355.

(23)　Lu, J.; Lee, Y. J.; Luo, X.; Lau, K. C.; Asadi, M.; Wang, H.; Brombosz, S.; Wen,
　　　　J.; Zhai, D.; Chen, Z.; Miller, D. J.; Jeong, Y. S.; Park, J.; Fang, Z. Z.; Kumar, B.;

Salehi-khojin, A.; Sun, Y.; Curtiss, L. A.; Amine, K. *Nature* **2016**, *529*, 377–382.

(24)   Mitchell, R. R.; Gallant, B. M.; Thompson, C. V.; Shao-Horn, Y. *Energy Environ. Sci.* **2011**, *4*, 2952–2958.

(25)   Wang, Z.-L.; Xu, D.; Xu, J.-J.; Zhang, L.-L.; Zhang, X.-B. *Adv. Energy Mater.* **2012**, *22*, 3699–3705.

(26)   Xu, D.; Wang, Z.-L.; Xu, J.-J.; Zhang, L.-L.; Zhang, X.-B. *Chem. Commun.* **2012**, *48*, 6948–6950.

(27)   Aetukuri, N. B.; McCloskey, B. D.; García, J. M.; Krupp, L. E.; Viswanathan, V.; Luntz, A. C. *Nat. Chem.* **2014**, *7*, 50–56.

(28)   Lau, S.; Archer, L. a. *Nano Lett.* **2015**, *15* (9), 5995–6002.

(29)   Olivares-Marín, M.; Palomino, P.; Enciso, E.; Tonti, D. *J. Phys. Chem. C* **2014**, *118*, 20772–20783.

(30)   Luntz, A. C. *J. Phys. Chem. Lett.* **2012**, *3*, 3043–3047.

(31)   McCloskey, B. D.; Speidel, A.; Scheffler, R.; Miller, D. C.; Viswanathan, V.; Hummelshøj, J. S.; Nørskov, J. K.; Luntz, A. C. *J. Phys. Chem. Lett.* **2012**, *3*, 997–1001.

(32)   Macdonald, J. R. *Solid State Ionics* **1984**, *13*, 147–149.

(33)   Hurt, R. L.; Macdonald, J. R. *Solid State Ionics* **1986**, *20*, 111–124.

(34)   Younesi, R.; Hahlin, M.; Roberts, M.; Edström, K. *J. Power Sources* **2013**, *225*, 40–45.

(35)   Lu, J.; Jung, H.-J.; Lau, K. C.; Zhang, Z.; Schlueter, J. a; Du, P.; Assary, R. S.; Greeley, J.; Ferguson, G. a; Wang, H.-H.; Hassoun, J.; Iddir, H.; Zhou, J.; Zuin, L.; Hu, Y.; Sun, Y.-K.; Scrosati, B.; Curtiss, L. a; Amine, K. *ChemSusChem*

2013, *6* (7), 1196–1202.

(36)   Kichambare, P.; Kumar, J.; Rodrigues, S.; Kumar, B. *J. Power Sources* **2011**, *196*, 3310–3316.

(37)   Zhang, T.; Zhou, H. *Nat. Commun.* **2013**, *4*, 1817–1823.

(38)   Sahapatsombut, U.; Cheng, H.; Scott, K. *J. Power Sources* **2013**, *227*, 243–253.

(39)   Hassoun, J.; Croce, F.; Armand, M.; Scrosati, B. *Angew. Chem. Int. Ed. Engl.* **2011**, *50*, 2999–3002.

(40)   Eswaran, M.; Munichandraiah, N.; Scanlon, L. G. *Electrochem. Solid-State Lett.* **2010**, *13*, A121–A124.

Chapter 4 – Strategies to improve the Li-O$_2$ battery performance

Li-O$_2$ batteries have not been able to match the expectations initially generated based on their high theoretical energy density. Thus, different strategies have been followed in order to improve their performance. In this chapter many of these strategies are followed and analyzed in detail.

4.1. Introduction

High charge overpotential in Li-O$_2$ batteries (1-1.5 V) has been one of the main challenges that researchers have had to deal with from the early beginnings of this technology.[1–3] The insulating nature of the Li$_2$O$_2$ generated during the discharge of the cell and its low solubility in the common organic electrolytes leads to high charge potentials for the oxidation of the discharge products accumulated in the oxygen electrode.[4–6] At those high potentials the organic electrolyte[1,7,8] and the carbon electrode[9–11] have been reported to undergo side reactions leading to the formation of carbonates that passivate the oxygen electrode and hinder the electrochemical performance of Li-O$_2$ batteries.

The most common strategy adopted to decrease charge overpotential has been the use of heterogeneous catalysts that dispersed in the oxygen electrode are supposed to facilitate the oxidation of Li$_2$O$_2$. In addition, many of them have also demonstrated to enhance the discharge capacity of the cell.[12,13] In the recent years several theories have been proposed to understand the mechanisms of catalytic activity. Some argue that this type of catalyst can provide lower overpotentials which result in improved stability of the battery components and may lead to enhanced cyclability.[14,15] Other authors associate the effect of these catalysts with the creation of alternative reaction pathways for the formation or reversion of the discharge products.[16,17] Catalysts, however, have also been demonstrated to catalyze degradation reactions also leading to an enhancement of the capacity.[1,18] Improvement of ORR and OER capacity and/or

overpotential by the use of heterogeneous catalyst, therefore, has to be accompanied by exhaustive material characterization using techniques that can accurately detect ORR products and side reaction by-products, such as Raman spectroscopy, infrared spectroscopy and X-ray photoelectron spectroscopy. In addition, in situ techniques can also give evidence of the real reactions occurring in the cell. Unfortunately, authors reporting the improvement of the electrochemical performance of the cell by the use of heterogeneous catalyst usually limits the discharge product characterization to XRD and SEM in which the detection of amorphous and soluble side-products is difficult.[12–14] Metal oxides[13,19,20] and precious metals[14,21,22] have been commonly reported as electrocatalysts for Li-O_2 batteries. In this work the catalytic activity of MnO_2, Pd and Au will be analyzed.

Other authors have studied the substitution of carbon by alternative materials in the oxygen electrode in order to avoid its oxidation at high charging potentials.[9–11] Metal oxides,[23–26] precious metals,[27–29] carbides[30] and polymeric materials[31] have been reported as positive electrode materials in Li-O_2 cells. In this chapter, Co_3O_4, NiO and TiC have been analyzed as carbon-free electrode materials based on the successful performance evidenced in literature by metal oxides and carbides.

Finally, improvement on the Li-O_2 cell chemistry by the inclusion of additives in the electrolyte has been proposed. On the one hand, the stabilization of the discharge products generated in ORR plays a key role in the prevention of side reactions, particularly by the nucleophillic attack of O_2^- radical. O_2^- coordinates stronger coordinates with softer acids based on Pearson's hard and soft acids and bases (HSAB) theory.[32] K^+ is a softer acid than Li^+ [33] and its addition is supposed to improve the stabilization of the discharge products in the electrolyte. On the other hand, oxidation of the electronic insulator Li_2O_2 during charge can be favored by the use of heterogeneous catalysts, also known as redox mediators (RMs).[34–36] These compounds, dissolved in the electrolyte, act as charge transfer carriers that diffuse

from the carbon electrode surface, where they are oxidized, to the discharge product particle surface and oxidize it (see Figure 4.1):[37]
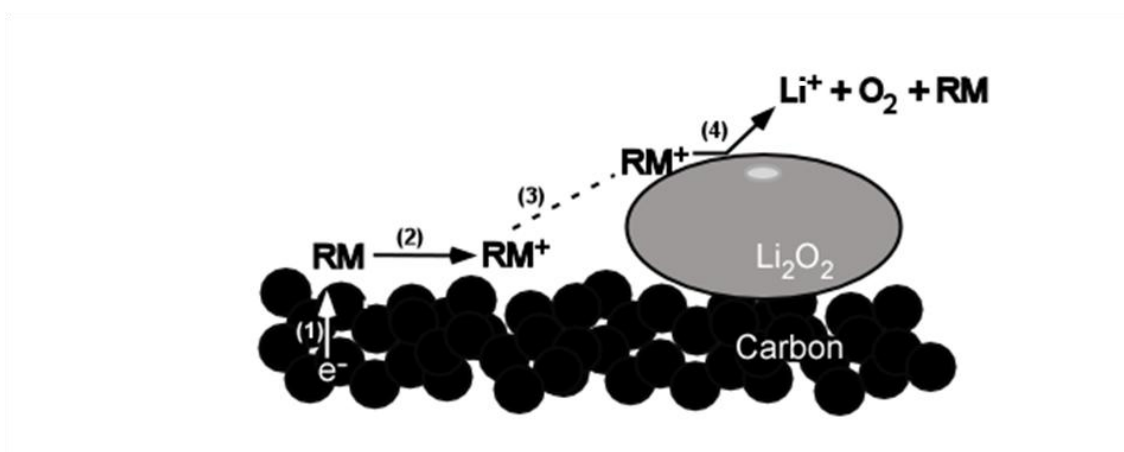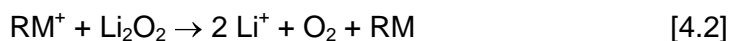
$$RM \rightarrow RM^+ + e^- \qquad\qquad [4.1]$$

$$RM^+ + Li_2O_2 \rightarrow 2\ Li^+ + O_2 + RM \qquad\qquad [4.2]$$

Figure 4.1. Schematic representation of the RM^+/RM redox couple mediated OER.

In this chapter the cell chemistry using iodide (I^-) as RM is analyzed in detail. In addition, the synergetic effect of the discharge product stabilizer K^+ and the charge RM I^- is demonstrated.

4.2. Catalyst assisted ORR and OER

4.2.1. MnO$_2$ characterization

MnO_2, Pd and Au were studied as catalyst in $Li-O_2$ batteries. MnO_2 powder synthesized by hydrothermal method (see Chapter 2 for experimental details) was firstly analyzed by XRD, SEM and TEM. XRD pattern (Figure 4.2) reveals the formation of the Ramsdellite phase ($R-MnO_2$), which was indexed to an orthorhombic structure with the space group *Pnam* (JCPDS 82-2169) with a = 9.0486, b = 4.5281 and c = 2.9138 as cell parameters.
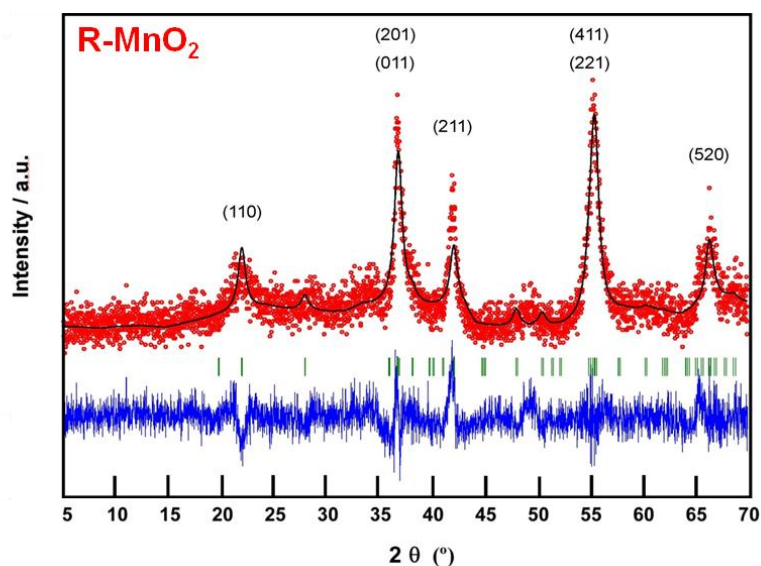
Figure 4.2. Fitted diffraction profile of the MnO_2 powder showing observed (red line), calculated (black line), difference (blue line) profiles and position of the theoretical reflections of R-MnO_2 (green lines).

In addition, the morphology of these systems was analyzed by SEM (Figures 4.3.a and 4.3.b) and TEM (Figures 4.3.c and 4.3.d).
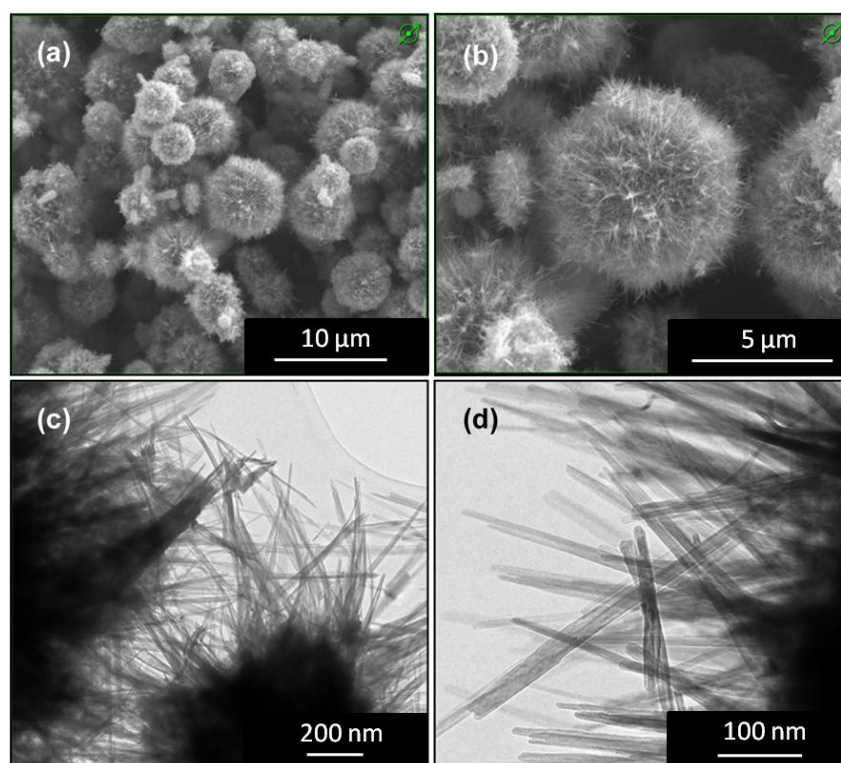

Figure 4.3. (a, b) SEM and (c, d) TEM images of the R-MnO_2 powder.

90

The images show the formation of acicular manganese oxide aggregates (5-10 µm wide) which tend to form spherical clusters, adopting urchin-shaped form of roughly 6 microns diameter. TEM images confirm the existence of very small dense clusters of nanorods (Figures 4.3.c and 4.3.d) with a diameter of about 10 nm and different lengths between 50 and 500 nm.

4.2.2. Analysis of the catalytic properties of MnO_2, Pd and Au

First galvanostatic cycle was stopped at different potentials (2.7, 2.6, 2.5, 2.3, 2.0, 3.0, 3.8, 4.2 and 4.5 V) and impedance spectroscopy of the catalyst containing cathodes was carried out at those stops (Figure 4.4), similarly to the experiments presented in Chapter 3.
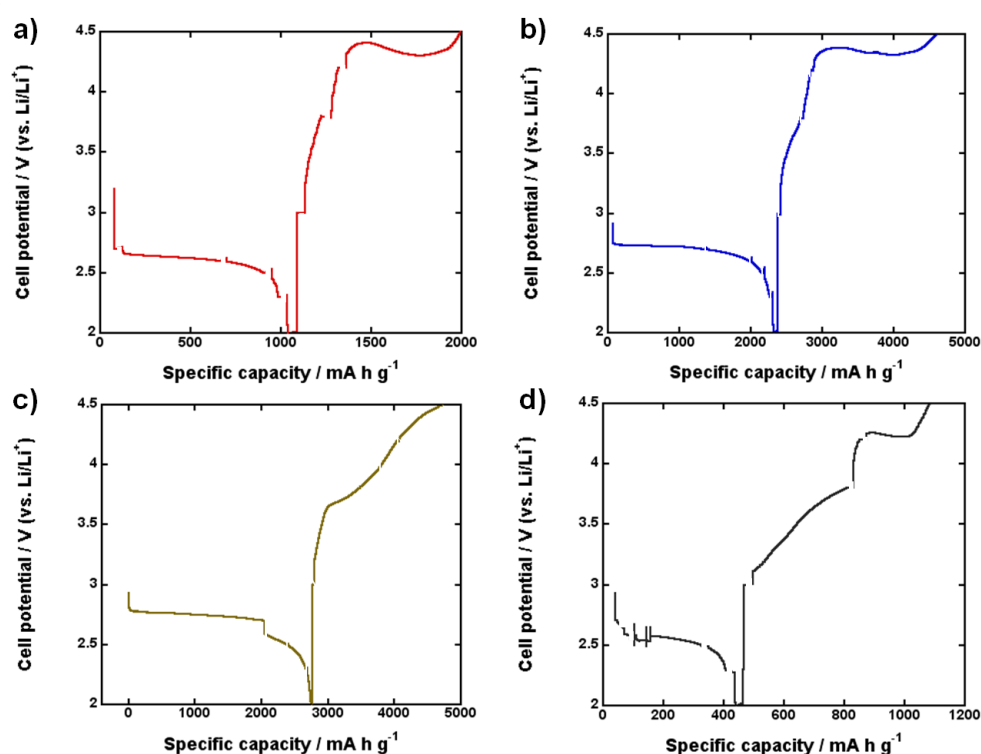

Figure 4.4. First galvanostatic cycles carried out (a) without catalyst, and using (b) R-MnO_2, (c) Au and (d) Pd as catalysts. Measurements were carried out at 0.1 mA cm^{-2} in a potential window of 2.0-4.5 V. Cycles were stopped at 2.7, 2.6, 2.5, 2.3, 2.0, 3.0, 3.8, 4.2 and 4.5 V to carry out impedance spectroscopy measurements.

Galvanostatic cycle of the catalyst-free cell (Figure 4.4.a) revealed that the ORR took place mostly between 2.7 and 2.6 V. After impedance measurement at 2.6 V the potential decay was progressively enhanced finishing in a deep discharge at 2.0 V. During the recharge of the cell no plateau was observed until the last potential window between 4.2 and 4.5 V. As previously mentioned carbon[9–11] and electrolyte[1,7,8] have been demonstrated to be unstable at those high potentials and that plateau might partly be attributed to side reactions. The addition of R-MnO$_2$ resulted in an enhanced discharge and charge capacity (Figure 4.4.b) and a small decrease of discharge overpotential. The shape of the galvanostatic profile, however, did not vary from the catalyst-free profile and the charge overpotential was not decreased. In addition, coulombic efficiency increased from 92% for the catalyst-free cathode to 102% after the addition of R-MnO$_2$; the excess of charge with respect to the discharge indicates the presence of side reactions associated to OER. Moreover, the almost identical cycle profile of the catalyst free and the MnO$_2$ added cells indicates that similar reactions are possibly taking place in both cases. Figure 4.5 shows a proposed mechanism to explain the effect of the addition of MnO$_2$ to the oxygen electrode.
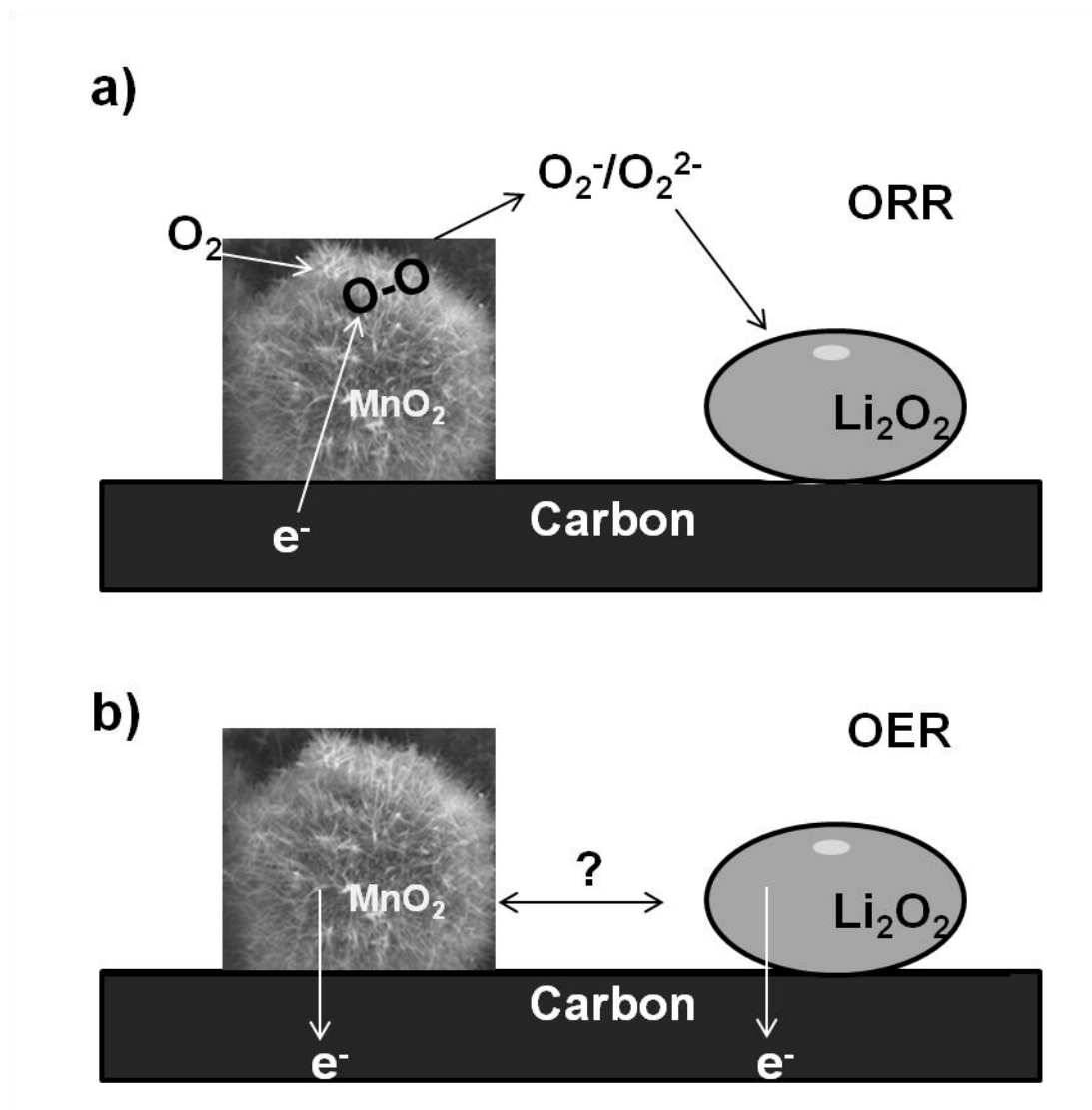
Figure 4.5. Schematic representation of the influence of MnO_2 in (a) ORR and (b) OER.

During the discharge of the cell O_2 can be adsorbed, reduced and finally accumulated at the electrode surface as Li_2O_2 in the typical toroidal shape (Figure 4.5.a). The MnO_2 catalyzed ORR can be responsible for the enhanced discharge capacity due to a more efficient electron transfer to the adsorbed O_2 molecules. Nevertheless, it is difficult to understand how a heterogeneously dispersed discrete urchin can assist in the oxidation of other discrete and dispersed compounds (Li_2O_2 toroids, as shown in Figure 4.5.b). This could be the reason for the similarities in the charge plateau between the catalyst-free and the R-MnO_2 containing oxygen electrodes.

The addition of 40% of Au in the carbon electrode resulted in a significant increase of the discharge capacity (2746.9 and 1040 mA h g^{-1} for the Au containing and the catalyst-free electrodes, respectively). There were differences in charge overpotential as it was decreased from ~4.3 V to ~3.7 V. Decrease in charge overpotential had been previously reported by Amine's group for LiO_2 oxidation[38] and Au was demonstrated to catalyze one-electron ORR by means of DEMS.[39] Whatever the reason for the reduction of charge overpotential coulombic efficiency was decreased from 92% without catalyst to 72% after the addition of Au, revealing that although at lower potentials the catalyst did not allow the cell to perform a promising galvanostatic cycle.

Finally, the discharge capacity exhibited by the addition of Pd to the oxygen electrode was lower than that of the catalyst-free electrode. Main differences between these two cycles, however, were observed during charge of the cells; opposite to all the other cells Pd-containing electrode performed the main part of the charge below 3.8 V. Actually, when the cell reached 3.8 V the coulombic efficiency was 102% also indicating the presence of side reactions. A final plateau similar to that in the MnO_2-containing and catalyst-free cells was observed between 4 and 4.5 V.

Impedance spectroscopy measurements were carried out at 2.7, 2.6, 2.5, 2.3, 2.0, 3.0, 3.8, 4.2 and 4.5 V of each galvanostatic cycle and, opposite to impedance analysis in Chapter 3, the obtained Nyquist plots were fitted using R_1-R_2CPE_2-R_3CPE_3 equivalent circuit (Figure 4.6.a). The use of a reference electrode allowed us to omit the contribution of the Li anode. In addition, R_4CPE_4 and R_5CPE_5 associated to O_2 diffusion from the atmosphere to electrode surface, O_2 adsorption and charge-transfer resistance of electrochemical reduction of oxygen species were analyzed together and labeled as R_3CPE_3. R_1 and R_2CPE_2 were assigned to ohmic resistance and charge transfer in the oxygen electrode/electrolyte interface, respectively. Some of these fittings carried out in the proximities of the full discharge and after charge are shown in Figure 4.6.
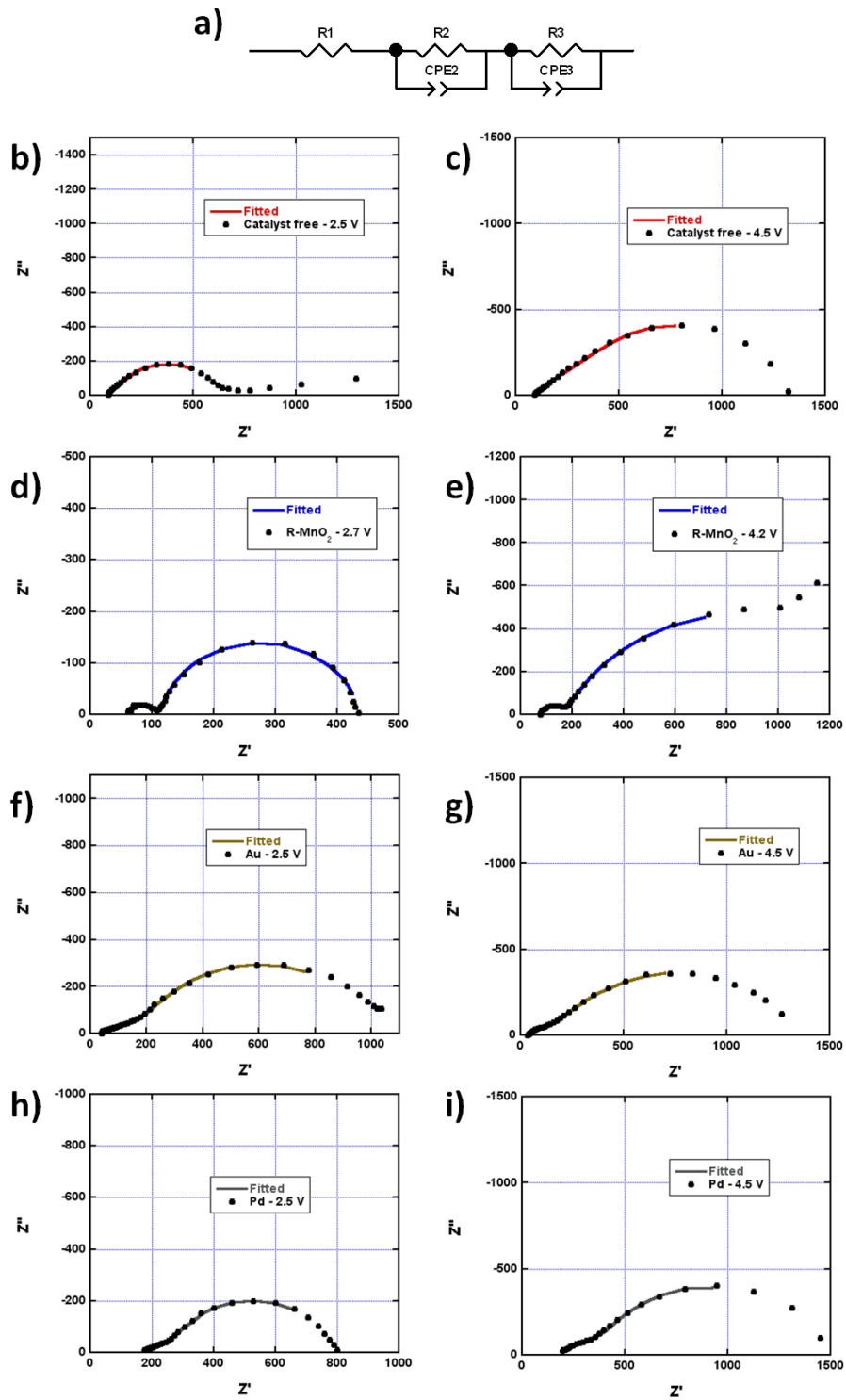
Figure 4.6. (a) Equivalent circuit proposed for the fitting of the experimental data. Experimental points recorded together with the fittings (b) without catalyst at 2.5 V and (c) 4.5 V, (d) with R-MnO$_2$ at 2.5 V and (e) 4.5 V, (f) with Au at 2.5 V and (g) 4.5 V and (h) with Pd at 2.5 V and (i) 4.5 V

In order to reasonably compare the evolution of the resistances during the galvanostatic cycles they were represented vs. the fraction of the maximum discharge capacity in which the impedance measurement was carried out. This method allowed us to compare, for example, the impedance measurement of the Au containing electrode at 2.7 V after 9520 mA h g^{-1} with the measurement performed in the catalyst-free electrode at 2.5 V after ~900 mA h g^{-1} as in both of them ~90% of the maximum depth of discharge was achieved. Resistance evolutions are shown in Figure 4.7.
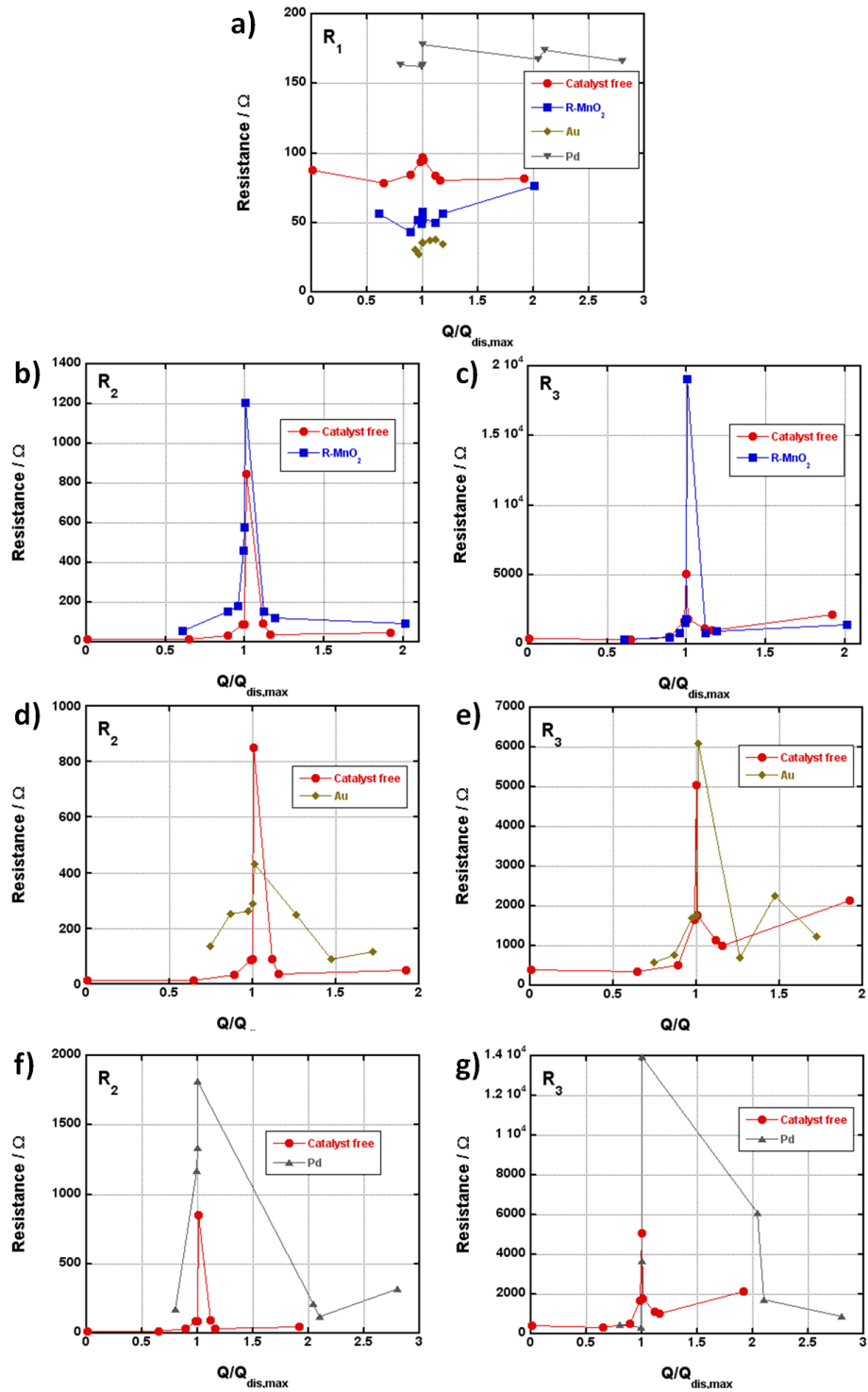
Figure 4.7. Evolution of the resistances associated to the oxygen electrode during the galvanostatic cycle. (a) Comparison of the evolution of R_1 with and without catalyst. (b) and (c) represent the evolution of R_2 and R_3, respectively, with and without R-MnO$_2$. (d) and (e) represent the evolution of R_2 and R_3, respectively, with and without Au. (f) and (g) represent the evolution of R_2 and R_3, respectively, with and without Pd.

Similarly to the measurements in Chapter 3, R_1 remained almost constant during all the measurements of each cycle (Figure 4.7.a). Both R_2 and R_3 increased during discharge showing the maximum resistance value at full discharge ($Q/Q_{dis,max} = 1$) and decreased during the charge of the battery ($Q/Q_{dis,max} > 1$) as can be observed in Figures 4.7.b-g. The addition of R-MnO_2 to the oxygen electrode revealed an increase of the resistance associated to the electrode/electrolyte interface (R_2) for all the measurements carried out (Figure 4.7.b), in good agreement to the insulating nature of MnO_2.[40] R_3, associated to the accumulation of discharge products was similar with and without catalyst (Figure 4.7.c) although the discharge capacity, and consequently the discharge product generated, was twofold higher with MnO_2 and might be indicative of a similar accumulation process (as previously exposed in Figure 4.5). It is worth noting that although the main part of the charge process of both cells took place between 4.2 and 4.5 V a slight increase of R_3 was observed in this period that can be indicative of the generation of insulating carbonate based species accompanying the Li_2O_2 removal (OER).

Electronic conductor Au containing electrode exhibited lower R_2 than bare Vulcan carbon (VC), what could be associated to the addition of the conductive Au (Figure 4.7.d).[41] It is worth mentioning that R_3 of the Au containing electrode associated to product accumulation was in the same range of that without catalyst (Figure 4.7.e) even though the discharge capacity was almost threefold higher. As can be observed in Figure 4.7.e R_3 decreased in the potential ranges of 3.0-3.8 V and 4.2-4.5 V and increased between 3.8 and 4.2 V. This increase suggests the formation of insulating species in the electrolyte surface that could be generated in side-reactions, revealing that Au does not only catalyze OER and can also facilitate undesired reactions.[18]

On the other hand, it is difficult to explain the resistance evolution of the Pd containing electrode. Although it is an electron conducting material[41] the electrode/electrolyte interface resistance is higher than that of the catalyst-free electrode during the whole

galvanostatic cycle (Figure 4.7.f). Higher resistance values were also observed for R_3 (Figure 4.7.g) although the discharge capacity was significantly lower than in the catalyst free cell. Besides the resistance evolution data and the lower discharge capacity, the galvanostatic charge also points out side reactions accompanying OER.

In summary, studied catalysts have not significantly improved the performance of the galvanostatic cell. Precious metals (Au and Pd) have been observed to catalyze side reactions in addition to OER. In turn, R-MnO_2 has demonstrated an improved ORR although drawbacks associated to OER such as high overpotential and derivative side reactions therefore were not overcome. Finally, despite the low coulombic efficiency and the presence of side-reactions during charge discharge capacity has been increased and the charge overpotential has been reduced by the addition of Au to the oxygen electrode. New strategies will be proposed in the following sections in order to improve the cell performance.

4.3. Carbon-free electrodes

Co_3O_4, NiO and TiC were the materials analyzed in order to replace carbon in the oxygen electrode of the Li-O_2 cell. Co_3O_4 and NiO were in situ grown on a Ni foam piece (see details in Chapter 2) and they were characterized before being tested as electrode materials.

4.3.1. Co_3O_4 and NiO characterization

XRD pattern of the powder scratched from the electrode confirmed the formation of Co_3O_4 (Figure 4.8.a) and NiO (Figure 4.8.b).
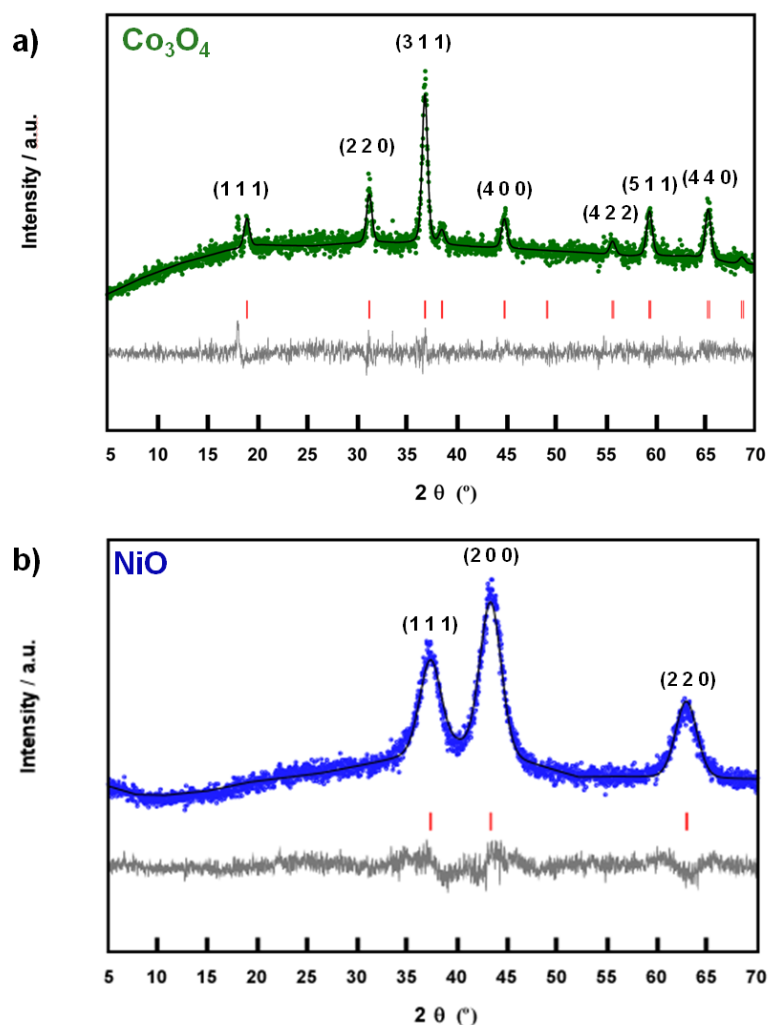
Figure 4.8. Fitted diffraction profile of the (a) Co_3O_4 and (b) NiO powder showing observed (green and blue lines, respectively), calculated (black line), difference (grey line) profiles and position of the theoretical reflections of these species (red lines).

Co_3O_4 presented a cubic unit cell with the space group F d -3 m (JCPDS 78-1970). The cell parameter of these cubes was a = 8.079 Å and the pure phase could not be obtained by the selected method as a reflection at 2θ = 18.1 ° can be observed. This specie could not be identified. On the other hand, the NiO synthesized by the same method did not show any impurities and could be ascribed to the cubic space group F m -3 m (JCPDS 70-0429) with a = 4.184 Å. The morphologies of both C-free electrodes are shown in Figure 4.8.
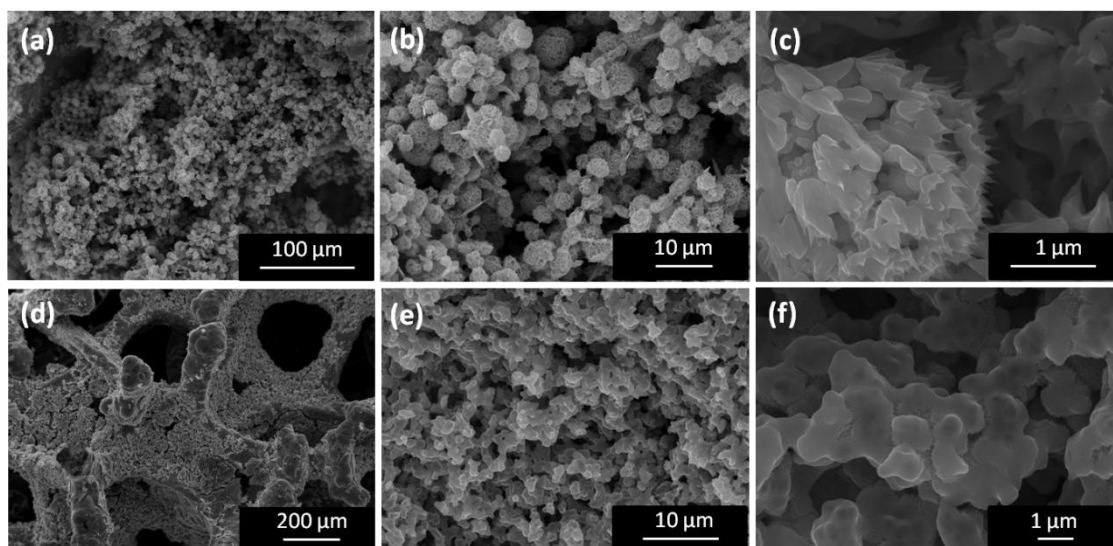
Figure 4.9. SEM images of the hydrothermally synthesized Co_3O_4 (a, b and c) and NiO (d, e and f) electrodes.

In contrast to the electrodes synthesized by Lin et al.[42] the Ni meshes were completely covered by Co_3O_4 (Figure 4.9.a) and NiO (Figure 4.9.d). Both oxides were growth forming aggregates of around 2 μm (Figures 4.9.b and 4.9.e); the Co_3O_4 aggregates were formed by sharpen particles (Figure 4.9.c) while the NiO aggregates consisted of particles with an undefined morphology (Figure 4.9.f). The electrochemical performance of these electrodes will be discussed in the following section.

4.3.2. Electrochemical tests

Hydrothermally growth carbon free Co_3O_4 and NiO electrodes together with the commercial TiC based electrode were tested as cathodes in Li-O_2 cells.
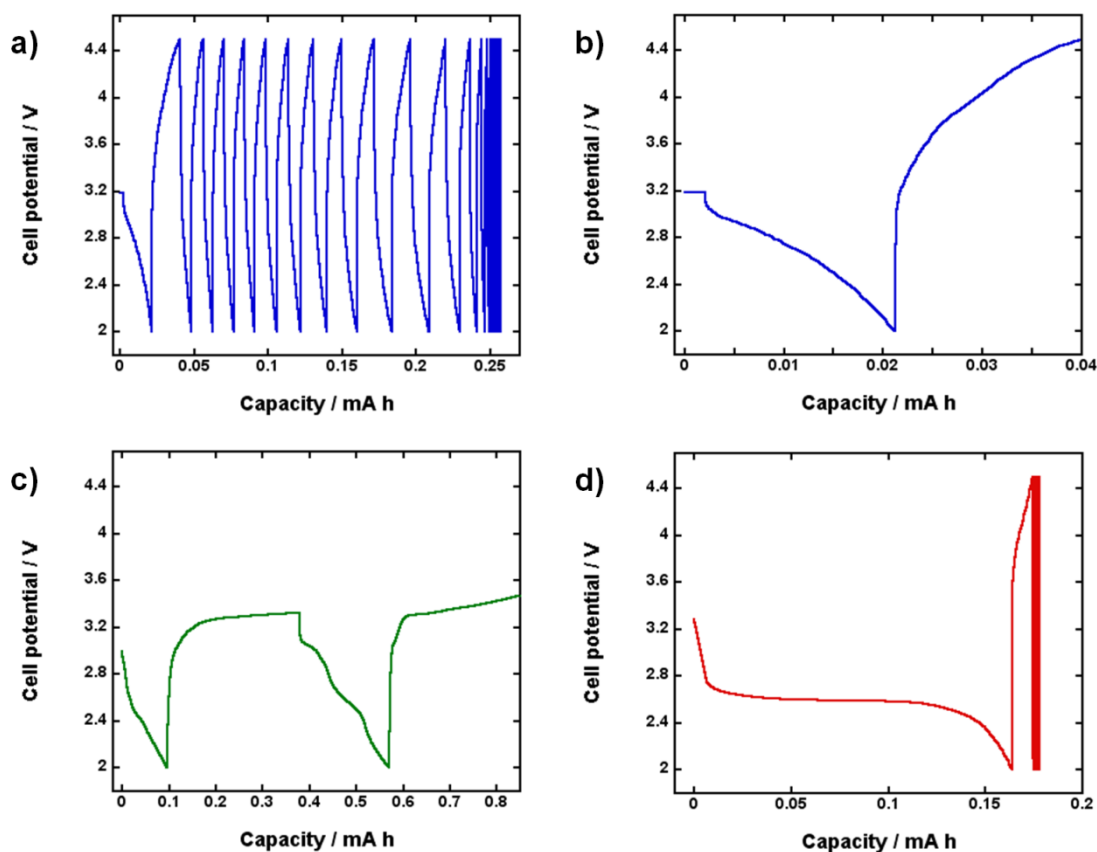
Figure 4.10. Galvanostatic cycles carried out using NiO (a, b), Co_3O_4 (c) and TiC (d) and oxygen electrodes in a Li-O_2 cell. The current density was 0.05 mA cm^{-1} and the potential window was set between 2.0 and 4.5 V,

Galvanostatic cycles carried out using the NiO oxygen electrode (Figure 4.10.a) showed an unsuccessful cycling performance in which the discharge capacity in all the cycles was negligible. Detail of the first galvanostatic cycle (Figure 4.10.b) evidenced the absence of a discharge plateau and a fast voltage drop leading to a discharge capacity of 0.021 mA h that was traduced in a fast charge. In addition, in the following cycles the capacity was even lower. The replacement of NiO by Co_3O_4 enhanced the discharge capacity by 5 (Figure 4.10.c), although it kept being insignificant. The first recharge, however, was much longer than the previous discharge what points out that side reactions were accompanying OER. The second discharge exhibited two different plateaus (the first around 3 V and the second at 2.5 V) that confirm the presence of other reactions apart from ORR. The low discharge capacity coupled with the presence

of parallel reactions indicates that Co_3O_4 is not an appropriate substitute for carbon. Finally, TiC was tested as oxygen electrode (Figure 4.10.d). The first discharge exhibited a flat plateau around 2.6 V that finished with a drop in the potential at 0.16 mA h. Although the discharge capacity was low, the stability of the pleateau could be considered promising. Nevertheless, the following null charge evidenced the lack of OER what in the following cycles was traduced in the absence of ORR.

In summary, experiments carried out with carbon free electrodes could not be considered successful and, coupled with the results obtained using heterogeneous catalysts point out the necessity of a change in the strategy; in the following section improvement in the cycling stability of the cell will be pursued by the addition of additives to the electrolyte.

4.4. K⁺ additive assisted ORR

The effect of the addition of potassium ions to the electrolyte was analyzed in the $Li-O_2$ batteries. Potassium-oxygen ($K-O_2$) batteries have been successfully cycled based on the formation and decomposition of potassium superoxide (KO_2)[43] and potassium impurities in the oxygen electrode have been demonstrated to improve the performance of $Li-O_2$ batteries.[44] In addition, Abraham et $al.$ observed that both oxygen reduction reaction (ORR) and oxygen evolution reaction (OER) were favored when Li^+ was substituted by larger monovalent cations, and explained this effect based on Pearson's HSAB theory:[32] Larger cations are softer Lewis acids that coordinate more strongly with the soft base O_2^-. Considering that the superoxide radical can react with both electrolyte[45] and carbon electrode[46,47] due to its high instability, a complexed state would also contribute to prevent the degradation of the cell components. Moreover, Sharon et $al.$ evidenced by the use of different anions in the electrolyte that the lower dissociation of the electrolyte salt delays the interaction between Li^+ and LiO_2 leading to an enhanced solution phase mechanism.[48]

The effect of K^+ addition to the electrolyte was studied comparing the electrochemical performance of two $Li-O_2$ cells with different electrolytes; one of them consisted of K^+ free, 1 M LiOTF in TEGDME while the second one was 0.1 M KOTF and 1 M LiOTF in TEGDME (Figure 4.11).
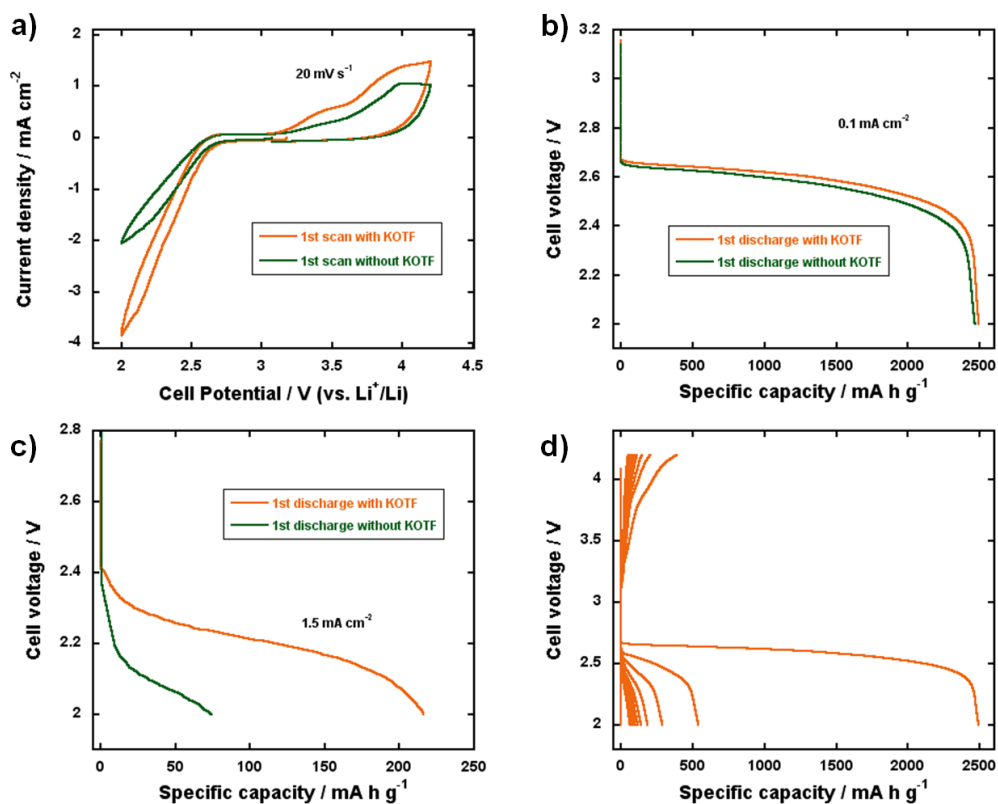

Figure 4.11. Electrochemical performance of lithium-oxygen batteries with (orange line) and without (green) 0.1 M KOTF in the electrolyte. (a) Cyclic voltammetry at a scan rate of 20 mV s^{-1}. (b) First galvanostatic discharge profiles at 0.1 mA cm^{-1}. (c) First galvanostatic discharge profile at 1.5 mA cm^{-1}. (d) Galvanostatic cycling of a battery with an electrolyte containing 0.1 M KOTF in a voltage range of 2 and 4.2 V at 0.1 mA cm^{-2}.

The CV measurement, carried out between 2 and 4.2 V at a scan rate of 20 mV s^{-1} (Figure 4.11.a), evidences that potentials of electrochemical processes (onsets at 2.6 V for the cathodic scan and 3.1 and 3.6 V for the anodic scan) were unaffected by the presence of K^+ in the electrolyte. However, both cathodic and anodic currents are enhanced by a factor of almost two. This was also observed by Abraham *et al.* when

they used salts of different monovalent cations at a concentration of 0.025 M.[33] In that work, however, the onset potentials during anodic scans were increased with smaller cations. Instead, the anodic scan in Figure 4.11.a reveals the same onset potential for the two observed processes after adding K^+. It is widely accepted that the first process in the anodic scan starting at 3.1 V corresponds to LiO_2 oxidation, while the second process at 3.6 V is related to Li_2O_2 oxidation.[38] In addition, the observed anodic current is only slightly higher in presence of K^+ revealing that it does not influence the OER chemistry.

Galvanostatic discharges of Li-O_2 cells with and without K^+ ions in the electrolyte were carried out at 0.1 mA cm^{-2} (Figure 4.11.b) and 1.5 mA cm^{-2} (Figure 4.11.c). At 0.1 mA cm^{-2} almost no differences were observed in the discharge profile or the capacity of the battery. Instead, at the higher current density of 1.5 mA cm^{-2} the electrolyte with K^+ showed both lower overpotential and higher discharge capacity. Galvanostatic discharges in Figure 4.11.c are similar to those reported using a ORR redox mediator.[49,50] In those cases, the higher rate capability was attributed to the electron transfer from the electrode to the mediator, which then promotes a solution-mediated ORR, that finally leads to higher discharge capacity. In the present case, no mediator was added, but a similar effect is achieved by the addition of K^+ that favors a solution-mediated mechanism. At low current densities, as demonstrated by Adams and coworkers,[51] ORR is solution-mediated leading to large toroidal particles. In addition, Aetukuri *et al.* attributed this morphology to solvating additives, including water.[52] In this regime the current density is low enough to allow LiO_2 stabilization and diffusion in the electrolyte and the contribution of K^+ is negligible. In contrast, at higher current densities when ORR is likely surface mediated, K^+ contributes to stabilize the superoxide anion in the bulk of the electrolyte as explained by Abraham[33] and, therefore, discharge capacity and the discharge voltage plateau are increased.

The rechargeability remains equally poor, as shown by a galvanostatic cycling at 0.1 mA cm^{-2} in a voltage range of 2-4.2 V, leading to a fast capacity fading (Figure 4.11.d). It has to be noted that by the addition of K$^+$ to the electrolyte one could expect the formation of KO_2, similarly to K-O_2 cells.[43] Experimental oxidation of KO_2 during charge, however, occurs at ~2.8 V vs. Li$^+$/Li (2.62 V vs. K$^+$/K in the work by Ren *et al.*)[43] and, therefore, the lack of a plateau at such potential evidences the absence of KO_2. This behavior proves that K$^+$ does not influence OER, which is in good agreement with the CV data in Figure 4.11.a. Consequently, an additional agent is required in order to improve the OER and the cycling performance of the cell.

4.5. K$^+$ and I$^-$ assisted ORR and OER

4.5.1. Effect in the electrochemical response

As mentioned in the introduction, I$^-$ addition to the electrolyte has been widely reported to improve the rechargeability of the Li-O_2 battery. The combined effect of I$^-$ and K$^+$ on the cycling performance of the cell was tested comparing cells with and without the addition of 0.1 M LiI or KI to the 1 M LiOTF in TEGDME electrolyte (Figure 4.12).
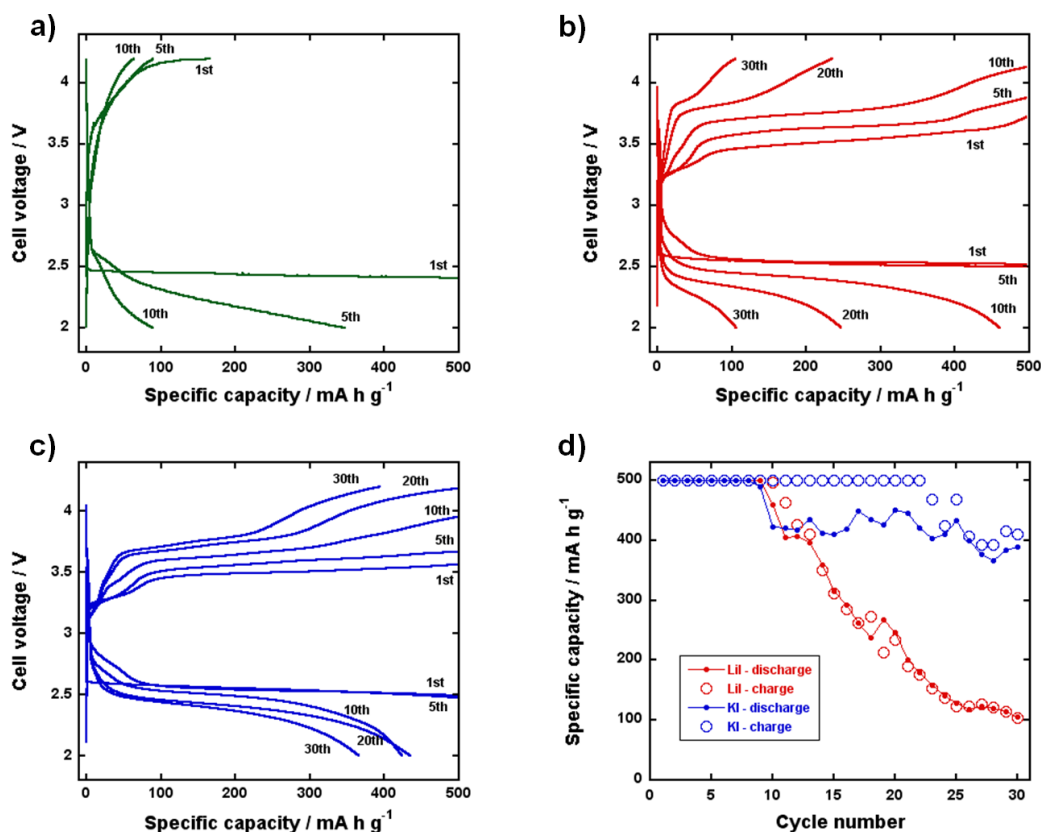
Figure 4.12. Galvanostatic cycles of Li-O_2 cells between 2 and 4.2 V at 0.1 mA cm^{-2} with a cutoff capacity of 500 mA h g^{-1}. (a) Profiles without additives, (b) with 0.1 M LiI redox mediator and (c) with 0.1 M KI redox mediator in the electrolyte. (d) Comparison of the discharge (line-connected dots) and charge (circles) capacities obtained with 0.1 M LiI and with 0.1 M KI.

These cells were cycled at a current density of 0.1 mA cm^{-2} limiting the discharge and charge capacity to 500 mA h g^{-1}. Even when the discharge capacity is limited, below 4.2 V the cell without redox mediator could only oxidize a small part of the discharge products deposited in the cathode, leading to a fast decay of the discharge capacity after few cycles (Figure 4.12.a). Thus, the cell could only reach 60 % of the cutoff capacity (500 mAh g^{-1}) already after 5 galvanostatic cycles. As expected, when LiI was used, the charge reaction was enhanced, with a clear plateau below 4 V, leading to an improved capacity retention, with over 60% of the capacity for at least 20 cycles (Figure 4.12.b). This capacity, however, decreased rather fast in the following cycles. After confirming enhancements of ORR with K$^+$, and of OER with I$^-$, KI was added to the

electrolyte in order to analyze their combined effect. Galvanostatic cycles of a Li-O_2 cell containing 0.1 M KI are shown in Figure 4.12.c. A stable first discharge plateau is observed at 2.55 V similar to the previous cases. The process occurring at 3.0 V, which was previously observed in the cell with LiI during charge, was also detected with an apparently similar evolution during the first 10 cycles. However, beyond this point discharge capacity was retained between 350 and 450 mA h g^{-1} when KI was used while the capacity fade was much faster in presence of LiI (see also Figure 4.12.d). Consequently, a synergetic effect of K$^+$ and I$^-$ is detected clearly improving the cycling performance of the Li-O_2 cell. At closer inspection, lower potentials of the charge plateaus in presence of K$^+$ are consistently observed, allowing a more complete removal of the discharge products before the upper voltage cutoff is reached, and thus a slower increase of the overpotentials.

In order to provide evidence of I$^-$ oxidation two cells, with and without 0.1 M KI in the electrolyte, were charged without a previous discharge (Figure 4.13). The potential of the cell without KI increased rapidly to reach the 4.2 V without showing any plateau. On the contrary, the cell with 0.1 M KI exhibited a plateau of 60 mA h g^{-1} at 3.2-3.4 V, similar to that at the first stages of the charge in Figures 4.12.b and 4.12.c, confirming its attribution to I$^-$ oxidation. A plateau with similar capacity appears from the second discharge, indicating reduction of the produced I$_2$.

Charge:	$2\ I^- \rightarrow I_2 + 2\ e^-$	[4.3]

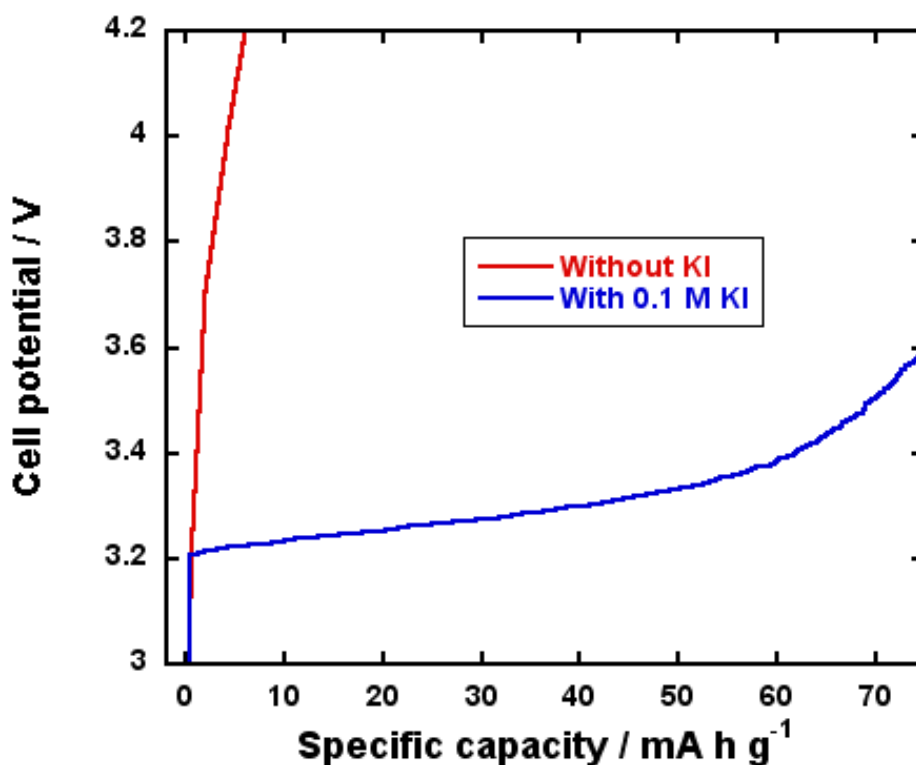| Discharge:	$I_2 + 2\ e^- \rightarrow 2\ I^-$	[4.4]
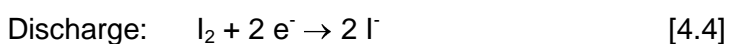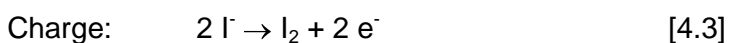
Figure 4.13. Charge profile of a lithum-oxygen cell with (blue line) and without (red line) 0.1 M KI in the electrolyte (1 M LiOTF in TEGDME) at 0.1 mA cm^{-1}.

In furtherance of obtaining more information about the reactions at the plateaus at 3.6 and 4.0 V the cycling evolution of two batteries with potential windows of 2-3.8 (Figure 4.14.a) and 2-4.2 V (Figure 4.14.b) was compared. The capacity retention was remarkably higher when the potential window was extended to 4.2 V. Consequently, it can be deduced that the oxidative activity of I$^-$ is not limited to the plateau at 3.6 V and the discharge products formed during discharge need potentials higher than 3.8 V to be completely oxidized.[53,54] It can be concluded that parasitic reactions contribute to the enhancement of the plateau at 3.6 V, as the capacity achieved at its end is similar to the previous discharge capacity and at that point (3.6 V) all the discharge products are not removed. To give further evidence of the incomplete OER at 3.6 V a cell with 0.1 M KI in the electrolyte was cycled limiting the discharge capacity to 500 mA h g^{-1} and without capacity limitation during charge in the potential range of 2-4.2 V (Figure 4.14.c). The first discharge was followed by an extremely long charge reaction of 1900

mA h g^{-1}. Charge capacity, however, rapidly decreased in the following cycles and the capacity of each charge approached to the value of their previous discharge. These results are compared to the previously presented limiting the charge of the cell to 500 mA h g^{-1} (Figure 4.14.d); the established maximum discharge capacity of 500 mA h g^{-1} could only be achieved in the first 8 cycles when charge capacity was limited, while this maximum discharge capacity was reached 15 times after a full recharge of the battery. Moreover, it was observed that when the discharge capacity of the cell without limiting charge capacity started to decay, charge overpotential increased tending to 4 V; after that the discharge capacity could be maintained in the following cycles at ~ 400 mA h g^{-1}. In addition, this trend was also observed in the battery with charge capacity limitation, and the discharge capacity of the cell was maintained at ~ 400 mA h g^{-1} after the cell became incapable of achieving the maximum discharge capacity of 500 mA h g^{-1}.
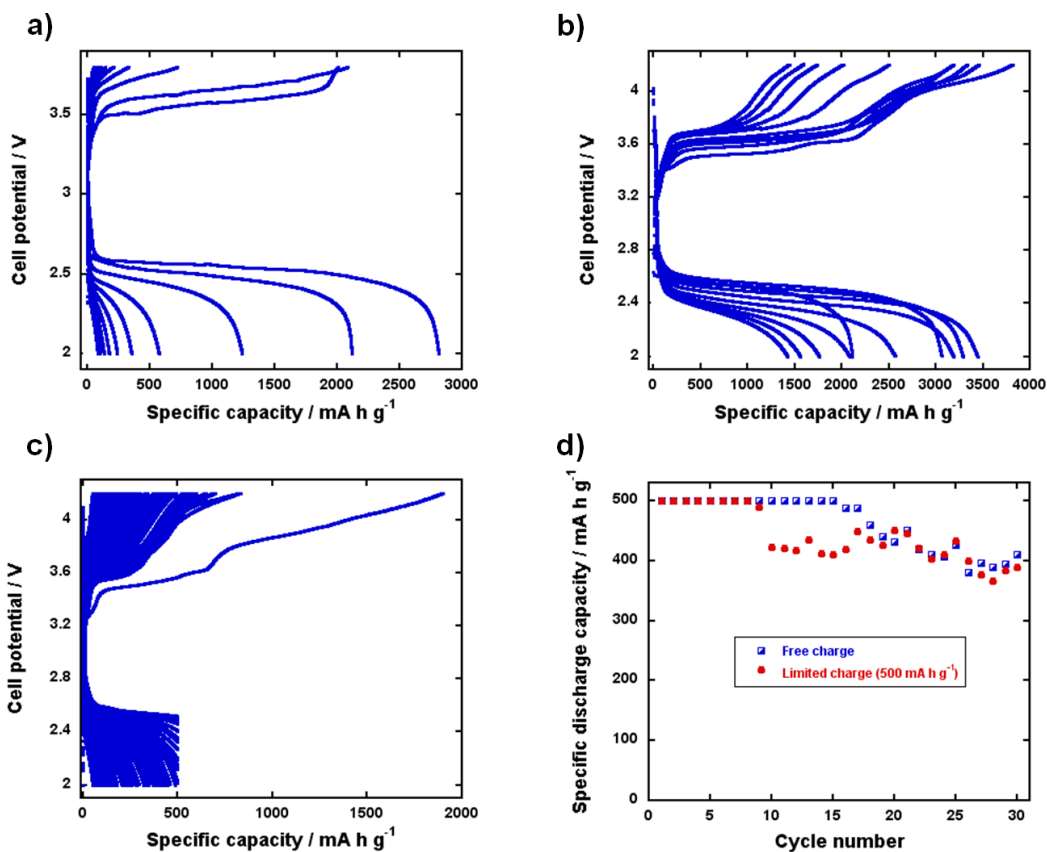
Figure 4.14. Galvanostatic cycles of a Li-O$_2$ cell with 0.1 M KI in the electrolyte without limiting the discharge capacity in a potential window between (a) 2 and 3.8 V and (b) 2 and 4.2 V. (c) Galvanostatic cycles of the same battery with a limited discharge capacity of 500 mA h g^{-1} without limiting the charge of the battery, in a potential window between 2 and 4.2 V. (d) Comparison between the discharge capacity recorded during the first 30 cycles with a fixed maximum discharge capacity of 500 mA h g^{-1} limiting the charge of the cell to 500 mA h g^{-1} (red cycles) and without limiting it (blue squares), in the range of 2 and 4.2 V.

4.5.2. Deeper insight into the effect of K$^+$ and I$^-$ addition

XPS analysis of the lithium anode reveals the presence of both I$^-$ and K$^+$ at the surface (Figures 4.15.a and 4.15.b). Both iodine and potassium signals can be detected by means of XPS at the Li anode. While K exhibits just one signal (highlighted in orange in Figure 4.15.a), three different signals can be observed for the case of iodine (Figure 4.15.b). The iodine spectrum evidence not only that I$^-$ is the main species, but also that secondary products such as I$_2$ or IO$_4^-$ can be deposited or chemisorbed at the anode

surface. Iodide species could be expected from the precipitation of the additive, their reaction with the anode or the reduction of the I_2 migrated from the cathode towards the anode during the charge process. This shuttling of I_2 was suggested in a previous work and these results confirm this feature.[56] Finally, the presence of oxidized species can be related with parasitic reactions. This fact discards a possibility that has been reported in literature by adding Ir^{3+};[55] the presence of K^+ does not influence the reaction of I^- with the Li electrode and its beneficial effect is limited to the oxygen electrode. Moreover, the deposition of K^+ on the anode points out the need of limiting its migration and deposition on this electrode; for this purpose the introduction of selective membranes is considered a promising approach.[57] In the other electrode, Li_2O_2 formation during discharge reaction with the KI additive was confirmed by XRD measurements of the oxygen electrode (Figure 4.14.c). Reflections at 32.9 and 34.9° were attributed to the gradual formation of Li_2O_2 and its removal after recharge to 3.8 V (JDCPS 74-0115). LiOH formation was not detected. Moreover, one could expect the deposition of KO_2 (JDCPS 77-0211) in the electrode due to the addition of K^+ to the electrolyte. XRD pattern, however, did not evidence the presence of such specie as no signal was detected at $2\theta = 31.37°$.
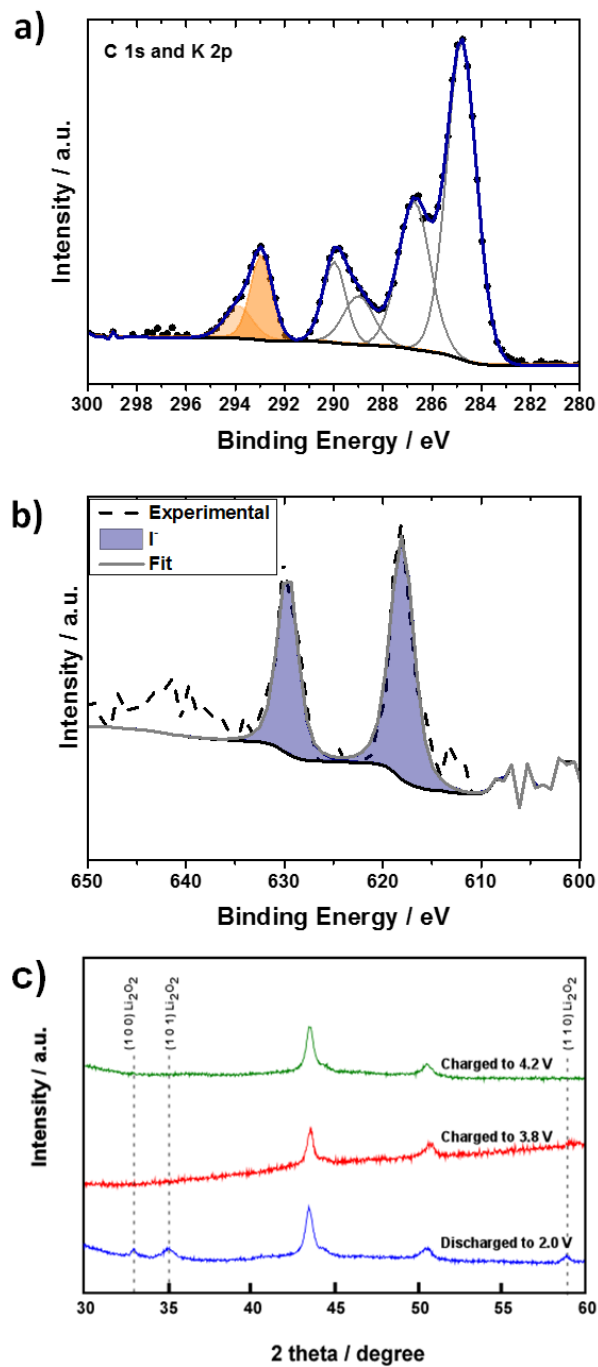
Figure 4.15. XPS measurements on the lithium anode after 1 cycle (2-4.2 V) using a KI additive in the electrolyte: (a) C 1s and K2p and (b) I 3d regions. (c) XRD patterns recorded in the oxygen electrode after discharge to 2.0 V (blue), charge to 3.8 V (red) and charge to 4.2 V (green) with 0.1 M KI redox mediator in the electrolyte.

In order to obtain detailed information on the discharge products deposited in the oxygen electrode transmission soft X-ray microscopy (TXM),[58] was applied to inspect whether the use of K^+ affected the distribution and composition of the deposits. Analyses of the O K-edge XANES spectra of the TEM grids (see Chapter 2) discharged in presence and absence of KOTF (Figure 4.16.a) reveal the presence of LiO_2, Li_2O_2 and Li_2CO_3 with very similar proportions for both electrolyte compositions. From the absence of superoxide and carbonate reflections in the XRD of the oxygen electrode it is inferred an essentially amorphous character for these components. TXM images revealed toroidal particles in both cases, but their size distribution was significantly different (Figure 4.16.b): the presence of K^+ led to a more homogeneous particle size. Instead, no significant chemical differences in the discharge products were observed, given the similar XANES spectra.
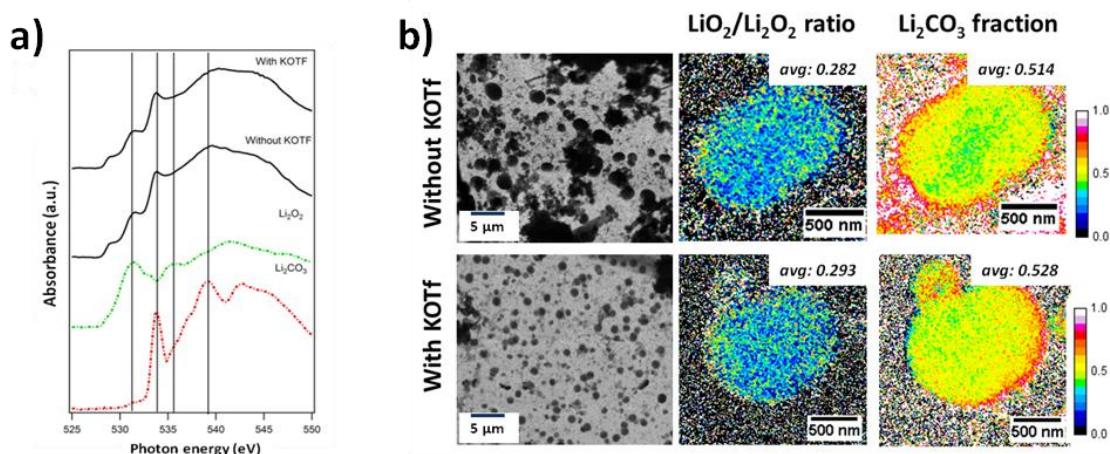

Figure 4.16. (a) O K-edge XANES spectra of the reference materials (Li_2O_2 and Li_2CO_3) and the discharge particles obtained at the carbon coated Au TEM grid after being fully discharged at 100 mA per total gram of carbon in a Li−O_2 cell in presence and absence of KOTF. (b) TXM images of the discharge products obtained in presence and absence of KOTF. Increase of the LiO_2/Li_2O_2 ratio and the Li_2CO_3 fraction are represented by increasing the color heat at each pixel.

The essentially similar chemistry of the discharge and charge processes was confirmed also quantitatively by monitoring the cell pressure during the galvanostatic experiments. These measurements allow quantifying the number of gas molecules consumed or released per electron exchanged at the electrode. Figure 4.17 shows the voltage and pressure profiles of the cells without RM and with 0.1 M LiI and 0.1 M in the electrolyte.

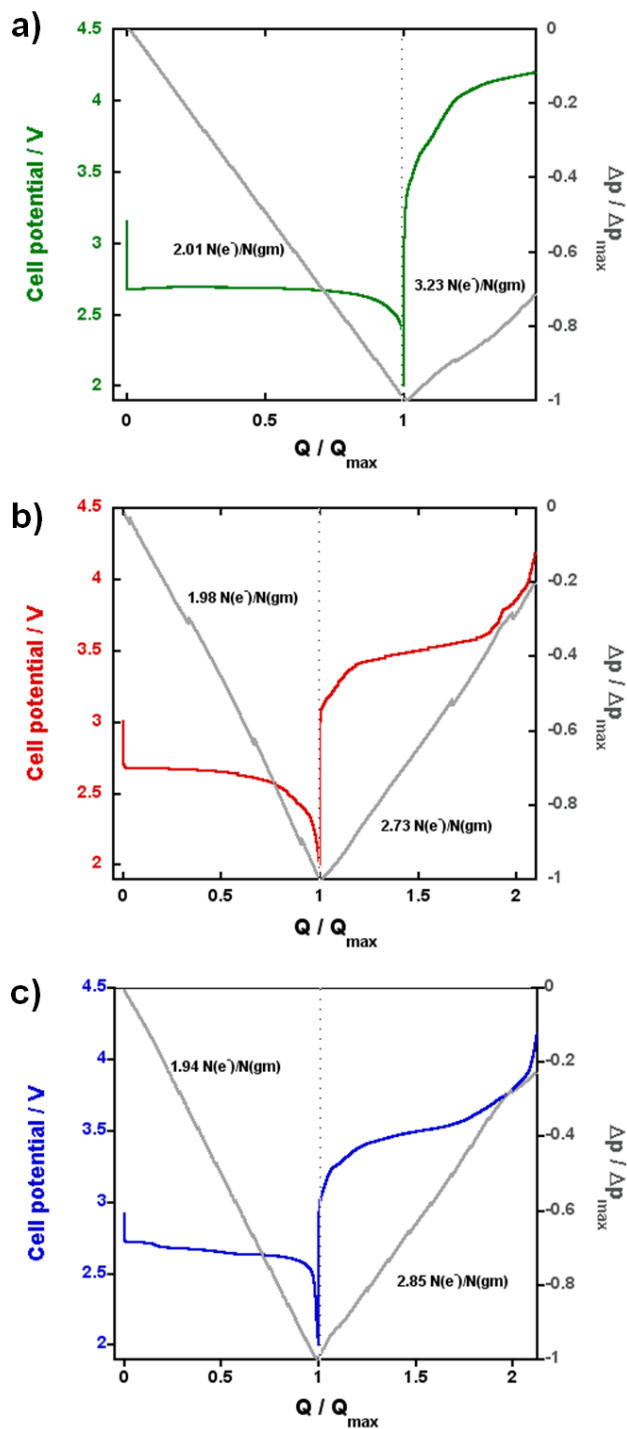**Figure 4.17**. First galvanostatic cycle of the Li-O$_2$ cell (a) without redox mediator, (b) adding 0.1 M Li and (c) adding 0.1 M KI to the electrolyte. Relative pressure variations are represented in grey for each galvanostatic cycle.

During discharge all values are close to the ideal 2 *N(e$^-$)/N(gm)* molecule for the formation of Li$_2$O$_2$, confirming that the electrochemically generated discharge products

were identical. After charge to 4.2 V not all the O_2 consumed during discharge was recovered, leading to ratios of $N(e^-)/N(gm)$ close to 3. This can be attributed to parasitic reactions following the ideal ORR process. Lower values were found with iodide mediator, confirming its role for a higher reversibility and efficient charge of the battery. Again, it can be inferred that differences using K^+ instead of Li^+ in the electrochemically generated products were negligible.

From these results is deduced that K^+ does not affect the cell chemistry or interfere in the reaction path, but enhances the kinetics of the precipitation process. Due to the high soft acid-base affinity with superoxide, K^+ promotes a higher rate capability displacing the reduction of dioxygen toward its superoxide product, and thus leading to a higher superoxide concentration in solution. This high concentration favors a more distributed peroxide precipitation, resulting in a slower passivation and an easier oxidation. In effect, previous reports have demonstrated a significant dependence of the charge potential on the size of the discharged particles.[51,2] The more homogeneous precipitate leads to lower overpotentials and thus larger cycle life is observed.

In furtherance of identifying side reactions associated to the cycling performance of the battery 4 cells were galvanostatically cycled and stopped at different stages: (i) after discharge to 2 V, (ii) after charge to 3.8 V, (iii) after charge to 4.2 V and (iv) after 10 cycles. The normalized IR spectra (Figure 4.18) of the wet separator after discharge showed reflections at 1620, 1500 and 1420 cm^{-1} (highlighted by dashed lines), which have been attributed to the presence of lithium acetate, formate and carbonate by several authors.[11,7] After the recharge to 3.8 V the presence of such species is severely reduced, probably involving their oxidation to CO_2 due to the presence of oxidative I_3^- concurrently to OER.[59] After charge to 4.2 V these reflections transitions appeared again indicating side reactions associated to the last part of the charge (3.8 V – 4.2 V). Finally, after 10 complete cycles (stopping the cell after the 10th charge to 4.2 V) the

presence of the signals at 1620, 1500 and 1420 cm^{-1} reveals the accumulation of these carbonate-based species in the electrolyte.
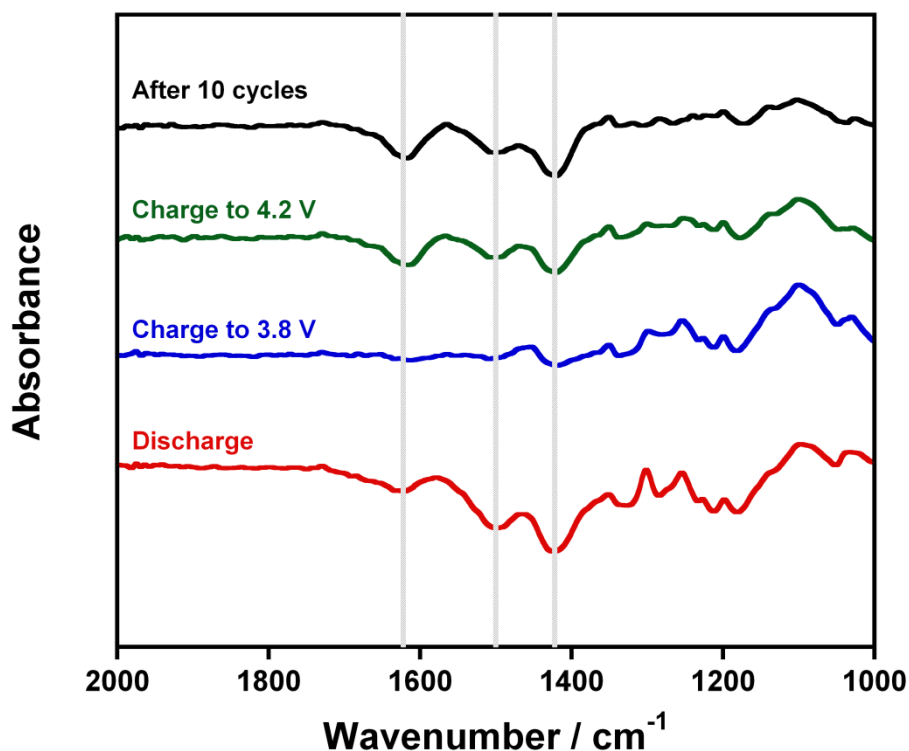

Figure 4.18. Normalized IR spectra of the electrolyte after discharge (red), charge to 3.8 V (blue), charge to 4.2 V (green) and 10 cycles (black) normalized and deducted from the IR spectrum of the pristine electrolyte. Grey lines highlight the signals associated to lithium carbonates, acetates and formats.

Recently, LiI has been studied as RM in a water containing Li-O$_2$ battery in which LiOH has been identified as the main discharge product.[60] In contrast to them, no LiOH was detected in our oxygen electrodes after discharge and, therefore, our results cannot be directly compared to that work. The experimental data in this work suggests the existence of side reactions by introducing iodide in our electrolyte. Pre-charge in Figure 4.13 demonstrates that indeed I$^-$ oxidation is the dominant reactions at low charge potentials. However, Figure 4.14 suggests that the presence of I$^-$ redox mediator

influences the coulombic efficiency of the galvanostatic cycle requiring higher charge capacities to remove all the discharge and side products generated.

4.5.3. Operando UV-visible spectroscopy evidence of the reactions of I^-

In order to shed some light into the use of iodide (I^-) as redox mediator in Li-O$_2$ batteries an *in situ* UV-visible spectroscopy cell was built up (described in Chapter 2) and used to analyze the formation and elimination of iodide species. This tool is particularly useful when the electrochemical reactions involve species that absorb visible light as is often the case for redox mediators and their side products.

The CV curve and the absorbance spectra collected at different stages of the experiment are shown in Figure 4.19.
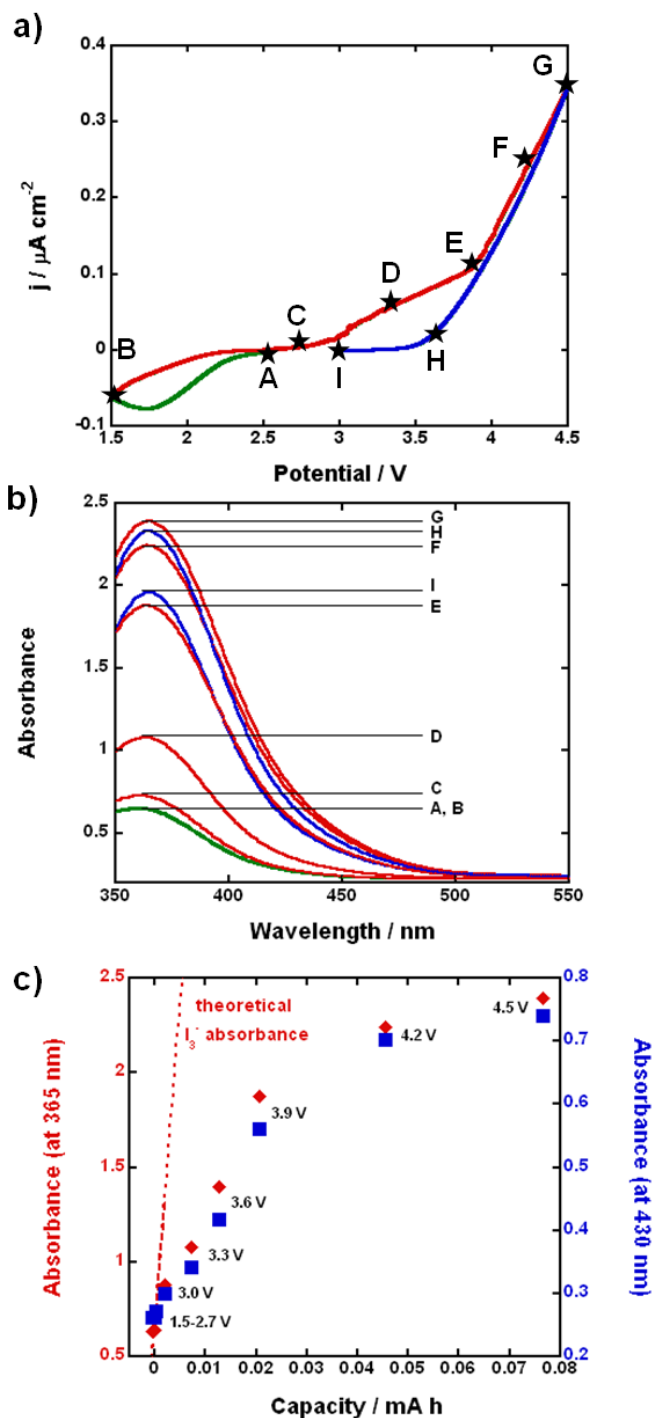
Figure 4.19.(a) Cyclic voltammetry carried out at a scan rate of 5 mV s^{-1} between 1.5 and 4.5 V. Blue stars correspond to the stages of the voltammetry for which the absorbance spectra is shown in Figure 19.b. (b) The absorbance spectra collected with the UV-vis spectroscopy at different stages of the cyclic voltammetry. (c) Absorbance values recorded at 365 nm (red diamonds) and at 430 nm (blue squares) vs. capacity of the cell during charge of the cell. Cell potential at each point is added next to each point and the dotted red line shows the theoretical absorbance at 365 nm.

During the cathodic scan a reduction process could be appreciated starting at 2.25 V, which can be ascribed to oxygen reduction reaction (ORR) (Fig. 4.19.a). This potential was lower than the typically reported 2.6-2.7 V when carbon-based oxygen electrodes are used, and can be related to the poor electronic conductivity of the ITO used as the oxygen electrode in this cell, compared to carbon and to the low surface area of these flat electrodes.[61] At OCV an absorbance peak with a maximum at 365 nm could be observed, which is typical for I_3^-.[62] The presence of this peak could be attributed to the reaction between I^- and trace amounts of hydrogen peroxide in TEGDME,[63] which is a common product formed during glyme storage:

$$3\ I^- + H_2O_2 + 2\ H^+ \quad I_3^- + 2\ H_2O \qquad\qquad [4.5]$$
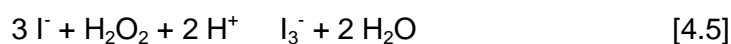
Yin *et al*. also reported the presence of this peak before charging their NaI-containing sodium-oxygen battery.[64] Based on this reaction it can be deduced that H_2O and I_3^- would be chemically formed. From the extinction coefficient in Awtrey and Connick's work[62] it is estimated a I_3^- concentration of about $4\cdot10^{-5}$ mol/L, two orders of magnitudes less than the I^- present in solution.

The absorbance spectrum during the cathodic scan (between points A and B in Figure 4.19.a) did not show relevant changes, evidencing that I^- did not participate to the ORR. Instead, in the reverse scan the 365 nm peak significantly increased, revealing the electrochemical production of I_3^-. The most important growth of the peak at 365 nm parallels the steeper slope in the anodic current between 3 and 3.9 V associated to the I_3^- formation (points C-F). Above 3.9 V an ohmic process takes place, with a linear current increase with voltage and nearly no hysteresis. The onset of this current is at about 3.6 V vs. Li, next to the redox potential of the I_3^-/I^- couple (3.35 V vs. Li according to Boschloo *et al.*[65]). This current is attributed to the shuttling of I_3^-/I^- between anode and cathode, which is limited by ohmic polarization in the electrolyte, given the large distance between the electrodes. This possibility was also discussed by Bergner *et*

al..[35] Above 3.9 V the UV-visible I_3^- signal has a small further increase to a maximum intensity that is kept during the following cathodic scan down to 3.6 V (point H). Finally, the I_3^- signal decreased between 3.6 and 3.0 V (point I), implying a decrease in I_3^- concentration in the electrolyte in spite of the positive current registered in the cell. This could be attributed to the decrease of the I_3^- electrochemical generation rate during the cathodic sweep, which becomes lower than chemical oxidation rate of the remaining peroxide.

A quantitative correlation between electrochemical and spectrophotometric data is represented in Figure 4.19.c, showing the absorbance at 365 nm and at 450 nm vs. the capacity during the anodic scan. The lower absorbance at 450 nm rules out saturation effects. Between 2.4 and 3.9 V absorbance steadily increased with capacity, with an inflexion above 3.0 V. However, above 3.9 V the gradient tended to 0 revealing I_3^- consumption, in agreement with the shuttling reaction discussed above. Below 2.4 V the cathodic current should form peroxide and suppress I_3^- formation. The charge between 2.4 and 3.0 V mostly forms I_3^-, in effect the slope, 100 $(mA\ h)^{-1}$, approaches the theoretical value of 344 $(mA\ h)^{-1}$ for a quantitative I^- oxidation reaction that was calculate considering the Faraday constant, the I_3^- extinction coefficient[66] and an electrolyte volume of 1.7 mL (represented in Figure 4.19.c by a dotted red line). Experimental errors, I_3^- consumption and side reactions, however, should be considered associated to the lower experimental slope compared to the theoretical. This slope decreases when the electrode potential is above 3 V and the produced I_3^- starts oxidizing peroxide. Above 3.9 V no peroxide seems available and the current is essentially due to the shuttling process, in which the increase in triiodide concentration should be proportional to the current rather than to the capacity.

A close inspection of spectra in Fig. 4.19.b evidences a small broadening between points C and G which is partially reverted between G and I, which seems to indicate the presence of a species centered around 400 nm. In order to analyze the stability of I_3^- in

the cell after the CV measurement the absorbance spectrum was recorded again after
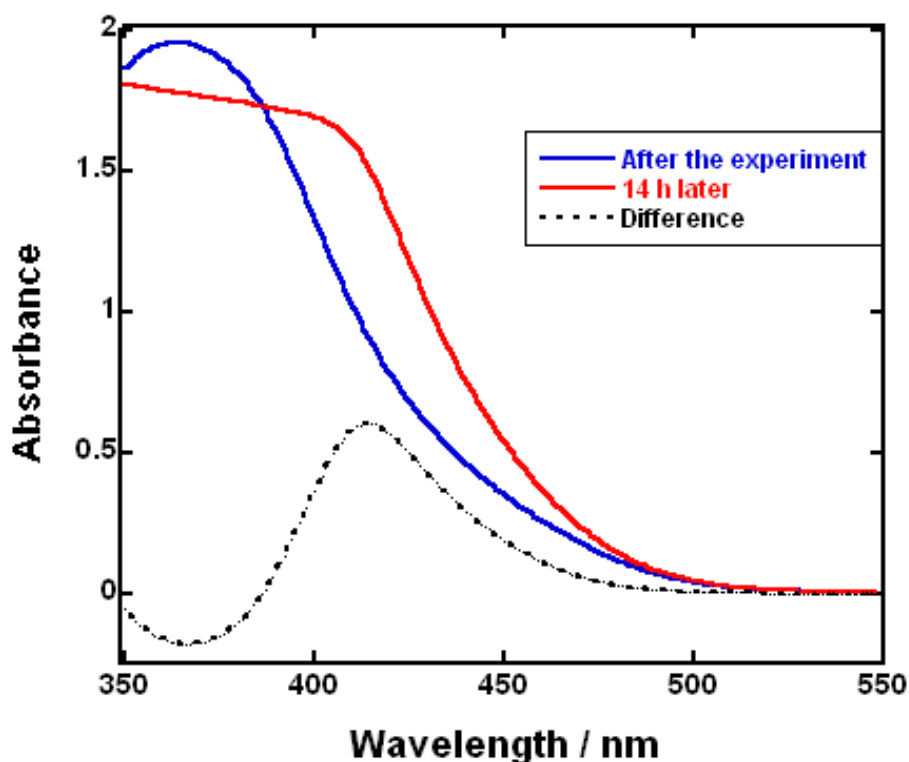
14 hours at OCV (Figure 4.20).

Figure 4.20. Absorbance spectra recorded in the homemade lithium-oxygen cell after the CV (blue line) and 14 hours later, kept at OCV (red line). The difference between these two lines is represented by the dashed black line.

Absorbance at 365 nm decreased, while a new component emerged at 410 nm (black dashed line), which corresponds to the absorbance wavelength of hypoiodus acid (HOI) according to Minaev[67] OI^- formation has been proposed by Kwak *et al.* as an intermediate in the decomposition of ether solvents in Li-O_2 cells containing LiI.[61] However this intermediate should be finally eliminated by reaction with the other intermediate HOO^-, contrasting with the increasing OI^- concentration that we observe. Allen *et al.* described HOI formation from water and iodine:[68]

$$I_2 + H_2O \rightarrow HOI + I^- + H^+ \qquad\qquad [4.6]$$
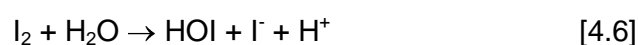
Even if in small amounts considering the large I$^-$ excess, iodine should be available from the equilibrium described in equation 4.5:[69]

$$I_2 + I^- \rightleftharpoons I_3^-$$ [4.7]
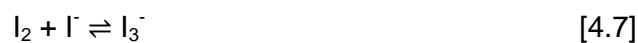
Freunberger *et al.* reported TEGDME decomposition leading to water formation in presence of oxidative species such as oxygen radicals and O_2.[7] In effect, we did only observe the characteristic I_3^- peak one week after dissolving I_2 in TEGDME. This indicates that water required for the formation of this OI$^-$ was electrochemically generated in the cell during the CV.[7] Therefore, electrolyte degradation processes probably involving water formation can be identified by this method based on the formation of HOI that absorbs radiation at 410 nm.

4.6. Conclusions

To sum up, the use of heterogeneous catalysts and carbon-free electrodes has not been traduced in a remarkable improvement of the electrochemical performance of the Li-O_2 cell. On the other hand, two positive effects of due to K$^+$ addition to the electrolyte have been observed: 1) an improved discharge rate capability; 2) sustained cycling in presence of an oxidation redox mediator such as iodide. K$^+$ does not affect the cell chemistry, but favors a more homogeneous discharge particle growth, which could be related to the stabilization of superoxide in the electrolyte by interaction with K$^+$. The easier and more distributed precipitation allows supporting higher discharge currents. This more homogeneous precipitate facilitates the attack by oxidized mediators during charge, which reduces overpotentials and the associated irreversible side reactions, therefore improving capacity retention. This synergetic improvement of the cycling performance makes KI a better choice than LiI as additive for Li-O_2 batteries. Indeed, an electrolyte additive as K$^+$ is one of the simplest, safest, and most stable species that can be conceived, and encourages research on alternative mechanisms of controlling the Li_2O_2 discharge process for increased cell reversibility. We believe that further

investigations on the chemistry of the I^-/I_3^- redox pair as RM in the Li-O$_2$ batteries are required in order to better understand the electrochemical improvement unequivocally obtained by its addition to the electrolyte. Nevertheless, our experience with the K$^+$ additives shows that, by controlling the morphology of insulating discharge products, it is indeed possible to significantly reduce overpotentials and thus, within the limits of thermodynamics, significantly decrease a charging potential.

Finally, it is provided *in situ* evidence of some of the reactions taking place when iodide is used as redox mediator in Li-O$_2$ batteries. We present a UV-visible spectrophotometry lithium-oxygen cell developed for the monitoring of such reactions, based in the formation of I_3^-, which absorbs visible radiation. I_3^- concentration has been observed to increase during the anodic scan. Oxidation of the discharge products by triiodide is confirmed by the decreased slope of absorption vs. charge. Shuttle reaction between Li and oxygen electrodes has also been identified above 3.9 V. In addition, side reactions on the electrolyte have been detected, leading to formation of OI$^-$ absorbing radiation at 410 nm. This anion may form from I$^-$ and I$_2$ reaction respectively with LiOOH and H$_2$O, both possible TEGDME degradation products in presence of electrochemically generated superoxide. The presence of these side reactions may influence the cycle life of a real Li-O$_2$ batteries using iodide as redox mediator.

4.7. References

(1)   McCloskey, B. D.; Scheffler, R.; Speidel, A.; Girishkumar, G.; Luntz, A. C. *J. Phys. Chem. C* **2012**, *116*, 23897–23905.

(2)   Gallant, B. M.; Kwabi, D. G.; Mitchell, R. R.; Zhou, J.; Thompson, C. V; Shao-Horn, Y. *Energy Environ. Sci.* **2013**, *6* (8), 2518–2528.

(3)   Marchini, F.; Herrera, S. E.; Torres, W.; Tesio, A. Y.; Williams, F. J.; Calvo, E. J. *Langmuir* **2015**, No. 3331, 9236–9345.

(4)   Burke, C. M.; Pande, V.; Khetan, A.; Viswanathan, V.; McCloskey, B. D. *Proc. Natl. Acad. Sci. U. S. A.* **2015**, *112* (30), 9293–9298.

(5)   Li, C.; Fontaine, O.; Freunberger, S. A.; Johnson, L.; Grugeon, S.; Bruce, P. G.; Armand, M. *J. Phys. Chem. C* **2014**, *118*, 3393–3401.

(6)   Xia, C.; Waletzko, M.; Chen, L.; Peppler, K.; Klar, P. J.; Janek, J. *ACS Appl. Mater. Interfaces* **2014**, *6* (15), 12083–12092.

(7)   Freunberger, S. a; Chen, Y.; Drewett, N. E.; Hardwick, L. J.; Bardé, F.; Bruce, P. G. *Angew. Chem. Int. Ed. Engl.* **2011**, *50* (37), 8609–8613.

(8)   Peng, Z.; Freunberger, S. A.; Hardwick, L. J.; Chen, Y.; Giordani, V.; Barde, F.; Novak, P.; Graham, D.; Tarascon, J. M.; Bruce, P. G. *Angew. Chem. Int. Ed. Engl.* **2011**, *50*, 6351–6355.

(9)   McCloskey, B. D.; Speidel, A.; Scheffler, R.; Miller, D. C.; Viswanathan, V.; Hummelshøj, J. S.; Nørskov, J. K.; Luntz, A. C. *J. Phys. Chem. Lett.* **2012**, *3*, 997–1001.

(10)   Itkis, D. M.; Semenenko, D. A.; Kataev, E. Y.; Belova, A. I.; Neudachina, V. S.; Sirotina, A. P.; Ha, M.; Teschner, D.; Knop-gericke, A.; Dudin, P.; Barinov, A.; Goodilin, E. A.; Shao-horn, Y.; Yashina, L. V. *Nano Lett.* **2013**, *13* (10), 4697–4701.

(11)   Ottakam Thotiyl, M. M.; Freunberger, S. a; Peng, Z.; Bruce, P. G. *J. Am. Chem. Soc.* **2013**, *135* (1), 494–500.

(12)   Sun, L.; Cong, L.; Gao, X.; Yao, C.; Guo, X.; Tai, L.; Mei, P.; Zeng, Y.; Xie, H.; Wang, R. *J. Phys. Chem. C* **2013**, *117*, 25890–25897.

(13)   Huang, B.-W.; Li, L.; He, Y.-J.; Liao, X.-Z.; He, Y.-S.; Zhang, W.; Ma, Z.-F. *Electrochim. Acta* **2014**, *137*, 183–189.

(14) Lei, Y.; Lu, J.; Luo, X.; Wu, T.; Du, P.; Zhang, X.; Ren, Y.; Wen, J.; Miller, D. J.; Miller, T.; Sun, Y.; Elam, W.; Amine, K. *Nano Lett.* **2013**, *13*, 4182–4189.

(15) Trahan, M. J.; Jia, Q.; Mukerjee, S.; Plichta, E. J.; Hendrickson, M. A.; Abraham, K. M. *J. Electrochem. Soc.* **2013**, *160* (9), A1577–A1586.

(16) Débart, A.; Paterson, A. J.; Bao, J.; Bruce, P. G. *Angew. Chem. Int. Ed.* **2008**, *47* (24), 4521–4524.

(17) Lim, H.-D.; Gwon, H.; Kim, H.; Kim, S.-W.; Yoon, T.; Choi, J. W.; Oh, S. M.; Kang, K. *Electrochim. Acta* **2013**, *90*, 63–70.

(18) McCloskey, B. D.; Scheffler, R.; Speidel, A.; Bethune, D. S.; Shelby, R. M.; Luntz, A. C. *J. Am. Chem. Soc.* **2011**, *133*, 18038–18041.

(19) Zhao, G.; Xu, Z.; Sun, K. *J. Mater. Chem. A* **2013**, *1* (41), 12862.

(20) Kim, D. S.; Park, Y. J. *J. Alloys Compd.* **2013**, *575*, 319–325.

(21) Lim, H.-D.; Song, H.; Gwon, H.; Park, K.-Y.; Kim, J.; Bae, Y.; Kim, H.; Jung, S.-K.; Kim, T.; Kim, Y. H.; Lepró, X.; Ovalle-Robles, R.; Baughman, R. H.; Kang, K. *Energy Environ. Sci.* **2013**, *6* (12), 3570.

(22) Yang, Y.; Shi, M.; Zhou, Q.-F.; Li, Y.-S.; Fu, Z.-W. *Electrochem. commun.* **2012**, *20*, 11–14.

(23) Cui, Y.; Wen, Z.; Liu, Y. *Energy Environ. Sci.* **2011**, *4*, 4727–4734.

(24) Riaz, A.; Jung, K.-N.; Chang, W.; Lee, S.-B.; Lim, T.-H.; Park, S.-J.; Song, R.-H.; Yoon, S.; Shin, K.-H.; Lee, J.-W. *Chem. Commun.* **2013**, *49*, 5984–5986.

(25) Yu, Y.; Zhang, B.; Xu, Z.-L.; He, Y.-B.; Kim, J.-K. *Solid State Ionics* **2013**, *4*, 2–6.

(26) Lee, H.; Kim, Y.; Jin, D.; Song, J.; Min, Y. *J. Mater. Chem. A* **2014**, *2*, 11891–11899.

(27)   Peng, Z.; Freunberger, S. a; Chen, Y.; Bruce, P. G. *Science* **2012**, *337* (6094), 563–566.

(28)   Zhao, G.; Niu, Y.; Zhang, L.; Sun, K. *J. Power Sources* **2014**, *270*, 386–390.

(29)   Yamada, A.; Zhou, H. *Nano Lett.* **2013**, *13*, 4702–4707.

(30)   Thotiyl, M. M. O.; Freunberger, S. A.; Peng, Z.; Chen, Y.; Liu, Z.; Bruce, P. G. *Nat. Mater.* **2013**, *12*, 1050–1056.

(31)   Cui, Y.; Wen, Z.; Liang, X.; Lu, Y.; Jin, J.; Wu, M.; Wu, X. *Energy Environ. Sci.* **2012**, *5* (7), 7893.

(32)   Pearson, R. G. *J. Am. Chem. Soc.* **1963**, *85* (22), 3533–3539.

(33)   Abraham, K. M. *J. Electrochem. Soc.* **2014**, *162* (2), A3021–A3031.

(34)   Chen, Y.; Freunberger, S. A.; Peng, Z.; Fontaine, O.; Bruce, P. G. *Nat. Chem.* **2013**, *5*, 489–494.

(35)   Bergner, B. J.; Schürmann, A.; Peppler, K.; Garsuch, A.; Janek, J. *J. Am. Chem. Soc.* **2014**, *136* (42), 15054–15064.

(36)   Sun, D.; Shen, Y.; Zhang, W.; Yu, L.; Yi, Z.; Yin, W.; Wang, D.; Huang, Y.; Wang, J.; Wang, D.; Goodenough, J. B. *J. Am. Chem. Soc.* **2014**, *136* (25), 8941–8946.

(37)   Lim, H.; Song, H.; Kim, J.; Gwon, H.; Bae, Y.; Park, K.; Hong, J.; Kim, H.; Kim, T.; Kim, Y. H.; Lepró, X.; Ovalle-, R.; Baughman, R. H.; Kang, K. *Angew. Chemie* **2014**, *126* (15), 4007–4012.

(38)   Zhai, D.; Lau, K. C.; Wang, H.-H.; Wen, J.; Miller, D. J.; Lu, J.; Kang, F.; Li, B.; Yang, W.; Gao, J.; Indacochea, E.; Curtiss, L. a; Amine, K. *Nano Lett.* **2015**, *2014* (1), 1–6.

(39) Bondue, C. J.; Abd-El-Latif, a. a.; Hegemann, P.; Baltruschat, H. *J. Electrochem. Soc.* **2015**, *162* (3), A479–A487.

(40) Kayan, A.; Tarcan, E.; Kadiroglu, U.; Esmer, K. *Mater. Lett.* **2004**, *58*, 2170–2174.

(41) Nazarpour, S.; Langenberg, E.; Jambois, O.; Ferrater, C.; Polo, M. C.; Varela, M. *Appl. Surf. Sci.* **2009**, *255*, 3618–3622.

(42) Lin, X.; Shang, Y.; Huang, T.; Yu, A. *Nanoscale* **2014**, *6*, 9043–9049.

(43) Ren, X.; Lau, K. C.; Yu, M.; Bi, X.; Kreidler, E.; Curtiss, L. a.; Wu, Y. *ACS Appl. Mater. Interfaces* **2014**, *6* (21), 19299–19307.

(44) Zhai, D.; Lau, C.; Wang, H.; Wen, J.; Miller, D. J.; Kang, F.; Li, B.; Zavadil, K.; Curtiss, L. A. *ChemSusChem* **2016**, *8* (24), 4235–4241.

(45) Freunberger, S. A.; Chen, Y.; Peng, Z.; Griffin, J. M.; Hardwick, L. J.; Bardé, F.; Novák, P.; Bruce, P. G. *J. Am. Chem. Soc.* **2011**, *133*, 8040–8047.

(46) Itkis, D. M.; Semenenko, D. a; Kataev, E. Y.; Belova, A. I.; Neudachina, V. S.; Sirotina, A. P.; Hävecker, M.; Teschner, D.; Knop-Gericke, A.; Dudin, P.; Barinov, A.; Goodilin, E. a; Shao-Horn, Y.; Yashina, L. V. *Nano Lett.* **2013**, *13* (10), 4697–4701.

(47) Landa-Medrano, I.; Pinedo, R.; Ortiz-Vitoriano, N.; Ruiz de Larramendi, I.; Rojo, T. *ChemSusChem* **2015**, *8*, 3932–3940.

(48) Sharon, D.; Hirsberg, D.; Salama, M.; Afri, M.; Frimer, A. A.; Noked, M.; Kwak, W.; Sun, Y.; Aurbach, D. *Appl. Mater. Interfaces* **2016**, *8* (8), 5300–5307.

(49) Yang, L.; Frith, J. T.; Garcia-Araez, N.; Owen, J. R. *Chem. Commun.* **2015**, *51*, 1705–1708.

(50)   Tesio, A. Y.; Blasi, D.; Olivares-Marín, M.; Ratera, I.; Tonti, D.; Veciana, J. *Chem. Commun.* **2015**, *51*, 17623–17626.

(51)   Adams, B. D.; Radtke, C.; Black, R.; Trudeau, M. L.; Zaghib, K.; Nazar, L. F. *Energy Environ. Sci.* **2013**, *6*, 1772–1778.

(52)   Aetukuri, N. B.; McCloskey, B. D.; García, J. M.; Krupp, L. E.; Viswanathan, V.; Luntz, A. C. *Nat. Chem.* **2014**, *7*, 50–56.

(53)   Ling, C.; Zhang, R.; Takechi, K.; Mizuno, F. *J. Phys. Chem. C* **2014**, *118*, 26591–26598.

(54)   Carboni, M.; Brutti, S.; Marrani, A. G. *ACS Appl. Mater. Interfaces* **2015**, *7* (39), 21751–21762.

(55)   Zhang, T.; Liao, K.; He, P.; Zhou, H. *Energy Environ. Sci.* **2016**, *9*, 1024–1030.

(56)   Landa-Medrano, I.; Olivares-Marín, M.; Pinedo, R.; Ruiz de Larramendi, I.; Rojo, T.; Tonti, D. *Electrochem. commun.* **2015**, *59*, 24–27.

(57)   Bergner, B. J.; Busche, M. R.; Pinedo, R.; Berkes, B. B.; Schröder, D.; Janek, J. *ACS Appl. Mater. Interfaces* **2016**, *8* (12), 7756–7765.

(58)   Olivares-Marín, M.; Sorrentino, A.; Lee, R.-C.; Pereiro, E.; Wu, N.-L.; Tonti, D. *Nano Lett.* **2015**, *15* (10), 6932–6938.

(59)   McCloskey, B. D.; Valery, A.; Luntz, A. C.; Gowda, S. R.; Wallra, G. M.; Garcia, J. M.; Mori, T.; Krupp, L. E. *J. Phys. Chem. Lett.* **2013**, *4*, 2989–2993.

(60)   Liu, T.; Leskes, M.; Yu, W.; Moore, A. J.; Zhou, L.; Bayley, P. M.; Kim, G.; Grey, C. P. *Science (80-.).* **2015**, *350* (6260), 530–533.

(61)   Kwak, W.-J.; Hirshberg, D.; Sharon, D.; Shin, H.-J.; Afri, M.; Park, J.-B.; Garsuch, A.; Chesneau, F. F.; Frimer, A. a.; Aurbach, D.; Sun, Y.-K. *J. Mater.*

Chem. A **2015**, *3*, 8855–8864.

(62)   Awtrey, A. D.; Connick, R. E. *J. Am. Chem. Soc.* **1951**, *73* (4), 1842–1843.

(63)   Liebhafsky, H. A.; Mohammad, A. *J. Am. Chem. Soc.* **1933**, *55* (10), 3977–3986.

(64)   Yin, W.; Shadike, Z.; Yang, Y.; Ding, F.; Sang, L. *Chem. Commun.* **2015**, *51*, 2324–2327.

(65)   Boschloo, G.; Hagfeldt, A. *Acc. Chem. Res. 42*, 1819–1829.

(66)   Hanson, K. J.; Tobias, C. W. *J. Electrochem. Soc.* **1987**, *134* (9), 2204–2210.

(67)   Minaev, B. F. *J. Physycal Chem. A* **1999**, *103*, 7294–7309.

(68)   Allen, T. M.; Feefer, F. M. *J. Phys. Chem.* **1955**, *77* (11), 2957–2960.

(69)   Marczenko, Z.; Balcerzak, M. *Separation, Preconcentration and Spectrophotometry in Inorganic Analysis*; Elsevier, **2000**.

Chapter 5 – Analysis of the discharge products evolution in Na-O$_2$ batteries

Sodium oxygen (Na-O$_2$) batteries have been presented as an alternative to lithium-oxygen (Li-O$_2$) batteries. In these batteries cube-shaped sodium superoxide (NaO$_2$) replaces toroid-shaped lithium peroxide (Li$_2$O$_2$) as the discharge product accumulated in the oxygen electrode. In this chapter the formation and evolution of the discharge products is analyzed.

5.1. Introduction

As mentioned in the previous chapters, lithium-oxygen (Li-O$_2$) batteries have attracted the interest of the research community due to their high theoretical gravimetric energy density (3456 W h kg^{-1}, based on the mass of lithium peroxide discharge product) which still remains far away from attained practical values.[1] Additionally, unsolved issues such as high overpotentials, low current densities and coulombic efficiencies and limited cycle life have given rise to some doubts about the future implementation of these batteries in EVs. In this context, sodium-oxygen (Na-O$_2$) batteries have emerged as a promising alternative to Li-O$_2$ batteries, which, despite their lower theoretical gravimetric energy density (1602 and 1105 W h kg^{-1} based on the mass of Na$_2$O$_2$ and NaO$_2$, respectively), do not present some of the aforementioned drawbacks.[2,3] This is attributed to the different and initially unexpected cell chemistry of Na-O$_2$ batteries with ether-based electrolytes, firstly reported by Hartmann *et al.*.[4] Actually, the cell chemistry in these sodium based batteries, in contrast to Li-O$_2$ batteries, has been a controversial point since their early steps, as at least three different discharge products, namely sodium superoxide (NaO$_2$), sodium peroxide (Na$_2$O$_2$) and sodium peroxide dihydrate (Na$_2$O$_2$·2H$_2$O), have been reported. The reasons still remain unclear and have attracted the interest of many research groups. While clear evidences of superoxide have been frequently reported,[4-8] those of peroxides are still under debate.[9]

Some light was shed by demonstrating the effect of gas moisture or air exposure in the evolution of NaO_2 to $Na_2O_2 \cdot 2H_2O$.[7,10] In contrast, no reports about the reduction of NaO_2 to Na_2O_2 are available, and the proposed alternative mechanisms for the generation of Na_2O_2 need to be experimentally demonstrated.[11] Hence, micrometer sized NaO_2 cubes are the usual discharge products in ether-based electrolytes, but their insulating nature[12] has fed another debate on the growth mechanism. On the one hand, in surface mediated growth, oxygen would be reduced and directly deposited on the carbon surface while in solution mediated growth, the superoxide ion formed on the electrode surface would be able to migrate and be deposited at other parts of the electrode after combining with sodium ions in the electrolyte. The latter agrees with the reaction mechanism proposed by Xia *et al.* in which protons (H^+) supplied by residual H_2O molecules in the electrolyte act as phase-transfer catalysts being combined with superoxide ions and stabilizing them in the electrolyte as HO_2.[6] Solution-mediated discharge product formation has been also proposed by Hartmann *et al.*, and further evidences obtained by electron paramagnetic resonance (EPR) are given in this chapter.[13]

Apart from the mentioned controversies, there is generally agreement in literature that $Na-O_2$ batteries can be a good alternative to overcome some of the drawbacks of $Li-O_2$ batteries. Thus, while their promising electrochemical performance could open new opportunities beyond lithium-ion batteries, other critical factors such as cell stability, poorly studied until now, need to be also understood and improved. Thus, in this chapter the stability of NaO_2 is called into question evidencing side reactions and highlighting the partial solubility of sodium superoxide in the cell that can hinder its re-oxidation at low overpotential. Moreover, this solubility process is closely related to the migration of the superoxide radical. The latter will be identified as one important factor for the incomplete reversibility of $Na-O_2$ batteries, above all in the first cycle, and to the cross-talk between both electrodes.

5.2. (In-)Stability of NaO$_2$ in the cell environment

In contrast to Li-O$_2$ batteries, where Li$_2$O$_2$ is reported as the discharge product, the chemical nature of Na-O$_2$ products is still under debate.[7,12,14,15] Thus, in order to analyze the presence of superoxide or peroxide, EPR measurements have been conducted in cathodes discharged at different depths of discharge (Figure 5.1).
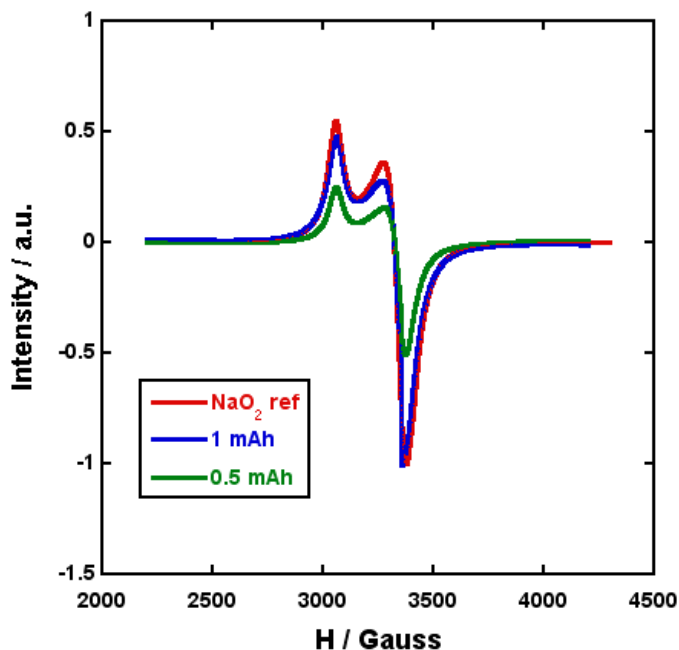

Figure 5.1. X-band (9.4 GHz) EPR spectra registered at 5 K on the oxygen electrodes after discharge to 1 mA h (blue) and 0.5 mA h (green). The spectra obtained are compared to NaO$_2$ reference (red).

The X-band EPR spectra registered below 100 K are characteristics of a rombic g-tensor: g1=2.192, g2=2.008, g3=1.998, <g>=2.066, in good agreement with the presence of NaO$_2$. The increasing intensity of the signal when extending the depth of discharge further supports this result. Nevertheless, despite the important advantages in terms of reversibility provided by NaO$_2$, the development of reversible Na-O$_2$ batteries requires also the stability of the discharge product in the cell environment, as side reactions could compromise its reversibility and consequently the coulombic efficiency, as will be analyzed in detail in the following section.

In order to analyze the stability of NaO_2 three different cells were discharged to 1.5 mA h at a current density of 0.2 mA cm^{-2} and were let resting for three different periods, i.e. 0, 24 and 48 h. After these resting periods, cells were charged at the same current density (Figure 5.2).
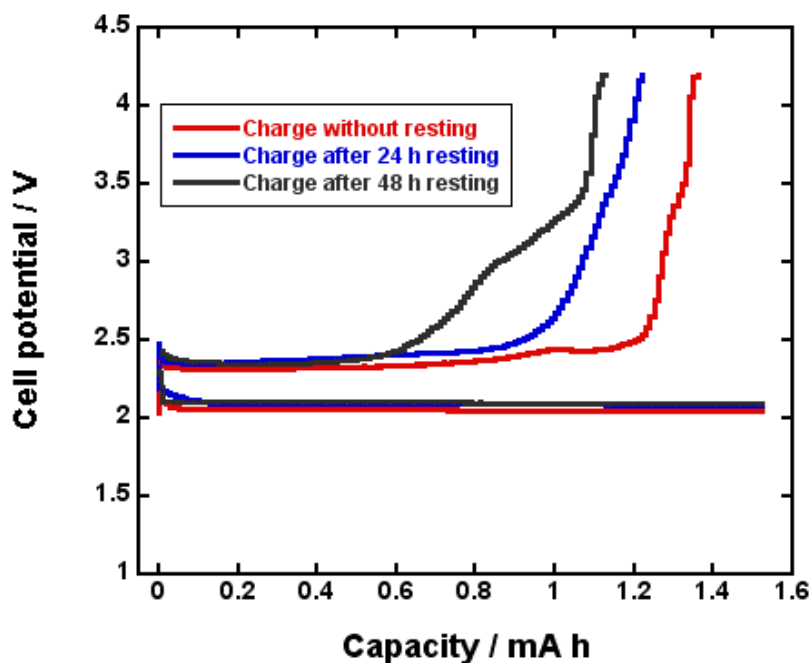

Figure 5.2. Galvanostatic cycles of three different cells that were let resting for 0 (red), 24 (blue) and 48 hours (black) between discharge and charge.

In contrast to Li-O$_2$ batteries, reversion rates above 90 % can be achieved even when limiting the voltage under 3 V.[16] Actually, if it is assumed that oxidation of NaO_2 takes place below 3 V,[6,16] it can be observed that coulombic efficiency fell from 84.7% when charge was carried out right after the discharge to 70.6 % and 57.3 % when the resting time was increased up to 48 hours. This fact proves that processes occurring in the cell during rest affect the reversibility of the previously formed NaO_2. Moreover, this behavior is extended to further cycles as shown in Figure 5.3.
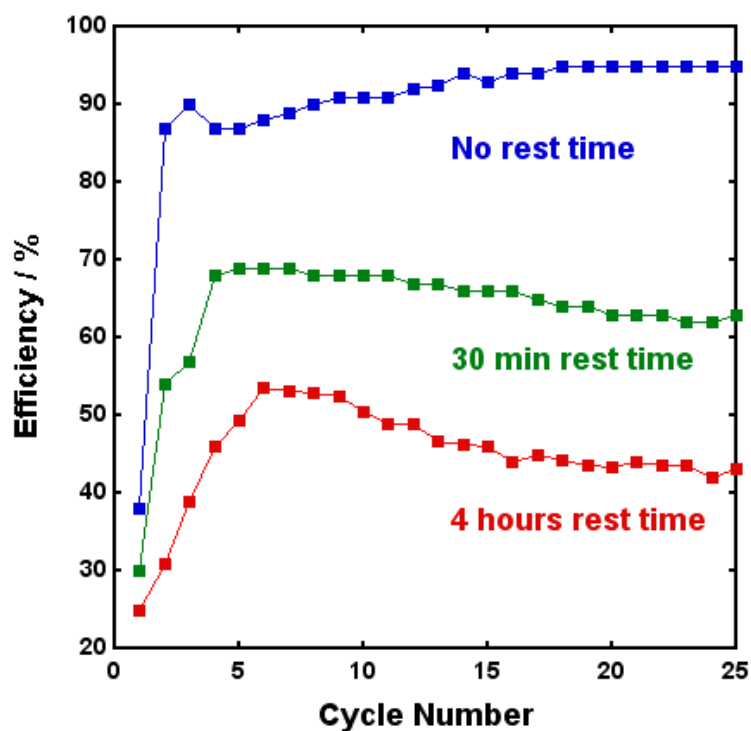
Figure 5.3. Evolution of the coulombic efficiency of the galvanostatic cycles with a resting period of 4 hours (grey), 30 minutes (orange) and without resting (blue) at a current density of 0.05 mA h limiting the discharge to 0.5 mA h.

In order to unveil the origin of the observed effect, two cells were discharged to 1.5 mA h at 0.2 mA cm^{-2}. One of these cells was directly transferred into the glovebox after discharge, dissembled and the oxygen electrode was washed and analyzed. The other cell was let assembled resting for 30 h before transferring it into the glovebox. Raman, SEM and EDX analyses of the discharge products were carried out to analyze the differences in these two oxygen electrodes.
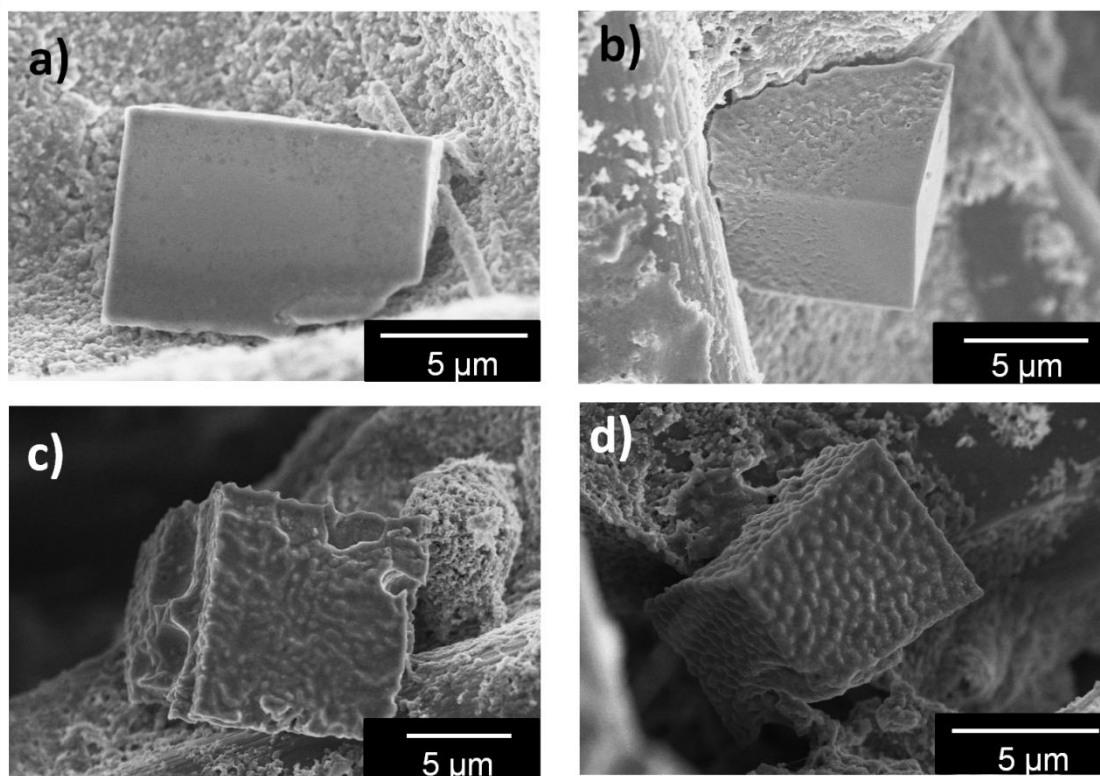
Figure 5.4. (a), (b), (c) and (d) SEM images of discharge products generated during discharge. Electrode in (a) and (b) was directly dissembled and analyzed after discharge while electrode in (c) and (d) was kept in the cell for 30 h after discharge.

SEM micrographs of the oxygen electrode analyzed just after discharge (Figures 5.4.a and 5.4.b) are consistent with the presence of the widely reported NaO_2 cubes,[4,6,7,17] with smooth faces and edges of 5-10 μm length. However, assuming that NaO_2 is thermodynamically unstable relative to Na_2O_2,[15] the observed surface side reactions when the electrode is exposed 30 hours to the cell environment without net current (Figures 5.4.c and 5.4.d), is not surprising. Moreover, EDX analyses of the cubes without and with resting period (Figure 5.5 and Table 5.1) were carried out, evidencing that the morphology differences also imply a variation of the atomic composition of the cubes.
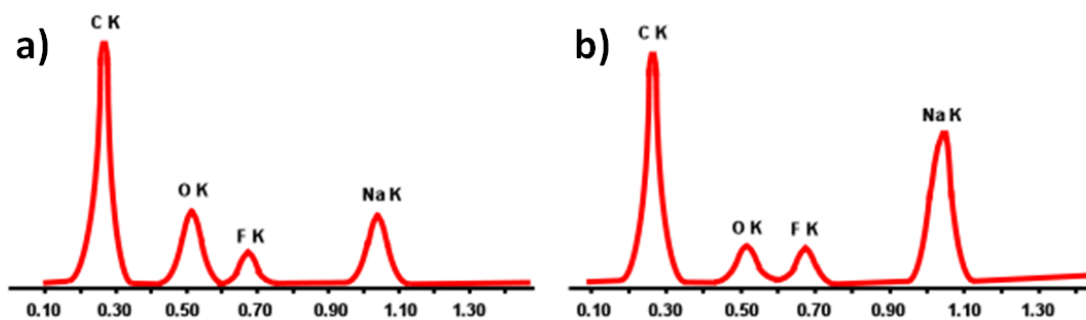
Figure 5.5. EDX spectra of a cube analyzed (a) after discharge (b) and after 30 h resting after discharge.

Table 5.1. Atom percentage obtained by EDX analysis of the discharge products in the electrode after discharge and after 24 h resting after discharge.

	Atom %	
Element	**Discharge**	**Discharge + 24 h rest**
C	71.2	69.9
O	14.1	5.8
F	4.3	4.2
Na	10.5	20.2

The main contribution to the total composition came from C (~70 %) that principally belongs to the carbon electrode, although species such as Na_2CO_3 could also contribute. In both samples around 4 % of F was detected, which coupled to the absence of S reveals the possible formation of NaF as side product from NaOTF.[18] However, the main difference is ascribed to the Na/O ratio. We observed that the Na

content rose from 10.5 % to 20.2 % during the resting period while the oxygen percentage falls from 14.1 % to 5.8 % (Table 5.1). Unfortunately, it was not possible to identify in detail the composition of the cubes before and after the resting period as the uncertainty in the exact oxygen amounts belonging to the functional groups of the carbon electrode and Na from possible NaF formation, making it difficult to reveal the exact quantification of oxygen and sodium amounts in the ORR product. The Na/O ratio is, however, unequivocally increased which can be attributed to chemical reactions of the discharge product during the resting period after discharge. Recently, Kim *et al.* described the reduction of NaO_2 to $Na_2O_2 \cdot 2H_2O$; the Na/O ratio increase observed by EDX in our experiment, however, dismisses the hypothesis of peroxide dihydrate formation, as Na/O ratio should the same for both NaO_2 and $Na_2O_2 \cdot 2H_2O$ (1:2).[7] Moreover, for the formation of $Na_2O_2 \cdot 2H_2O$ a large amount of water needs to be present in the electrolyte, and this is not likely to occur under the closed conditions employed in this study.[7] In addition, this compound usually exhibits several charge plateaus, which are not observed in this study.[2] It must be noted that the change in the Na:O ratio can also be ascribed to the formation of secondary products such as Na_2CO_3, NaOH and NaF. In order to shed some light on the observed changes, Raman spectroscopy was carried out before and after the resting period (Figures 5.6.a and 5.6.b).
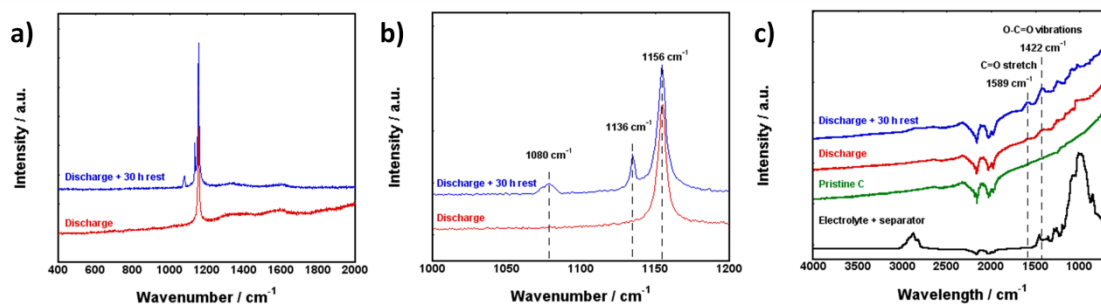
Figure 5.6. (a) Raman spectra (400-2000 cm^{-1}) obtained focusing the laser beam on a discharge particle in an oxygen electrode analyzed after the discharging the cell (red) and an oxygen electrode letting rest inside the cell for 30 hours after discharge (blue). (b) Detail of the previous Raman spectra (1000-1200 cm^{-1}). (c) Normalized FTIR spectra (650-3500 cm^{-1}) of the discharged electrode (red), the discharged electrode stored in the cell for 30 hours (blue), the pristine carbon electrode (green) and the NaOTF in DEGDME soaked separator (black).

Raman spectroscopy of the discharge particles shows that NaO_2 was the sole discharge product in ORR. After 30 hours resting in the cell environment, however, two additional peaks were detected in the Raman spectrum; one at 1080 cm^{-1} and the other at 1136 cm^{-1}. The signal at 1080 cm^{-1} can be assigned to Na_2CO_3, which could be formed by the reaction of NaO_2 with the electrolyte and / or the carbon electrode, in line with analogous studies on Li-O_2 batteries.[1] However, we also found sodium carbonate in a pristine electrode after contact with the electrolyte and oxygen for 64 h, even without any current being applied (Figure 5.7). Thus, it appears that Na_2CO_3 can also be formed without reaction with NaO_2.
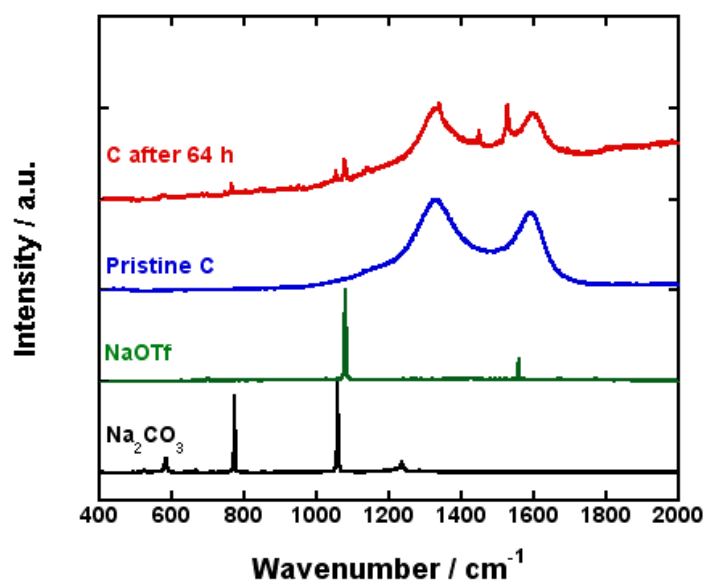
Figure 5.7. Raman spectra of a carbon electrode stored in the electrochemical cell for 64 h with oxygen (red line). Spectrum of the pristine C (blue), Na_2CO_3 (black) and NaOTF (green) were also collected for comparison.

More interestingly, the peak at 1136 cm^{-1} was also detected by Ortiz-Vitoriano *et al*. when the discharged oxygen electrode was exposed to ambient air, and attributed to $Na_2O_2.2H_2O$ formed by the reaction of NaO_2 with water.[7] In their work, simple Na_2O_2 showed two peaks at 740 and 790 cm^{-1} and the double-hydrated phase showed an additional peak at 1136 cm^{-1}. In this work, however, none of these peaks at 740 and 790 cm^{-1} could be detected suggesting that no peroxide was formed in our electrode and, consequently, the band at 1136 cm^{-1} cannot be assigned to $Na_2O_2.2H_2O$. Moreover, a detailed Raman study of peroxides and hydrated peroxides[19] attributed this peak to superoxide impurities, probably in a slightly different chemical environment, while suggests just a small shift in the bands of hydrated peroxides ($\sim$ 800 cm^{-1}). This data are consistent with our results, but also points out the necessity of clarifying the chemical nature of hydrated peroxides. Finally, FTIR of the electrodes (Figure 5.6.c) exposed to the cell environment for 30 h after discharge to 1.5 mA h evidenced signals at 1422 and 1589 cm^{-1}, which can be ascribed to the presence of Na_2CO_3.

142

In order to monitor the oxygen loss of the NaO_2 cubes under resting conditions, pressure evolution analyses of the cell were performed (Figure 5.8).
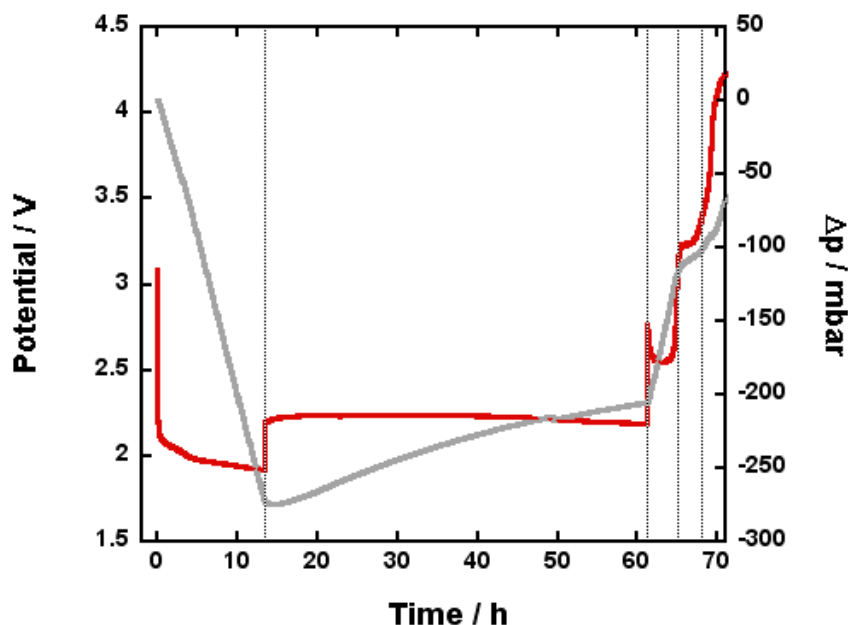

Figure 5.8. Potential (red) and pressure (grey) variations in a Na-O_2 cell during discharge and the resting period after discharge.

During the discharge reaction cell pressure decreased due to oxygen consumption for ORR. The electron per oxygen molecule ratio (z) during such period was close to 1.00 in good agreement to experimental results reported by McCloskey *et al.* and Hartmann *et al.*[5,18] After discharge, however, a gradual increase of the cell pressure was recorded which fits with the O atomic % decrease observed in the aforementioned EDX measurements. One could expect that NaO_2 could be self-charging. Gas pressure inside the cell after charge to 4.2 V, however, is much lower than the initial pressure evidencing that the oxygen consumed during discharge reaction was not completely reversed during charge reaction. This oxygen, therefore, should have undergone side reactions during the resting period. O_2 formation from the discharge products was also reported by Black *et al.* for Li/O_2 batteries.[20] The process associated to this oxygen evolution is not clear but three different pathways can be considered:

i. NaO_2 reacts with water and is reduced to $Na_2O_2.2H_2O$ and oxygen is evolved;

ii. NaO_2 reacts with the carbon electrode and/or the electrolyte producing Na_2CO_3 and O_2;

iii.   a disproportionation process ($O_2^- + O_2^- \rightarrow O_2 + O_2^{2-}$) takes place.

The first reaction pathway was proposed by Kim *et al.* suggesting the transformation from superoxide to peroxide during the resting period of the cell based on XRD and Raman spectroscopy data.[21] In good accordance to our experimental results, they observe the appearance of the peak at 1136 cm^{-1} in their Raman measurements when they let the cell resting after discharge, which was assigned to hydrated peroxide species. Unfortunately, their Raman spectra did not show frequencies under 1000 cm^{-1}, which is crucial to observe the characteristic Raman bands of peroxide (700 cm^{-1}) and to identify this specie.[4,7] Moreover, our EDX results evidence a Na/O ratio decrease that would not occur in the NaO_2 to $Na_2O_2 \cdot 2H_2O$ transformation as for both species Na/O ratio is the same. It must be noted that superoxide ions do not attack the organic solvent[22] and, thus, water must came from an external source in good agreement to Grey *et al.*.[23] Moreover, if superoxide radical could abstract protons from the organic solvent, no water would be needed for the NaO_2 formation, which is contradictory with previous results reported by the group of Nazar.[6] Furthermore, Gasteiger *et al.* proved the stability of superoxide in the electrolyte solvent in absence of water.[24] These results are consistent with the superoxide signal detected in EPR measurements even after several days, in opposite to Kim *et al.*.[21] Thus, although the instability of NaO_2 cubes in the cell environment is evidenced in both studies, factors such as the presence of water could alter and/or accelerate the reaction process.

The second reaction pathway is supported by the appearance of carbonate species when increasing the resting period. Moreover, Freunberger *et al.* proposed a similar mechanism for $Li-O_2$ systems.[25] Lithium peroxide discharge product reacts with the

ether based solvent leading to the formation of lithium carbonate and O_2. Nevertheless, there are some facts that contradict this hypothesis; the mechanism involves the formation of intermediate oxalate that was not detected in our cell. In addition, as previously mentioned, superoxide has been described to be stable in ether-based solvents and this was further confirmed as we were able to dissolve a small fraction of NaO_2 in DEGDME and detect it after several weeks.[22]

The third pathway was recently reported as a plausible mechanism for the formation of sodium peroxide.[11] This theory implies the dissolution of NaO_2 and then the disproportonation of superoxide anions. It must be noted that no evidence of peroxide were found in our measurements. However, the possibility that the formed anions (both peroxide and superoxide) migrate towards the anode side cannot be excluded. Shuttle effects have been already reported for Li-O_2 systems,[26,27,28,29] and for Na, both superoxide and peroxide species have been detected at the anode side.[8]

Although further studies are required to provide stronger evidences about these mechanisms, we believe that options ii) and iii) are more likely to occur than i).

5.3. Electrochemical methods to evidence discharge product passivation

Discharge product passivation was more accurately analyzed by means of three different electrochemical methods:

i. Electrochemical impedance spectroscopy (EIS)
ii. Quarz crystal microbalance (QCM)
iii. Cyclic voltammetry (CV)

Impedance evolution during the first galvanostatic cycle in a Na-O_2 cell was analyzed similarly to that of the Li-O_2 cell previously discussed in Chapter 3. The 2-electrode cell was discharged to 1.5 V at 0.1 mA cm^{-2} stopping the galvanostatic measurement every 30 minutes in order to carry out an impedance measurement. After the full discharge

both the sodium anode and the oxygen electrode impedance spectra were recorded using a sodium reference electrode in furtherance of distinguishing between anode and cathode processes (3-electrode set up). After that the 2-electrode set up was recovered and impedance spectra were recorded every 30 minutes until the cell was charged to 3.0 V. Finally, after the charge process impedance of the anode and the cathode was re-analyzed using the 3-electrode set up. The galvanostatic cycle, equivalent circuit proposed and some of the experimental Nyquist spectra are shown in Figure 5.9.
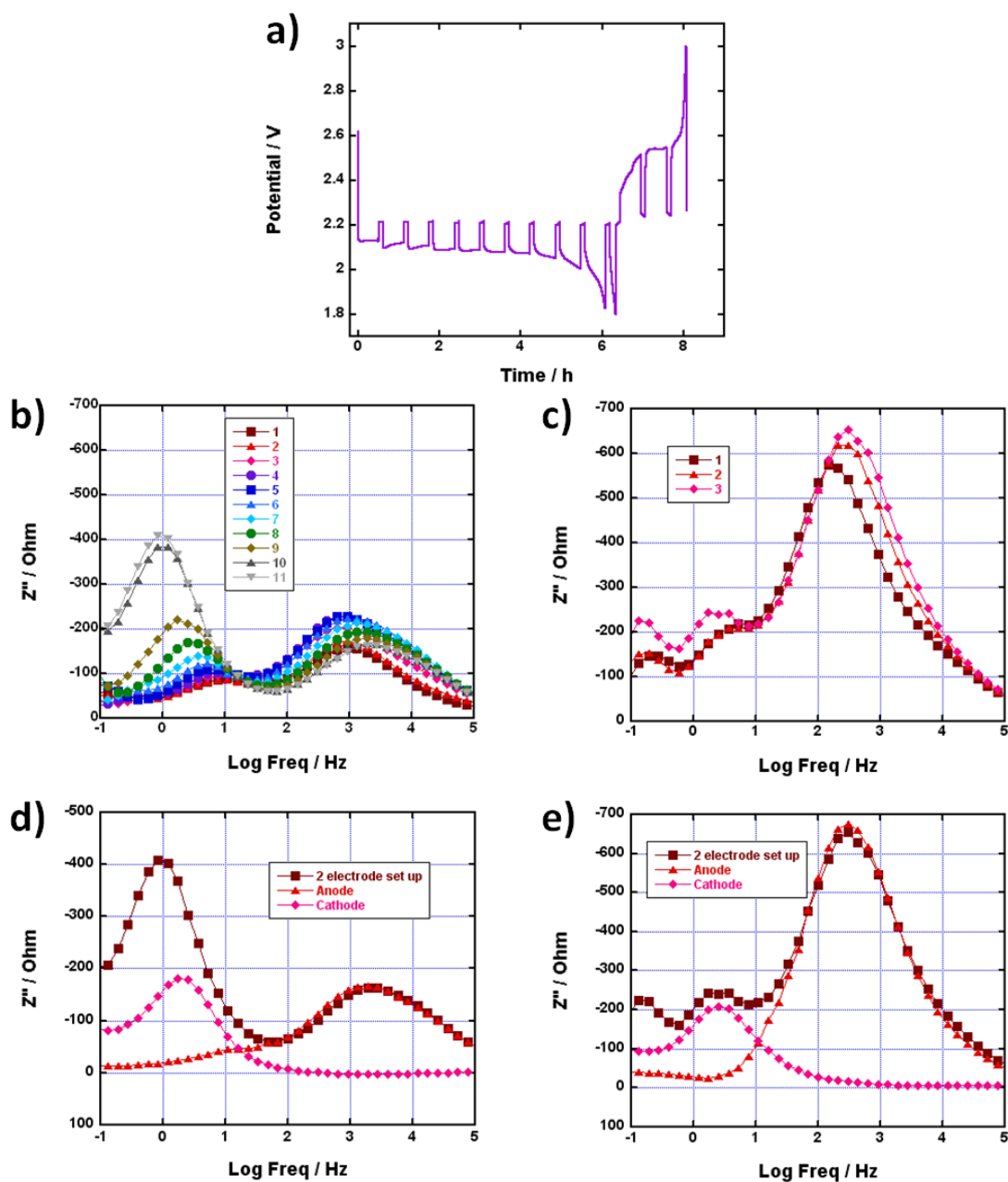
Figure 5.9. (a) First galvanostatic cycle of the Na-O$_2$ cell with the 2-electrode set up between 1.5 and 3.0 V at 0.1 mA cm^{-2}. Experimental Bode plots recorded (b) during discharge and (c) during charge. Comparison of the Bode plots obtained using the 2-electrode set up, and the anode and the cathode contribution using a reference sodium electrode after (d) full discharge and (e) full charge.

The galvanostatic cycle (Figure 5.9.a) revealed a stable discharge plateau at ~2.1 V that took almost 75% of the full discharge capacity. The subsequent charge showed an

average potential of 2.55 V and the Coulombic efficiency was 26%. From the Bode plots of the impedance measurements carried out during the discharge (Figure 5.9.b) it is deduced that three main processes take place in the cell; one at low frequencies ($\sim10^0 - 10^1$ Hz) and two at higher frequencies (approximately at 10^3 and 10^4 Hz). Contribution at lower frequencies is increased as discharge goes on, while contributions at 10^3 and 10^4 Hz are slightly decreased and increased, respectively. During the galvanostatic charge of the cell, however, two process can be observed at low frequencies (Figure 5.9.c), one at $\sim10^{-1}$ Hz and the other at $\sim10^1$ Hz. There are two possible reasons for this fact: on one hand, it is possible that both processes at low frequencies were overlapped during the discharge of the cell, being separated during the charge. On the other hand, it is also possible that during the discharge of the cell only one process took place, and during the charge of the cell the contribution of this process was decreased while a new process appeared. It is worth mentioning that all the contributions increase during the charge of the cell, although there is a decrease in the low frequency process between the measurements after full discharge and the first charge step.

Next step in the characterization process was the determination of the origin the contributions; for that aim impedance of the anode and the cathode was measured separately against a sodium reference electrode which did not undergo electrochemical oxidation and reduction reactions. Bode diagrams of the anode and cathode compared to those of the 2 electrode set up after full discharge (Figure 5.9.d) and full charge (Figure 5.9.e) unequivocally revealed that processes at low frequency were originated in the oxygen electrode, while those at high frequencies were related to the sodium anode. In both figures processes at high frequencies fit well when 2 electrode and anode contribution are compared. Contributions at lower frequencies, however, were not that accurately overlapped, which considering that each impedance measurement lasted over 6 minutes could be indicative of some kind of small variation in the oxygen

electrode while measurements were being carried out. Consequently, it must be considered the presence of chemical reactions accompanying the aforementioned electrochemical ORR and OER.

After that, contributions in the impedance measurements were quantified by fitting the obtained spectra with the R_1-R_2CPE_2-R_3CPE_3-R_4CPE_4 equivalent circuit for the 2 electrode set up, R_1-R_2CPE_2-R_3CPE_3 for the anode and R_1-R_2CPE_2 for the cathode (Figure 5.10).
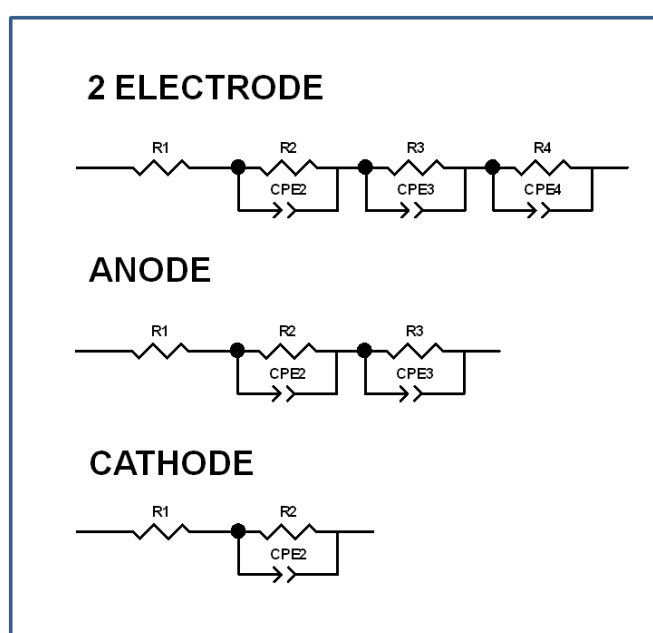

Figure 5.10. Equivalent circuits selected for the fitting of the 2 electrode, anode and cathode measurements.

Nyquist plots of the impedance data recorded at half discharge (Figure 5.11.a, 5th measurement during discharge) and at half charge (Figure 5.11.b, 1st measurement during charge) reveal the presence of two main semicircles that could consist of one or two overlapped minor semicircles each due to their flat shape. R_1-R_2CPE_2-R_3CPE_3-R_4CPE_4 equivalent circuit fits accurately as shown in Figures 5.11.a and 5.11.b. Examples of anode and cathode fittings are displayed in Figures 5.11.c and 5.11.d, respectively, evidencing that the equivalents circuits were correctly selected.
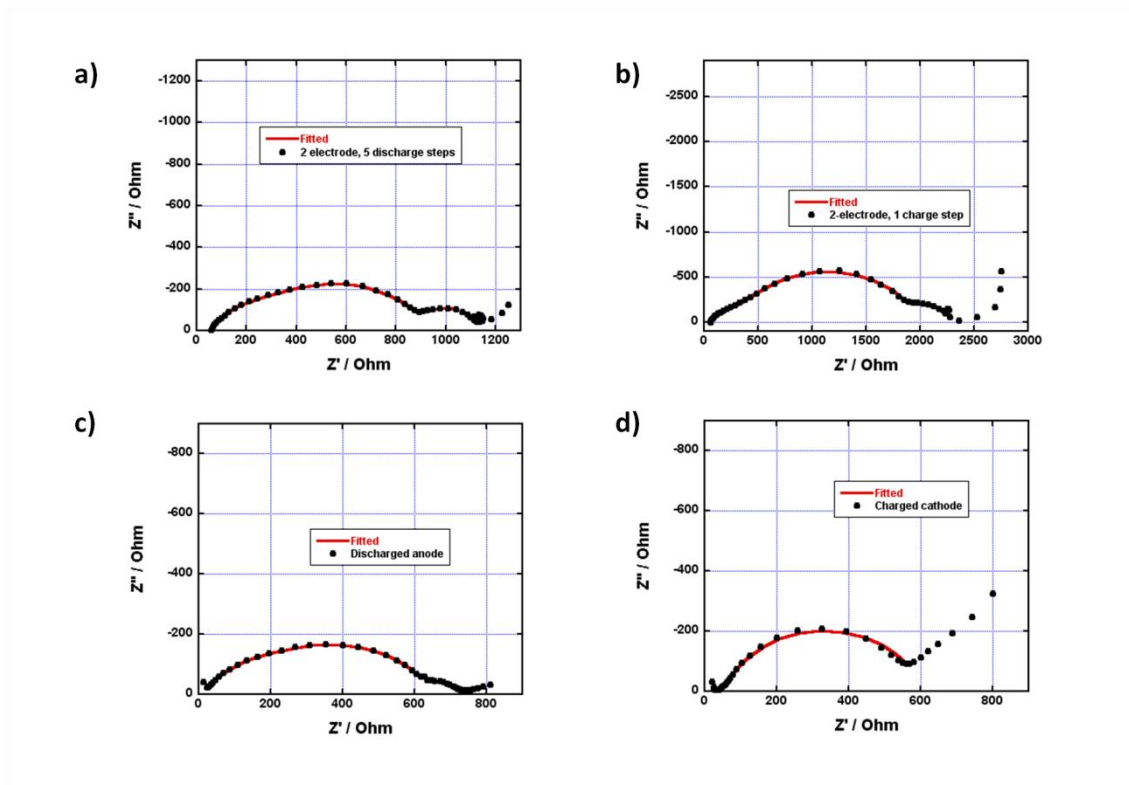
Figure 5.11. Experimental Nyquist plots with the 2 electrode set up recorded (a) at half discharge and (b) half charge fitted with the R_1-R_2CPE_2-R_3CPE_3-R_4CPE_4 equivalent circuit. Experimental Nyquist plots of the (c) sodium anode after full discharge and (d) oxygen electrode after full charge fitted with the R_1-R_2CPE_2-R_3CPE_3 and the R_1-R_2CPE_2 equivalent circuits, respectively.

Finally, Figure 5.12 shows the evolution of the resistances associated to each process with the galvanostatic cycle. It can be observed that based on the resistance values obtained for the cathode and the anode it is possible to relate R_2, R_3 and R_4 in the 2 electrode set up to R_2, and R_3 of the anode and R_2 of the cathode, respectively. It is worth mentioning that R_2 in the cathode after discharge is lower than that for R_4 in the 2 electrode set up, in good agreement with the lower signal observed at low frequencies in the Bode plot after discharge (Figure 5.9.d). Furthermore, capacitances and frequencies of the contributions fitted on well for both the anode and cathode processes (see Table 5.2).

Table 5.2. Capacitances and frequencies obtained after the galvanostatic discharge associated to each electrochemical process identified by the equivalent circuits in Figure 5.10.

Resistance	Capacitance / F	Frequency / Hz
2 electrode-R_2	$2.66 \cdot 10^{-6}$	$2.32 \cdot 10^4$
Anode-R_2	$4.41 \cdot 10^{-6}$	$2.81 \cdot 10^4$
2 electrode-R_3	$9.25 \cdot 10^{-7}$	$1.32 \cdot 10^4$
Anode-R_3	$1.16 \cdot 10^{-6}$	$1.08 \cdot 10^4$
2 electrode-R_4	$2.27 \cdot 10^{-4}$	5.84
Cathode-R_2	$2.09 \cdot 10^{-4}$	13.3

Finally, R_1 was associated with the ohmic resistance and keeps constant during all the galvanostatic cycle. Recently, Knudsen *et al.*[30] carried out a similar experiment in which they observed a similar trend in the cathode resistance during the first cycle: resistance increased with the depth of discharge, obtaining a maximum value after full discharge. Similar to them, during the charge of the battery resistance value was decreased in the first stage and slightly increased in the subsequent stages. In our experiment, however, anode contribution was significantly higher than that reported by Knudsen *et al.*.[30]
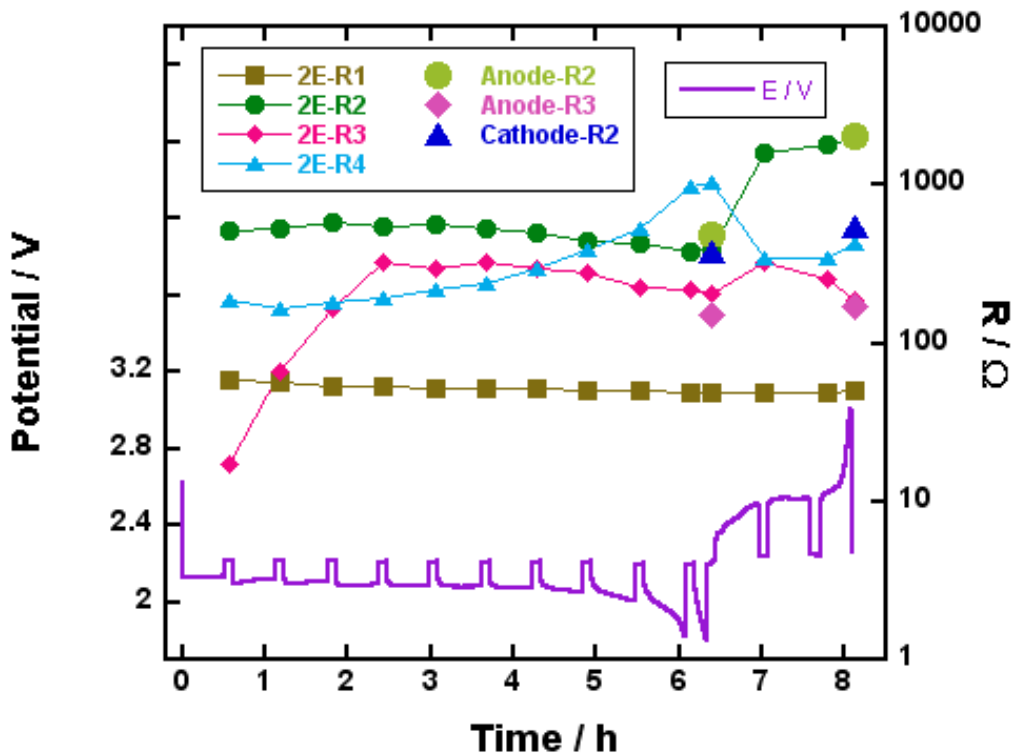
Figure 5.12. Analysis of the evolution of the resistances with the galvanostatic cycle.

The origin of such difference remains unclear and in furtherance of analyzing the cathode processes the experiment was repeated with a 3 electrode set up monitoring in detail the evolution of the oxygen electrode without the influence of the sodium anode. Galvanostatic cycle carried out using the 3 electrode set up was slightly longer than the cycle with the 2 electrode set up (Figure 5.11.a). This difference, however, cannot be attributed to the cell set up; it is accepted that it is challenging to accurately reproduce galvanostatic cycles in non-aqueous metal-oxygen batteries.[31] Nevertheless, cycle overpotential is reduced in approximately 200 mV; this behavior was also observed by Knudsen *et al.* and is indicative of side reactions in the sodium counter electrode (anode) that influence the cell potential.[30] The reference Na electrode does not undergo these reactions as electrochemical oxidation and reduction reactions are not continuously occurring on its surface and it is therefore more reliable to analyze processes taking place in the oxygen electrode.
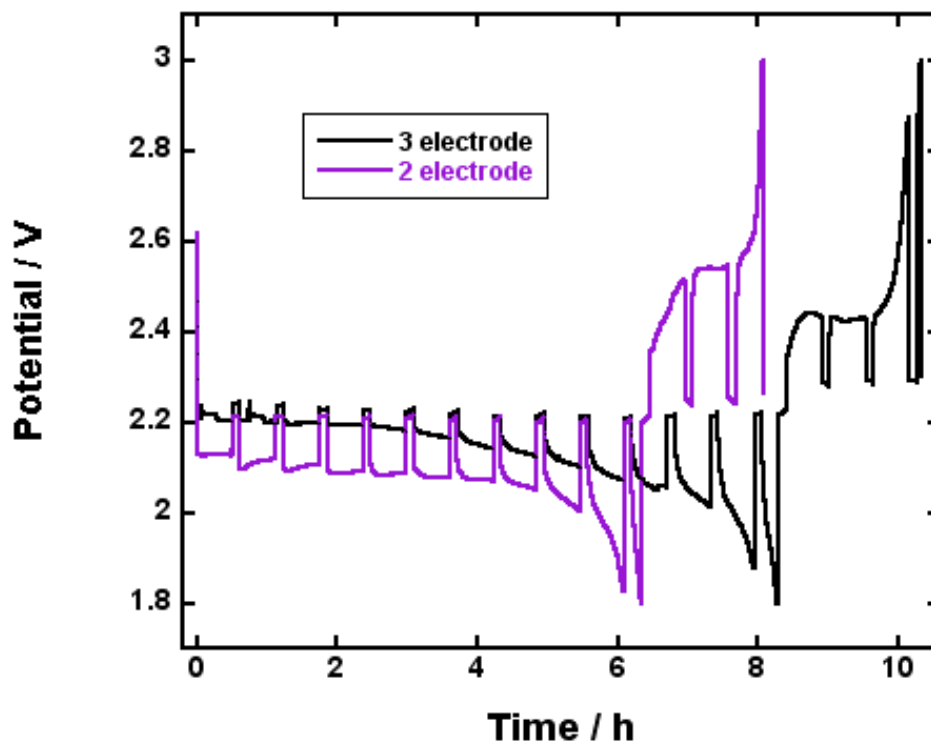
Figure 5.13. (a) Galvanostatic cycles carried out with the 2-electrode (purple line) and 3-electrode set up (black line).

As expected, no evidence of anode processes (at high frequencies) was observed in the Bode plots recorded during discharge (Figure 5.14.a) and charge (Figure 5.14.b) with the 3-electrode set up. This time, however, Nyquist plots could not be fitted using the R_1-R_2CPE_2 equivalent circuit as in the cathode analysis in Figure 5.10 and it was necessary to use the R_1-R_2CPE_2-R_3CPE_3-R_4CPE_4 equivalent circuit. This difference suggests that different processes can be overlapped in these measurements, making challenging to distinguish between them. Figures 5.14.c and 5.14.d are some examples of the Nyquist plots recorded and the fittings carried out. R_1 is assigned again to the ohmic resistance and has negligible differences through the cycle. R_2 shows a capacitance value of 10^{-6} F, the same as R_2 and R_3 in the 2-electrode set up (anode contribution), and both R_3 and R_4 are around 10^{-4} F. This allows us to identify R_3 and R_4 as the oxygen diffusion from outer atmosphere to oxygen-electrode surface and oxygen adsorption together with the charge-transfer resistance of electrochemical

153

reduction of oxygen species (and will be therefore analyzed together, as we did in Chapter 3). Furthermore, the capacitance and the low resistance value (discussed later) of R_2 suggest that its presence can be attributed to the charge transference in the electrolyte/RE interface. Consequently, although negligible, the reference electrode also has a small contribution in the impedance spectra.
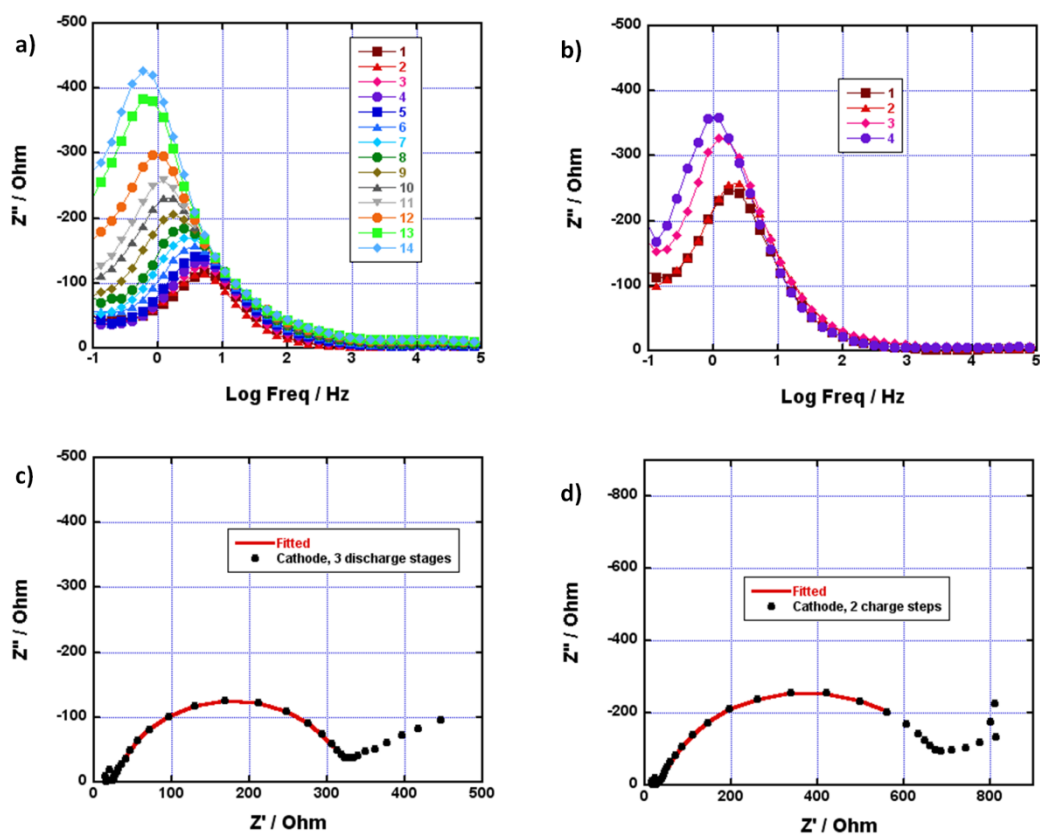

Figure 5.14. Bode plots of the oxygen electrode recorded during (a) discharge and (b) charge. Experimental Nyquist plots obtained with the 3-electrode set up (c) after 3 discharge steps and (d) after 2 charge steps fitted with the R_1-R_2CPE_2-R_3CPE_3-R_4CPE_4 equivalent circuit.

Resistance evolution with the galvanostatic cycle is shown in Figure 5.15. R_2 grows since the early beginning of the discharge, reaching its maximum before the plateau starts to decay. After that, there is a small decrease in its contribution in the first stages of the charge, with a final growth by the end of the charge. Nevertheless, R_2 is between 8 and 28 ohms during all the cycle, and consequently variations recorded may not be

significant, or can perhaps be attributed to the fitting. On the other hand, R_3+R_4 evolution has a similar shape to the inverted discharge plateau; it was constant while potential plateau was flat and increased significantly as the discharge came to an end. R_3+R_4 are decreased during the first stages of the charge and increased by the end. Knudsen *et al.* attributed this fact to the side reactions that can occur in the oxygen electrode surface and the discharge products, leading to the formation of species that cannot be eliminated at these low working potentials, such as carbonates[30] in good agreement with the results shown in Section 5.2.
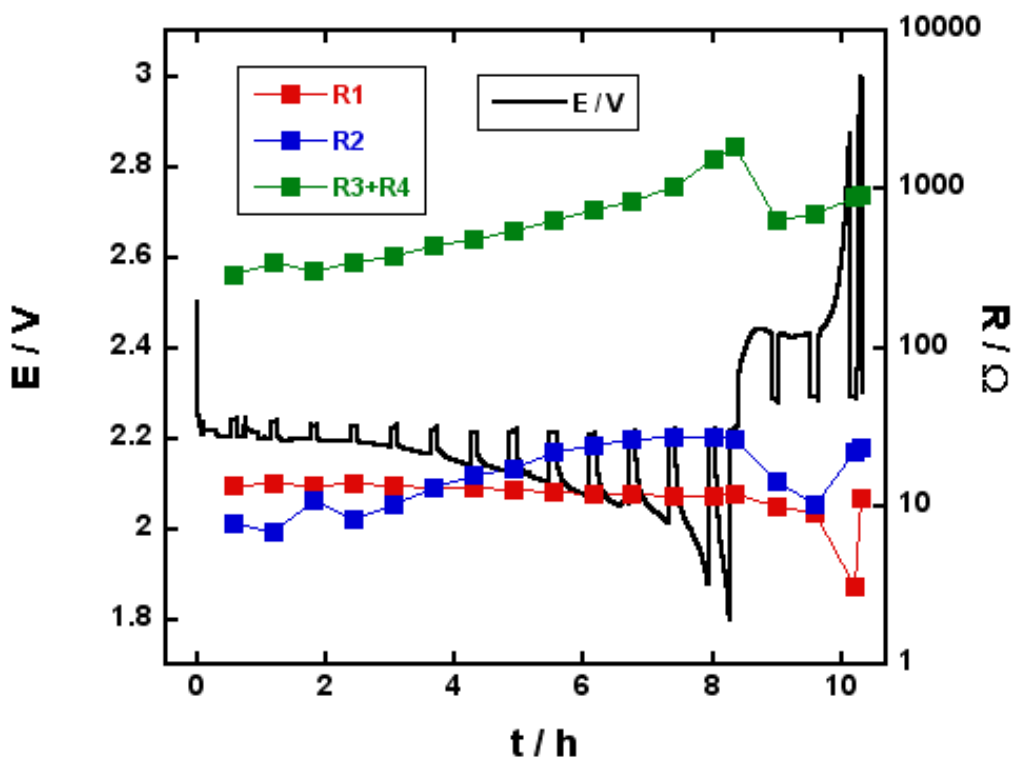

Figure 5.15. Analysis of the evolution of the resistances measured with the 3-electrode set up during the galvanostatic cycle.

In order to shed some light into the discharge product accumulation and removal in the oxygen electrode quartz crystal microbalance (QCM) measurements were carried out (Figure 5.16).
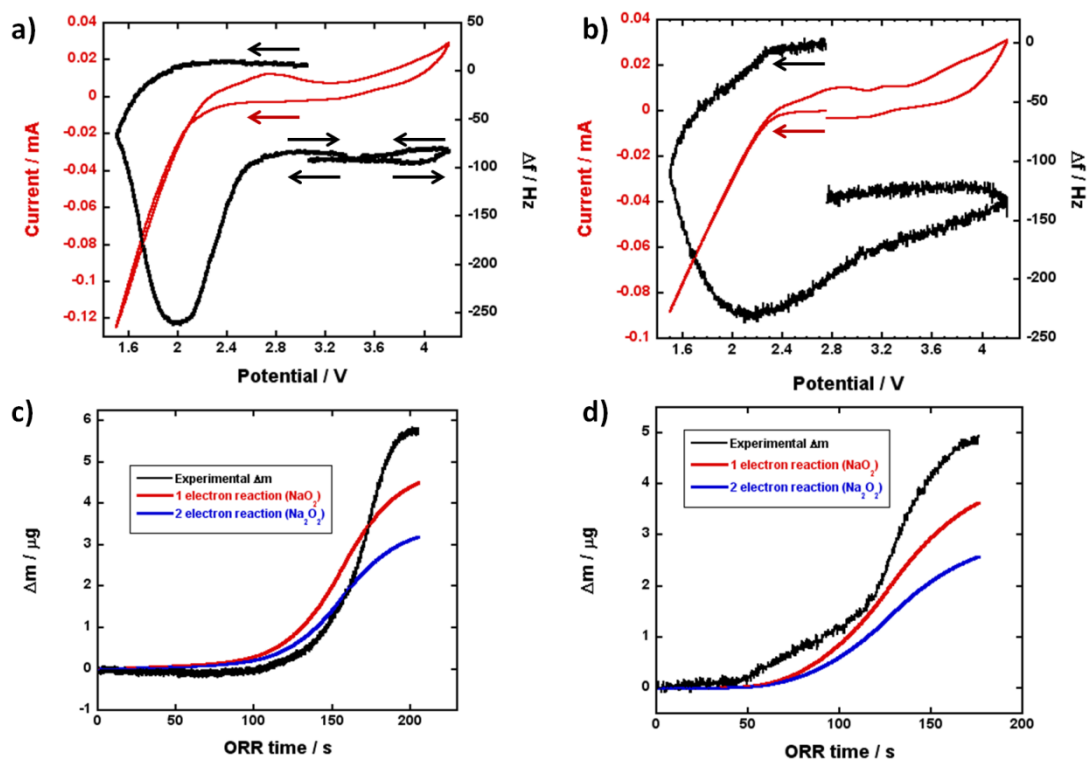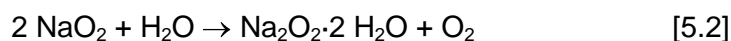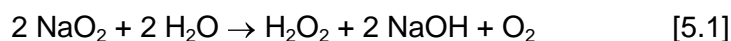
Figure 5.16. Cyclic voltammetries (CVs) carried out with the QCM cell in (a) absence and (b) presence of leaks. Mass gain in the electrode calculated using Sauerbrey equation in (c) absence and (d) presence of leaks. Ideal formation of NaO_2 (red) and Na_2O_2 (blue) are calculated from the CV curves.

Figure 5.16.a shows the frequency variation associated to a CV measurement in a QCM cell. The accumulation of discharge product during the cathodic scan leads to a negative frequency variation (Δf) (in good agreement to the $Li-O_2$ literature) that continues increasing even in the first stages of the anodic sweep in the region that the current is still negative. Δf is decreased between 2.1 and 2.6 V evidencing OER activity and, therefore, confirming that ORR products were accumulated in the cathodic scan. Between 2.8 and 3.8 V, however, slight mass accumulation is registered and gives us interesting information: based on the work by Pinedo *et al.* if we had leaks in our cell we would expect the formation of $Na_2O_2\cdot2H_2O$ in the cathodic sweep, that would lead to the formation of NaOH in the OER potential.[10]

$$2\ NaO_2 + 2\ H_2O \rightarrow H_2O_2 + 2\ NaOH + O_2 \qquad [5.1]$$

$$2\ NaO_2 + H_2O \rightarrow Na_2O_2 \cdot 2\ H_2O + O_2 \qquad [5.2]$$

$$Na_2O_2 \cdot 2H_2O \rightarrow H_2O_2 + 2\ NaOH \qquad [5.3]$$

NaOH was demonstrated to be eliminated between 2.8 and 3.5 V, and its presence in our cell would be traduced in a decrease in the mass recorded in this potential range together with the appearance of a peak in the CV:[10]

$$2\ NaOH \rightarrow 2\ Na^+ + H_2O_2 + 2\ e^- \qquad [5.4]$$

$$2\ H_2O_2 \rightarrow 2\ H_2O + O_2 \qquad [5.5]$$
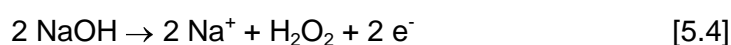
In our experiment we did not observe an electrochemical oxidation peak and we observed Δf was decreased, what involves mass gain in our electrode. This mass gain could be due to accumulation of passivation products that are in good agreement with the resistance increase observed in the last stage of the impedance measurements. Actually, as potential increased and got close to 4.2 V we could observe a Δf which can be due to carbonate elimination. After the anodic sweep the Δf decrease between 3.8 and 2.8 V is observed again. It is worth noting that Δf does not get back to the initial value meaning that we still have some product in the oxygen electrode after the complete cycle, in good agreement to the passivation of the discharge products demonstrated in section 5.2.

As a comparison we assembled an alternative QCM cell set up that due to the higher amount of connections in its structure was more likely to present leaks. The electrochemical response during the cathodic scan obtained with this set up is very similar to that with the original cell (Figure 5.16.b). Anodic scan, however, revealed an additional peak at 3.3 V that is in good agreement with the NaOH oxidation reported by Pinedo *et al.*. The appearance of an oxidation peak at 3.1 V confirms the appearance

of an additional specie that is oxidized at that potential being NaOH the most likely option. As with the leak-less set up the initial Δf cannot be recovered demonstrating that this cell is also affected by passivation.

Passivation also hinders the identification of the discharge products in ORR: Figure 5.16.c shows the discharge product mass formed for 1 and 2 electron reductions if each electron in the cathodic scan was converted into discharge product and accumulated in the oxygen electron for the leak-less set up. These curves are compared to the experimental mass accumulation in this electrode, calculated from the registered Δf using the Sauerbrey equation.[32,33] In the first 160 s of ORR the registered mass is lower than that of the theoretical 1 and 2 electron reduction; this indicates that although electrons were being transferred into the electrode this was not traduced in the accumulation of discharge products evidencing that these discharge products were stable in the electrolyte. However, once accumulated the discharge product deposits can be passivated and the experimental mass accumulation exceeded those for the ideal 1 and 2 electron reductions. On the other hand, mass gain analysis in presence of leaks (Figure 5.16.d) reveals that the experimental mass gain is over the ideal for the formation of both NaO_2 and Na_2O_2. Consequently, it is likely that the resultant products were not stable in the electrolyte and were therefore accumulated in the electrode since the early beginning of the cathodic scan. In addition, reaction of ORR products with moisture is fast, leading to the production of heavier species than the initial superoxide and/or peroxide since the early beginning of the scan.

Although it was impossible to identify the discharge product generated in ORR two main conclusions were obtained from this experiment:

i.   It is demonstrated that ORR is solution mediated as suggested in literature.[6]

ii. The presence of moisture leads to the incapability to carry out a solution mediated ORR.

iii.   It is confirmed that the discharge product is passivated in the cell, gaining mass in the regions at which carbonates cannot be oxidized.

Moreover, effect of the passivation of the discharge products was further analyzed using a glassy carbon (GC) electrode. CV measurements were carried out limiting the anodic scan to 4.2, 3.8 and 3.5 V in order to analyze the capacity of the cell to retain the cathodic current depending on the anodic limiting potential (Figure 5.17).
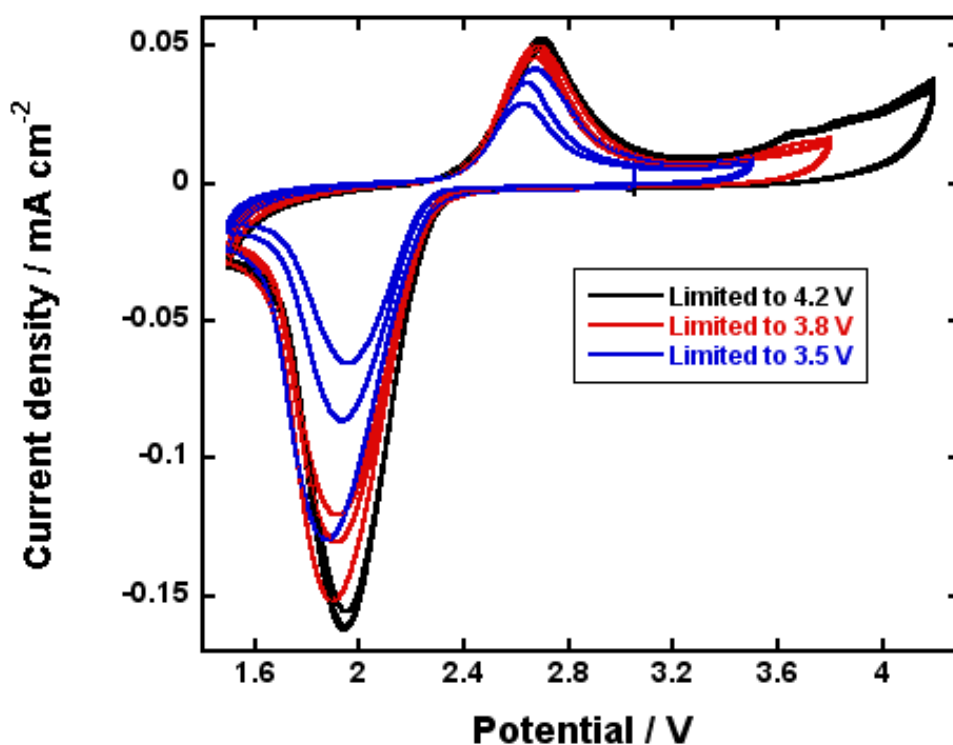
Figure 5.17. Cyclic voltammetries carried out limiting the anodic sweep to 4.2 (black line), 3.8 (red line) and 3.5 V (blue line).

Na-O_2 cell in which the anodic scan was limited to 4.2 V could retain the ORR for the first three cycles (0.5088, 0.5289 and 0.5203 mC in the first, second and third cycles, respectively). Nevertheless, when the anodic sweep limit was decreased to 3.8 V the ORR charge was decreased from 0.4727 to 0.388 mC in the second cycle and to 0.383 mC in the third cycle. The incapability to retain the ORR was enhanced when the

anodic sweep was limited to 3.5 V, decreasing from 0.4295 mC in the first cycle to 0.2602 and 0.2128 mC in the second and the third cycles, respectively.

Based on the impedance and QCM data it is possible to propose the discharge product formation and removal model that is schematized in Figure 5.18. In the initial stages of the discharge (Figure 5.18.a) superoxide is formed at the oxygen electrode surface and stabilized in the electrolyte, as demonstrated by QCM measurement in absence of leaks. Once the solution saturates some discrete nuclei are formed and growth as more superoxide is generated. These nuclei, however, are discrete and resistance associated to the discharge products is kept almost constant. At that stage we observe a flat plateau in the potential vs. time (or capacity) graph. As discharge goes on (Figure 5.18.b) more nuclei are generated, resistance is increased, and oxygen adsorption is hindered leading to a potential fall that is slowly increased. Consequently, it can be said that ORR slowly turns from a solution-process to a surface-process. By the end of the discharge (Figure 5.18.c) oxygen electrode gets saturated of discharge products and the impedance is quickly increased, reaching to its maximum. ORR almost completely stops being solution mediated and very small nuclei (or a thin film) appear. Finally, the electrode is not able to adsorb and reduce more oxygen and cell potential falls. In addition, during all this period the discharge product nuclei are slowly passivated.
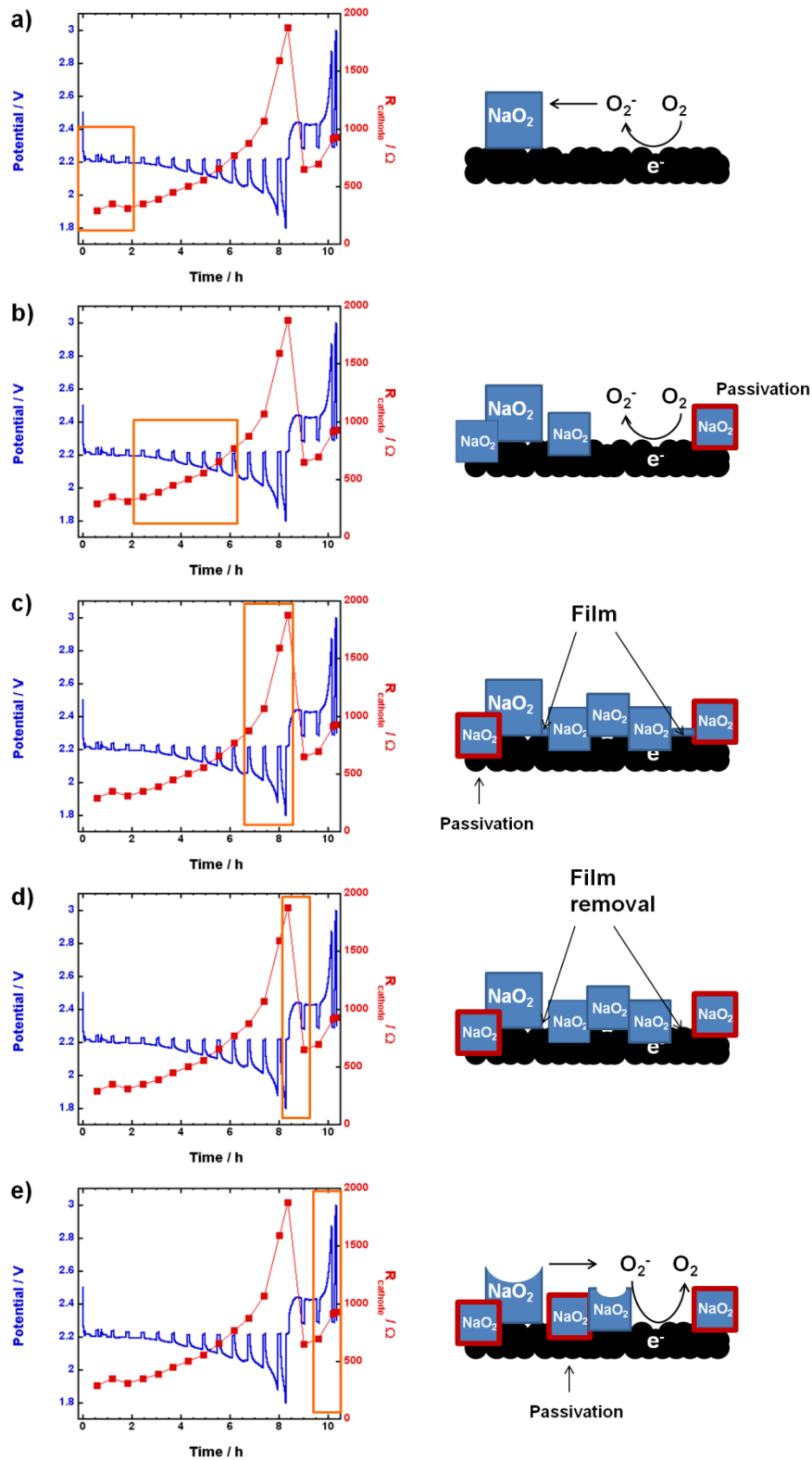
Figure 5.18. Schemes of the model proposed for the discharge product accumulation and removal. Orange boxes in the galvanostatic cycle indicate the part to which each scheme corresponds.

When positive current is applied (charge) the smallest nuclei are oxidized and resistance is significantly decreased (Figure 5.18.d). OER re-takes its solution-mediated nature and although we have a flat charge plateau, resistance is not decreased as electrode/electrolyte interface is not being recovered; we still have nuclei that are being slowly re-dissolved and then oxidized (Figure 5.18.e). In parallel, our electrode/products are passivated and impedance is increased.

In order to further validate the discharge product growth and removal model Na-O$_2$ cells were discharged to approximately 75, 44 22 and 7.5 % of their depth of discharge (DoD) and then recharged to 3.0 V (galvanostatic cycles are displayed in Figure 5.19.a). Meanwhile, impedance was measured every 30 minutes. Based on the model proposed in Figure 5.18 the discharge deposits by the end of the discharge should be more isolated as the DoD is decreased and, therefore, the resistance decrease in the first stages of the charge should be less noticeable, as the ORR becomes a surface-process as discharge goes on. Resistance evolution of the different cells is presented in Figure 5.19.b, highlighting the end of each discharge by a vertical line. As previously shown, resistance after full discharge (100 %) was decreased after the first fraction of the charge. Nevertheless, when the cell was discharged to the 75 % of the DoD resistance kept almost constant after 1 charge step evidencing the lack of product saturation in the oxygen electrode before charge. For the rest of the measurements resistance after charge was even higher than that before. It can therefore be concluded that for "early cutoffs" there is not a significant removal of discharge products from the electrode surface affecting the cell impedance; products are removed from the solution. However, when we turn to "late cutoffs" electrode surface is covered by discharge products that are partly removed until the OER can be carried out by the solution mechanism.
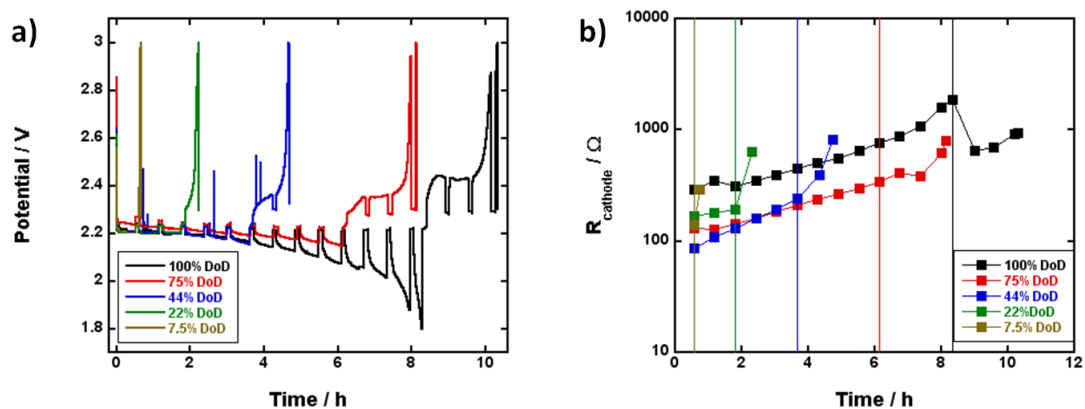
Figure 5.19. (a) Galvanostatic cycles carried out to the 7.5 (olive line), 22 (green line), 44 (blue line) 75 (red line) and 100% (black line) of the depth of discharge. (b) Resistance evolution of the cathode with the galvanostatic cycle. Vertical lines correspond to the measurement between the last discharge and the first charge periods.

5.4. Superoxide migration and Coulombic efficiency

As demonstrated by Hartmann *et al*. O_2^- is formed at the cathode surface and dissolved in the electrolyte, and it can migrate within the cell.[13] In this work we will successfully demonstrate that the loss of efficiency is caused by the migration of the formed superoxide out of the diffusion layer of the positive electrode. For this purpose, Na-O_2 cells were discharged to 0.1 and 0.5 mA h at a current density of 0.2 mA cm^{-2} and carbon electrodes were analyzed by means of SEM (Figure 5.20).
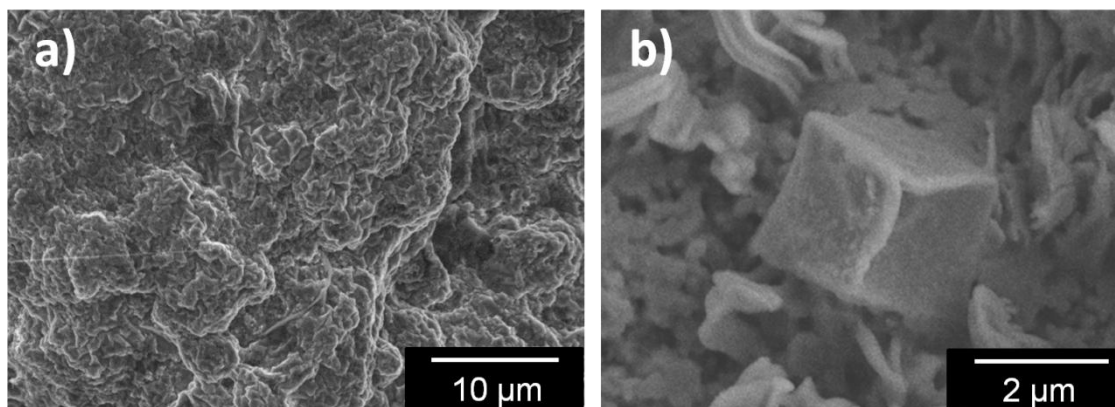
Figure 5.20. SEM images of an oxygen electrode discharged to a) 0.1 mA h and b) 0.5 mA h at a current density of 0.2 mA cm^{-2}.

No discharge product could be detected in the carbon electrode at capacities lower than 0.5 mA h. The aforementioned pressure evolution measurement (Figure 5.8), however, unequivocally demonstrates ORR activity even for these small capacities and gives evidence for the formation of discharge product in the electrolyte. In order to further analyze the effect of the electrolyte-mediated O_2^- storage, different Na-O_2 cells were cycled at different current densities limiting the discharge capacity to 0.05 mA h, a low value in which no discharge product should be accumulated in the carbon electrode, based on SEM measurements shown in Figure 5.20. The use of different current densities allowed us to carry out discharges of different duration (Table 5.3).

Table 5.3. Different current densities and the corresponding discharge length set to discharge the Na-O$_2$ cell to 0.05 mA h.

Current density / mA cm^{-2}	Discharge time
1	0:03:10
0.5	0:06:19
0.2	0:15:47
0.1	0:31:34
0.05	1:03:08
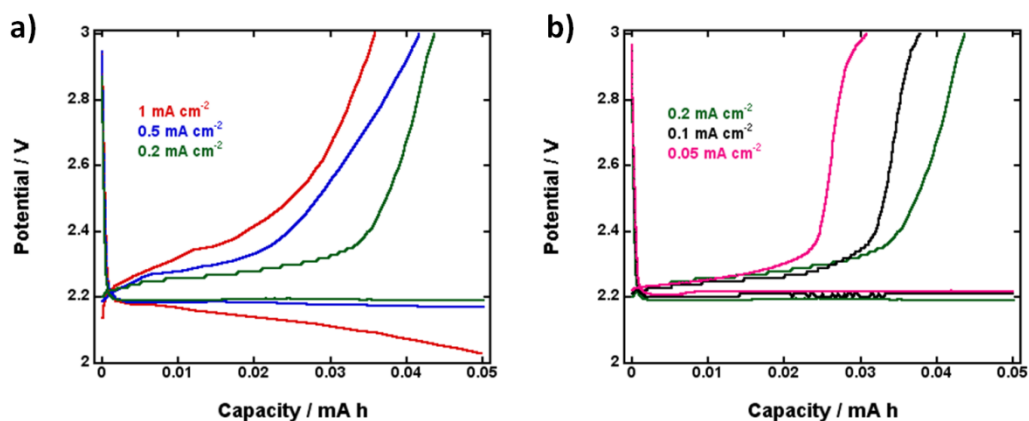
Figure 5.21. Galvanostatic curves obtained for the Na-O$_2$ cell at (a) higher and (b) lower current densities. Current density and NaO$_2$ exposure time to the cell environment govern the coulombic efficiency at higher and lower current densities, respectively.

The experimental results reveal that two different effects govern the performance of the cell. At high current densities (Figure 5.21.a) the tendency usually reported for Li-O$_2$ batteries is observed: increase in the current density leads to an increase of the

165

overpotential and a decrease of the coulombic efficiency due to the limited mass transport of O_2 to the electrode.[4] On the other hand, at lower current densities (Figure 5.21.b), the effect of the current density is reduced as no significant overpotential variations are detected. In turn, discharge time is increased from 15 minutes for the cell cycled at 0.2 mA cm^{-2} to over 1 hour for the one at 0.05 mA cm^{-2}. The lack of overpotential variations coupled to the loss of efficiency with the decrease of the current density (and therefore discharge length) can be taken as the first evidence of O_2^- migration affecting the rechargeability of the cell, as longer discharge duration would allow more time for migration leading to wider diffusional spreading of these anions within the electrolyte. This migration brings a larger fraction of the produced O_2^- out of the Nernst layer and therefore makes it unavailable for the upcoming charge. To support this hypothesis, CV experiments were carried out. The experiment was initiated with a standard cycle consisting of a cathodic scan to 1.5 V followed by an anodic scan to 4.2 V at a scan rate of 5 mV s^{-1} in order to identify the different processes taking place at each potential (Figure 5.22.a).
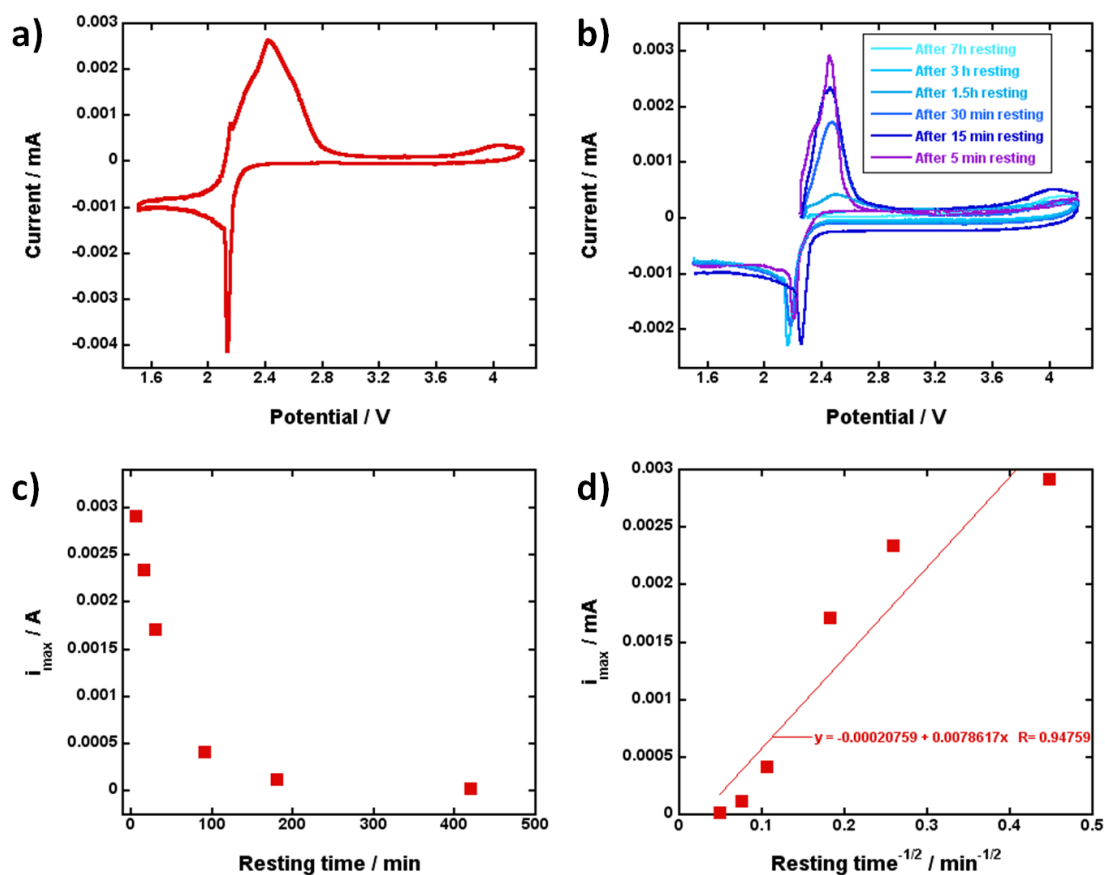
Figure 5.22. (a) First cycle of a cyclic voltammetry carried out in a Na-O_2 cell between 1.5 and 4.2 V at a scan rate of 5 mV s-1. (b) Cyclic voltammetry carried out following different resting periods after the cathodic scan. (c) Maximum intensities obtained in the anodic scan after the mentioned resting periods. (d) Square root dependence of the I_{max} to the resting time.

In the cathodic scan a sharp peak was recorded starting at 2.29 V attributed to the oxygen reduction reaction (ORR). No additional peaks were observed, concluding that the sole reaction in the cathodic scan was the reduction of O_2 to O_2^-. In the anodic scan, a broad peak with a maximum in 2.4 V was observed, starting at 2.07 V and finishing at 2.85 V attributed to oxygen evolution reaction (OER) in which NaO_2 is re-oxidized to O_2. It has to be mentioned that no additional processes were observed until 3.7 V, where the electrolyte degradation was initiated. After establishing the potentials of each electrochemical process, the CV analyses were modified, stabilizing a variable resting time between the cathodic and anodic scans, which allow us to evaluate the evolution of the peak associated to the OER, and therefore, the capability of the cell to

re-oxidize the previously formed superoxide. As seen in Figure 5.22.b, the peak attributed to OER is reduced when increasing the resting period. Interestingly, the OER peak was significantly reduced even after 30 minutes resting. In addition, almost no OER was observed after resting for 3 and 7 h. Analyses of the maximum current observed after each resting period (Figure 5.22.c) reveals a fast decrease of these values for resting times below three hours, while almost no difference was detected in the maximum current following 3 and 7 hour rest. The obtained NaO_2 oxidation peak intensities were observed to be square root dependent of the waiting time (Figure 5.22.d), matching the requirements of the Cottrell equation:

$$i = n \cdot F \cdot A \cdot c_j^0 \cdot D_j^{1/2} \cdot \pi^{-1/2} \cdot t^{-1/2} \qquad\qquad [5.6]$$

F represents the Faraday constant, A the area of the electrode, n the number of the electrodes involved in the process of the oxidation/reduction of the specie j, D_j the diffusion coefficient of j, c the initial concentration of j, and t and i are time and the current of the oxidation/reduction process, respectively. Fitting of the data in Figure 5.22.d reveals that maximum current obtained for NaO_2 oxidation after each resting period process is dependent on the square root of the resting period and is, therefore, a diffusion limited process.

The migration of the O_2^- formed was also observed to influence the performance of the cell discharged to higher capacities. A $Na\text{-}O_2$ cell was discharged to 0.5 mA h at 0.05 mA cm^{-2} and SEM analysis of the oxygen electrode was carried out (Figure 5.23) and compared to the one observed at 0.2 mA cm^{-2} (Figure 5.20).
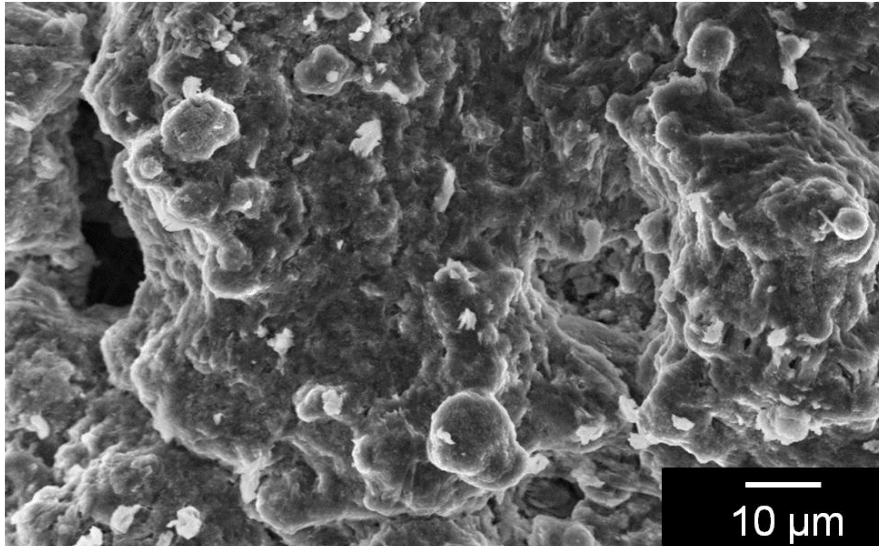
Figure 5.23. SEM image of a carbon electrode discharged to 0.5 mA h at a current density of 0.05 mA cm^{-2}.

Opposite to the cell discharged at 0.2 mA cm^{-2}, no discharge product could be detected at the cell discharged at 0.05 mA cm^{-2} for the same discharge capacity (0.5 mA h). If NaO_2 deposition in the electrode surface occurs after saturation of the electrolyte nearby the electrode surface is accepted,[18] lower current densities cause a slower O_2^- formation and, therefore, this discharge product can be distributed more effectively in the electrolyte.[34] The more effective diffusion decreases the O_2^- concentration in the vicinity of the electrode and, consequently, higher discharge capacities are required to detect discharge product accumulation on its surface. Evidence of such migration was demonstrated by EPR measurements when analyzing the separator exposed to the sodium electrode in which O_2^- was detected (Figure 5.24).
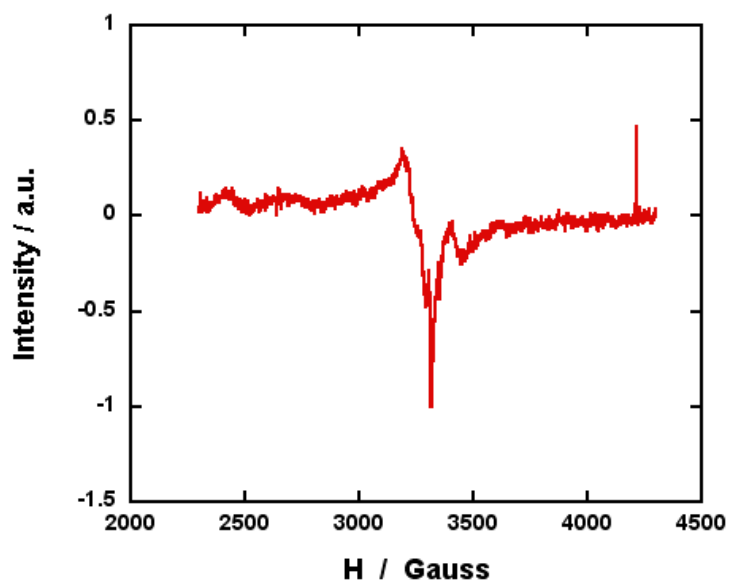
Figure 5.24. Electromagnetic paramagnetic resonance (ESR) measurements carried out on the separator facing the sodium electrode.

Furthermore, coulombic efficiency was 9 % lower at 0.05 mA cm^{-2} than that at 0.2 mA cm^{-2} (Figure 5.25.a) evidencing that lower reduction rates, and consequently lower superoxide formation rates, allow the migration of a higher amount of superoxide before saturation and resulting in a decrease of the efficiency of the subsequent recharge. Finally, analysis of the second galvanostatic cycle evidences higher coulombic efficiency than the first cycle (Figure 5.25.b).
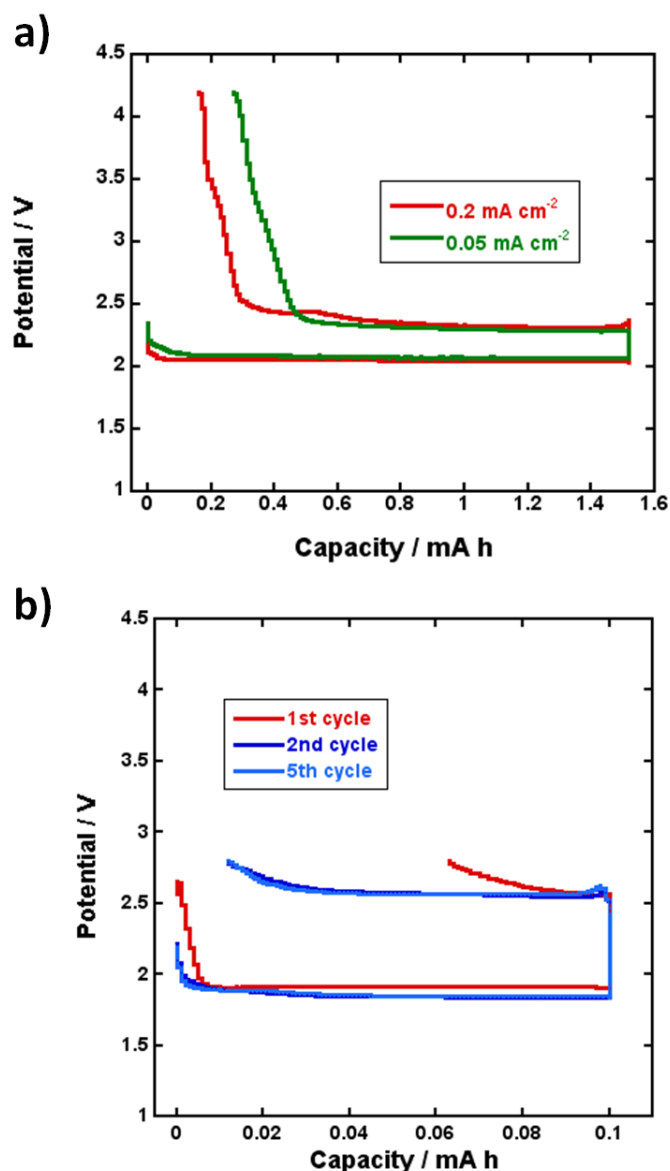
Figure 5.25. (a) First galvanostatic cycle of Na-O$_2$ cells discharged at a current density of 0.2 (red) and 0.05 (green) mA cm^{-2}. (b) 1st, 2nd and 5th galvanostatic cycles of a Na-O$_2$ cell limited to 0.1 mA h. Profile of the 1st cycle is colored in red.

In addition, NaO$_2$ deposits could be detected by means of SEM on the oxygen electrode at the very early steps of the discharge (Figure 5.26). This is in good agreement with the O$_2^-$ migration hypothesis; superoxide is present in the electrolyte outside the Nernst layer and, therefore, newly formed O$_2^-$ migration is not facilitated outside this layer. This leads to fast electrolyte saturation in the electrode vicinities for

low discharge capacities and early NaO_2 deposits formation. The decrease of the O_2^- migration increases such O_2^- availability during charge and, therefore, coulombic efficiency is increased.
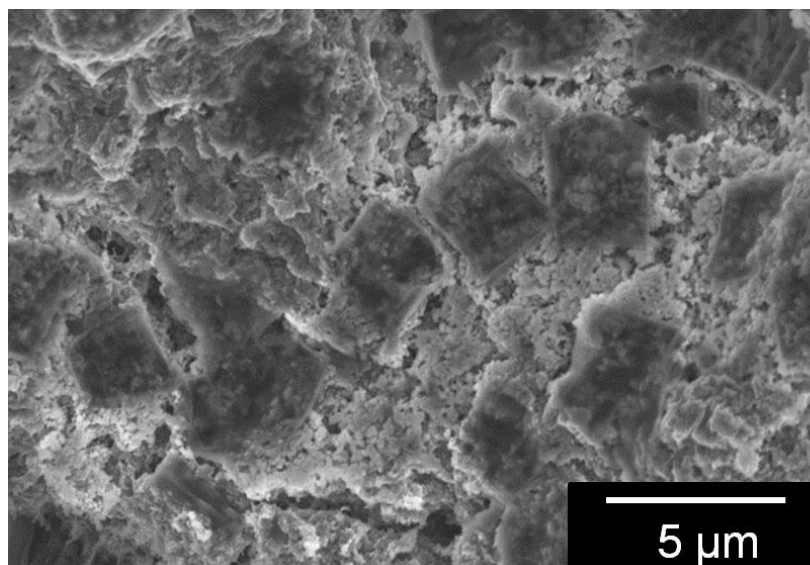
Figure 5.26. SEM images of discharge products generated during discharge of the second galvanostatic cycle limited to 0.1 mA h.

5.5. Conclusions

In this chapter the evolution in the cell environment of the superoxide formed in the ORR has been analyzed. It has been shown that the solubility and the diffusion of the discharge product O_2^- is the reason for the lower coulombic efficiency during the first galvanostatic cycle. The effect of O_2^- migration is reduced during the second galvanostatic discharge as O_2^- in the electrolyte hinders such migration leading to higher availability of O_2^- during the second charge, which leads to a higher coulombic efficiency compared to the first cycle. More importantly, NaO_2 is unstable in the cell environment and Na/O ratio of the cubes formed during discharge is decreased, evidencing chemical reactions. In addition, the gas pressure of the cell is increased during these resting periods and coupled to the Na/O ratio decrease, it can be deduced that oxygen is being released from these NaO_2 cubes. This instability leads to the

reduction of both the coulombic efficiency and the battery life. In addition, discharge product formation and removal have been analyzed by means of EIS and QCM. Both discharge product deposition and removal have been demonstrated to be solution-process for the NaO_2 nuclei formed in the initial stages of the discharge. As ORR goes on, however, oxygen electrode gets covered by smaller nuclei that lead both ORR and OER to be surface-process.

5.6. References

(1)   Landa-Medrano, I.; Pinedo, R.; Ortiz-Vitoriano, N.; Ruiz de Larramendi, I.; Rojo, T. *ChemSusChem* **2015**, *8*, 3932–3940.

(2)   Adelhelm, P.; Hartmann, P.; Bender, C. L.; Busche, M.; Eufinger, C.; Janek, J. *Beilstein J. Nanotechnol.* **2015**, *6*, 1016–1055.

(3)   Landa-Medrano, I.; Li, C.; Ortiz-Vitoriano, N.; Ruiz de Larramendi, I.; Carrasco, J.; Rojo, T. *J. Phys. Chem. Lett.* **2016**, *7*, 1161–1166.

(4)   Hartmann, P.; Bender, C. L.; Vračar, M.; Dürr, A. K.; Garsuch, A.; Janek, J.; Adelhelm, P. *Nat. Mater.* **2013**, *12* (3), 228–232.

(5)   Mccloskey, B. D.; Garcia, J. M.; Luntz, A. C. *J. Phys. Chem. Lett.* **2014**, *5*, 1230–1235.

(6)   Xia, C.; Black, R.; Fernandes, R.; Adams, B.; Nazar, L. F. *Nat. Chem.* **2015**, *7*, 496–501.

(7)   Ortiz-Vitoriano, N.; Batcho, T. P.; Kwabi, D. G.; Han, B.; Pour, N.; Yao, K. P. C.; Thompson, C. V.; Shao-Horn, Y. *J. Phys. Chem. Lett.* **2015**, *6*, 2636–2643.

(8)   Bi, X.; Ren, X.; Huang, Z.; Yu, M.; Kreidler, E.; Wu, Y. *Chem. Commun.* **2015**, *51*, 7665–7668.

(9)   Yadegari, H.; Li, Y.; Norouzi Banis, M.; Li, X.; Wang, B.; Sun, Q.; Li, R.; Sham,

T.-K.; Cui, X.; Sun, X. *Energy Environ. Sci.* **2014**, *7*, 3747–3757.

(10) Pinedo, R.; Weber, D. A.; Bergner, B. J.; Schröder, D.; Adelhelm, P.; Janek, J. *J. Phys. Chem. C* **2016**, *120* (16), 8472–8481.

(11) Bender, C. L.; Schröder, D.; Pinedo, R.; Adelhelm, P.; Janek, J. *Angew. Chemie (International Ed.* **2016**, *55*, 2–12.

(12) Arcelus, O.; Li, C.; Rojo, T.; Carrasco, J. *J. Phys. Chem. Lett.* **2015**, *6*, 2027–2031.

(13) Hartmann, P.; Heinemann, M.; Bender, C. L.; Graf, K.; Baumann, R.-P.; Adelhelm, P.; Heiliger, C.; Janek, J. *J. Phys. Chem. C* **2015**, *119* (40), 22778–22786.

(14) Bender, C. L.; Hartmann, P.; Vračar, M.; Adelhelm, P.; Janek, J. *Adv. Energy Mater.* **2014**, *4* (12), 1301863.

(15) Kang, S.; Mo, Y.; Ong, S. P.; Ceder, G. *Nano Lett.* **2014**, *14* (2), 1016–1020.

(16) Hartmann, P.; Grübl, D.; Sommer, H.; Janek, J.; Bessler, W. G.; Adelhelm, P. *J. Phys. Chem. C* **2014**, *118* (3), 1461–1471.

(17) Zhao, N.; Li, C.; Guo, X. *Phys. Chem. Chem. Phys.* **2014**, *16* (29), 15646–15652.

(18) Hartmann, P.; Bender, C. L.; Sann, J.; Dürr, A. K.; Jansen, M.; Janek, J.; Adelhelm, P. *Phys. Chem. Chem. Phys.* **2013**, *15* (28), 11661–11672.

(19) Eysel, H. H.; Thym, S. *J. Inorg. Gen. Chem.* **1975**, *411*, 97–192.

(20) Black, R.; Oh, S. H.; Lee, J.; Yim, T.; Adams, B.; Nazar, L. F. *J. Am. Chem. Soc.* **2012**, *134*, 2902–2905.

(21) Kim, J.; Park, H.; Lee, B.; Seong, W. M.; Lim, H.; Bae, Y.; Kim, H.; Kim, W. K.;

Ryu, K. H.; Kang, K. *Nat. Commun.* **2016**, *7*, 1–9.

(22)   Todres, Z. V. *Ion-Radical Organic Chemistry: Principles and Applications*,
         Second.; CRC Press, **2008**.

(23)   Liu, T.; Leskes, M.; Yu, W.; Moore, A. J.; Zhou, L.; Bayley, P. M.; Kim, G.; Grey,
         C. P. *Science (80-.).* **2015**, *350* (6260), 530–533.

(24)   Schwenke, K. U.; Meini, S.; Wu, X.; Gasteiger, H. A.; Piana, M. *Phys. Chem.
         Chem. Phys.* **2013**, *15* (28), 11830–11839.

(25)   Freunberger, S. a; Chen, Y.; Drewett, N. E.; Hardwick, L. J.; Bardé, F.; Bruce, P.
         G. *Angew. Chem. Int. Ed. Engl.* **2011**, *50* (37), 8609–8613.

(26)   Bergner, B. J.; Schürmann, A.; Peppler, K.; Garsuch, A.; Janek, J. *J. Am. Chem.
         Soc.* **2014**, *136* (42), 15054–15064.

(27)   Bergner, B. J.; Busche, M. R.; Pinedo, R.; Berkes, B. B.; Schröder, D.; Janek, J.
         ACS Appl. Mater. Interfaces **2016**, *8* (12), 7756–7765.

(28)   Landa-Medrano, I.; Olivares-Marín, M.; Pinedo, R.; Ruiz de Larramendi, I.; Rojo,
         T.; Tonti, D. *Electrochem. commun.* **2015**, *59*, 24–27.

(29)   Zhang, T.; Liao, K.; He, P.; Zhou, H. *Energy Environ. Sci.* **2016**, *9,* 1024–1030.

(30)   Knudsen, K. B.; Nichols, J. E.; Vegge, T.; Luntz, A. C.; Mccloskey, B. D.; Hjelm,
         J. *J. Phys. Chem. C* **2016**, *120* (20), 10799–10805.

(31)   Landa-Medrano, I.; Pinedo, R.; Ruiz de Larramendi, I.; Ortiz-vitoriano, N. *J.
         Electrochem. Soc.* **2015**, *162* (2), 3126–3132.

(32)   Sauerbrey, G. *Zeitschrift Für Phys.* **1959**, *155*, 206–222.

(33)   Schaltin, S.; Vanhoutte, G.; Wu, M.; Bardé, F.; Fransaer, J. *Phys. Chem. Chem.
         Phys.* **2015**, *17* (19), 12575–12586.

(34)   Schröder, D.; Bender, C. L.; Osenberg, M.; Hilger, A.; Manke, I.; Janek, J. *Sci. Rep.* **2016**, *6*, 1–7.

Chapter 6 – Characterization of Na-O$_2$ discharge products by Synchrotron X-ray Transmission Microscopy

The nature of the discharge products in Na-O$_2$ batteries has been under debate since the early steps of this technology. In this chapter discharge products are generated under different experimental conditions and their composition is studied by means of Synchrotron X-ray transmission microscopy.

6.1. Introduction

The identification of discharge products has been one of the main hotspots in Na-O$_2$ batteries; although sodium superoxide (NaO$_2$) has been the most widely reported discharge product some authors have evidenced the formation of sodium peroxide (Na$_2$O$_2$) and sodium peroxide dehydrate (Na$_2$O$_2$·2H$_2$O).[1–3] In a previous work Dr. Tonti's group at ICMAB used Synchrotron X-ray Transmission Microscopy (TXM) at the Mistral beamline of the ALBA synchrotron[4,5] in Li-O$_2$ batteries to quantify and localize, with spatial resolution, the distribution of the oxygen discharge products and appreciate several compositional, structural, and morphological aspects.[6] TXM allowed simultaneously mapping and discriminating between the principal possible reaction products involved as oxygen and its chemical state was directly detected obtaining a full O K-edge absorption spectrum at each pixel. In this chapter this technique will be used to analyze the composition of the discharge products generated in Na-O$_2$ cells under different experimental conditions.

6.2. Reference samples

Na$_2$O$_2$, NaOH and Na$_2$CO$_3$ were analyzed by means of TXM in order to be used as references for the products accumulated in the oxygen electrodes under different conditions. O K-edge XANES spectra of these compounds are shown in Figure 6.1.
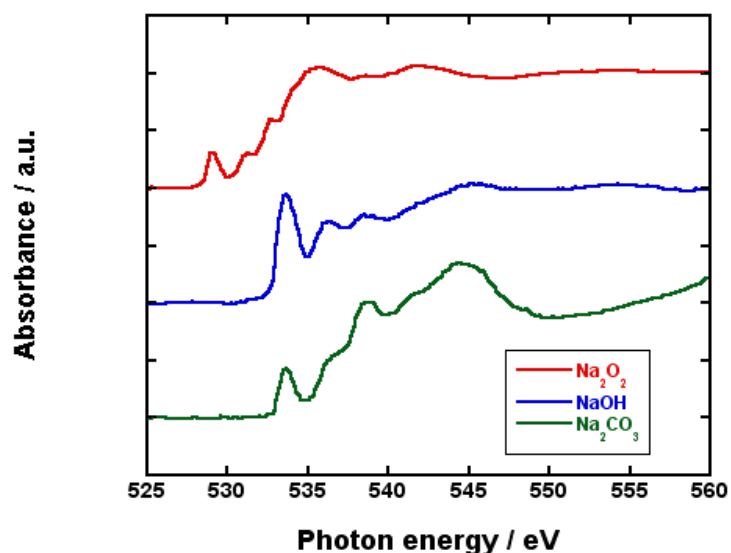
Figure 6.1. O K-edge XANES spectra of the reference materials: Na_2O_2 (red line), NaOH (blue line) and Na_2CO_3 (green line).

Based on the spectra obtained by the reference materials one could expect that the main signal of Na_2O_2 is that at 529.15 eV and Na_2CO_3 and NaOH should be detected at 535.5 eV. Yadegari *et al*, however, related the presence of NaO_2 and Na_2O_2 to the features at 532.9 eV and 534.3 eV, respectively.[7] As far as we know, there has not been published any other work using XANES to identify the discharge products in Na-O_2 batteries and, therefore, we needed to turn to XANES spectra carried out in Li-O_2 batteries in order to shed some light into the differences observed between our work and that of Yadegari *et al.*.[7] Shao-Horn's group related the presence of Li_2O_2 and Li_2CO_3 to the signals at 532.1 and ~534 eV, respectively,[8] similar to the results reported by Olivares-Marín *et al.*, achieved following the same procedure as in the present work, which related the presence of LiO_2 , Li_2O_2 and Li_2CO_3 to features at 528.75, 531.25 and 533.8 eV.[6] Interestingly, our Na_2O_2 reference spectrum showed a feature at 531.2 eV that would be in good agreement to the mentioned peroxide characterization, based on the 1s $\rightarrow$ σ* (O-O) transition. This assignment could drive us to relate the feature at 529.15 eV to the 1s $\rightarrow$ π* (O-O) transition in NaO_2, implying the presence of NaO_2 impurities in the Na_2O_2 reference. In order to confirm the

presence of these impurities EPR measurements were carried out in the Na_2O_2 reference (Figure 6.2).
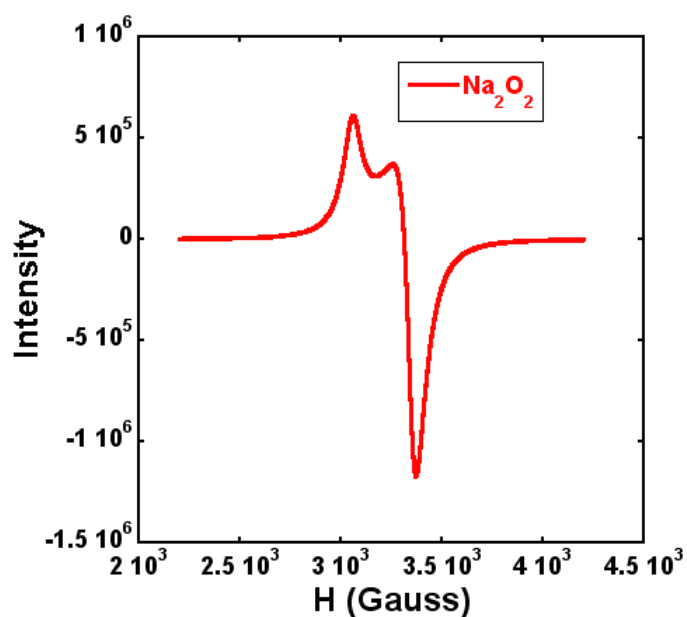
Figure 6.2. X-band (9.4 GHz) EPR spectra registered at 100 K on the Na_2O_2 reference.

Presence of NaO_2 in the Na_2O_2 reference was unequivocally demonstrated as the resultant spectrum was the same to the NaO_2 reference previously reported in Chapter 5. The feature at 529.15 eV can be therefore associated to the presence of NaO_2.

Finally, we can conclude from Figure 6.1 that it is not possible to distinguish between NaOH and Na_2CO_3 based on the O K-edge XANES spectra of the reference samples as they show signals for the same photon energies. Due to the impossibility to identify them in the samples presented in this work we will henceforth refer to both of them as side products (SP).

6.3. Discharge product characterization

6.3.1. Galvanostatic discharge

As described in previous chapters, during the discharge of the cell molecular oxygen is reduced in the oxygen electrode (oxygen reduction reaction, ORR) while sodium is oxidized in the sodium electrode:

Sodium electrode: $Na \rightarrow Na^+ + e^-$ [6.1]

Oxygen electrode: $O_2 + e^- \rightarrow O_2^-$ [6.2]

                     $O_2^- + Na^+ \rightarrow NaO_2\downarrow$ [6.3]
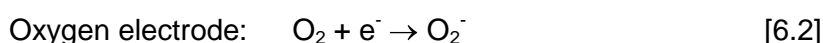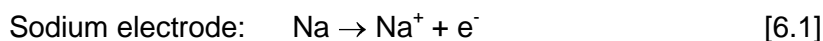
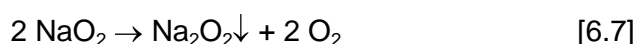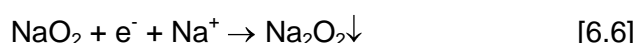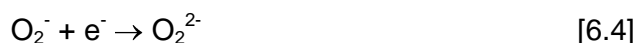The most widely reported ORR is the reduction of O_2 to superoxide radical (O_2^-) (equation 6.2) which coupled with the Na^+ formed in the sodium electrode (equation 6.1) is deposited in the oxygen electrode in a characteristic cubic shape (equation 6.3). The presence of NaO_2 as the ultimate discharge product involves the consumption of one electron per reduced oxygen molecule, as evidenced by several groups by means of an electrochemical cell coupled with a pressure sensor.[9,10] Nevertheless, other authors have reported the formation of Na_2O_2 in the oxygen electrode, that should be obtained by the reduction of the superoxide radical formed in eq.2 as described in equations 6.4 and 6.5, by the reduction of the previously formed sodium superoxide (equation 6.6), or by the disproportionation of NaO_2 (equation 6.7):

$O_2^- + e^- \rightarrow O_2^{2-}$ [6.4]

$O_2^{2-} + 2\ Na^+ \rightarrow Na_2O_2\downarrow$ [6.5]

$NaO_2 + e^- + Na^+ \rightarrow Na_2O_2\downarrow$ [6.6]

$2\ NaO_2 \rightarrow Na_2O_2\downarrow + 2\ O_2$ [6.7]

NaO_2 and Na_2O_2 exhibit similar standard reduction potentials (2.33 and 2.27 V vs. Na^+/Na for peroxide and superoxide, respectively)[11] and the reason for the accumulation of one or the other remain still unclear. Pinedo *et al.* provided *operando* X-ray diffraction (XRD) evidence of $Na_2O_2 \cdot 2H_2O$ formation in presence of constant oxygen flux containing moisture traces following equation 6.7.[10] In addition, Ortiz-Vitoriano *et al.* reported the accumulation of $Na_2O_2 \cdot 2H_2O$ after the exposure of NaO_2 to ambient air,[12] reinforcing the key role of moisture in the determination of the discharge product. Moreover, Kim *et al.* and Black *et al.* reported the instability of NaO_2 discharge product in the cell environment leading to the formation of $Na_2O_2 \cdot 2H_2O$ and $Na_2O_2 \cdot 8H_2O$,[13,14] respectively that in turn could not be observed by our group following similar procedures (Chapter 5).[15] It is worth mentioning that water in the electrolyte does not seem to affect to the superoxide/peroxide balance as in the Raman spectroscopy and XRD data provided by Ortiz-Vitoriano after the addition of 6000 ppm of water to the electrolyte NaO_2 was found the sole discharge product. In our experiments, however, both NaO_2 and Na_2O_2 were found in the oxygen electrode after a galvanostatic discharge by means of TXM (Figure 6.3).
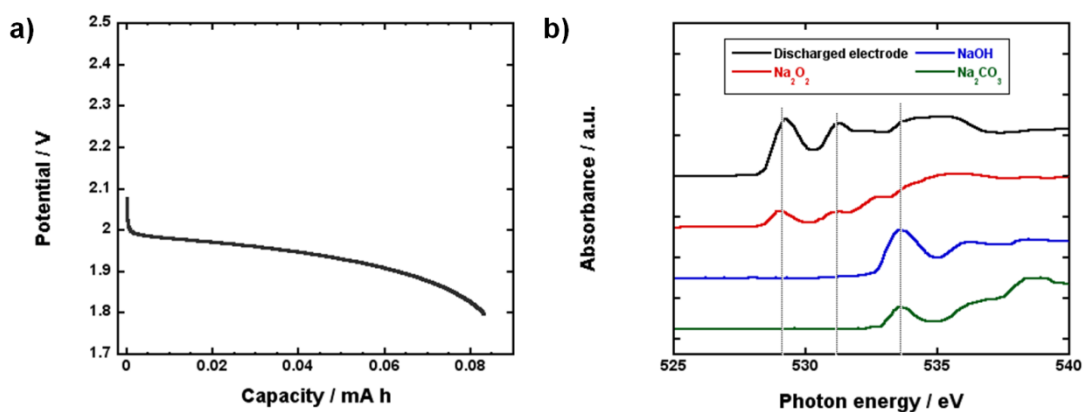

Figure 6.3. (a) Discharge profile of the Na-O_2 cell at 0.2 mA cm^{-2}. (b) O K-edge XANES spectra of the oxygen electrode after a galvanostatic discharge (black line) compared to the reference materials: Na_2O_2 (red line), NaOH (blue line) and Na_2CO_3 (green line).

The discharge capacity of the galvanostatic measurement (Figure 6.3.a) was low compared to those at Chapter 5 as the carbon paper used in the experiments performed in this chapter (Toray TGP-060) had a lower surface area than that in Chapter 5 (H2315, Freudenberg). In addition, the main part of the plateau was located between 2.0 and 1.9 V as a 2-electrode set up was used for the measurements. On the other hand, quantitative analysis of the XANES spectra (Figure 6.3.b) revealed a relative content in NaO_2, Na_2O_2 and SD in the oxygen electrode of 62, 29 and 9 %, respectively. Surprisingly, analyses of the cubes revealed the presence of peroxide in their structure, although cubic morphology was believed to be characteristic of superoxide,[1] in similar proportion to that observed in the bulk electrode. Several possibilities can be considered in order to explain the presence of Na_2O_2 in the oxygen electrode:

i. Leaks in the electrochemical cells in which the galvanostatic discharge was carried out.

ii. Excess of water in the electrolyte.

iii. Reduction of NaO_2 due to the exposure to the photon beam.

iv. Electrocatalysis by the Au TEM grid.

Effect of moisture in the oxygen added to the cell is excluded as the measurements were not carried out under continuous gas flux. In addition, possibilities (i), (ii) and (iii) will be analyzed in detail later, but we can reveal that are not responsible for the presence of Na_2O_2. Is Au, therefore, a 2 e$^-$ oxygen reduction electrocatalyst? Unfortunately, it is not possible for us to confirm such hypothesis, but it is a possibility that should be considered. DFT studies carried out by Krishnamurthy *et al.* suggest that NaO_2 nucleation is favored rather than Na_2O_2 nucleation in Au (111) and (110) although it is mentioned that an appropriate solvent/electrode couple could drive to the 2 e$^-$ reduction.[16] In addition, Aldous and Hardwick recently reported the formation of Na_2O_2 utilizing surface-enhanced Raman spectroscopy (SERS), in which a Au-based

oxygen electrode and DEGDME were used.[17] Moreover, Reinsberg *et al.*, in their novel work about calcium-oxygen (Ca-O_2) batteries, observed that after replacing the carbon electrode by an Au based one reduction reaction turned from a 1 e^-/O_2 process to a 2 e^-/O_2 process.[18] Albeit we do not have definitive evidence of this we cannot exclude the possibility of peroxide being formed in smaller fractions than superoxide in presence of both Au-based TEM grid and the carbon paper.

The spatial distribution of these products was also determined. Figure 6.4 shows the O K-edge absorption map of a specific region of the TEM grid. TXM image evidences that the discharge products were present in the typical cubic-shape. Absorbance gradients are present on apparently flat surfaces of the cube. This should be due to orientations that are not parallel to the substrate, as suggested by the 3D reconstruction below. .
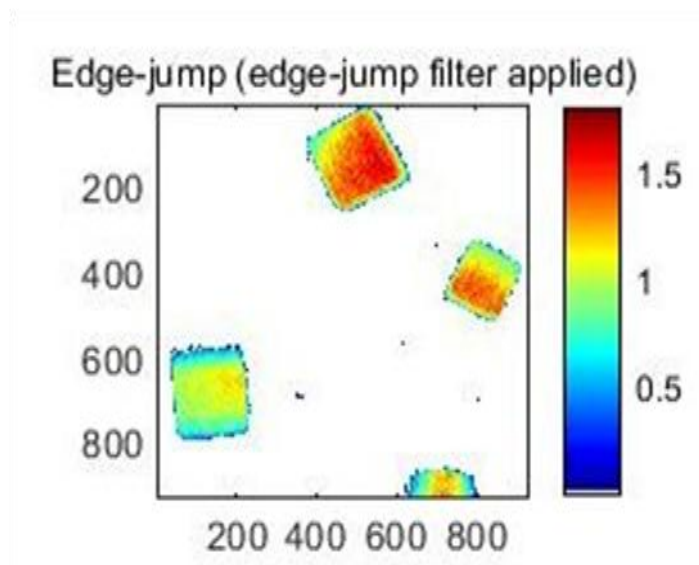
Figure 6.4. TXM images of the discharge products. Absorbance in the O K-edge region at each pixel of the image is specified by its color.

Figure 6.5.a shows the relative absorbance of NaO_2, Na_2O_2 and SPs in a cubic discharge deposit and the surrounding electrode surface. Both Na_2O_2 and NaO_2 have their maximum absorbance in the cube and their presence is almost limited to this discharge products deposit (particularly in the case of superoxide). SPs, however,

could be found more homogeneously distributed through the grid although the maximum absorbance values were obtained on the cube. In addition, although it could be expected a significant presence of SPs on the grid (outside the cube), analyses of the XZ and YZ planes (Figure 6.5.b) demonstrated that the total absorbance of these SPs was similar to that of peroxide and superoxide outside the cubes and, consequently, negligible.
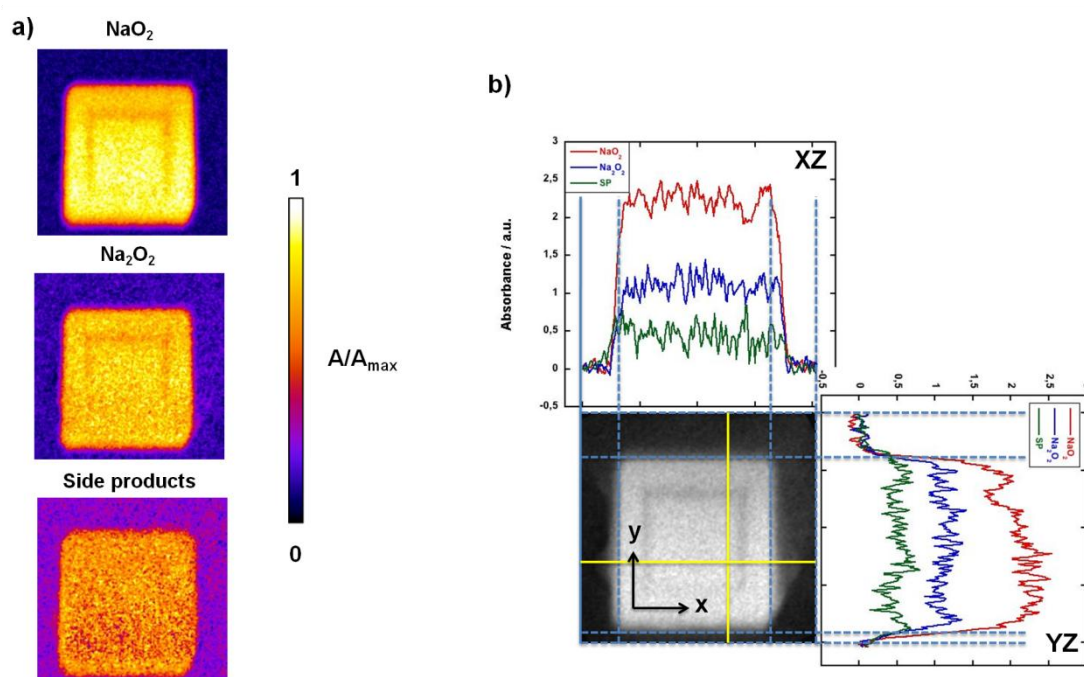
Figure 6.5. (a) TXM images of a cubic discharge product deposited. Relative absorbance at each pixel of the image at the established NaO_2, Na_2O_2 and side product photon energies is represented by its color. (b) Absorbance values at the NaO_2 (red), Na_2O_2 (blue) and side product (green) photon energies for the XZ and XY planes highlighted by the yellow lines in the TXM image.

Finally, the tomographic reconstruction of the cubes displayed in Figures 6.6.a and 6.6.b evidenced an outer layer of ~100 nm with higher density (1.6-1.8 times the density of the inner cube) and lower oxygen content, although superoxide was identified as the main product in this layer. The O-poor layer could not be detected in the cube face exposed to the electrode (Figures 6.6.c and 6.6.d) evidencing that this

surface layer was formed by the interaction of the electrolyte and the cube. The information provided by this reconstruction fits with the oxygen concentration decrease observed by EDX in Chapter 5 although this time the electrode was not let ageing inside the cell. It is therefore possible that this oxygen loose and passivation starts since the moment that the electrochemical measurement is stopped, although requires from an extraordinarily powerful characterization technique such as Synchrotron X-ray Transmission Microscopy in order to be detected.
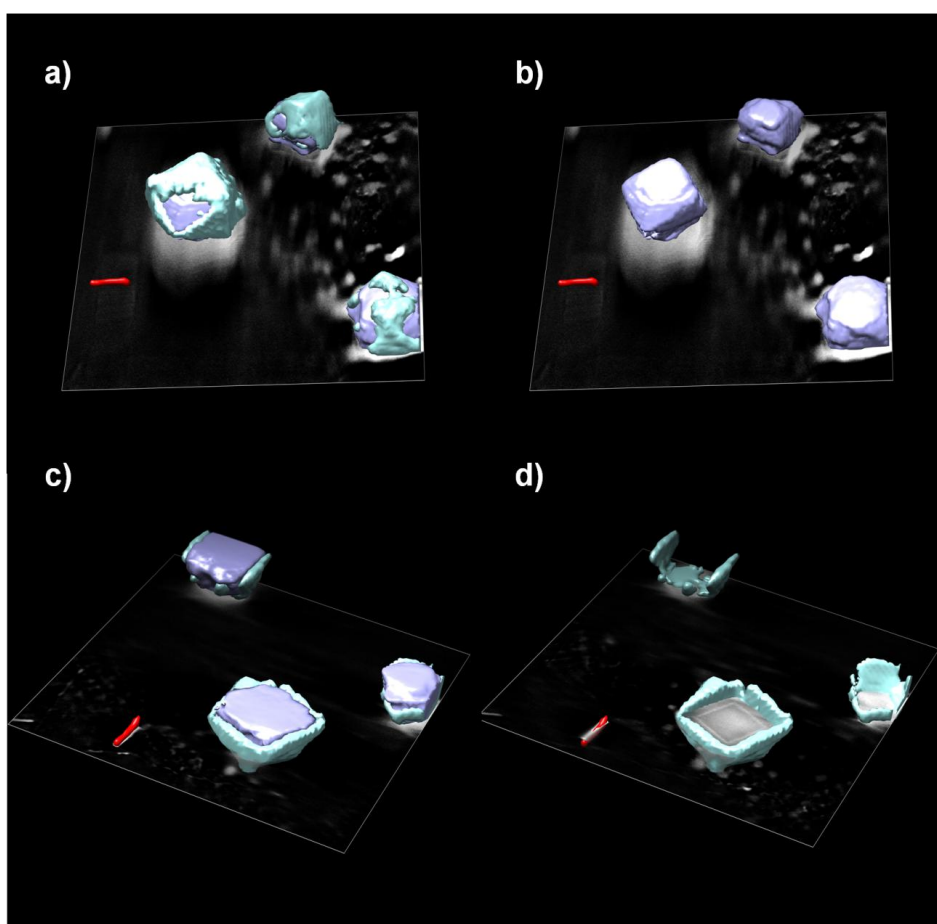

Figure 6.6. Three-dimensional reconstruction of some discharge particles. The particle nuclei and the covering O-deficient layer are colored in grey and green, respectively. Top view of these particles (a) including and (b) excluding the O-deficient layer. Down view of the discharge particles (c) including and (d) excluding the particle nuclei.

6.3.2. Effect of beam-exposition

As previously mentioned, the possibility of NaO_2 reduction to form Na_2O_2 due to beam exposure should be considered. In furtherance of checking this hypothesis the TEM grid analyzed in section 3.2 was re-analyzed after the first scan evidencing negligible variations in their composition (summarized in Table 6.1).

Table 6.1. Evolution of the relative contents in NaO_2, Na_2O_2 and side products in the Au grid and the cubes 1, 2 and 3 before and after being exposed to the beam.

	% NaO$_2$	% Na$_2$O$_2$	% SP
Discharged grid	61.95	29.32	8.73
Discharged grid, beam exposed	57.82	30.80	11.37
Cube 1	62.45	29.18	8.37
Cube 1, beam exposed	58.95	29.85	11.21
Cube 2	59.39	31.23	9.38
Cube 2, grid exposed	54.37	32.78	12.86
Cube 3	64.13	27.50	8.37
Cube 3, beam exposed	59.01	30.51	10.49

It can be observed a small decrease in the NaO_2 fraction in parallel to a minimal increase in the Na_2O_2 and SP. Although these variations can in part be attributed to instrumental deviations, it cannot be ruled out that a fraction of the peroxide and the SP could be formed by the exposition of superoxide to the photon beam. In any case, this

fraction is negligible and the Na_2O_2 fraction observed was significant after the first scan (~ 30%). Na_2O_2 formation, therefore, cannot be attributed to beam exposition.

6.3.3. Effect of water-exposition

Water in the electrolyte has been analyzed and discarded in literature as a possible explanation for peroxide formation in Na-O_2 cells.[12,19] In these works NaO_2 was found as the sole discharge product in the oxygen electrode after adding significant amounts of water to the electrolyte. In order to confirm their findings a Na-O_2 cell was discharged adding 7000 ppm of water in the electrolyte and the TEM grid in contact with the oxygen electrode was analyzed by TXM (Figure 6.7).
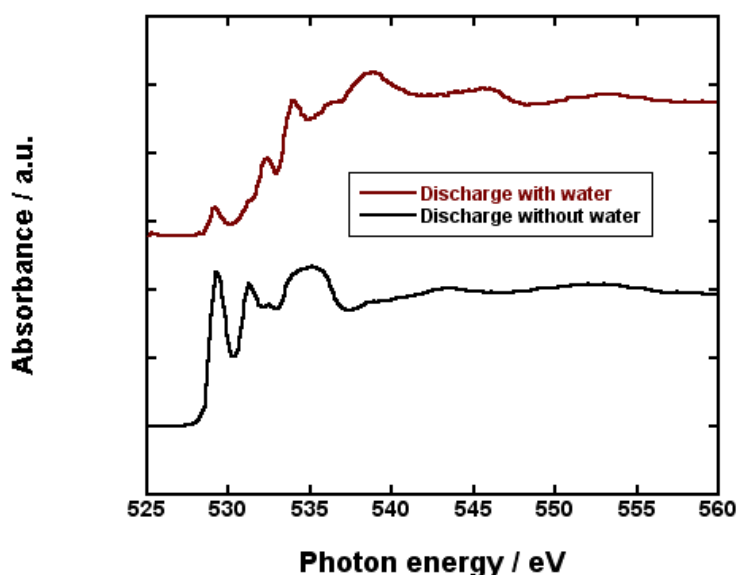
Figure 6.7. O K-edge XANES spectra of the oxygen electrode after a galvanostatic discharge with 7000 ppm of water in the electrolyte (maroon line) and without water (black line).

O k-edge XANES spectra of the TEM grid discharged in presence of 7000 ppm of water revealed the presence of both NaO_2 and Na_2O_2 together with SPs. The Na_2O_2 fraction in the grid was 20.22 %, slightly lower than that obtained in absence of water (29.32 %). In spite of the observed difference it can be concluded that (i) peroxide is formed in a similar fraction in presence and absence of water and (ii) a higher

concentration of water is not responsible for the formation of Na_2O_2, in good agreement to the works in literature.[12,19] Significant variations were, however, observed in the NaO_2 and the SP fraction; NaO_2 content was decreased to 27.30 % while SPs were increased to 52.48 %. In absence of CO_2 (and consequently discarding the formation of carbonates) and without an increase in the peroxide content the most probable reaction would be that reported by Pinedo *et al.*:[10]

$$2\ NaO_2 + 2\ H_2O \rightarrow 2\ NaOH\downarrow + H_2O_2 + O_2 \qquad [6.8]$$
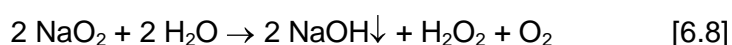
It is possible that the NaOH formed is not crystalline and therefore cannot be detected by XRD, the most commonly used technique for Na-O_2 discharge product characterization.[3] In addition, NaOH is detected at ~3500 cm^{-1} by Raman spectroscopy and discharge product characterization is usually focused in lower wavenumber windows in which peroxide (two peaks between 700 and 800 cm^{-1}), Na_2CO_3 (1080 cm^{-1}) and superoxide (1156 cm^{-1}) are detected.

In summary, the addition of significant amounts of water leads to the formation of NaOH by the reaction of this H_2O with the electrochemically generated NaO_2. Despite the high concentration of 7000 ppm of water the 27.30 % of the deposited material consisted of NaO_2. Finally, no peroxide was formed by after adding 7000 ppm of water to the electrolyte.

6.3.4. Effect of air-exposition

The conversion of galvanostatically generated superoxide into peroxide was reported by Ortiz-Vitoriano *et al.*;[12] in their work a discharged electrode was exposed to air for 3 hours and analyzed by Raman spectroscopy and XRD. Analysis of the air-exposed electrode revealed the formation of $Na_2O_2\cdot 2H_2O$. Consequently, air-contamination of our electrodes was considered as the reason for the presence of peroxide in our samples. Following their procedure, the TEM grid previously analyzed was exposed to air for 5 minutes and re-analyzed evidencing unexpected variations (Figure 6.8).
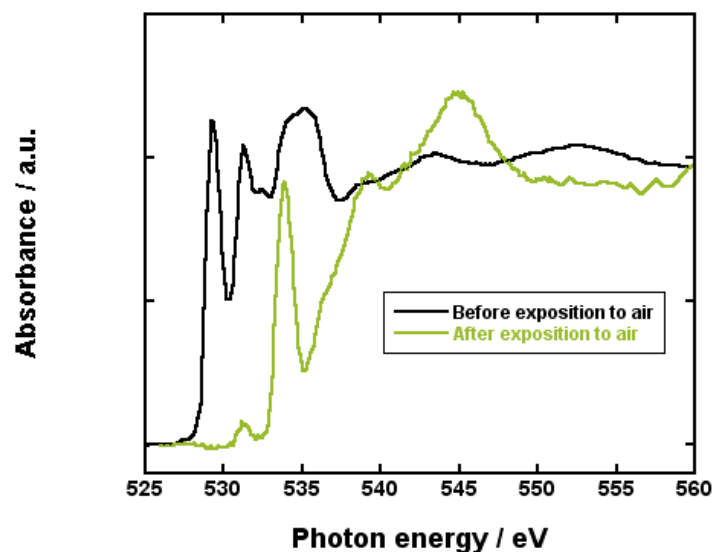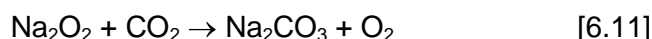
Figure 6.8. O K-edge XANES spectra of the oxygen electrode after a galvanostatic discharge before (black line) and after (green line) exposition of the TEM grid to ambient air for 5 minutes.

It is worth mentioning that opposite to Ortiz-Vitoriano *et al.*[12] no NaO_2 was detected (0.00%) after 5 minutes of exposition of the TEM grid to ambient air. In addition, Na_2O_2 concentration was also reduced to 9.44% and SPs were considerably increased to 90.56%. Reaction of NaO_2 to form Na_2O_2 (or $Na_2O_2 \cdot 2H_2O$) is therefore ruled out based on our experiments. On the other hand, analyses in section 6.3.3 reveal the formation of NaOH from NaO_2 in presence of water, which should also take place in presence of moisture. Carbon dioxide (CO_2) in ambient air must also be considered; Das *et al.* reported that in presence of CO_2 the discharge product formed is Na_2CO_3.[20] The reaction could occur as follows:

$$2 \ NaO_2 + CO_2 \rightarrow Na_2CO_3 + 3/2 \ O_2 \qquad [6.9]$$

$$Na_2O_2 + CO_2 \rightarrow Na_2CO_3 + 1/2 \ O_2 \qquad [6.10]$$

$$Na_2O_2 + CO_2 \rightarrow Na_2CO_3 + O_2 \qquad [6.11]$$
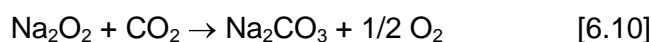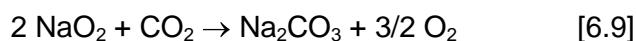
The formation of both Na_2CO_3 and NaOH would be in good agreement with the spectrum present in Figure 6.8. In order to give further evidence of the formation of SP

in presence of ambient air a cell with leaks was discharged and the TEM grid on the oxygen electrode was analyzed by means of TXM (Figure 6.9).
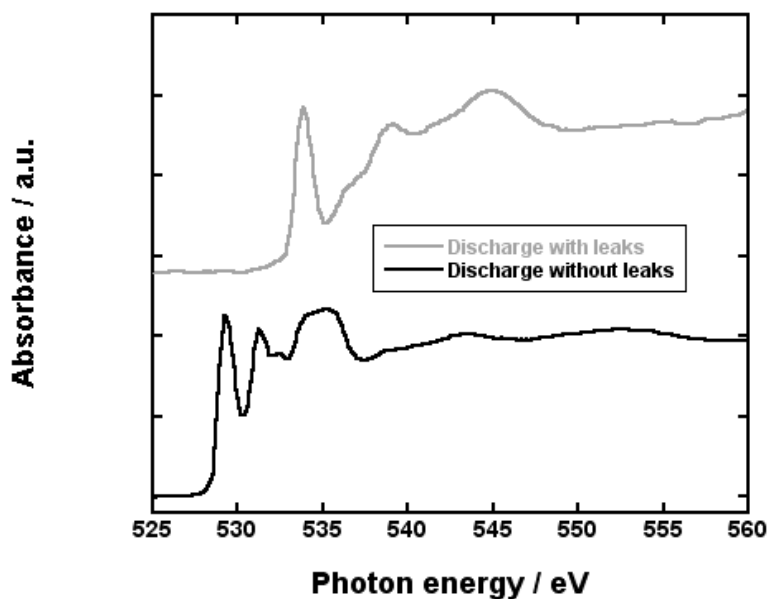
Figure 6.9. O K-edge XANES spectra of the oxygen electrode after a galvanostatic discharge in a cell with (grey line) and without (black line) leaks.

It is worth mentioning that no superoxide was detected in the TEM grid discharged in presence of leaks while peroxide content was similar to the previously registered after the unexposed grid was exposed to ambient air (7.06 % in the cells with leaks vs. 9.46 % in the electrode exposed for 5 minutes). On the other hand, and in good agreement with Das *et al.*,[20] the fraction of SPs unequivocally increased.

To sum up, exposure of the ORR products to ambient air and discharge in presence of ambient air (in presence of moisture and CO_2) leads to the formation of NaOH and/or Na_2CO_3, which could compromise the performance of these batteries. In addition, opposite to other works, no evidence of peroxide concentration increase was observed when the discharge products were exposed to ambient air.[12]

6.3.5. Charge reaction

It is generally accepted that oxidation of NaO_2 during the charge of $Na\text{-}O_2$ cells can be carried out at low potential of ~ 2.5 V.[1,10,12,21,22] Nevertheless, there is not such agreement on the potential at which oxidation of peroxide occurs; on the one hand, most of the research groups reporting peroxide as the discharge product suffer from high overpotential during the charge of the cell.[2,3] On the other hand, Pinedo *et al*. demonstrated by means of *in situ* XRD that $Na_2O_2 \cdot 2H_2O$ could be oxidized at the same overpotential as NaO_2 although it could lead to the formation of NaOH, which requires from higher overpotential to be removed.[10] We carried out two different experiments in order to analyze the removal of superoxide and peroxide below 3.0 V. In the first one the cell was charged to the 17% of the capacity of the previous discharge in furtherance of analyzing the oxidation of both peroxide and superoxide at the early stage of the charge. Second experiment consisted in 5 complete galvanostatic cycles limiting charge potential to 3.0 V to determine the accumulation of NaO_2 and Na_2O_2 upon cycling. Spectra obtained are shown in Figure 6.10 and summarized in Table 6.2.
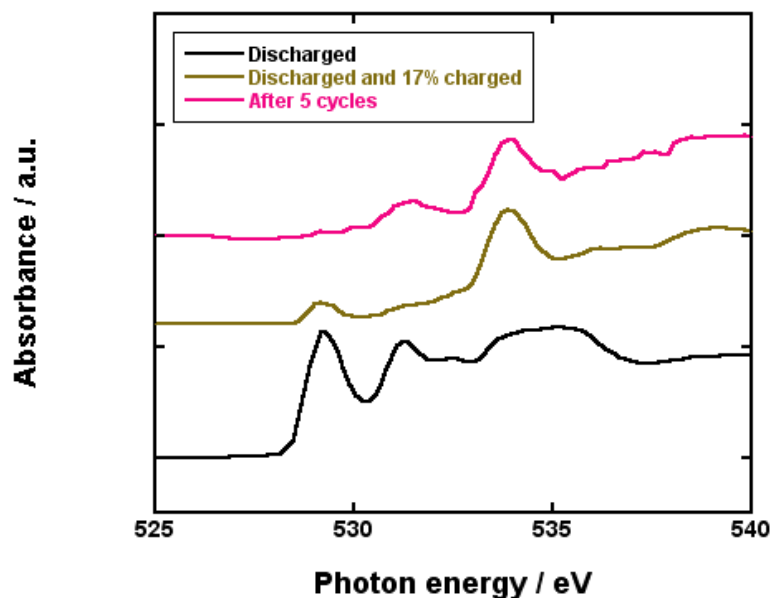
Figure 6.10. O K-edge XANES spectra of the oxygen electrode after a galvanostatic discharge (black line) in the early stages of the charge (gold-colored line) and after 5 galvanostatic cycles (pink line).

Table 6.2. NaO_2, Na_2O_2 and SP fractions quantified in the TEM grids after discharge, after a discharge followed by the 17% of the charge and after 5 complete galvanostatic cycles.

	After discharge	Discharge-17% charge	After 5 cycles
% NaO_2	61.95	23.84	5.33
% Na_2O_2	29.32	11.74	30.17
% SP	8.73	64.42	64.50

Both NaO_2 and Na_2O_2 fractions were decreased by 3 after 17 % of the charge confirming the reversal of peroxide at low overpotential together with superoxide. The increase in the SP percentage could be attributed to two main reasons: (i) after the removals of ORR products the only detectable species are SPs and (ii) NaOH could be alternatively formed as proposed by Pinedo *et al*. in the removal of $Na_2O_2 \cdot H_2O$.[10] Analyses after 5 cycles revealed insignificant accumulation of NaO_2 (5.33%) in the oxygen electrode proving the efficient OER of this discharge product at potentials lower

than 3.0 V. On the other hand, 30 % of peroxide could be detected in the electrode after these cycles, similar to that observed after the first discharge. Even though analysis after 17% of the charge reveals that peroxide can be reverted at low overpotentials it can be deduced that its removal is not as effective as in the case of superoxide.

6.4. Conclusions

In this chapter the composition of the discharge products generated under different experimental conditions has been analyzed by means of TXM. Unexpectedly, it was determined that the typical superoxide cubes were in this case composed of both NaO_2 and Na_2O_2. Water in the electrolyte and leak were demonstrated not to be responsible for the formation of peroxide and 2 e^-/O_2 catalysis performed by the Au TEM grids used for the TXM analysis are the most likely option in order to explain the formation of Na_2O_2. In addition, an oxygen deficient layer covering the discharge particles was detected in good agreement to the gas pressure increase observed under resting conditions after discharge in Chapter 5, reinforcing the argument of the instability of discharge products in the NaOTf-DEGDME electrolyte. Finally, measurement after several cycles reveal that superoxide is more efficiently reversed than peroxide, being this last one slowly accumulated in the electrode with the galvanostatic cycles. .

6.5. References

(1)   Landa-Medrano, I.; Li, C.; Ortiz-Vitoriano, N.; Ruiz de Larramendi, I.; Carrasco, J.; Rojo, T. *J. Phys. Chem. Lett.* **2016**, *7*, 1161–1166.

(2)   Yadegari, H.; Sun, Q.; Sun, X. *Adv. Mater.* **2016**, *28* (33), 7065–7093.

(3)   Bender, C. L.; Schröder, D.; Pinedo, R.; Adelhelm, P.; Janek, J. *Angew. Chemie (International Ed.* **2016**, *55*, 2–12.

(4)   Pereiro, E.; Nicolas, J.; Ferrer, S.; Howells, M. *J. Synchrotron Radiat.* **2009**, *16*,

505–512.

(5)   Sorrentino, A.; Nicolás, J.; Valcárcel, R.; Chichón, F. J.; Rosanes, M.; Avila, J.; Tkachuk, A.; Irwin, J.; Ferrer, S.; Pereiro, E. *J. Synchrotron Radiat.* **2015**, *22*, 1112–1117.

(6)   Olivares-Marín, M.; Sorrentino, A.; Lee, R.-C.; Pereiro, E.; Wu, N.-L.; Tonti, D. *Nano Lett.* **2015**, *15* (10), 6932–6938.

(7)   Yadegari, H.; Banis, M. N.; Xiao, B.; Sun, Q.; Li, X.; Lushington, A.; Wang, B.; Li, R.; Sham, T.-K.; Cui, X.; Sun, X. *Chem. Mater.* **2015**, *27* (8), 3040–3047.

(8)   Gallant, B. M.; Kwabi, D. G.; Mitchell, R. R.; Zhou, J.; Thompson, C. V; Shao-Horn, Y. *Energy Environ. Sci.* **2013**, *6* (8), 2518–2528.

(9)   McCloskey, B. D.; Garcia, J. M.; Luntz, A. C. *J. Phys. Chem. Lett.* **2014**, *5*, 1230–1235.

(10)   Pinedo, R.; Weber, D. A.; Bergner, B. J.; Schröder, D.; Adelhelm, P.; Janek, J. *J. Phys. Chem. C* **2016**, *120* (16), 8472–8481.

(11)   Adelhelm, P.; Hartmann, P.; Bender, C. L.; Busche, M.; Eufinger, C.; Janek, J. *Beilstein J. Nanotechnol.* **2015**, *6*, 1016–1055.

(12)   Ortiz-Vitoriano, N.; Batcho, T. P.; Kwabi, D. G.; Han, B.; Pour, N.; Yao, K. P. C.; Thompson, C. V.; Shao-Horn, Y. *J. Phys. Chem. Lett.* **2015**, *6*, 2636–2643.

(13)   Black, R.; Shyamsunder, A.; Adeli, P.; Kundu, D.; Murphy, G. K.; Nazar, L. F. *ChemSusChem* **2016**, *9*, 1–10.

(14)   Kim, J.; Park, H.; Lee, B.; Seong, W. M.; Lim, H.; Bae, Y.; Kim, H.; Kim, W. K.; Ryu, K. H.; Kang, K. *Nat. Commun.* **2016**, *7*, 1–9.

(15)   Landa-Medrano, I.; Pinedo, R.; Bi, X.; Ruiz de Larramendi, I.; Lezama, L.; Janek,

J.; Amine, K.; Lu, J.; Rojo, T. *ACS Appl. Mater. Interfaces* **2016**, *8* (31), 20120–20127.

(16)   Krishnamurthy, D.; Hansen, H. A.; Viswanathan, V. *ACS Energy Lett.* **2016**, *1* (1), 162–168.

(17)   Aldous, I. M.; Hardwick, L. J. *Angew. Chemie* **2016**, *128* (29), 8394–8397.

(18)   Reinsberg, P.; Bondue, C. J.; Baltruschat, H. *J. Phys. Chem. C* **2016**, *120* (39), 22179–22185.

(19)   Xia, C.; Black, R.; Fernandes, R.; Adams, B.; Nazar, L. F. *Nat. Chem.* **2015**, *7*, 496–501.

(20)   Das, S. K.; Xu, S.; Archer, L. a. *Electrochem. commun.* **2013**, *27*, 59–62.

(21)   Hartmann, P.; Bender, C. L.; Vračar, M.; Dürr, A. K.; Garsuch, A.; Janek, J.; Adelhelm, P. *Nat. Mater.* **2013**, *12* (3), 228–232.

(22)   Hartmann, P.; Heinemann, M.; Bender, C. L.; Graf, K.; Baumann, R.-P.; Adelhelm, P.; Heiliger, C.; Janek, J. *J. Phys. Chem. C* **2015**, *119* (40), 22778–22786.

Chapter 7 – Discharging a Na-O$_2$ cell using a redox mediator

In this chapter ethyl viologen ditriflate (EtV(OTf)$_2$) is analyzed as a discharge redox mediator (RM) in Na-O$_2$ cells. In a first step chemical oxidation and reduction of the EtV^{2+}/EtV$^+$ couple is explored. After that EtV^{2+} mediator is electrochemically tested in a Na-O$_2$ cell.

7.1. Introduction

As commented in previous chapters, RMs have been widely analyzed in order to improve the performance of Li-O$_2$ batteries. In most of the cases the target of such attempts has been charge reaction;[1,2] high overpotential and low coulombic efficiency of the re-charge of these batteries have lead to the use of species that dissolved in the electrolyte can be electrochemically oxidized at lower potentials than Li$_2$O$_2$ in the surface of the electrode, migrate to these peroxide deposits and chemically oxidize them.[3] The research group headed by Prof. Owen and Dr. García-Araez, however, has focused their research in the use of EtV^{2+}/EtV$^+$ redox couple as discharge RM in furtherance of obtaining the following benefits:[4,5]

i.   Facilitate the solution-mediated ORR and prevent from the accumulation of discharge products in electrochemically active sites of the oxygen electrode.[4]

ii. Promote the complete reduction of dioxygen (O$_2$) to peroxide (O$_2^{2-}$) in order to prevent the formation of the incomplete reduction product superoxide (O$_2^-$), which can react with the carbon electrode and/or the electrolyte.[5]

The use of charge RMs was introduced to Na-O$_2$ cells by Jin *et al.*.[6] They used iodide (I$^-$) to reproduce the promising coulombic efficiency improvement usually reported for Li-O$_2$ batteries. In a later work Yin *et al.* successfully replaced I$^-$ by ferrocene in furtherance of avoiding iodine volatilization, which decreases the I$_3^-$/I$^-$ redox couple

concentration in the electrolyte hindering the capability to mediate in the OER as cycling of the cell goes ahead.[7]

As far as we know, however, discharge redox shuttles have not been studied in Na-O_2 cells. In this chapter the use of EtV(OTf)$_2$ as soluble redox mediator in these batteries is explored in order to improve the discharge performance of these batteries. Apart from the already mentioned battery application[4,5] the methyled form of the molecule is used in biological membranes as a mediator in oxygen reduction leading to the ultimate formation of superoxide.[8] For that aim ethyl viologen presents three reversible oxidation states (EtV^{2+}/EtV^{+}/EtV^{0}) that are resumed in Figure 7.1.a.[9] The presence of double bonds and aromatic rings in its structure allows ethyl viologen to absorb at different wavelengths of the visible range depending on the oxidation state and this property will be used to analyze the reactions in section 7.2.[9,10] On the other hand, the bases of the EtV^{2+} mediated ORR are summarized in Figure 7.1.b.

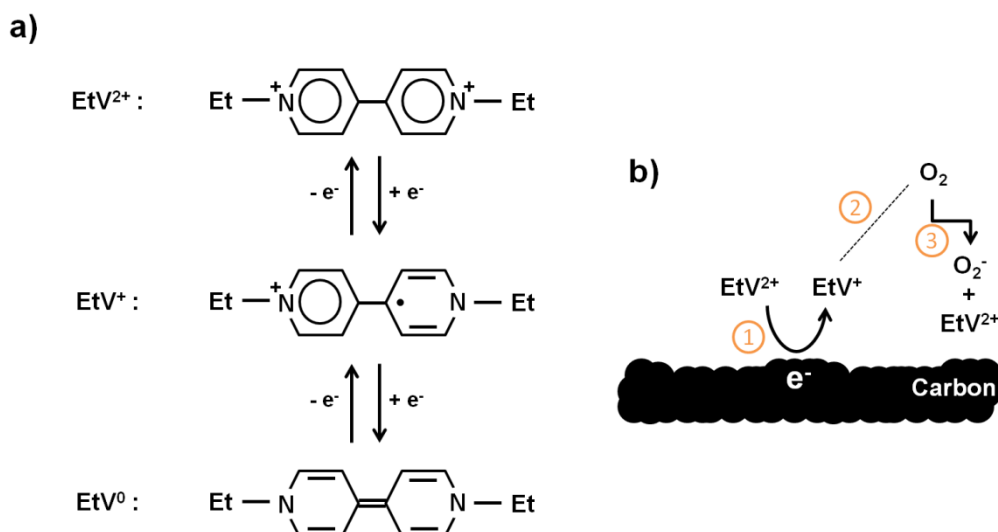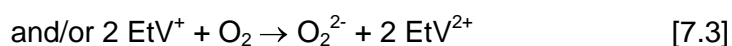**Figure 7.1.** (a) Representation of ethyl viologen at its three oxidation states.[9] (b) Schematic representation of the EtV^{2+}/ EtV^{+} redox couple mediated ORR. Numbers inside the orange circles highlight the three main steps in the process: (1) EtV^{2+} electrochemical reduction to EtV^{+}, (2) EtV^{+} migration and (3) chemical reduction of O_2 with EtV^{+} to obtain O_2^{-} and EtV^{2+}.[4]

For a successful RM mediated ORR EtV^{2+} should be reduced to EtV^+ at a potential higher than O_2 reduction. Electrochemically generated EtV^+ would reduce O_2 dissolved in the electrolyte going back to the initial 2+ oxidation state:

$$EtV^{2+} + e^- \rightarrow EtV^+ \qquad\qquad [7.1]$$

$$EtV^+ + O_2 \rightarrow O_2^- + EtV^{2+} \qquad\qquad [7.2]$$

$$\text{and/or } 2\,EtV^+ + O_2 \rightarrow O_2^{2-} + 2\,EtV^{2+} \qquad\qquad [7.3]$$

Reduced oxygen species should be stabilized in the electrolyte until saturation and precipitation in the electrode as described in Chapter 5. The main benefit of the use of EtV^{2+} would be the more effective ORR as O_2 molecules far from the oxygen electrode could be reduced due to the migration of the EtV^+ molecules.

The experiments in this chapter will be divided into two sections: in the first section we will focus our interest in the demonstration of the capability of the EtV^{2+}/EtV^+ redox pair to be chemically reduced, oxidized and re-reduced. In the second section this redox pair will be electrochemically tested in Na-O_2 cells.

7.2. EtV^{2+}/EtV^+ redox reactions evidence

Yang *et al*. demonstrated that the presence of EtV^{2+} and EtV^+ in a solution can be quantified using UV-vis spectroscopy;[5] EtV^{2+} absorbs radiation at 260 nm while the formation of EtV^+ leads to the appearance of absorption bands at 396 and 605 nm.[9,10] The experiment was based on the quantification of EtV^{2+} and EtV^+ in an electrolyte solution by the addition of reduction and oxidation agents, lithium titanate oxide (LTO, $Li_{6.8}Ti_5O_{12}$) and dioxygen gas (O_2), respectively. We prepared a 1 mM $EtV(OTf)_2$ and 10 mM NaOTf acetonitrile solution in furtherance of reproducing the experiments carried out by Yang *et al.*. As they demonstrated the chemical reduction process is quite slow; consequently, we added 1.8 times the stoichiometric amount of LTO to accelerate the process and let it stirring for two days allowing the following redox reaction:[5]
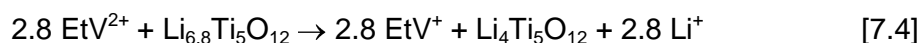
$$2.8 \text{ EtV}^{2+} + \text{Li}_{6.8}\text{Ti}_5\text{O}_{12} \rightarrow 2.8 \text{ EtV}^+ + \text{Li}_4\text{Ti}_5\text{O}_{12} + 2.8 \text{ Li}^+ \qquad [7.4]$$

Figure 7.2 shows the absorption spectra of the initial EtV^{2+} 1 mM solution and that obtained after the reaction with LTO, both diluted by 1/24. Before the addition we had a sole peak around 260 nm that corresponded to EtV^{2+}; the lack of absorbance at 396 and 605 nm confirmed the absence of EtV$^+$ impurities in the sample. In addition, extinction coefficient for EtV^{2+} was calculated using the Lambert-Beer law and was 2.5·10^4 M^{-1} cm^{-1}, similar to the reported in literature.[9,10]
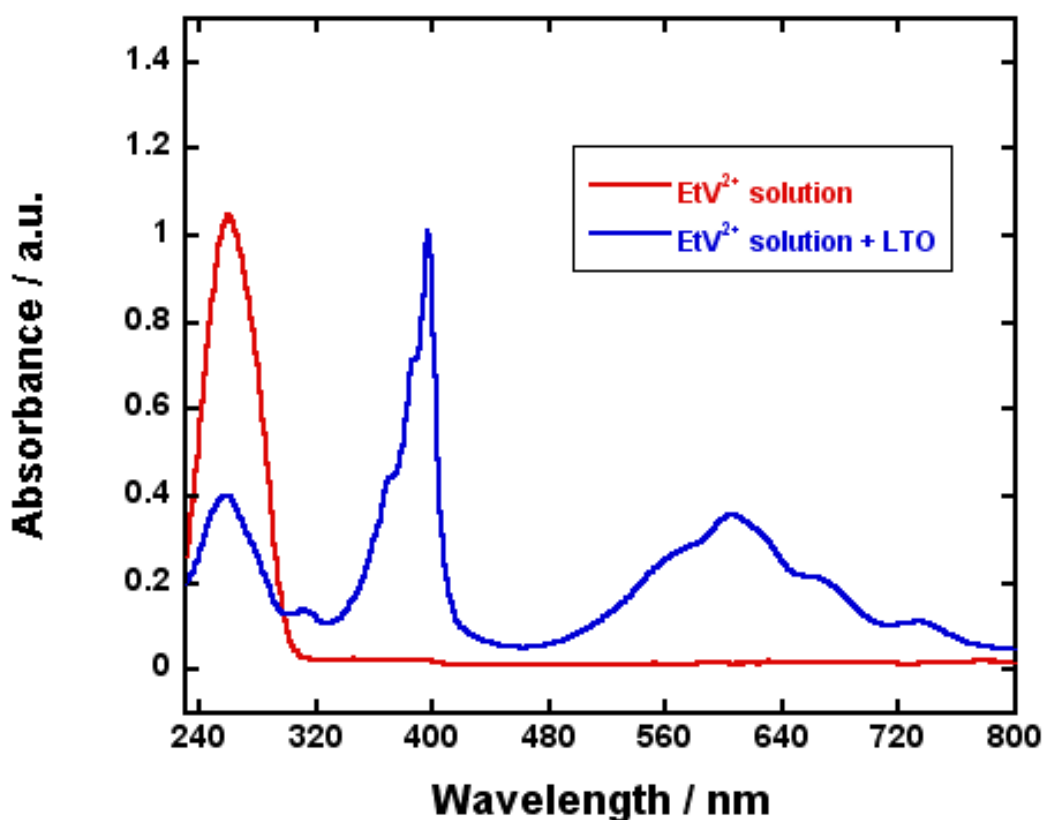
Figure 7.2. Absorption spectra of the 1 mM EtV^{2+} and 10 mM NaOTf in acetonitrile solution before (red line) and after (blue line) the addition of 1.8 times the stoichiometric amount of Li$_{6.8}$Ti$_5$O$_{12}$.

Although not a complete elimination of the signal corresponding to EtV^{2+}, the addition of L-LTO caused a decrease of the peak at 260 nm and the appearance of two absorption bands at 396 and 605 nm, in good agreement with Yang's work.[5] Using the

experimental extinction coefficient value previously obtained it was calculated that EtV^{2+} concentration decreased from 1 mM to 0.38 mM; we could therefore estimate that EtV$^+$ concentration after LTO addition was 0.62 mM. Based on that estimation we calculated the extinction coefficient of EtV$^+$ at 396 nm ($3.9 \cdot 10^4$ M^{-1} cm^{-1}) and 605 nm ($1.4 \cdot 10^4$ M^{-1} cm^{-1}), also in good agreement with literature.[9,10] The causes of the low efficiency in the EtV^{2+} reduction remain unclear, but Yang *et al.* observed that reaction time is a key factor in the reduction;[5] it is possible that allowing the reaction for longer would be traduced in a improved efficiency. In addition, it is also possible that LTO was not such reduced and the number of lithium atoms per molecule could be something between 6.8 and 4. Whatever the reason was, the reduction of a significant amount of EtV^{2+} was successfully carried out and quantified.

Reversion of EtV$^+$ to EtV^{2+} was performed by adding O$_2$ to the solution, based on reactions 7.2 and 7.3. O$_2$ was added to the solution in 1:1 proportion to the EtV$^+$ previously generated and the absorption spectrum was recorded (Figure 7.3).
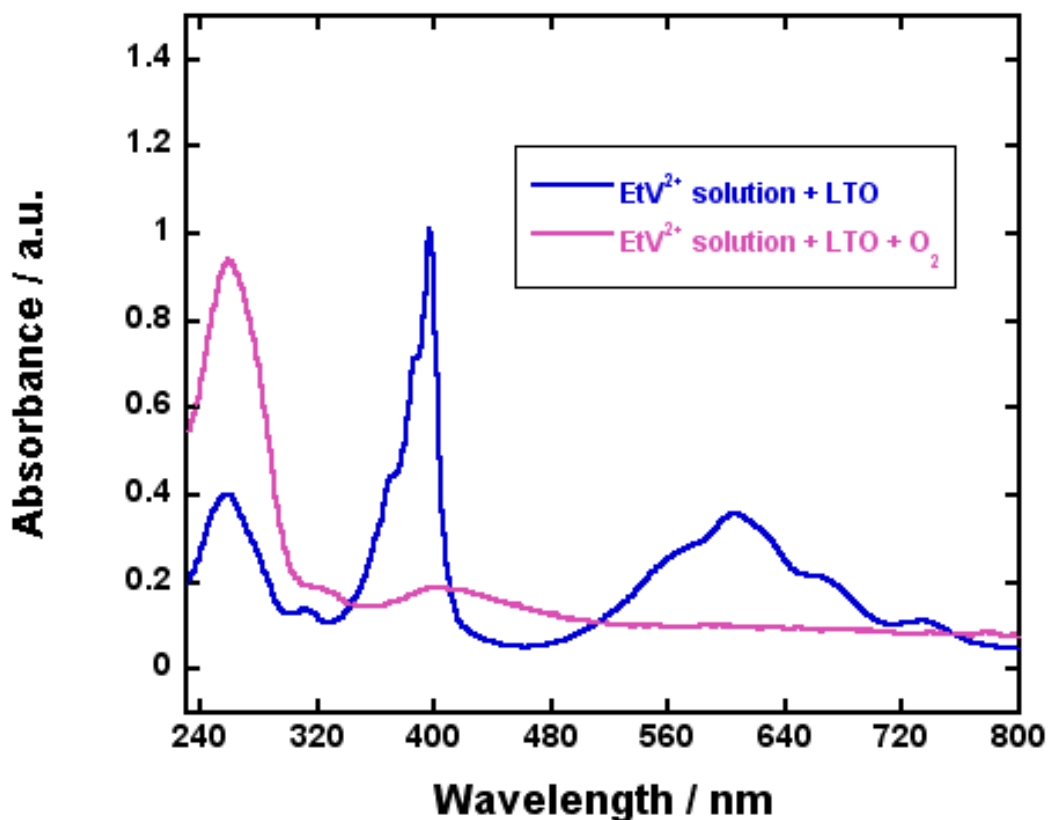
Figure 7.3. Absorption spectra of the 0.68 mM EtV$^+$, 0.38 mM EtV^{2+} and 10 mM NaOTf in acetonitrile solution before (blue line) and after (pink line) the addition of O$_2$.

The oxidation of EtV^{2+} by the addition of O$_2$ was demonstrated as the absorption bands at 396 and 605 nm were almost disappeared. Concurrently, absorption band at 260 nm increased again; based on the extinction coefficient previously calculated it was determined that the concentration of EtV^{2+} rose to 0.9 mM. Once again, we could not achieve 100 % efficiency. On the other hand, the EtV$^+$ analyses band revealed a concentration of 0.11 and 0.16 mM based on the absorptions registered at 396 and 605 nm, respectively. These results almost discard the presence of side reactions involving the use of EtV^{2+}/EtV$^+$ redox couple, as all the EtV^{2+} initially added (1 mM) remain as EtV^{2+} and/or EtV$^+$. It is also noticeable that a background increase was observed after O$_2$ addition. This could be attributed to the presence of particles remaining suspended in the solution, although this solution was filtered prior to the absorbance analysis. The origin of such particles could be the formation of NaO$_2$ after the reduction of O$_2$.

In their work, Yang *et al.* observed that by adding oxygen in a 1:2 proportion to the previously generated EtV$^+$, they had a 100 % conversion, revealing that it was a 2 electron reduction process and dismissing the formation of lithium superoxide in presence of EtV(OTf)$_2$.[5] In our experiment 75 % of the EtV$^+$ was re-oxidized after adding oxygen in 1:1 proportion, leading to a 0.75 e$^-$/O$_2$ reduction. Nevertheless, that reaction ratio is not likely; it is known that water traces can influence oxygen solubility and the O$_2$ saturated solution we used could therefore have slightly different O$_2$ concentration than that estimated.[11,12] The results obtained, however, suggest that ORR in presence of EtV$^+$ is a 1 e$^-$ reduction reaction as it was carried out in the same conditions as in previous works[5] and the value obtained is far from the 2 electron reduction.

In the last part of the experiment EtV^{2+} was reduced back to EtV$^+$ by the addition of 1.8 times the stoichiometric amount of LTO (Figure 7.4). EtV^{2+} band decreased and the quantification revealed that concentration was diminished from 0.9 mM to 0.51 mM. In addition, EtV$^+$ concentration quantification revealed a concentration of 0.44 and 0.49 mM based on the bands at 396 and 605 nm, respectively.
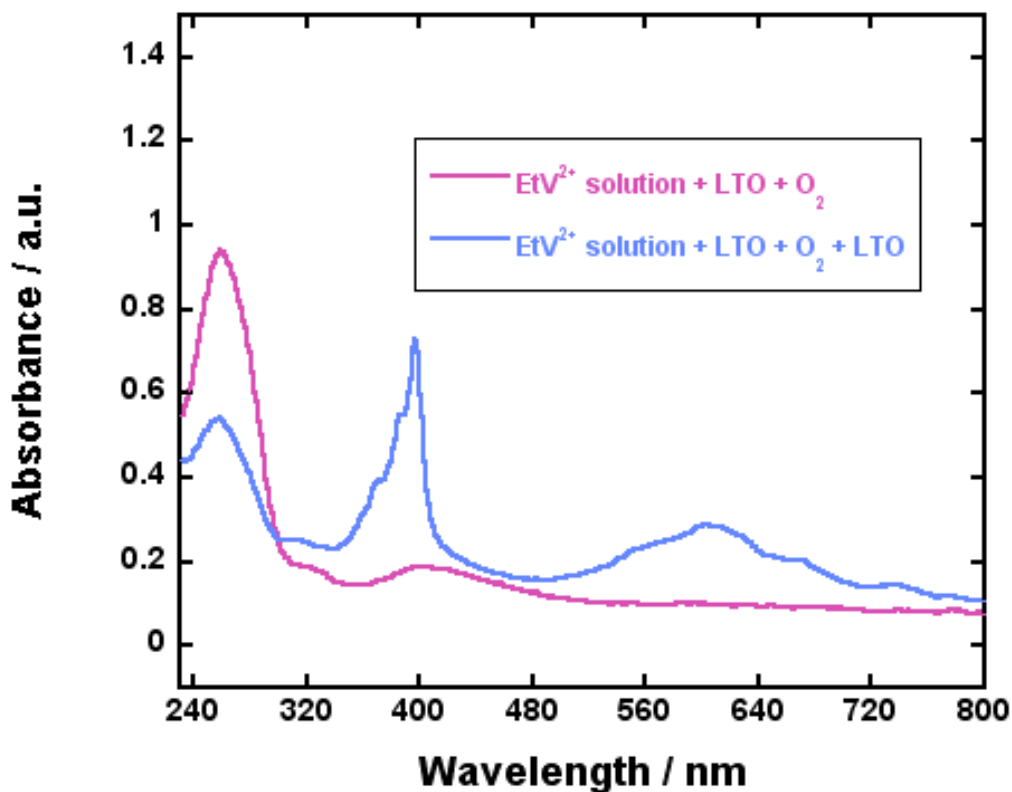
Figure 7.4. Absorption spectra of the 0.9 mM EtV^{2+}, 0.11/0.16 mM EtV^{+} and 10 mM NaOTf in acetonitrile solution before (pink line) and after (blue line) the addition of 1.8 times the stoichiometric amount of Li$_{6.8}$Ti$_{5}$O$_{12}$.

In summary, EtV^{2+}/EtV^{+} redox pair has been demonstrated to be reversible and stable in the electrolyte and, consequently, in the following section will be analyzed as a RM in a Na-O$_2$ cell.

7.3. EtV^{2+}/EtV^{+} redox pair mediated Na-O$_2$ cell

After the proof of concept in section 7.2, EtV^{2+} was added into a U-cell with a glassy carbon working electrode in order to analyze its mediation capacity in a Na-O$_2$ cell. A cell with 1 mM EtV(OTf)$_2$ and 0.5 M NaOTf in diethylene glycol dimethyl ether (DEGDME) electrolyte was analyzed by cyclic voltammetry (CV) under Ar and O$_2$ atmosphere and compared to a RM-free electrolyte cell under O$_2$ atmosphere (Figure 7.5).
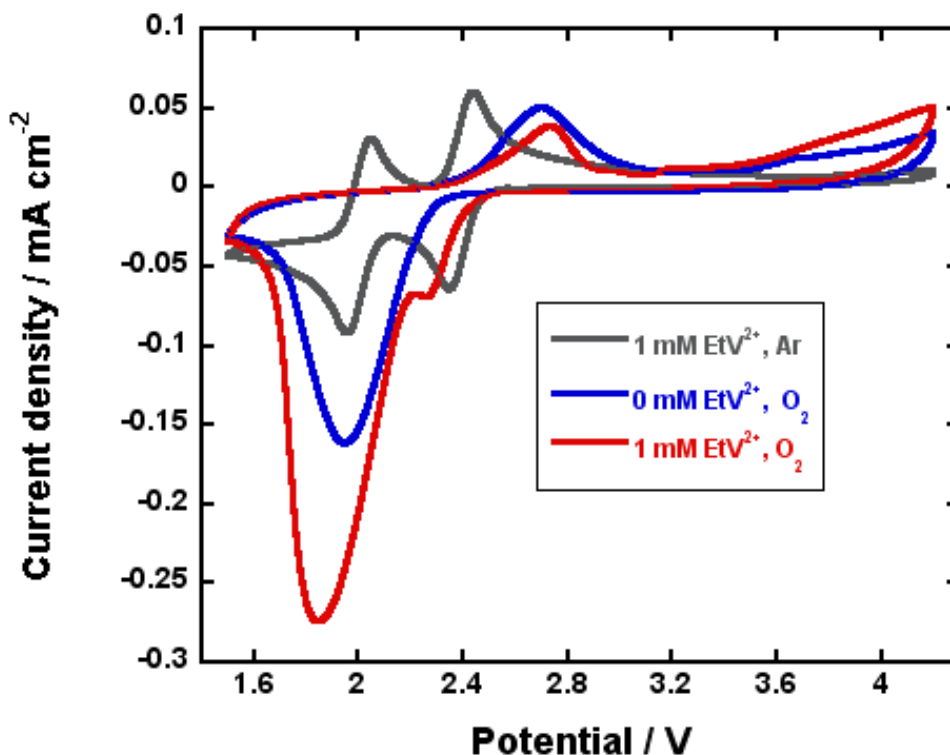
Figure 7.5. Cyclic voltammetries carried out in the Na-O_2 U-cell using a glassy carbon working electrode at 10 mV s^{-1} between 1.5 and 4.2 V. Grey and red line were obtained in presence of 1 mM EtV^{2+} under Ar and O_2 atmosphere, respectively. Blue line was obtained in absence of EtV^{2+} under O_2 atmosphere.

CV of the EtV^{2+} containing cell under Ar atmosphere at 10 mV s^{-1} revealed the presence of two reduction peaks in the cathodic scan. First peak at 2.35 V was attributed to the EtV^{2+}/EtV$^+$ reduction, while the second peak at 1.9 V was assigned to the EtV$^+$/EtV^0 reduction. Both processes were reversed in the anodic scan.

After replacing Ar by O_2 in the electrochemical test an IR drop of 0.05 V was observed in the first EtV^{2+} reduction peak, while the EtV$^+$ reduction peak almost disappeared due to the presence of the O_2 reduction peak. Comparison of the RM containing cell to the RM-less cell reveals an extraordinary enhanced rate capability by the addition of EtV^{2+}, possibly due to an enhanced solution-mediated ORR.[4] This enhanced ORR rate capability, however, was not traduced in an enhanced OER rate capability in the anodic

scan. EtV^0/EtV^+ and EtV^+/EtV^{2+} signals also disappeared; this means that the EtV^{2+} reduction products were chemically oxidized back to EtV^{2+}. The reason for that similarity in the OER currents remains unclear, but could be related to the migration of the electrochemically generated EtV^+, that could oxidize O_2 molecules far from the oxygen electrode and were not able to reach to the oxygen electrode in the cathodic scan or nucleate in different locations of the cell. Whatever the reason this behavior was also observed in Prof. Owen's works with EtV^{2+} in $Li-O_2$ in which a U-cell and a glassy carbon working electrode were used.[4,5]

In order to demonstrate the fast oxidation of the electrochemically generated EtV^+ in presence of oxygen chronoamperometry experiments were carried out in presence and absence of O_2. The first pulse was carried out at a potential at which EtV^{2+} was reduced to EtV^+ but O_2 is not reduced to O_2^-, based on the CV curve (2.4 V, see Figure 7.5). After that, a second pulse was applied at a potential in which EtV^+ is oxidized to EtV^{2+}, but O_2^- is not oxidized to O_2 (2.45 V). The charge obtained at 2.45 V can therefore only be attributed to the oxidation of EtV^+ to EtV^{2+}. Comparing the experiment under Ar and O_2 atmospheres, charge at 2.45 V should be lower under O_2 atmosphere as a fraction of the EtV^+ chemically reacts with dioxygen to form EtV^{2+} and O_2^- and consequently less EtV^+ can be reduced at 2.45 V. Experimental chronoamperometry results for 2, 5 and 10 second pulses under Ar and O_2 atmospheres are shown in Figures 7.6.a and 7.6.b, respectively. In addition, coulombic efficiencies obtained for the experiment under Ar and O_2 atmospheres are shown in Figure 7.6.c.

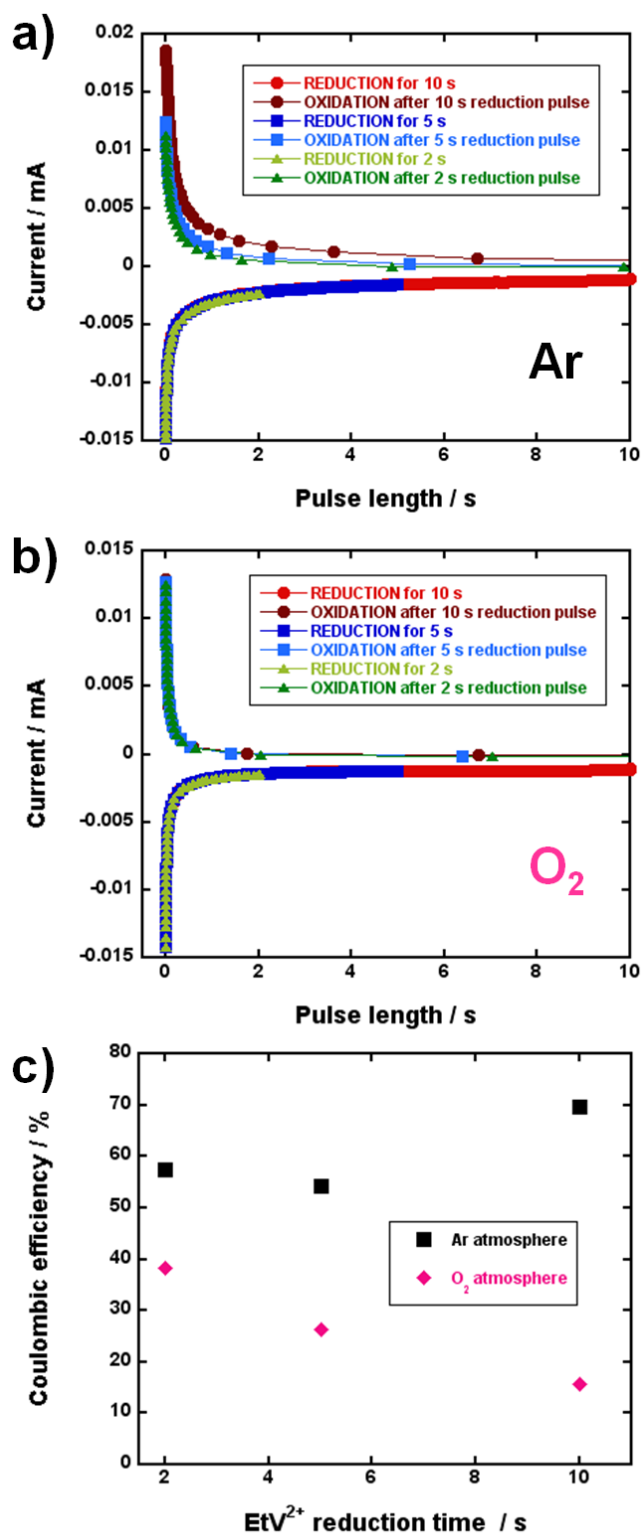**Figure 7.6.** Chronoamperometries carried out in the Na-O$_2$ U-cell using a glassy carbon working electrode at 2.4 and 2.45 V for EtV^{2+} reduction and EtV$^+$ oxidation, respectively. (a) Experiments under Ar atmosphere. (b) Experiments under O$_2$ atmosphere. (c) Coulombic efficiencies obtained in (a) and (b).

Chronoamperometry under Ar atmosphere (Figure 7.6.a) shows that the area below the charge curve was enhanced as reduction pulse at 2.4 V was extended; the longer the reduction pulse the higher EtV^+ amount produced and, consequently, the higher oxidation current. When Ar was replaced by O_2, however, charge curves seem to be overlapped obtaining similar EtV^+ oxidation currents despite the previous reduction pulses had different lengths (Figure 7.6.b). Moreover, coulombic efficiencies under Ar atmosphere remained between 50 and 70 % for all pulses while the addition of oxygen to the cell leaded to a decrease in the efficiency (Figure 7.6.c). Actually, the longer the pulse the lower the coulombic efficiency, evidencing that a higher fraction of the electrochemically generated EtV^+ was chemically oxidized back to EtV^{2+} in presence of oxygen. It was therefore demonstrated that the EtV^+ rapidly reacts in presence of O_2.

In addition, chronoamperometries at 2.4 V and Cottrell equation were used to obtain and compare the diffusion coefficients of EtV^{2+} under Ar and O_2:
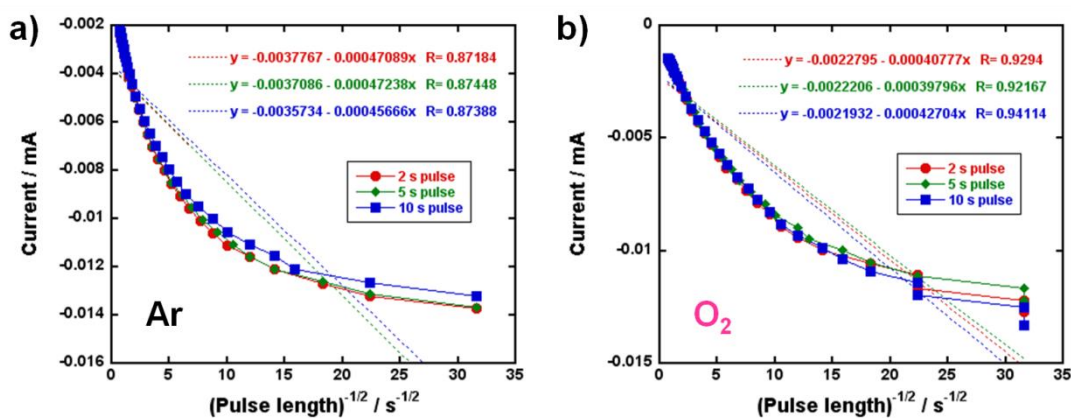
Figure 7.7. Current vs. time$^{-1/2}$ plots of the EtV^{2+} reductions carried out at 2.4 V in the Na-O_2 U-cell using a glassy carbon working electrode under (a) before and (b) after bubbling O_2 in the electrolyte.

$$i = n \cdot F \cdot A \cdot c_j^0 \cdot D_j^{1/2} \cdot \pi^{-1/2} \cdot t^{-1/2} \qquad [7.5]$$

As commented in previous chapters, F represents the Faraday constant, A the area of the electrode (0.0707 cm^{-2}), n the number of the electrodes involved in the process of

the oxidation/reduction of EtV^{2+} (1), D_j and c the diffusion coefficient and concentration (1 mM) of EtV^{2+}, respectively. It is therefore possible to calculate the diffusion coefficient of EtV^{2+} from the gradient of the curves in Figure 7.7: $(1.47 \pm 0.05) \cdot 10^{-8}$ and $(1.14 \pm 0.08) \cdot 10^{-8}$ cm^2 s^-1 before and after bubbling O_2 in the electrolyte, respectively. Thus, O_2 saturation in the electrolyte slightly decreases the diffusion coefficient of EtV^{2+} in the electrolyte, possibly leading to the IR drop observed in the CVs in Figure 7.5.

Finally, galvanostatic discharges were carried out in presence and absence of EtV^{2+} and under O_2 and Ar atmospheres in order to definitively demonstrate the favored ORR in presence of this RM (Figure 7.8). Once again the experiment was carried out in the U-cell using a glassy carbon working electrode. This type of electrode has a very low specific area and, consequently, the experiments performed at the very little current density of 20 μA cm^{-2}.
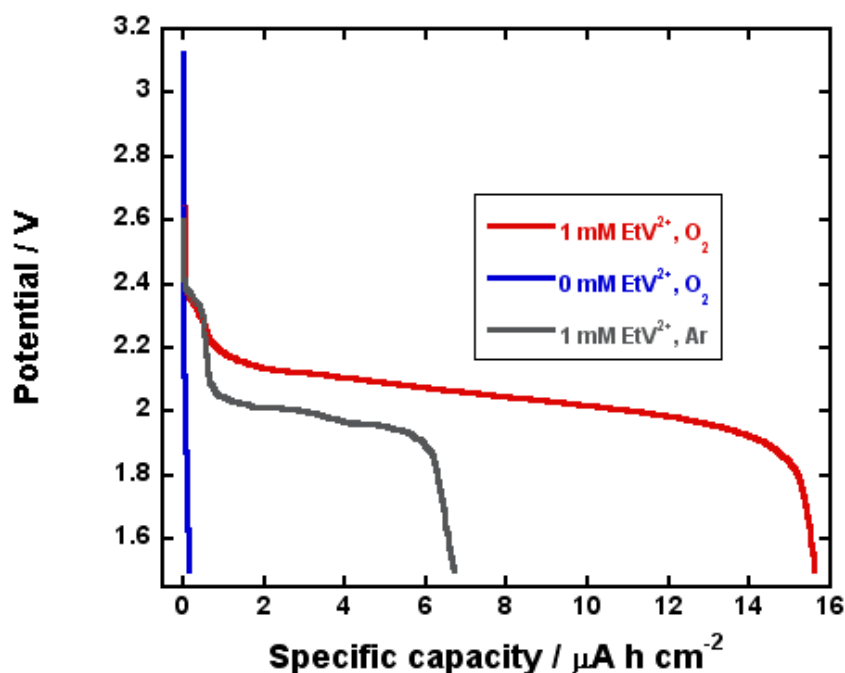

Figure 7.8. Galvanostatic discharges carried out in the Na-O_2 U-cell using a glassy carbon working electrode at 20 mA cm^{-2}. Grey and red lines were obtained in presence of 1 mM EtV^{2+} under Ar and O_2 atmospheres, respectively. Blue line was obtained in absence of EtV^{2+} under O_2 atmosphere.

Galvanostatic discharge of the EtV^{2+} containing cell under Ar atmosphere revealed the presence of two plateaus, being the second plateau (EtV^+/EtV^0 reduction plateau) longer that the first one (EtV^{2+}/EtV^+ reduction plateau). This could mean that in this second plateau both reductions took place. On the other hand, reduction in absence of the RM was insignificant and we should probably requere lower current densities to obtain a better plateau. Finally, ORR in presence of both O_2 and EtV^{2+} was enhanced showing a small initial plateau of the same capacity of the EtV^{2+}/EtV^+ reduction plateau recorded under Ar atmosphere. After that we could observe a second plateau at higher potential than that of the EtV^+/EtV^0 + EtV^{2+}/EtV^+ reductions under Ar atmosphere. In overall, the enhanced discharge capacity in presence of O_2 together with the higher rate capability and the EtV^+ elimination demonstrated by CVs and chronoamperometries unequivocally demonstrate the improvement of the ORR in presence of EtV^{2+}.

7.4. Conclusions

In this chapter the use of ethyl viologen redox shuttle in Na-O_2 batteries has been explored. As a proof of concept, reduction and oxidation of the EtV^{2+}/EtV^+ redox pair has been analyzed and quantified by UV-vis spectrometry. The reversibility of the redox pair has been demonstrated and it is worth mentioning that the oxidation of EtV^+ by the addition of O_2 has been confirmed.

The electrochemical reduction and oxidation of the EtV^{2+}/EtV^+ in a Na-O_2 has been also analyzed evidencing an improvement in the ORR in presence of the mediator. Charge following the ORR, however, is the same in presence and absence of the RM our working conditions. As a solution, it could be interesting to move to the usual Swagellok-based cells in order to give a step forward in their implementation in Na-O_2 batteries.

7.5. References

(1)   Chen, Y.; Freunberger, S. A.; Peng, Z.; Fontaine, O.; Bruce, P. G. *Nat. Chem.* **2013**, *5*, 489–494.

(2)   Bergner, B. J.; Schürmann, A.; Peppler, K.; Garsuch, A.; Janek, J. *J. Am. Chem. Soc.* **2014**, *136* (42), 15054–15064.

(3)   Sun, D.; Shen, Y.; Zhang, W.; Yu, L.; Yi, Z.; Yin, W.; Wang, D.; Huang, Y.; Wang, J.; Wang, D.; Goodenough, J. B. *J. Am. Chem. Soc.* **2014**, *136* (25), 8941–8946.

(4)   Lacey, M. J.; Frith, J. T.; Owen, J. R. *Electrochem. commun.* **2013**, *26*, 74–76.

(5)   Yang, L.; Frith, J. T.; Garcia-Araez, N.; Owen, J. R. *Chem. Commun.* **2015**, *51*, 1705–1708.

(6)   Yin, W.; Shadike, Z.; Yang, Y.; Ding, F.; Sang, L. *Chem. Commun.* **2015**, *51*, 2324–2327.

(7)   Yin, W.; Yue, J.; Cao, M.; Liu, W.; Ding, J.; Ding, F.; Sang, L.; Fu, Z. *J. Mater. Chem. A Mater. energy Sustain.* **2015**, *3*, 19027–19032.

(8)   Sawyer, D. T. *Oxygen Chemistry*; Oxford University Press, **1991**.

(9)   Bockman, M.; Kochi, J. K. *J. Org. Chem.* **1990**, *55*, 4127–4135.

(10)   Watanabe, T.; Honda, K. *J. Phys. Chem.* **1982**, *86*, 2617–2619.

(11)   Horstmann, S.; Grybat, A.; Kato, R. *J. Chem. Thermodyn.* **2004**, *36*, 1015–1018.

(12)   Calvo, E. J.; Mozhzhukhina, N. *Electrochem. commun.* **2013**, *31*, 56–58.

Chapter 8 – Summary and conclusions

In this work, the insights of Li- and Na-O_2 batteries have been analyzed and novel pathways have been provided in furtherance of improving their electrochemical processes. In Chapter 1 the state of the art of both types of batteries was analyzed in order to contextualize the experiments performed later. Moreover, the basis of the experimental techniques and methods selected were explained in detail in Chapter 2.

In Chapter 3 non-aqueous Li-O_2 system was analyzed in detail by electrochemical (galvanostatic cycles and EIS) and material characterization (XRD, SEM and XPS) techniques. It was found that oxygen solubility and diffusion are key factors limiting the electrochemical performance of Li-O_2 batteries as the electrode surface facing the O_2 gas deposit was able to accumulate more discharge product than the surface facing the separator (and consequently opposite to the O_2 deposit). Electrode/separator interface evidenced negligible activity towards ORR if the electrode was thick enough (and consequently the diffusion path of oxygen from the deposit to this surface long enough). Nevertheless, as cycling of the battery went on activity towards ORR in this interface was enhanced and, actually, thicker electrodes had a better cycling performance than thinner ones. In addition, the formation and decomposition of the discharge products was *in situ* monitored by means of EIS. A Li-O_2 cell was stopped at different stages of the galvanostatic cycle in order to follow the impedance evolution. Electrolyte/cathode interface contribution increased in resistance during the discharge of the cell as discharge products were accumulated. During charge it was initially decreased with the oxidation of Li_2O_2; at high voltages, however, a small increase in the resistance associated to the formation of solid side products was observed. EIS was therefore determined as a valuable technique to *in situ* follow the accumulation and elimination of discharge products and the formation of side products, coupled with complementary techniques capable of identifying such species.

Different strategies were followed in Chapter 4 in furtherance of improving the electrochemical performance of the Li-O$_2$ cell. The use of heterogeneous catalysts (MnO$_2$, Au and Pd) dispersed in the oxygen electrode was not traduced in an improved ORR and/or OER performance as was confirmed by means of EIS. Moreover, the galvanostatic cycles performed by the carbon-free oxygen electrodes studied (Co$_3$O$_4$, NiO and TiC) were disappointing. The addition of I$^-$ redox mediator to the electrolyte, however, leaded to an improved OER, which was traduced in an enhanced cycle life. The I$^-$/I$_3^-$ redox pair mediated in the discharge product oxidation and better efficiencies were therefore obtained. An *in situ* UV-vis Li-O$_2$ cell was built up in order to monitorize the formation and decomposition of the visible radiation absorbing I$^-$ and I$_3^-$ species. Although it was possible to follow both triiodide formation and decomposition by its reaction with oxygen, some undesired reactions such as shuttling effect and IO$^-$ side product formation were also detected. On the other hand, the addition of K$^+$ additive to the electrolyte further improved the rate capability of the Li-O$_2$ cell; TXM characterization revealed that in presence of K$^+$ the discharge products were deposited more homogeneously, suggesting a stabilization effect of the discharge products in the electrolyte promoted by these ions, based on HSAB theory. Finally, the combined effect of K$^+$ and I$^-$ resulted in an enhanced cycling performance.

In Chapter 5, the first about non-aqueous Na-O$_2$ batteries in this thesis, an exhaustive analysis of the discharge product is performed; starting from the identification of the product (NaO$_2$) to its stabilization in the electrolyte, migration vs. deposition balance and stability. Superoxide radical migration was demonstrated by means of EPR and identified as an important factor limiting the Coulombic efficiency in the first cycles; as electrolyte got saturated of superoxide the efficiency was enhanced. In addition, NaO$_2$ discharge deposit was found unstable in the cell environment as gas pressure increase together with lower charging efficiencies and lower O fraction (measured using EDX) were detected when the cell was let resting after discharge. Na$_2$CO$_3$ deposition and

discharge particles passivation were also demonstrated by QCM and EIS. This reveals the necessity of finding alternative electrolyte systems alternative to the commonly used NaOTf in DEGDME and capable of successfully storing the NaO_2 deposits.

TXM experiments were performed in Chapter 6 in furtherance of analyzing the composition and spatial distribution of the discharge products. XANES analysis of the commonly reported cubic-shaped deposits revealed a significant content of peroxide together with the predominant superoxide. Several experimental conditions were studied in order to clarify the presence of this peroxide: adding water to the electrolyte, allowing the contact of the discharge products and ambient air, exposing the cubes for prolonged time to the photon beam… however, none of these variables lead to the formation of Na_2O_2. Furthermore, the addition of water and contact with air was traduced in the reaction of the ORR products to form NaOH and Na_2CO_3, while beam exposition did not affect the chemical nature of such products. SERS experiments in Na-O_2 and electrochemical tests in Ca-O_2 batteries performed by other authors leaded us to the hypothesis of a 2 electron reduction reaction catalyzed by the Au TEM grids used for the synchrotron characterization. On the other hand, analysis spatial distribution of the products revealed that superoxide and peroxide were almost exclusively present in the cubes, while a very small fraction of side products (SPs, NaOH and/or Na_2CO_3) was homogeneously distributed through all the discharge deposits and the electrode. The SP fraction was remarkably enhanced after 5 galvanostatic cycles. Finally, 3D reconstruction of the cubes revealed the presence of a thin O-deficient ORR product layer, in good agreement with the gas rehearsal monitored in Chapter 5. Although this time the electrode was not let aging inside the cell, the use of such a powerful technique allow us to detect it from its early formation.

In Chapter 7, EtV^{2+} was studied as ORR redox mediator; in a first approach the chemical reduction and oxidation of this compound in a Na^+-based solution is demonstrated and quantified by UV-vis spectroscopy. Lithiated LTO and O_2 were used

as reduction and oxidation agents, respectively, and both reduction and oxidation were demonstrated to be reversible. After that, EtV^{2+} was added to a Na-O_2 cell and the electrochemical reduction of EtV^{2+} and its reaction with O_2 was demonstrated by chronoamperometry. Moreover, EtV^{2+} significantly increased the ORR rate capability and discharge capacity in the experiments performed in the U-cell with a glassy carbon oxygen electrode. Results using EtV^{2+} as a redox mediator can therefore be considered as promising and will be subject of a more detailed analysis in Swagelok cells in the future.

List of contributions

Publications

1. *In situ monitoring of discharge/charge processes in Li-O$_2$ batteries by electrochemical impedance spectroscopy*, Landa-Medrano, I.; Ruiz de Larramendi, I.; Ortiz-Vitoriano, N.; Pinedo, R.; Ruiz de Larramendi, J.I.; Rojo, T., Journal of Power Sources 2014, 249, 110-117.

2. *Monitoring the Location of Cathode-Reactions in Li-O$_2$ Batteries*, Landa-Medrano, I.; Pinedo, R.; Ruiz de Larramendi, I.; Ortiz-Vitoriano, N.; Rojo, T., Journal of the Electrochemical Society 2015, 162(2), 3126-3132.

3. *Operando UV-visible spectroscopy evidence of the reactions of iodide as redox mediator in Li-O$_2$ batteries*, Landa-Medrano, I.; Olivares-Marín, M.; Pinedo, R.; Ruiz de Larramendi, I.; Rojo, T.; Tonti, D., Electrochemistry Communications, 2015 59, 24-27.

4. *Carbon-free cathodes: a step forward in the development of stable lithium-oxygen batteries*, Landa-Medrano, I.; Pinedo, R.; Ortiz-Vitoriano, N.; Ruiz de Larramendi, I.; Rojo, T., Chem. Sus. Chem, 2015, 7, 1161-1166.

5. *The Sodium-Oxygen Battery: Steps Toward Reality*, Landa-Medrano, I.; Li, C.; Ortiz-Vitoriano, N.; Larramendi, I. R. de; Carrasco, J.; Rojo, T., The Journal of Physical Chemistry Letters, 2016, 7, 1161–1166.

6. *New Insights into the Instability of Discharge Products in Na−O$_2$ Batteries*, Landa-Medrano, I.; Pinedo, R.; Bi, X.; Ruiz de Larramendi, I.; Lezama, L.; Janek, J.; Amine, K.; Lu, J.; Rojo, T., ACS Applied Materials and Interfaces 2016, 8 (31), 20120–20127.

Conferences

1. *Urchin-Shaped R-MnO$_2$ Nanoparticles: A Promising Catalyst for Li-O$_2$ Batteries*, Landa-Medrano, I.; Ruiz de Larramendi, I.; Jimenez de Aberasturi, D.; Pinedo,

R.; Ortiz-Vitoriano, N; Rioja-Monllor, L.; Ruiz de Larramendi, J.I.; Rojo T., Materials Research Society (MRS) Symposium, December 2013, Boston, Massachusetts, USA (Oral)

2. *High Performance Catalyst Free Sodium-Oxygen Battery*, Pinedo, R.; Landa-Medrano, I.; Ruiz de Larramendi, I.; Ortiz-Vitoriano, N; Jimenez de Aberasturi, D.; Ruiz de Larramendi, J.I.; Rojo T., 1st Symposium on Na batteries, October 2013, Vitoria, Spain (Poster)

3. *Improved Electrochemical Performance In Na-O$_2$ Batteries By Controlling The Measurement Parameters*, Landa-Medrano, I.; Pinedo, R.; Ruiz de Larramendi, I.; Ortiz-Vitoriano, N.; Ruiz de Larramendi, J.I.; Rojo T., The 2nd International Forum on Progress and Trends in Battery and Capacitor Technologies, Vitoria, Spain (Poster)

4. *Monitoring The Location Of Cathode-Reactions In Li-O$_2$ Systems*, Landa-Medrano, I.; Pinedo, R.; Ruiz de Larramendi, I.; Ortiz-Vitoriano, N; Jimenez de Aberasturi, D.; Ruiz de Larramendi, J.I.; Rojo T., International Meeting on Lithium Batteries (IMLB), June 2014, Como, Italy (Poster)

5. *KI Homogeneous Catalyst For Li-O$_2$ Batteries*, Landa-Medrano, I.; Olivares-Marín, M.; Pinedo, R.; Ruiz de Larramendi, I.; Rojo, T.; Tonti, D., 8th International Conference on Advanced Lithium Batteries for Automobile Applications (ABAA8), September 2015, Bilbao, Spain (Poster)

6. *Stability issues in Na-O$_2$ batteries*, Landa-Medrano, I.; Lu, J.; Ruiz de Larramendi, I.; Rojo, T.; Amine, K., 2nd Metal-Air Batteries International Congress, March 2016, Santander, Spain (Oral)

Curriculum Vitae

Imanol Landa-Medrano

Date of birth: 11th of August, 1988
Gudari kalea 20, 5. eskubia
20400 Tolosa, Gipuzkoa (Spain)
Phone: 0034-661-277-028
Email: landa.imanol@gmail.com

Academic Formation

2012-2016	**B.Sc. in Chemistry**
	Universidad Nacional de Estudios a Distancia (UNED)
2011-2012	**M.Sc. in Novel Materials**
	UPV/EHU
2006-2011	**B.Sc. in Environmental Sciences**
	UPV/EHU

Work Experience

2013-2016 **PhD Student**

Project: Energy Storage Systems based on alkali-O_2

(UPV/EHU-Inorganic Chemistry)

15/03/2012- **Post-Graduate Researcher**

30/12/2012 **Project:** Materials synthesis for Li-O_2 cathalysis applications

(UPV/EHU-Inorganic Chemistry)

Stays in International Research Centers

28/08/2016- **Project:** Electrochemistry in Na-O_2 batteries

06/06/2016 *University of Southampton (UK)*

08/11/2015- **Project:** Characterization of Na-O_2 discharge products by

30/11/2015 Synchrotron based techniques.

Institut de Ciència de Materials de Barcelona (ICMAB) / Synchrotron Alba (Spain)

15/07/2015-	**Project:** Stability analyses in Na-O$_2$ batteries
15/10/2015	*Argonne National Laboratory (USA)*
01/11/2014-	**Project:** Redox Mediators in Li-O$_2$ batteries
30/12/2014	*Institut de Ciència de Materials de Barcelona (ICMAB)*

Languages

- **English:** High Level

Complementary Formation

- " Basics and applications of XPS", (2013)
- " Basics and applications of SEM", (2011)
- "Materials characterization by XRD" (2012)
- "Environmental Management in the Industry" (2011)

List of Publications

1. **New Insights into the Instability of Discharge Products in Na−O$_2$ Batteries**
   Landa-Medrano, I.; Pinedo, R.; Bi, X.; Ruiz de Larramendi, I.; Lezama, L.; Janek, J.; Amine, K.; Lu, J.; Rojo, T.
   ACS Applied Materials and Interfaces 2016, 8 (31), 20120−20127.

2. **The Sodium-Oxygen Battery: Steps Toward Reality**
   Landa-Medrano, I.; Li, C.; Ortiz-Vitoriano, N.; Ruiz de Larramendi, I.; Carrasco, J.; Rojo, T.
   The Journal of Physical Chemistry Letters, 2016, 7, 1161−1166.

3. **Carbon-free cathodes: a step forward in the development of stable lithium-oxygen batteries**
   Landa-Medrano, I.; Pinedo, R.; Ortiz-Vitoriano, N.; Ruiz de Larramendi, I.; Rojo, T.
   Chem. Sus. Chem, 2015, 7, 1161-1166.

4. **Operando UV-visible spectroscopy evidence of the reactions of iodide as redox mediator in Li-O$_2$ batteries**
   Landa-Medrano, I.; Olivares-Marín, M.; Pinedo, R.; Ruiz de Larramendi, I.; Rojo, T.; Tonti, D.
   Electrochemistry Communications, 2015 59, 24-27

5. **Monitoring the Location of Cathode-Reactions in Li-O$_2$ Batteries**
Landa-Medrano, I.; Pinedo, R.; Ruiz de Larramendi, I.; Ortiz-Vitoriano, N.; Rojo, T.
Journal of the Electrochemical Society 2015, 162(2), 3126-3132.

6. **In situ monitoring of discharge/charge processes in Li-O$_2$ batteries by electrochemical impedance spectroscopy**
Landa-Medrano, I.; Ruiz de Larramendi, I.; Ortiz-Vitoriano, N.; Pinedo, R.; Ruiz de Larramendi, J.I.; Rojo, T.
Journal of Power Sources 2014, 249, 110-117.

Conferences

- **Urchin-Shaped R-MnO$_2$ Nanoparticles: A Promising Catalyst for Li-O$_2$ Batteries**
Landa-Medrano, I.; Ruiz de Larramendi, I.; Jimenez de Aberasturi, D.; Pinedo, R.; Ortiz-Vitoriano, N; Rioja-Monllor, L.; Ruiz de Larramendi, J.I.; Rojo T., Materials Research Society (MRS) Symposium, December 2013, Boston, Massachusetts, USA (Oral)

- **High Performance Catalyst Free Sodium-Oxygen Battery**
Pinedo, R.; *Landa-Medrano, I.*; Ruiz de Larramendi, I.; Ortiz-Vitoriano, N; Jimenez de Aberasturi, D.; Ruiz de Larramendi, J.I.; Rojo T., 1st Symposium on Na batteries, October 2013, Vitoria, Spain (Poster)

- **Improved Electrochemical Performance In Na-O2 Batteries By Controlling The Measurement Parameters**
Landa-Medrano, I.; Pinedo, R.; Ruiz de Larramendi, I.; Ortiz-Vitoriano, N.; Ruiz de Larramendi, J.I.; Rojo T., The 2nd International Forum on Progress and Trends in Battery and Capacitor Technologies, Vitoria, Spain (Poster)

- **Monitoring The Location Of Cathode-Reactions In Li-O$_2$ Systems**
Landa-Medrano, I.; Pinedo, R.; Ruiz de Larramendi, I.; Ortiz-Vitoriano, N; Jimenez de Aberasturi, D.; Ruiz de Larramendi, J.I.; Rojo T., International Meeting on Lithium Batteries (IMLB), June 2014, Como, Italy (Poster)

- **KI Homogeneous Catalyst For Li-O$_2$ Batteries**
Landa-Medrano, I.; Olivares-Marín, M.; Pinedo, R.; Ruiz de Larramendi, I.; Rojo, T.; Tonti, D., 8th International Conference on Advanced Lithium Batteries for Automobile Applications (ABAA8), September 2015, Bilbao, Spain (Poster)

- **Stability issues in Na-O2 batteries**
Landa-Medrano, I.; Lu, J.; Ruiz de Larramendi, I.; Rojo, T.; Amine, K., 2nd Metal-Air Batteries International Congress, March 2016, Santander, Spain (Oral)

- **Characterization of Na-O$_2$ discharge products by Synchrotron X-ray Transmission Microscopy**

Landa-Medrano, I.; Sorrentino, A.; Ruiz de Larramendi, I.; Pereiro, E.; Rojo, T.; Tonti, D., 3rd International Conference on Sodium Batteries, December 2016, Geelong, Australia (Poster) (*Accepted*)